UNIVERSIDADE FEDERAL DE MINAS GERAIS
Escola de Engenharia
Departamento de Engenharia Elétrica

Abraão Regis Guia

An Overview of a Silicon Carbide In-Wheel Converter for Automotive Application

Belo Horizonte

August 2022

Abraão Regis Guia

An Overview of a Silicon Carbide In-Wheel Converter for Automotive Application

Thesis submitted to the examining board of the Graduate Program in Electrical Engineering at the Universidade Federal de Minas Gerais, as part of the requirements for obtaining the Master's degree in Electrical Engineering.

Advisor: Prof. Thales Alexandre Carvalho Maia

Belo Horizonte

August 2022

Guia, Abraão Regis.
G943d An overview of a silicon carbide in-wheel converter for automotive application [recurso eletrônico] / Abraão Regis Guia. - 2022.
1 recurso online (214 f. : il., color.) : pdf.

Orientador: Thales Alexandre Carvalho Maia.

Dissertação (mestrado) - Universidade Federal de Minas Gerais, Escola de Engenharia.

Apêndices: f. 193-214.
Bibliografia: f.181-192
Exigências do sistema: Adobe Acrobat Reader.

1. Engenharia Elétrica - Teses. 2. Veículos elétricos – Teses. 3. Conversores de corrente elétrica – Teses. 4. Carbeto de silício – Teses. I. Maia, Thales Alexandre Carvalho. II. Universidade Federal de Minas Gerais. Escola de Engenharia. III. Título.

CDU: 621.3(043)

Ficha catalográfica elaborada pela Bibliotecária Letícia Alves Vieira - CRB-6/2337
Biblioteca Prof. Mário Werneck - Escola de Engenharia da UFMG

UNIVERSIDADE FEDERAL DE MINAS GERAIS
ESCOLA DE ENGENHARIA
PROGRAMA DE PÓS-GRADUAÇÃO EM ENGENHARIA ELÉTRICA

FOLHA DE APROVAÇÃO

"AN OVERVIEW OF A SILICON CARBIDE IN-WHEEL CONVERTER FOR AUTOMOTIVE APPLICATION"

ABRAÃO REGIS GUIA

Dissertação de Mestrado submetida à Banca Examinadora designada pelo Colegiado do Programa de Pós-Graduação em Engenharia Elétrica da Escola de Engenharia da Universidade Federal de Minas Gerais, como requisito para obtenção do grau de Mestre em Engenharia Elétrica. Aprovada em 16 de agosto de 2022. Por:

Prof. Dr. Thales Alexandre Carvalho Maia
DEE (UFMG) - Orientador

Prof. Dr. Braz de Jesus Cardoso Filho
DEE (UFMG)

Prof. Dr. Tomas Perpetuo Correa
DELT (UFMG)

Prof. Dr. Menaouar Berrehil El Kattel
DEE (UFC)

Documento assinado eletronicamente por **Thales Alexandre Carvalho Maia**, **Professor do Magistério Superior**, em 18/08/2022, às 18:30, conforme horário oficial de Brasília, com fundamento no art. 5º do Decreto nº 10.543, de 13 de novembro de 2020.

A autenticidade deste documento pode ser conferida no site https://sei.ufmg.br/sei/controlador_externo.php?acao=documento_conferir&id_orgao_acesso_externo=0, informando o código verificador **1662002** e o código CRC **B5B59528**.

" Beware that you do not forget the Lord your God by not keeping His commandments, His judgments, and His statutes which I command you today,

lest—when you have eaten and are full, and have built beautiful houses and dwell in them

and when your herds and your flocks multiply, and your silver and your gold are multiplied, and all that you have is multiplied

when your heart is lifted up, and you forget the Lord your God who brought you out of the land of Egypt, from the house of bondage

who led you through that great and terrible wilderness, in which were fiery serpents and scorpions and thirsty land where there was no water; who brought water for you out of the flinty rock

who fed you in the wilderness with manna, which your fathers did not know, that He might humble you and that He might test you, to do you good in the end

then you say in your heart, 'My power and the might of my hand have gained me this wealth.'

And you shall remember the Lord your God, for it is He who gives you power to get wealth, that He may establish His covenant which He swore to your fathers, as it is this day. "

(Holy Bible, Deuteronomy 8:11-18)

Acknowledgements

I thank the only God and His son Jesus for His sacrifice. He who comforted and guided me through the desert and to whom I owe my heart of flesh and all that I have here and hereafter: that "is not corrupted".

To my father Anibal, who was so dedicated to his family. May you know that I will not forget the endless years you drove us to school and waited (often in the car) until we left, to bring us back home. I would like to have more Star Wars days, laying down in the mattress in the hallway.

To my mother Ester, for the heart in my chest and emotional health. I admire your affection and strength too much and I miss the afternoons walking to Minas Shopping.

To my grandma Bertha, for being my greatest example of life. Only God knows how I would like to be half of what you are, always helping so many people and giving an example of what it is to follow Jesus.

To my sister Hadassa, for being my best friend. For sharing her heart, her jokes, and her pains with me.

To my brother Caleb, preferably called Diplodocus, Predalien or Batman, for the brief and intense friendship. Now I have a cat named Tesoura -but we call her Titi-, and still not a day goes by without the pain of missing you. The wait to meet and hold you again is sickening. May God make us better people, Caebinho, to reduce all this suffering that exists in the world.

To my supervisor Thales. His goal of transforming Brazil is inspiring. I continue to be amazed by his early morning answers. I can state without a doubt that I received real guidance. Thank you for your impact on my knowledge, career and research, and the understanding of my limitations.

To my other family members and friends who really supported me. I wish I had room to name so many more, but I will paraphrase my mother: "feel embraced!"

"Except the Lord build the house, they labour in vain that build it: except the Lord keep the city, the watchman waketh but in vain. It is vain for you to rise up early, to sit up late, to eat the bread of sorrows: for so he giveth his beloved sleep."

(Holy Bible, Psalm 127:1-2)

Resumo

A propulsão elétrica têm sido uma resposta mundial à necessidade de transportes mais eficientes e com baixo índice de emissões. Neste trabalho é projetado um conversor trifásico alocado dentro das rodas (in-wheel) com utilização de carbeto de silício, para aplicação automotiva. A proposta de incorporar o sistema trativo à roda agrega diversas vantagens, incluindo flexibilidade de controle, melhoras na dinâmica veicular e aumento de eficiência. Adicionar o conversor ao sistema in-wheel libera ainda mais espaço interno no veículo, auxiliando também o desenvolvimento de sistemas de tração híbrida. A solução de chaveamento em carbeto de silício se encaixa bem à proposta in-wheel, aumentando a eficiência e reduzindo o volume e peso do sistema. A programação do firmware é realizada em micropython, com o objetivo de estudo do seu desempenho e de acelerar a prototipagem de conversores na indústria e academia.

Palavras-chave: Veículos elétricos, Motor nas rodas, Conversor de potência, Micropython, Carbeto de Silício.

Abstract

Electric propulsion has been a worldwide response to the need for more efficient and low-emission transport. In this work, a three-phase in-wheel converter using silicon carbide is designed for automotive application. The proposal to incorporate the traction system to the wheel adds several advantages, including control flexibility, improvements in vehicle dynamics and increased efficiency. Adding the converter to the in-wheel system frees up even more space inside the vehicle, also aiding the development of hybrid powertrain systems. The silicon carbide switching solution fits well with the in-wheel proposal, increasing efficiency and reducing the volume and weight of the system. Firmware programming is carried out in micropython, with the aim of studying its performance and accelerating the prototyping of converters in academia and industry.

Keywords: Electric vehicles, In-wheel motor, Power converter, Micropython, Silicon carbide.

List of Figures

List of Tables

List of abbreviations and acronyms

4WD	Four Wheel Drive
ABS	Anti-lock Brake System
AC	Alternating Current
AFPM	Axial Flux Permanent Magnet
ASQ	American Society for Quality
AWD	All Wheel Drive
BEV	Battery Electric Vehicle
BJT	Bipolar Junction Transistor
BMS	Battery Management System
BVSC	Bidirectional Voltage Source Converter
CAN	Controller Area Network
CMTI	Common-Mode Transient Immunity
CMV	Common-Mode Voltage
CSI	Current Source Inverter
DC	Direct Current
DSP	Digital Signal Processor
EAQF	*D'Evaluation D'Aptitude Qualite Fournisseurs*
EMF	Electromotive Force
EMI	Electromagnetic Interference
ESC	Electronic Stability Control
EV	Electric Vehicle
FCEV	Full Cell Electric Vehicle
FEMM	Finite Element Method Magnetics

FET	Field Effect Transistor
FHEV	Full Hybrid Electric Vehicle
FOC	Field Oriented Control
FPGA	Field Programmable Gate Array
FSPMSM	Fractional slot permanent magnet synchronous machines
H2-ICEV	Hydrogen Internal Combustion Engine Vehicle
HEV	Hybrid Electric Vehicle
HV	High Voltage
KPI	Kingpin Inclination
IATF	International Automotive Task Force
IBM	In-Board Motor
IC	Integrated Circuit
ICE	Internal Combustion Engine
ICEV	Internal Combustion Engine Vehicle
IGBT	Insulated Gate Bipolar Transistor
IM	Induction Machine
ISO	International Organization for Standardization
IWM	In-Wheel Motor
JVM	Java Virtual Machine
LV	Low Voltage
mHEV	Mild Hybrid Electric Vehicle
MOSFET	Metal Oxide Semiconductor Field Effect Transistor
MTPA	Maximum Torque per Ampere
NDA	Non Disclosure Agreement
PCB	Printed Circuit Board
PMSM	Permanent Magnet Synchronous Machine

PI	Proportional-Integral
PHEV	Plug-in Hybrid Electric Vehicle
PMSM	Permanent Magnet Synchronous Machine
PWM	Pulse Width Modulation
R&D	Research and Development
RMS	Root mean square
RTOS	Real-Time Operating System
SiC	Silicon Carbide
SPI	Serial Peripheral Interface
SPWM	Sinusoidal Pulse Width Modulation
SVPWM	Space Vector Pulse Width Modulation
TCS	Traction Control System
TIM	Thermal Interface Material
UFMG	*Universidade Federal de Minas Gerais*
VDA	*Verband der Automobilindustrie*
VSI	Voltage Source Inverter
WBGS	Wide Band Gap Semiconductor
ZSI	Z-source Inverter

List of symbols

a_{pcb}	Transversal area of PCB traces (m²)
b	Motor damping coefficient (Ns/m)
C_{bus}	DC bus total capacitance (F)
$C_{bus,self}$	DC bus capacitor capacitance (F)
$C_{parallel}$	Number of parallel capacitors in DC bus
C_{series}	Number of series capacitors in DC bus
$C_{th,j}$	Junction thermal capacitance (J/K)
$C_{th,tim}$	TIM thermal capacitance (J/K)
$C_{th,s}$	Heat sink thermal capacitance (J/K)
d_c	Duty cycle (%)
e_{pcb}	PCB trace thickness (m)
f_{el}	Machine's electrical frequency (Hz)
$f_{el,max}$	Machine's maximum electrical frequency (Hz)
f_{sw}	Switching frequency (Hz)
$f_{sw,min}$	Minimum switching frequency (Hz)
f_{mod}	Modulating frequency (Hz)
i	Instantaneous current (A)
$\hat{I}_g$	Peak gate current (A)
I_{in}	Inverter input current (A)
$I_{in,rip}$	Inverter input ripple current (A)
$I_{in,rip,rms}$	Inverter input RMS ripple current (A)
I_{bar}	Bus-to-Switches bus bar RMS current (A)
$I_{sw,max,cap}$	Capacitor maximum switched current (A)

J	Motor inertia (kg*m²)
L	Inductance (H)
L_{bus}	DC bus total inductance (H)
$L_{bus,self}$	DC bus capacitor self inductance (H)
L_d	Direct-axle inductance (H)
l_{pcb}	PCB traces length (m)
L_{pcb}	PCB traces inductance (H)
L_{bar}	Bus-to-Switches bus bar inductance (H)
L_s	Synchronous inductance (H)
L_q	Quadrature-axle inductance (H)
m_a	Modulation index
$n_{m,max}$	Maximum motor speed (RPM)
$n_{m,nom}$	Nominal motor speed (RPM)
n_{par}	Number of parallel power switches
P	Power (W)
P_{max}	Maximum converter power (W)
$P_{m,max}$	Maximum motor power (W)
P_{bar}	Bus-to-Switches bus bar power loss (V)
Q	Charge (C)
Q_g	Total gate charge (C)
R	Resistance (Ω)
R_a	Phase resistance (Ω)
R_{bus}	DC bus total resistance (Ω)
$R_{bus,self}$	DC bus capacitor resistance (Ω)
r_{din}	Dynamic tire radius (m)
R_{disc}	DC bus discharge resistance (V)

$R_{g,ext,off}$	External gate resistance for off state (Ω)
$R_{g,ext,on}$	External gate resistance for on state (Ω)
$R_{g,gd,off}$	Internal gate driver resistance for off state (Ω)
$R_{g,gd,on}$	Internal gate driver resistance for on state (Ω)
$R_{g,int}$	Internal MOSFET gate resistance (Ω)
$R_{g,off}$	Equivalent gate resistance for off state (Ω)
$R_{g,on}$	Equivalent gate resistance for on state (Ω)
R_{pcb}	PCB trace resistance (Ω)
R_{bar}	Bus-to-Switches bus bar resistance (Ω)
$R_{th,c-s}$	Case to heat sink thermal resistance (K/W)
$R_{th,cap}$	Capacitor thermal resistance (K/W)
$R_{th,j-c}$	Junction to case thermal resistance (K/W)
$R_{th,s-ext}$	Heat sink to exterior thermal resistance (K/W)
s_{pcb}	Mean separation of PCB traces (m)
S_x	Switching function
t	Time (s)
$T_{c,cap}$	Capacitor case temperature (ºC)
t_{dead}	Switching deadtime (s)
t_{disc}	DC bus discharge time (s)
$T_{j,max}$	Maximum junction temperature (ºC)
T_m	Motor torque (Nm)
t_{off}	Switch turn-off time (s)
t_{on}	Switch turn-on time (s)
T_{bar}	Bus-to-Switches bus bar temperature (ºC)
$T_{bar,ref}$	Reference Bus-to-Switches bus bar temperature (ºC)
T_{sw}	Switching period (s)

V	Voltage (V)
V_{ab}	Line voltage (V)
V_{ao}	Converter output voltage of phase A (V)
V_{an}	Phase A voltage (V)
$V_{bus,max}$	DC bus voltage limit (V)
$V_{bus,mean}$	Average DC bus voltage (V)
$V_{C,bus}$	Voltage ripple due to integral of inverter input current (V)
V_{dc}	DC bus voltage (V)
$V_{dc,disc}$	Discharged DC bus voltage (V)
$V_{gs,off}$	Gate-source voltage for off state (V)
$V_{gs,on}$	Gate-source voltage for on state (V)
$V_{in,max}$	Power switches voltage limit (V)
$V_{line,RMS}$	Line RMS voltage (V)
$V_{L,bus}$	Voltage ripple due to inverter input current in $Lbus$ (V)
$V_{L,bar}$	Voltage ripple due to inverter input current in $Lbar$ (V)
V_{bar}	Bus-to-Switches bus bar voltage drop (V)
$V_{R,bus}$	Voltage ripple due to inverter input current in $Rbus$ (V)
$V_{R,bar}$	Voltage ripple due to inverter input current in $Rbar$ (V)
v_{max}	Maximum vehicle speed (km/h)
V_{no}	Voltage between neutral and midpoint of the busbar (V)
$V_{xo,samp}$	Converter sampled output phase voltage (V)
w_{pcb}	PCB trace width (m)
t_r	Rise time of the power switches drain current (s)
ΔT_{bar}	Bus-to-Switches bus bar temperature rise (ºC)
δ_t	Phase pulse duration (s)
α	Resistance temperature coefficient

$\eta_{m,nom}$	Rated motor efficiency
μ	Adhesion coefficient road-tire
$\rho_{pcb,ref}$	PCB conductor resistivity in reference temperature (Ωm)
$\rho_{bar,ref}$	Bus-to-Switches bus bar conductor resistivity in reference temperature (Ωm)
ω	Rotational speed (rad/s)

Contents

1 Introduction

As we enter the third decade of the 21st century, quite some statistics show that traffic solutions for mobility are undergoing a revolution. This movement is mostly strengthened by environmental and sustainable arguments, to the detriment of non-renewable, gas-emitting solutions.

Among the main possibilities for vehicular traction without fossil fuels are ICEVs (Internal Combustion Engine Vehicles) with biofuels, H2-ICEVs (Hydrogen Internal Combustion Engine Vehicles), FCEVs (Fuel Cell Electric Vehicle) and BEVs (Battery Electric Vehicle). A relevant topic in the automotive industry is the debate between which is the best option to reduce pollutant emissions: biofuels, hydrogen solutions or electric traction.

Even though it is a global trend, Brazil is still somewhat reluctant to transform the traction technology, with its development focused more on biofuels technologies, the country's technological highlight (BLAND, 2022). Despite this, political initiatives are found in the sense of encouraging the beginning of the transition out of fossil fuels, such as the Rota2030 (FUNDEP, 2021) and similar programs, which bring investments both for electrification and for the biofuels sector.

The scope of this work involves the specific development of one of the main components of an electric traction system: the Traction Converter. A series of discussions are presented related to the design methodology, seeking to increasing the effectiveness and efficiency of the system and to popularize this technology. However, before delving into the technicalities of this system, it is important to present the global context that surrounds and justifies this work. The development of technology with environmental objectives demonstrates how engineering solutions can help society in highly relevant issues for its well-being.

1.1 Alternatives to fossil fuels

Seeking for alternative transport technologies to fossil fuels is a global trend motivated basically by two central issues: maintenance of the population's health and quality of life, and maintenance of the environment in general.

Regarding the health and quality of life, the issue is mainly evaluated in relation to air pollution, and to a lesser extent noise pollution. According to EPA-USA (2020), the transportation sector is responsible for 27% of 2020 greenhouse gas emissions, being the sector that generates the largest share of greenhouse gas emissions. The effects on the population's health are disastrous. Nationally, Rodrigues et al. (2015) study indicated that in the State of São Paulo, Brazil, a decrease in pollution of around 5% in a period of 15 years would lead to a reduction

of 10,777 deaths, 1,021 hospital admissions and savings of more than R$40 million in public hospitalizations for young people, demonstrating the acute criticality of air pollution. Chinese studies have shown that the impacts go beyond that, and chemicals from traffic exhaust, such as lead, CO and NO_2, can affect neurobehavioral functions mainly in children, due to their fast growth stage (YE; FU; GUIDOTTI, 2007). Air polution can also be critical to the neurobehavior of adults who have been occupationally exposed to traffic exhaust (LIU et al., 2001). Wang et al. (2009) further explored this association, showing that participants living in air polluted areas performed poorer on all neurobehavioral function tests made.

Regarding the environment in general, the issue is much more complex, since the impacts are multivariable, from the extraction of raw materials and energy generation, to the disposal and eventual recycling of components. According to the (DOE-USA, 2021), highway vehicles release about 1.7 billion tons (1.5 billion metric tons) of greenhouse gases into the atmosphere each year, mostly in the form of carbon dioxide (CO_2), contributing to global climate change. As that the impacts of pollution generated by fossil fuels traction are considerable, it remains to be evaluated how the other main solutions impact the environment. The objective is to bring, in a concise way, which factors can impact the decision for one or another of these technologies.

Biofuels are a potential direct solution for helping the environment. Zah et al. (2007) sought to analyze this issue in a more wholesome way, evaluating the entire life-cycle for 26 different biofuels. The harming impacts of each biofuel were determined utilizing two distinct criteria: greenhouse-gas emissions relative to gasoline, and overall environmental impact, including damage to human health and ecosystems and natural resource depletion. The authors found that almost 50% of the biofuels have more prominent ecological expenses than petroleum. However, when it comes to greenhouse emissions, 21 out of 26 biofuels present a reduction of 30% compared with fossil fuels. Biodiesel made from waste cooking oil and methanol and methane derived from wood, presented the greatest emissions reductions, above 50%. These fuels, plus bioethanol made from whey, also performed very well when taking into account their full environmental impact. On the other hand, biodiesel made from Brazilian soy, and bioethanol made from potatoes, rye and soy, presented the worst environmental friendly performance: they had low reductions in greenhouse gas emissions and high negative environmental impact.

For the hydrogen based alternatives to fossil fuels, H2-ICEV and FCEVs are the main ones. The difference between the two is that the first will use hydrogen for combustion and direct propulsion in an ICE, while the second will use hydrogen to power a fuel cell, and through it generate electrical energy to recharge the electric traction vehicle. F-S, J-M et al. (2009) developed a study analyzing the environmental impacts of these solutions, concluding that the FCEV has greater efficiency, being more eco-friendly than the H2-ICEV. In his analysis, he considered the production, logistics and use of hydrogen, and the impact of the solution on noise pollution, greenhouse gases impact on air quality, human health and potential global warming. Even with all the considerations made, it is not so straightforward to assert hydrogen comparative

environmental impact to fossil fuels or electric vehicles. One of the factors that makes this analysis more complex is that, like electricity, hydrogen has to be produced from primary energy sources such as fossil fuels, nuclear or renewable energy. These different production methods, combined with different storage and transport methods, result in a wide range of energy uses and environmental impacts.

BEVs are a widely used alternative to fossil fuels worldwide. While their operation does not emit pollutant gases, the electrical power generation, their manufacturing and disposal have considerable and multiple impacts. The only way to not base this issue on opinions is to present a comprehensive evaluation of the entire life cycle of the vehicle, and a well-to-wheel analyzes, including variables related to the energy matrix and kilometers driven. Helms et al. (2010) proposed this analysis, and indicated that a BEV using the German electric matrix at the time, with 120 thousand kilometers driven, ended up emitting slightly more pollutant gases than a diesel vehicle, and little less than a gasoline vehicle, see Figure 1. Since the environmental advantages of BEVs exist mainly in their operating phase, the positive impacts will weight more based on the kilometers they run. Likewise, it is clear that their impact is enhanced by the transition to a cleaner energy matrix.

Figure 1 – Emissions of pollutant gases in the life cycle of a compact vehicle with varied drivetrains (120'000km ; cycle 70% urban)

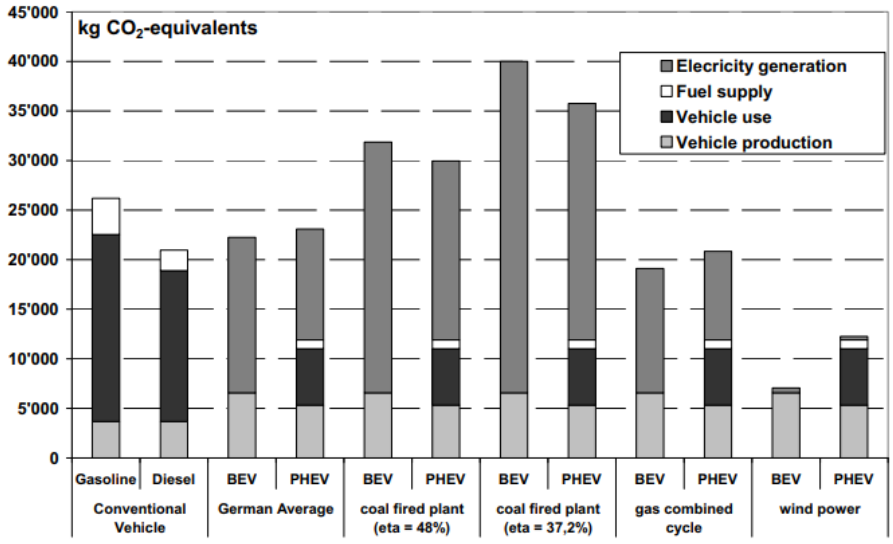

In short, as explained in this section, deciding which are the best solutions to reduce environmental impact is a non-trivial task, which depends on a series of variables, such as mineral extraction, hydrogen production, electricity generation matrix, disposal and eventual recycling of materials, among other factors. Among the four major solutions proposed, the technology developed in this work is applied in two, namely FCEVs and BEVs, remaining relevant for different applications with potential sustainable impact.

Concerning hybrid combustion-electric solutions, such as mHEVs (Mild Hybrid Electric Vehicle), FHEVs (Full Hybrid Electric Vehicle) and PHEVs (Plug-in Hybrid Electric Vehicle),

this work also has an interesting highlight, since in these cases the electric powertrain needs to compete for space with the ICE (Internal Combustion Engine). Bringing components to the wheel of vehicles avoids this volume competition with the ICE, which can facilitate hybridization.

This work now proceeds to more specific issues, namely providing the context of BEVs themselves, until later reaching the traction converter.

1.2 Electric Vehicles

It is difficult to point out a historical beginning for BEVs, because it relates to a series of disruptive developments, mainly concerning batteries and electric motors, present in the late 18th century, early 19th century. Hungarian, Dutch, Scottish and American researchers began to develop BEVs, but prototypes only became more feasible in the second half of the 19th century (DOE-USA, 2014).

Rechargeable batteries only came on the market due to the invention in 1859 of the lead-acid battery, by the French physicist Gaston Planté (KURZWEIL, 2010), industrially commercialized from 1881. This year also marked the possible first manned BEV, a tricycle invented by Gustave Trouvé's (WAKEFIELD, 1998). It outlined a future in making electric vehicles feasible for general consumer applications.

But instead of BEVs, a boom in combustion vehicles happened with the expansion and optimization of the US road network in the early 20th century, a history also marked by the launch in 1908 of the Ford Motor Company's Model T. The ICEV's proved to be cheaper and with better autonomy, making longer trips and broad access to vehicles possible.

1.2.1 Electric mobility market

Since the ICEVs takeover of the market in the early 20th century, fossil fuel-based traction has reigned supreme and somewhat unchallenged. In 2022, more than 110 years after the first major Fordist impact, it can be seen that the re-electrification of mobility, once a distant promise, has begun to transcend the character of a trend and is shaping up as a major market power.

Governments around the world have implemented regulations on carbon dioxide emissions and plans for the gradual increase of these restrictions. The effect on car manufacturers was considerable, generating a great search for technical solutions that increase powertrain efficiency, impacting the presence of hybrid-electric-fuel and pure electric topologies in the market (IEA, 2021b).

Even with the global 2020 drop of 16% in automotive vehicle sales, influenced by the impacts of the COVID-19 pandemic, EV registrations showed global growth of 41% in the same year (IEA, 2021a).

The world's prominent markets remain China, Europe and the United States, with a historical dominance of the asian giant, with around 45% of the world fleet. But the year 2020 surprised the world, presenting for the first time more European (1.4 million) than Chinese (1.2 million) new registrations (IEA, 2021a).

Other critical indications regarding this issue are corporate plans to increase sales of BEVs and even stop production of ICEVs. Announcements from automakers are presented in Figure 2. This data strongly support that the market is betting considerably on the electrification of mobility, but it is important to point out again that this movement has a significant political influence, as will be discussed below.

Figure 2 – Carmaker announcements related to small electric vehicles (light-duty vehicles) (IEA, 2021a)

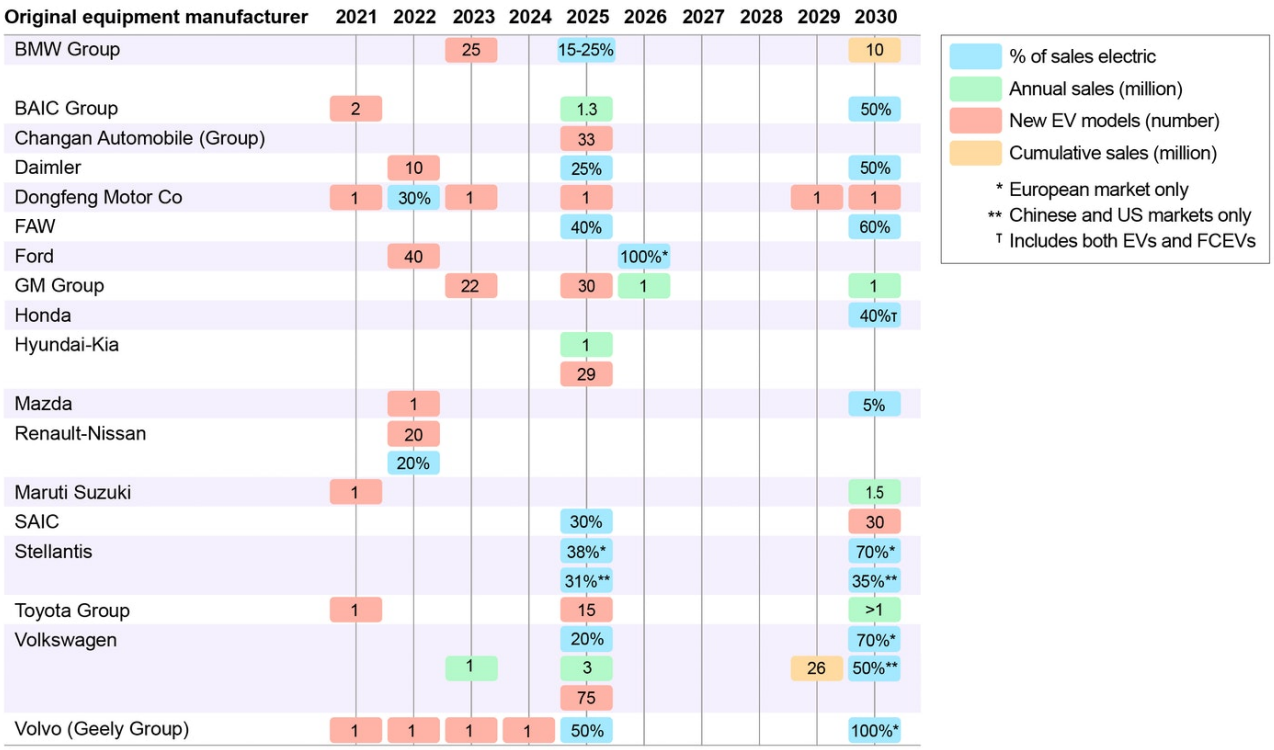

1.2.2 Political influence on electric mobility

Even though in recent decades the environmental impact factor has grown in relevance in the consumer decision to purchase a vehicle, it is still one of the most expensive common goods of human life, making its cost often still a critical and decisive factor. This effect is even more pronounced in second and third world countries.

In the cost department, despite the good reputation of electric vehicles with regard to their environmental impact, historically there has been a need for political input to the cause,

in the form of subsidies for BEVs and HEVs and restrictions on ICEVs. Figure 3 presents the countries plans related to encouraging the transition to electric mobility.

Figure 3 – Country plans regarding electrification, banning ICEVs and net-zero emissions (IEA, 2021a)

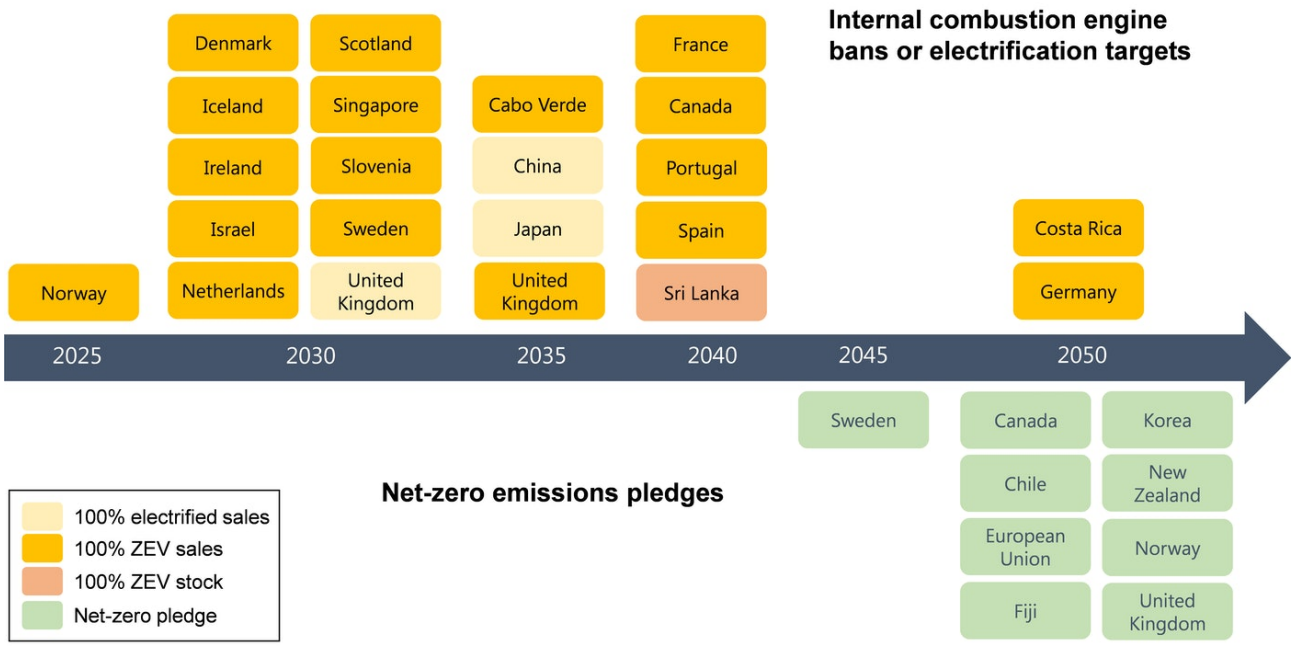

If in one hand all this movement is seen by some as an environmental investment, it has also configured itself as a historical reason for criticism of the growth of electric mobility, with the argument that it is an artificial and mostly political event, not coming directly from market and consumer interests.

While the scope of this work does not propose to delve deeper into this issue, it is also important to note the national political situation regarding electric mobility. The advancement of these political decisions at the national level is complicated, since Brazil is a country with considerable oil capacity and high proficiency in the manufacture of biofuels. No bill has succeeded in planning a complete ban on ICEVs, with bills that only gradually ban fossil fuels, maintaining the use of biofuels, still in progress of approval. Some examples include Bill PLS 304/2017, Bill 3339/2019 and Senate Bill 454/2017.

Having presented the macro environmental, market and political context in which this work is inserted, and that justifies the relevance of the development and improvement of the technology involved, a technical explanation of the powertrain that contains the traction converter is presented below.

1.2.3 Electric powertrain system

A simplified diagram of the electric powertrain is shown in Figure 4. A vehicle topology discussion can be found in Appendix A.

Figure 4 – Electric powertrain system for a BEV. From left to right: accumulator, inverter, motor, reduction, differential

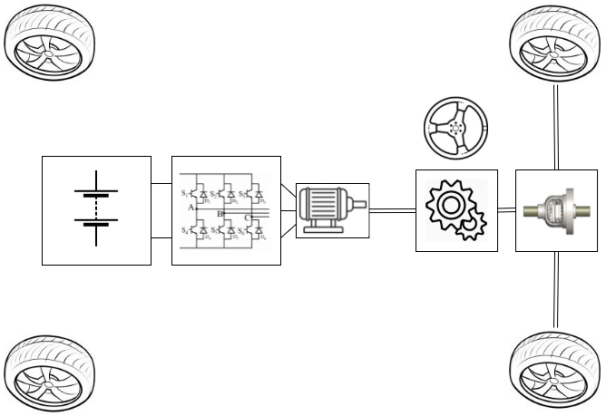

According to Chan et al. (2001), the accumulator, traction converter and the electric motor are the 3 main components of what the author calls the first generation of BEVs. The second generation brings the inclusion of energy management systems, which were not presented in this diagram for the sake of visual simplification.

- Accumulator: energy storage system, usually composed of batteries, supercapacitors, or a combination of both;
- Traction converter: DC to AC conversion, and in case of a bidirectional converter, it also performs AC to DC conversion. Responsible for controlling the powertrain. Commonly known as inverter;
- Electrical machine: conversion system between electrical and mechanical energy. Commonly referred to as electric motor

If the converter is bidirectional, the energy flow can occur either in the direction of vehicle traction or in the opposite direction, an event known as regenerative braking. The amount of energy that can be recovered in this process varies considerably, depending on the accumulator sizing, the driver's braking behavior and the powertrain efficiency. McIntosh (2021) points out variations between 16 to 70 percent of regeneration. One of the causes of this wide range of values is the battery's charge current capacity, which limits energy recovery under braking, so that light braking tends to recover more energy.

In automotive applications, powertrain efficiency, mass and volume are particularly relevant, since all these factors affect the sizing of the accumulator. A more efficient powertrain

can maintain the vehicle's autonomy, with less battery/supercapacitor energy, reducing the cost and size of the accumulator, and consequently the environmental impact.

Vehicle mass reductions also exhibit these trends. Any solution to reduce volume and mass such as to remove the gearbox from the vehicle, in addition to reducing the amount of batteries needed, reduces the need for other raw materials, which also tends to reduce final costs and environmental impact.

It is interesting to note how to a certain extent these effects have a certain positive feedback characteristic, that is, again, to a certain extent, the more volume and mass you remove from a vehicle, the less volume and mass it needs to have (due to powertrain downsizing).

Vehicle performance is also affected by powertrain topology decisions. Again, in order not to lose focus on the scope of this work, a more in-depth discussion of powertrain topologies is presented in Appendix A.

Keeping these factors in mind, a powertrain solution with the potential to prove itself relevant is the in-wheel drive. Without the need for a transmission, the solution tends to increase powertrain efficiency. Moreover, inserting components inside the wheel frees up space inside the vehicle itself, so it also tends to a reduction in the overall size and mass of the vehicle.

Finally, in the topology proposed in this work the inverters are attached to the motors, and the entire assembly is inserted into the wheels, see Figure 5.

Figure 5 – Topology of this work: BEV with AWD-IWM (all wheel drive, in-wheel motor) motorization and in-wheel inverters.

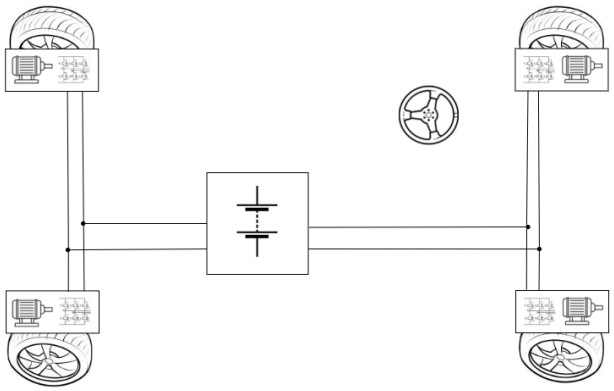

The converter integration to the in-wheel electric machine, provides the following advantages when compared to on-board converters:

- Reducing the length of the electrical connection between inverter and motor;
- Reduction of Joule losses in the electrical connection between inverter and motor (FUKUDA; AKATSU, 2019);
- Need to bring only 2 power cables to the wheel (positive and negative of the accumulator), instead of three cables (the three phases of the electric machine);

- Reduction of mass and volume of the motor-inverter set, due to shared use of housing, although this does not mean that there will be an overall reduction in vehicle mass;
- Release of internal space in the vehicle, which can facilitate BEVs size reduction or ICEVs hybridization processes.

Between the disadvantages and challenges related to this solution, are the following:

- Insertion of the converter in an environment of greater exposure to intrusion, dust, accidental contact and water;
- Insertion of the converter in an environment of greater vibration, and potential failures resulting from this;
- Increase in unsprung mass, and consequent issues for the vertical actuation of the suspension.

Vibration growth brings the need for additional attention with solutions to avoid failures resulting from it. As for environment difficulties, the result is a greater need for ingress protection. Finally regarding unsprung mass, Bravo et al. (2012) suggest that for commercial small passenger-carrying vehicles, the increase in unsprung mass should not exceed 40 kg per wheel, also pointing to the need to redesign the suspension. This change is necessary to ensure that there is no loss of tire contact with the pavement under transient damping conditions. Schalkwyk e Kamper (2006) evaluated vehicles with similar mass and suspension coefficients characteristics, pointing out that an increase of 50 kg per wheel is not able to alter the natural frequencies to the point of impairing passenger comfort levels.

Having presented these more general matters about the powertrain, this work proposes the design of a specific component of the system: the traction converter. A basic explanation of its operation follows.

1.3 Traction converter

Converters are essential components for electric traction, as they have the following functions:

- DC to AC conversion and vice versa;
- Control of the electric machine, generally through a current control loop and speed control loop, also defining if the operation mode is motor or generator.

For better compreension of the system, Figure 6 presents the major components of Tesla Model S Traction Converter. It is presented as an example, so that others will have a similar structure.

Figure 6 – Tesla Model S Traction Converter (REIMERS et al., 2019). Exploded component for view purposes. 1) Control board 2) Aluminium shield 3) Phase current sensor ferrite ring 4) Gate driver board 5) Phase busbars 6) Heat sinks 7) Power switches 8) Power switches clips 9) DC-link capacitors

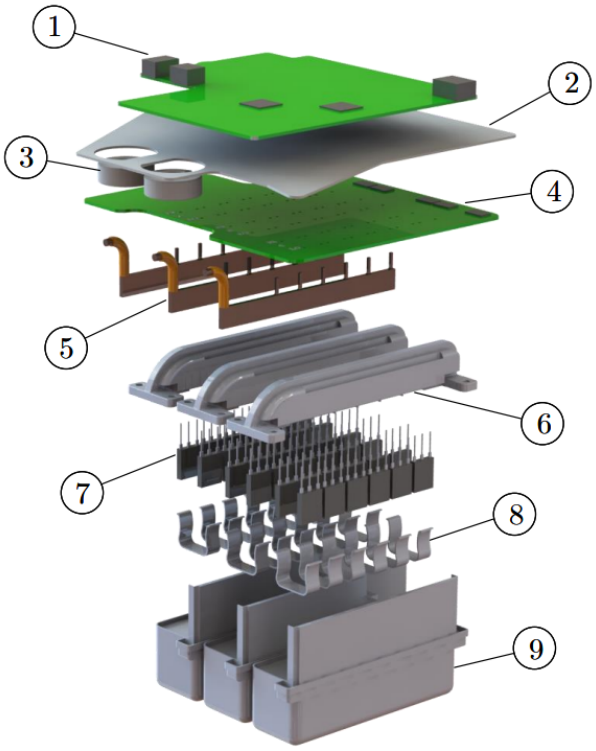

As for the topologies observed in traction converters for automotive applications, the most common is the one used in this work, called Three Phase Bidirectional Voltage Source Converter (BVSC), see Figure 7. More about topologies can be found in Section 2.3.

Figure 7 – Three Phase Bidirectional Voltage Source Converter diagram

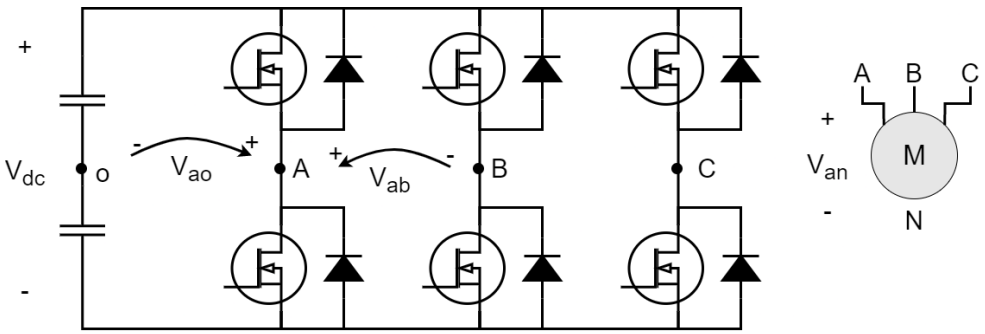

The accumulator can be either directly connected to the traction converter DC input, or a DC/DC converter can be used as interface, controlling the DC voltage (REIMERS et al., 2019). The first section of the converter is a DC-bus that acts as a low pass filter, smoothing the ripple

currents and voltages generated by the switching action of the active devices and the battery voltage sag. It protects both the accumulator and the power switches from large current and voltage spikes. The last section is composed by the power switches. Their switching pattern is responsible for the conversion between DC and AC.

A more in-depth discussion about the technologies related to the converter will be presented in this work mainly in the state of the art's Chapter 2, but also in the Chapters 4 and 5, related to hardware and software. However, in order to provide an introductory overview of the work, some considerations are carried out beforehand.

Regarding the hardware of these converters, a lot of development has been carried out in this field. In recent years, the dominant switching technology has been silicon IGBTs (Insulated Gate Bipolar Transistor), but it is also possible to observe the growth of the application of silicon carbide MOSFETs (Metal Oxide Field Effect Transistor), due to their characteristics that allow the increase of the frequency of switching, reduction of losses and consequent increase of efficiency (BIELA et al., 2010), see Figures 16 and 17. Mass and volume reduction are also trends related to the use of wide bandgap semiconductors, both in the converter itself and in the cooling systems, due to lower heat generation.

Despite this, there are not only pros in using these technologies. A disadvantage that can be presented in advanced, is that increasing the switching frequency increases the effects of parasitic capacitances and inductances. This effects work against system performance by increasing losses and voltage ripple. Therefore, applying these technologies brings new challenges, which need to be properly analyzed and taken care of. A relevant part of the scientific process is to provide solutions to overcome the difficulties of implementing new technologies, and this work is inserted in this context.

Regarding the software of these converters, there is also a wide development of technology for control systems in general, which also includes the automotive applications. Klerk e Saha (2021) provides an automotive review of the issue, demonstrating that the objectives of control systems vary, which can be machine torque control, machine power factor control, flux weakening, cruise speed control, DC bus and battery current control for protection and development of regenerative braking, among others. The scope of this work is limited to the torque and speed control design, leaving other developments for future work.

The converters are usually programmed in C, with the common use of DSPs (Digital Signal Processors) or FPGAs (Field Programmable Gate Array), due to their performance in signal processing (BUCCELLA; CECATI; LATAFAT, 2012). The MCUs (Microcontroller Unit) can be integrated with high-level programming solutions that provide automatic code generation, such as MATLAB/Coder and LabVIEW Embedded Module/LabVIEW Real Time Module, accelerating and simplifying the programming process. With the growth in the use of other programming languages, mainly at high level, see Figures 20 and 21, and their use in embedded systems, the question arises if their performance is suitable for automotive application in traction

systems. In case these solutions turn out to fit, they can be presented as alternatives to automatic code generation, accelerating the design process in academia and industry, while also reducing development costs, through less dependence on paid software. These costs are particularly relevant for micro and small companies.

Having briefly presented the converter, and some elements of the development of this work, the contributions and objectives are described below.

1.4 Motivation, contribution and objectives

The main difference between an ICEV and a BEV is present in the powertrain. Thus, the development of electric powertrain technology is a relevant element to popularize electric mobility. As R&D (Research and Development) in this regard can be highly costly, both in terms of time and actual budget, this type of technology is often developed and protected by automakers and/or auto parts manufacturers via NDAs (Non Disclosure Agreement) and patents. The R&D here financed by public entities of the Brazilian government, seeks to provide the population of the country and the world with easy open access to this technology and to methodologies to accelerate the learning and development process.

This work focus on this mission, with the main objective being the design of a Bidirectional Three-Phase Converter for automotive traction application. It is not an in-depth work on optimizing some specific part of the converter development, but it is an overview of the design of this component, generating supporting documentation for future in-depth studies. The specific objectives are as follows.

- Develop traction solution with characteristics of power, frequency, communication, etc., suitable for automotive application;
- Increase the efficiency of the traction system as a whole;
- Facilitate vehicle electrification procedures and/or vehicle volume reduction;
- Facilitate power converter prototyping for academia and companies.

It is proposed the use of in-wheel powertrain packaging without mechanical reduction and SiC (silicon carbide) switching technology. The control systems and switching control programming are developed and implemented in micropython. Throughout this work, it will be presented how this design solutions are related to the objectives presented.

1.5 Methodology

Developing a system like the proposed one involves different fields of science and engineering, including Electrical and Mechanical. More specifically, knowledge is required that ranges from control systems and programming, through low and high power electronics, to heat transfer, among others. Therefore, a multiphysics electro-thermal-structural analysis and/or modeling may be the most suitable way, as performed in the work of Zeng et al. (2019).

For reasons of simplicity and speed of development, the methodology performed in this work focused on a thermo-electric design development, with subsequent analysis on mechanical assembly implications. Opting for this type of solution can generate more iteration loops in the design phase, until it converges to assembly feasibility, but considerably simplifies the modeling of the system, which can be performed initially by limiting it to two fields of knowledge.

As the design is multivariable, even correlated with the suspension, brake and in-wheel engine designs, the complete algorithm is not feasible to be presented graphically in this work. The solution in this case was to use free mindmap tools to help monitor the project, and to present sections of the design algorithm in their respective applications.

1.6 Textual organization

This work is organized in 7 chapters. In Chapter 1, the introduction was made to acquaint the reader historically and in the current situation of the world in relation to this emerging technology. The issue of the electric mobility market, its political factors and actual impacts on the environment were discussed. A basic explanation of the functioning and topology of the developed system was also carried out.

In Chapter 2 the state of the art of the scope of this work is presented. The aim is to demonstrate the current state of development and market trends for the future, allowing the reader to better understand where this work is situated in a global R&D context. The reasoning for some of the major design decisions are presented, based on the results of the research.

Chapter 3 creates the basis for the development of the project, limiting its scope and establishing the requirements that seek to be achieved. This issue is evaluated in terms of torque and power targets, automotive standards, as well as limits on volume, mass, among others.

In Chapter 4 the subject is the development of the converter hardware, in all its main elements, such as power switches and DC bus. Main attention is given to the thermal and electrical issues involved, with subsequent analysis on assembly implications.

In Chapter 5 the software and control are discussed. The control methodologies are presented and attention is given to the development and implementation of the algorithm.

Chapter 6 presents the results and discussions, leading to the conclusion of the work in

Chapter 7.

2 State of Art

This chapter consists of a survey of information concerning the technology, in order to establish the basis on which this work gives its engineering contributions.

As presented in Chapter 1, the traction converter is a multivariable system, and in this work its development is subdivided into two large groups: hardware and software. Presenting the state of the art of traction converters, includes many fields of knowledge related to Electrical and Mechanical Engineering, such as Heat Transfer, Power Electronics, Analog and Digital Electronics, Control Systems and Programming. In order to provide an overview on the market and academia in relation to these subjects, this chapter has been subdivided into the following sections:

- Mechanical assembly solutions;
- Thermal management solutions;
- Converter topology;
- Operating voltage and frequency;
- Components state of the art;
- Modulating techniques;
- Software developments

2.1 Assembly solutions

The design of a system such as the traction converter must correlate a series variables and analyses from different fields of knowledge. One of the relevant issues of implementing an in-wheel system is packaging, since the converter has to compete for space with the braking, steering and suspension systems, along with the motor. The assembly and packaging solutions of the converter will also influence a wide variety of performance variables, such as power density, voltage ripple, cooling effectiveness, among others.

Regarding in-wheel powertrain, two major companies spearheaded the development worldwide, namely Elaphe Propulsion Technologies and Protean Electric, see Figures 8 and 9.

It is possible to observe some differences between the solutions of each company. The first is that Protean also develops Power Electronics solutions coupled to the in-wheel motor, while Elaphe maintains the in-board converters. Another direct difference that can be observed

Figure 8 – In-wheel drive solution from Elaphe (ENGINEERING, 2021)

Figure 9 – In-wheel drive solution from Protean (KLIMOV, 2021)

is in relation to the brake system solutions. Elaphe opted for the allocation of the brake system radially to the traction assembly and the use of a external brake caliper. Protean on the other hand, preferred the allocation of the brake system axially to the traction assembly and the use of a internal brake caliper.

The design decision regarding these geometries depends on the application and availability of in-wheel space, and there are no superior solutions in all cases. One of the factors that influences the decision is the availability of brake calipers. Due to common brake system geometries, commercial solutions tend to be with external calipers, i.e. calipers that access the brake disc through its external diameter. When the application is specific, as in the case of in-wheel traction, it may be desirable to use internal calipers, in which case the company usually has to develop the component itself. This work aims to simplify and popularize the solution through the use of a commercial brake system, with possible minor changes.

Due to the lack of axial space available, the choice was to allocate the brake system radially to the traction assembly (internally to the motor and inverter), and the solution ended up similar to Elaphe's design.

The problem with this solution is that it reduces the radial space available. As will be demonstrated during this work, with this design choices, it was feasible to develop the solution

for a 17-inch wheel, but it is indicated to analyze in future developments whether the same decisions would still be feasible for smaller rim wheels.

Another factor that can present a considerable volume, affecting the packaging of the system is the cooling solutions.

2.2 Thermal management solutions

The converter operation tends to have considerable losses, mainly generating heat, but to a lesser extent other forms of energy such as sound, one of the reasons for designers to distance the switching frequency from the human audible spectrum (MALFAIT; REEKMANS; BELMANS, 1994). Due to heat generation and limited operating temperature of the components, some cooling system is required. Their selection will influence a wide array of factors, such as the cost and power density of the converter. In general, the cooling system can be:

- Natural cooling with backplate/finless heatsink;
- Forced air cooling;
- Liquid cooling, direct (electrowetting, jet impingement, immersion) and indirect methods (cold plates).

If the heat generated in the converter can be removed by a finless heatsink, this solution tends to be selected. This type of cooling is usually achieved by attaching the power switches and DC bus to a backplate at the base of the inverter. The heat transfer occurs by conduction to this plate and then, is dissipated to the environment through conduction, natural convection and irradiation. This backplate is usually made of aluminum for its good thermal conductivity. As the heat transfer occurs naturally, the designer seeks to operate on the thermal capacitance (specific heat times mass) of the backplate, so that rapid heat generation events do not damage the component. This solution is very simple, cheap and low maintenance, but its heat transfer capacity, with fixed volume, is relatively low.

When the thermal demand increases, forced air cooling systems become relevant. They can be made with or without the aid of fins and/or fans, to help the heat transfer process. The installation and maintenance of this solutions are more expensive than the simple natural cooling solution, but they allow to use more power in the converter. On the other hand, when compared to liquid cooling, the solution has a lower power density, but with reduced cost and maintenance (ZENG et al., 2019).

For further increase in heat rejection, liquid cooling systems are used. Compared to natural cooling and forced air cooling solutions, it has the best heat rejection capability (ZENG et al., 2019) and it is generally used in high power density applications. Several researches

have been carried out to implement advanced methods for liquid cooling, and it can be done directly (electrowetting, jet impingement, immersion) and indirectly (cold plates). Immersion cooling is a possibility, been successfully applied to large scale traction inverters for locomotives and mining equipment (BARNES; TUMA, 2009), and now making some appearances in the automotive industry. A market example is the Cadillac CT6 inverter, that fully immerses the power switching module package in the coolant (MORENO et al., 2022). Jet impingement, spray cooling, microchannel heatsinks and heatpipes are another possibilities (BROUGHTON et al., 2018).

Another relevant point, is that in the case of a coupling to a motor that already has liquid cooling, it may be feasible to integrate the two systems with proper thermal analysis and sizing. As disadvantages, Lajunen, Yang e Emadi (2018) point out that it is possible to cite extra weight, greater complexity and higher cost. Coolant leakage and corrosion are also factors that should be taken into account. It is also important to remember that technology is not only being developed to improve cooling systems, but also to reduce losses, increasing efficiency and reducing the need for cooling itself, see Subsection 2.5.1.

The decision on this work was to operate with liquid cooling, and this analysis is closely related to the thermal sizing of the power switches, the desired power density, the decision on the power switch technology and the selection of the packaging, as shown in Section 2.5, Figure 17.

2.3 Converter topology

As for the topologies observed in traction converters for automotive applications, the most common is the one used in this work, called Three Phase Bidirectional Voltage Source Converter (BVSC) (JIN; GAN; GUO, 2017), see Figure 7. It is also known as Three Phase Voltage Source Inverter (VSI), but this denomination can be deceiving, since it is not just an inverter, since it acts as a rectifier in regenerative braking. Some of the advantages of this topology are pointed by Reimers et al. (2019):

- Single stage conversion, generating low cost, ease to manufacture, simple switches control, low volume and weight;
- Extensive use in the past decades, making the solution mature, robust and reliable;
- High efficiency.

A disadvantage of the BVSC topology is their poor CMV (Common-mode Voltage) characteristics. The existence of (usually capacitive) common-mode paths between the converter and the ground allows leakage currents to flow with CMV variation, thus high-frequency PWM produces high common-mode leakage currents. This may lead to EMI (Electromagnetic Inter-

ference) (BOILLAT et al., 2013), partial discharges, and motor bearing faults (HADDEN et al., 2016).

To start presenting alternatives to this topology, and treating its disadvantages, some extensions of the two level BVSC can be presented, such as the H8 architecture and four-leg inverters, see Figures 10 and 11.

Figure 10 – BVSC H8 architecture diagram (CONCARI et al., 2017)

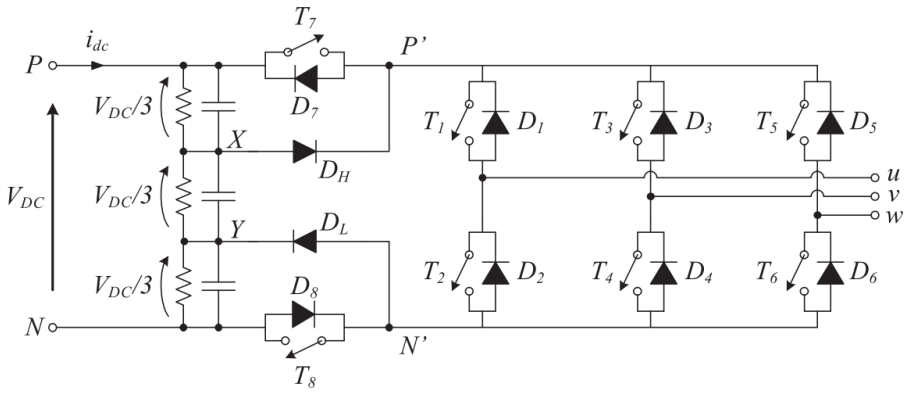

Figure 11 – BVSC four-leg architecture diagram (HASANZAD; RASTEGAR; PICHAN, 2018)

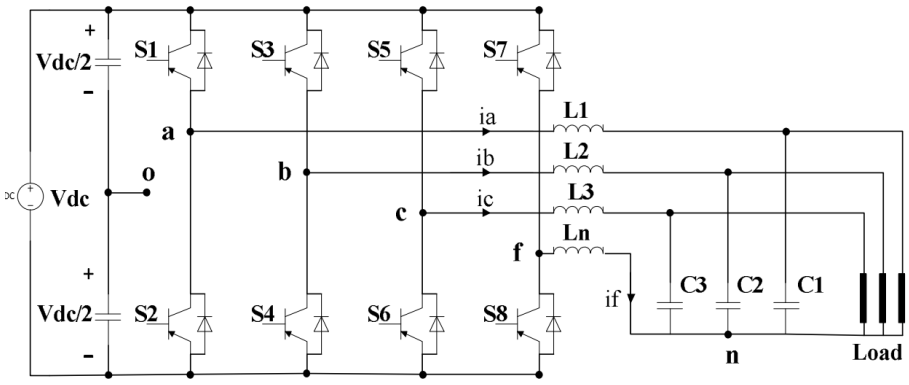

In the H8 architecture, the two additional switches on the DC side allow a reduction of the CMV by disconnecting the source from the load during the freewheeling intervals. A further optimized modulation also allows obtaining low-frequency CMV, at the expense of the maximum modulation index (CONCARI et al., 2017).

The VSI four-leg architecture is commonly used in applications where balanced three-phase voltage should be supplied when the loads are unbalanced or non-linear, such as distributed power generation, three-phase uninterruptible power supplies and islanded operation of a three-phase system. For supplying unbalanced and nonlinear loads, a neutral connection is needed so that the zero sequence component can pass through it (HASANZAD; RASTEGAR; PICHAN, 2018).

Both of these topologies are able to reduce the high frequency CMV variation within the electric machine. On the other hand, the required additional power switches and passive elements

increases cost, control complexity, volume and weight of the converter. This work evaluated that for automotive application, the cons of these solutions outweight the pros.

Another topologies that can be cited are the Current Source Inverter (CSI) and the Z-source Inverter (ZSI). The CSI circuit is composed of six switching devices with bidirectional voltage blocking and unidirectional current flow capability (RASHID, 2017), see Figure 12. Symmetric IGBTs in series with diodes are commonly used. The DC input can also have a voltage source, such as the accumulator, if it is connected in series with a large inductor. For motor drive applications, capacitor filters are required on the AC output due to the high distortion of the line currents caused by the switching action.

Figure 12 – CSI architecture diagram (RASHID, 2017)

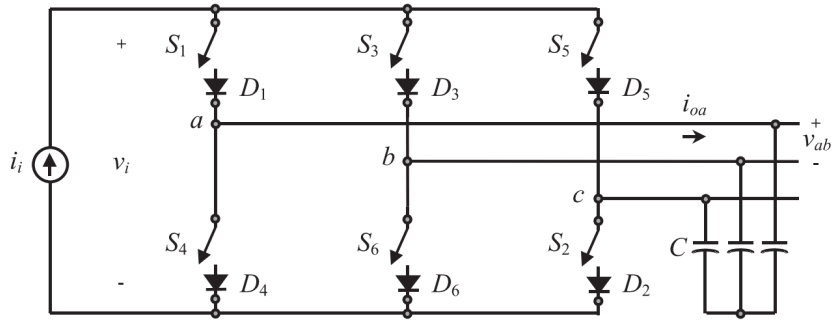

The main advantage of the CSI topology is to boost AC output voltage. If there was a need of this boost, the use of a CSI converter can eliminate the separate DC/DC boost converter. It is able to provide sufficient output voltage even as the electric machine's back EMF (Electromotive Force) rises above the DC-link (WU; SU, 2008). The disadvantage of the topology is its lower efficiency and higher cost, when compared to the BVSC, since there is still a need for a DC-link inductor that is usually bulky and heavy in high power applications (REIMERS et al., 2019). This disadvantages prevents major adoption of the topology in automotive traction.

The Z-source Inverter (ZSI) combines characteristics of the VSI and the CSI (PENG, 2003), see Figure 13. The ZSI is also able to lower as well as boost AC output voltage. The ZSI provides similar or higher efficiency than the BVSC and the combination of the BVSC with a DC/DC boost converter respectively (SHEN et al., 2007). However, the need of more passive components, negatively affects cost and volume, also preventing major adoption in automotive traction.

As for the number of phases, others solutions are present, such as the five-phase topologies, shown in the work of Fukuda e Akatsu (2019). Since it needs 5/3 more power switches, the volume tends to increase. The five-phase solution has the following advantages:

- Higher fault tolerance, since the three-phase system cannot operate with the loss of a phase, while the five-phase system can perform phase shifting, still generating the rotating magnetic field;

Figure 13 – Z-source Inverter architecture diagram (PENG, 2003)

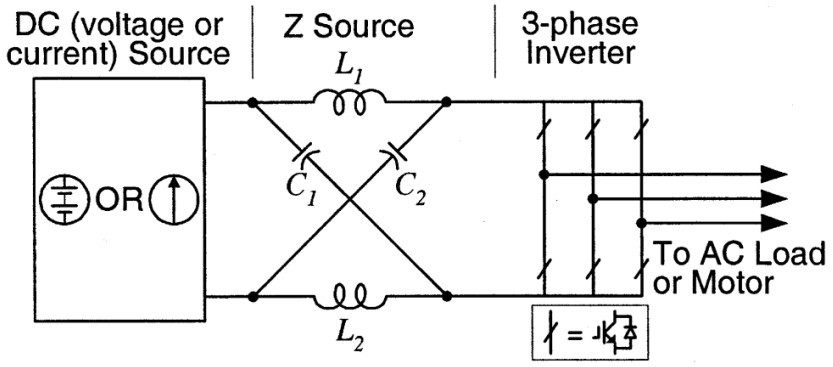

- It reduces the phase current for the same output power

Despite the advantages, this work still chose the three-phase solution, not having been part of the scope the development of systems with more phases, with the caveat that extra care should be taken both in the mechanical design of the solution and in the manufacturing process, considering the lower fault tolerance.

Finally, as discussed, operating voltage selection is correlated with a number of design variables. It can vary along with the design objectives, whether they are simplifying assembly, increasing efficiency, decreasing system mass and volume, among others.

After considering the converter topology, the next factor to be analyzed is the system operating voltage.

2.4 Operating voltage and frequency

Another characteristic of power converters that has been a subject to research and revolutionized the automotive market is the operating voltage. This parameter has a relevant impact on vehicle performance.

As electric power depends on current and voltage levels, increasing traction power has direct effects in one or both of this variables. To assess this issue, some considerations are necessary, including safety analysis, feasible range of operation, and supportability of the systems and components involved. Pros and cons of increasing voltage levels are show in Table 1.

Table 1 – Pros and cons of increasing the voltage of the powertrain

Pros	Cons
Reduction of losses in conductors	Increase in electromagnetic interference
Reduction of conductors mass	Increase in electric shock hazards

The same accident, with higher voltage, results in higher levels of current in the human body, causing more damage. All due care must be taken so that there is no direct contact with high voltage, neither in vehicle operation nor in maintenance, without proper protections. SAE (2020) defines low voltage as equal to or less than $60V_{dc}$ or $25V_{ac}$.

Despite these considerations, the voltage increase generates good results in the reduction of conduction losses, implying less volume and mass of components such as conductors and fuses. Low power applications, such as bicycles, motorcycles and tricycles, commonly present low voltage systems, first because there will not be much need for large levels of current, and secondly because low voltage-low power systems tend to be simpler to assemble, due to the lesser need to insert batteries in series. On the other hand, in applications that demand more power, such as light passenger vehicles BEVs, the industry common voltage levels are from around $400V_{dc}$ (JOHNSON, 2019).

On the other hand, the automotive market is currently showing a tendency to increase this values to $800V_{dc}$ solutions, technology that has gone hand in hand with reduced recharging time (CHAPMAN, 2021). Porsche, Hyundai and Fisker have both announced $800V_{dc}$ architectures with the goal of enabling faster charging rates (REBER, 2016; GITLIN, 2021; JENKINS, 2019).

Operating with low voltage in high power systems, besides decreasing efficiency, generates issues in the packaging of the traction systems, causing oversizing of the power connections and accumulator, and sometimes even packaging unfeasibility generated by the high bend radius of the power cables.

As in this project, the objectives are to increase the efficiency of the powertrain, and to reduce its mass and volume, these requirements tend to increase the operating voltage. Although the ideal may be to use the voltage amplitude as a variable to be optimized in the design, the voltage of 800V was selected as a design constraint based on these analyzes presented here.

Finally, for the switching frequency, common values for IGBT converters are in the range of 5 to 20 kHz. SiC MOSFETs, however, are capable of reaching higher frequencies, being found developments in the 100 kHz range (MEHRABADI et al., 2016), and studies performing zero-voltage-switching to bring the technology up to 300 kHz (HE et al., 2018). Higher switching frequencies tends to increase the motor efficiency but tends to decrease the inverter efficiency (due to commutation losses) (WEG, 2022). Selecting the exact value will depend on a cross thermal design between converter and motor. In this work, to reduce the design time, the value of 100kHz was selected, leaving to further tests to observe how a change in frequency can affect the thermal characteristics for the two systems.

2.5 Traction converter components

As presented in Chapter 1, the traction converter is a multivariable system, and has been subdivided in this work into two large groups: hardware and software. As for the hardware part, the electronic components are varied, with a series of subsystems that composes the final module. The state of the art of the main components is presented in this section.

2.5.1 Power switches status

Historically, Power Electronics has used a huge number of technologies for switching, including BJTs (Bipolar Junction Transistor), thyristors, IGBTs (Insulated Gate Bipolar Transistor), FETs (Field Effect Transistor), among others. Deepening into all these possibilities for power switches is beyond the scope of this work, as the analysis will focus on the main technologies of current impact in the automotive and industrial applications: IGBTs and MOSFETs.

In addition to selecting the type of the power switch, it is still necessary to evaluate the technology used. In the last decades, the Power Electronics market was dominated by silicon switching solutions. However, other solutions have been gaining space in the market, such as GaN (gallium nitride) and SiC (silicon carbide) (GUO, 2017). Both technologies are very promising for application in Power Electronics, including in the automotive sector. They are also known as wide bandgap semiconductors. Figure 14 shows a comparison between some of their characteristics.

Figure 14 – Comparison of Si, GaN and SiC technologies (ALVES et al., 2017)

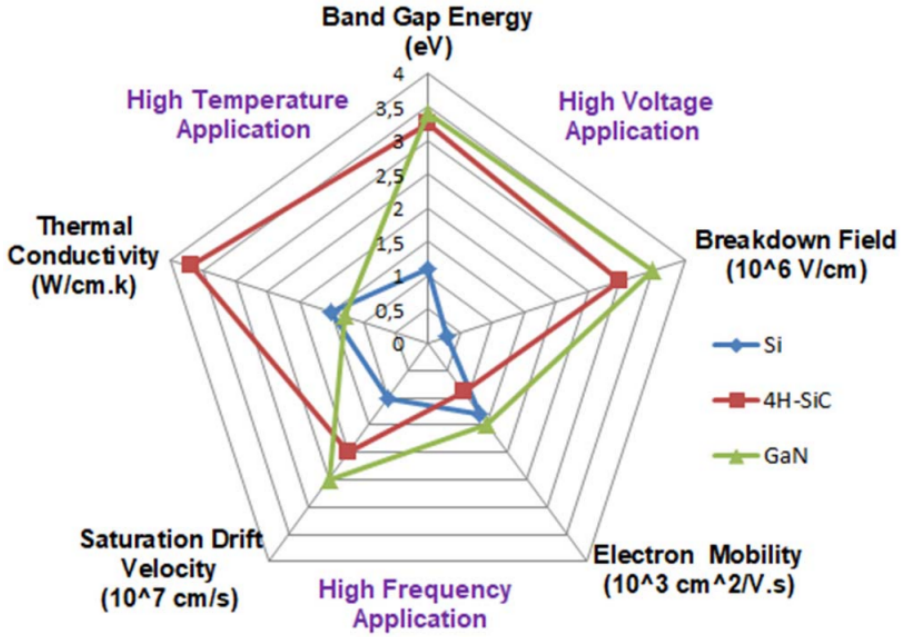

High breakdown field and high band gap energy allow operation with high voltage and high temperature levels. Increasing switching frequency is related to high saturation drift velocity

and high electron mobility (BIELA et al., 2010). GaN technology is a good choice for high voltage and high switching frequency applications. However, its performance decreases in high power and high temperature applications, due to its low thermal conductivity, being in some cases even lower than Si solutions. SiC, on the other hand, is shown to be a good choice for high voltage, high switching frequency and high temperature applications (ALVES et al., 2017). Going deeper into the comparison, Figure 15 also brings implications of the choice to operate with SiC.

Figure 15 – Approximate comparison of Si, GaN and SiC power switches and the implications of using SiC (GUO, 2017)

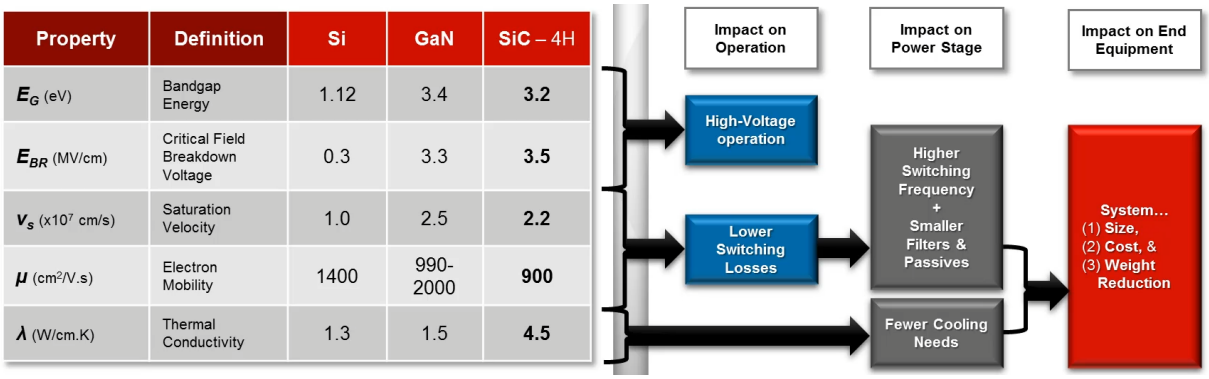

SiC is a technology with considerably better performance than the classical Si solutions. Initially presented at unfeasible prices, SiC has shown a constant cost reduction, tending more and more to economic viability. While silicon power switches withstand temperatures of 120ºC to 150ºC, silicon carbide solutions can withstand temperatures above 200ºC, with switching at high frequencies. With their lower losses, generating greater efficiency, their use may mean the reduction of the inverter volume, both in space for the switches themselves, and in the cooling system. In some cases, it is even indicated the transition to air cooling, since the conditions of dissipated heat may no longer imply the need for liquid cooling (ZHANG; TOLBERT; OZPINECI, 2010).

The higher operating temperatures raise concerns about the packaging of SiC power switches. With old encapsulations used in Si solutions, the possibility of them limiting SiC performance is considerable. Developments are being made in the areas of Materials Engineering and power module structures, seeking to achieve suitable encapsulations for SiC performance, withstanding the high temperatures and high power density (NEUDECK; OKOJIE; CHEN, 2002) (NING; WANG; ZHANG, 2013).

The advantages of SiC over Si are presented below:

- Possibility of achieving higher switching frequencies, reducing the need for capacitance in the DC bus, making the inverter more compact (WANG et al., 2015);
- Higher high temperature supportability;

- High power density, implying volumetric reduction of the cooling system and of the drive as a whole;
- Higher efficiency.

The disadvantages are shown below:

- Higher costs;
- High switching frequencies may generate EMI (electromagnetic interference) problems, due to high time derivatives of voltage and current;
- Comparing SiC MOSFET's with Si IGBT's, SiC components have lower short circuit supportability, and require better protection systems. This is because they exhibit a transition from the linear region to the saturation region at higher Vds voltages, causing this transition often not to occur and the drained current not to self-limit (GUO, 2017).

In order to present the most used solutions currently on the market, Figure 16 shows information regarding the year and peak power of inverters for electric traction. It can be seen the current market dominance of liquid-cooled IGBT's (Insulated Gate Bipolar Transistor) Si inverter solutions, with the tendency to be replaced by liquid-cooled SiC FET's (Field Effect Transistor). Air-cooled SiC solutions are appearing in considerable numbers in lower power applications, as the higher efficiency of SiC reduces the need for cooling.

Figure 16 – State of the Art in peak power of converters for electric traction (ZENG et al., 2019)

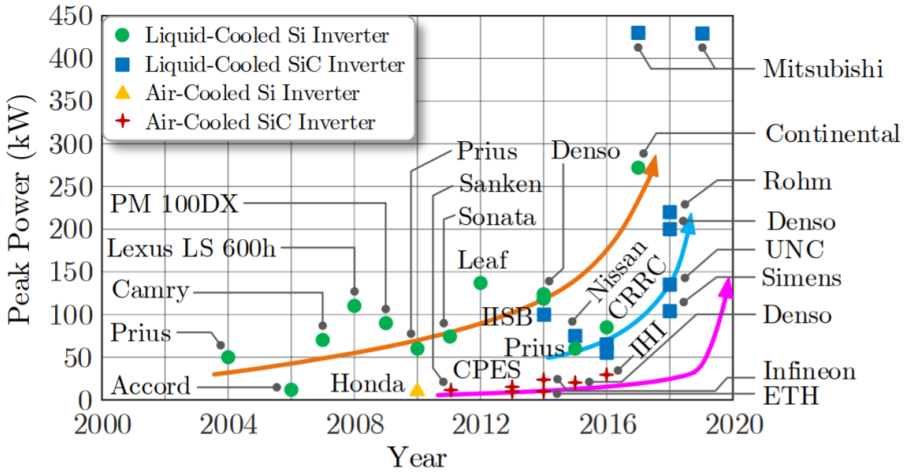

Figure 17 presents information regarding the power density. From the power density standpoint, other observations can be made. While Si IGBT's show less variation in this performance variable over the past few years, SiC FET's demonstrate themselves as a rising technology, presenting a wide range of power densities in the converters surveyed. The SiC FET solutions with air cooling present similar values to the Si IGBT's with liquid cooling, demonstrating

that the new switching technology can also be explored with the objective of simplifying and cheapening the cooling system.

Figure 17 – State of the Art in power density of converters for electric traction (ZENG et al., 2019)

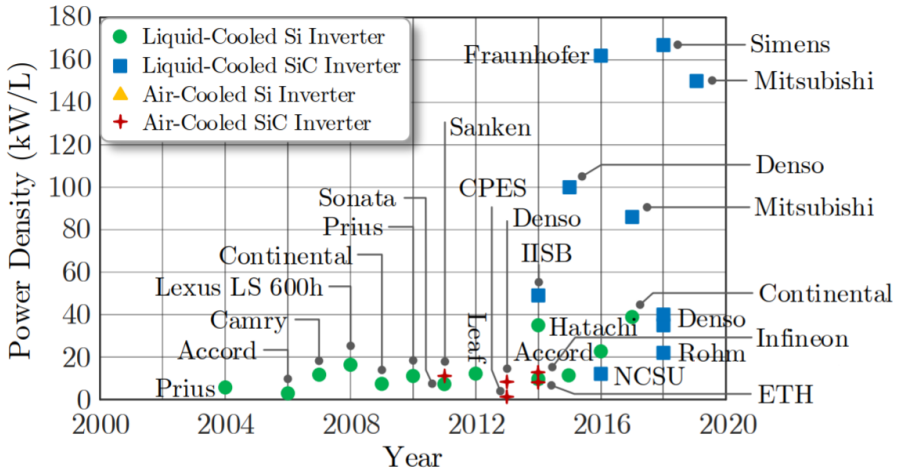

The characteristics of SiC make it interesting for a number of applications, see Figure 18. But they have not only made it a solution in Power Electronics, but also in a number of other products in various industrial sectors, such as automotive brake discs (in the form of carbon ceramics), bullet proof vests (due to its diamond like strength), steel making (due to its high thermal conductivity and melting point) and even wedding rings (due to its diamond like structure).

Figure 18 – SiC applications in Power Electronics (GUO, 2017)

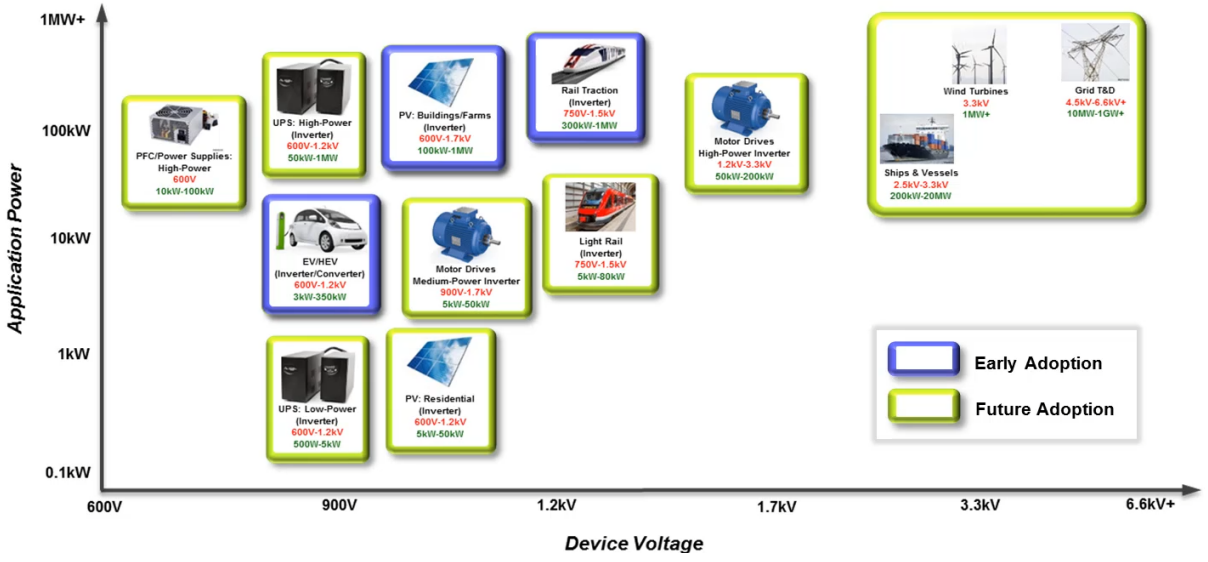

It is relevant to point out that SiC tends to be a better solution at higher power and voltages, see Figure 19, and other cheaper technologies may be more cost-effective for microhybrids, micromobility and other lower power applications.

Figure 19 – Variations of powers and voltages and implication on cost-effectiveness of switching technology (GUO, 2017)

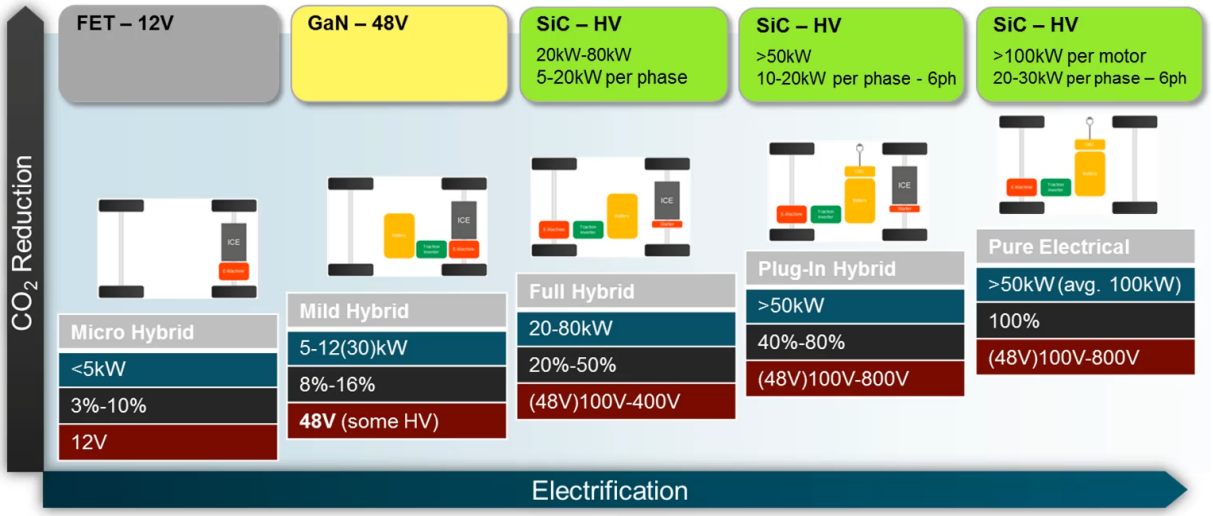

2.5.2 DC-link status

As stated in Section 1.3, the DC-link acts as a low pass filter, smoothing the voltage ripples generated by the switching action of the active devices. Once sized for the required power, the DC-link tends to occupy considerable space in the traction converter, usually being on of the heavier and most voluminous converter components (ZENG et al., 2019).

In power converter applications, three types of capacitors stand out, each with a type of dielectric material, namely: ceramic, electrolytic, and film capacitors.

Ceramic capacitors are suitable for high temperatures, but have as disadvantages their high cost, low capacitance values, and their sensitivity to humidity.

Electrolytic capacitors on the other hand have high capacitance, but their drawback is related to their low temperature supportability. Electrolytic capacitors are particularly sensitive to high temperatures, with every 10 ºC rise beyond their limit reducing the lifetime of the component by approximately half (VOGELSBERGER; WIESINGER; ERTL, 2010). Also, thermal runaway can dry out the electrolyte and generate serious damage. Other issue present, is as the frequency increases, so does the ESR (ZENG et al., 2019), affecting losses and decreasing efficiency.

Film capacitors can be used in automotive applications, presenting intermediate characteristics between ceramic and electrolytic, and being a cost-effective solution. While its power density tends to be the lowest among the three, it may still have lower capacitance requirements, due to its very good ripple current supportability characteristic (ZENG et al., 2019). The application on a power converter suits film capacitors well, since high current ripple capability is a concern. Indeed, a more power-dense, efficient, and low cost design can be achieved with film capacitors (WEN et al., 2012).

Advanced developments can also be pointed out, such as the novel polyyetherimide (PEI) capacitor dielectric film developed by Delphi Technologies and General Electric, that can operate at higher temperatures (ROGERS, 2013), and the TDK's CeraLink capacitors, which is a family of very compact capacitors based on PLZT ceramics optimized for high frequency switching applications.

In addition to the chemical technology of the capacitor itself, great advances have been made with a focus on the mechanical assembly of these components. As the switching will generate high current derivatives, the series inductance is a critical electrical factor for the converter, since voltage peaks tend to be generated on it. Its reduction is the focus of these advances in mechanical assembly, increasing voltage safety margin. This integration of the capacitor with the DC side bus bar, reduces inductance and increases power density and efficiency (BRUBAKER et al., 2014; SAWYER; BRUBAKER; HOSKING, 2015; BRUBAKER et al., 2016).

2.5.3 Other components

In addition to power switches and DC-link, a lot of technology development has been carried out on other components as well, such as the gate-drivers and MCUs (Microcontroller Unit).

Gate drivers are the components responsible for receiving the PWM signal from the MCU and generating the power switches command with the required charge and current characteristics. As they command the power switches, they affect directly their dynamic behavior and efficiency. Different design approaches have been developed, from passive circuits using external gate emitter capacitors and gate resistors, to advanced solutions using closed-loop control to adjust the gate driver output based on the operation status (LOBSIGER; KOLAR, 2013). For high voltage applications, such as traction inverters, isolation between the MCU circuit and the high voltage circuit is tipically achieved with the use of optocouplers or pulse transformers (WARD et al., 2013).

Traction Converter's intelligence is concentrated in the MCU. In this component, the necessary calculations are made for the implementation of PWM and current and speed controls. Given the high computational requirements of the motor control, 32-bit floating point processors clocked at over 100 MHz are the norm for traction converters (REIMERS et al., 2019). As mentioned in Section 2.6, DSPs are widely used solutions, since they are microcontrollers that have a high data processing capacity.

As switching frequency rises, mainly due to the advance in WBGSs (Wide Band Gap Semiconductor), and control algorithms continue to increase in complexity, some researches suggested to split the computational work between DSPs and other hardware solutions, such as FPGAs (Field Programmable Gate Array). There are many high speed and high sampling

rate applications that an FPGA does easily, while the DSP could not. Equally, there are many complex software problems that the FPGA cannot address (HUNT, 2016). Bearing this in mind, the proposal of this researches is to use FPGAs in the sampling process and the PWM, while the DSP is responsible for the control algorithms (DIAO et al., 2017; LAKKA; KOUTROULIS; DOLLAS, 2013). This solution can improve timing accuracy and reduce the DSP requirements, but the presence of two processing units increases system complexity and development time.

A completely opposite direction can be proposed, simplifying the development of these systems to reduce the financial and time investment. In this diverse approach, the solutions move towards applications with lower switching frequencies, simpler control algorithms, and high-level programmed MCUs.

2.6 Modulating techniques

Beyond the developments found related to converter topology, there is also various possibilities regarding the modulating techniques to establish the power switching pattern. The general technique used in power converters is called PWM (Pulse Width Modulation). The PWM consists in controlling the pulse duration in a certain frequency. The relation between pulse duration and period is called duty cycle, see Equation 2.1. Although the duty cycle is a dimensionless number, it is usually expressed as a percentage. By varying d_c, the system can control the mean output voltage.

$$d_c = \frac{\Delta t_x}{T_{sw}} \times 100\% \tag{2.1}$$

where d_c is the duty cycle (%), Δt_x is the duration of the pulse (s) and T_{sw} is the switching period (s)

Within this subject, two major concepts emerge to describe the modulation process: the switching frequency (f_{sw}) and the modulating frequency (f_{mod}). While f_{sw} refers to the rate of the switching events, f_{mod} refers to the motor currents and voltages fundamental frequency.

For didactic and historical reasons, PWM generation is known as a comparison between a triangular wave and a modulating wave. Regarding the PWM operation mode, not all PWM are the same, being divided into edge-aligned mode (also called Fast PWM) or center-aligned mode (also called Phase correct PWM). To analyze the differences, it is necessary to understand how they work.

In edge-aligned mode, the timer counts from 0 to its maximum and resets to zero when the maximum is reached, a so called overflow. It can also implement a countdown from its maximum to zero. Plotting the counter value versus time, it would look like a sawtooth signal. In centered mode, the timer/counter counts from 0 to its maximum, and then instead of resetting, it counts downward until it reaches zero. Thus, the counter value over time would look like a

triangle signal (GARCIA, 2019). In this case, care is needed to set the frequency of the PWM Timer, since it need to be twice the switching frequency.

In short, center-aligned mode needs to do twice as many counts, so its frequency cap is half that of edge-aligned mode. But what keeps its relevance its the effects on harmonics. In the case of the edge-aligned PWM, additional harmonics are presented at f_{sw} +- multiples of f_{mod}. The center-aligned PWM also has harmonics, but fewer: they are located at F_{sw} +- multiples of $2xf_{mod}$.

Centered mode produces less harmonics, but has a smaller maximum counter frequency, thus, depending on the application, the harmonics can get forcibly closer to our main signal in the spectrum. For machine drive applications, in general, center-aligned will be prioritized for its harmonics advantage, with consequently less losses and more efficiency, as long as the frequency limit of the counter is smaller than the desired switching frequency.

Also inside the context of PWM, a series of techniques that use this method have emerged, with some of the relevant ones been Sinusoidal Pulse Width Modulation (SPWM), Six-step Modulation and SVPWM (Space Vector Pulse Width Modulation). Further explanation follows.

SPWM is one of the most classic techniques used in the industry due to its simplicity (HOLMES; LIPO, 2003). It consists in using a sinusoidal f_{mod}, i.e varying the d_c with a sinusoidal reference. When compared to other modulation techniques, SPWM has relatively high THD (Total Harmonic Distortion), increasing harmonic losses, and low DC bus utilization. Being V_{dc} the DC bus voltage, the maximum amplitude of the fundamental output phase voltage is V_{dc}/2. So, despite having historical relevance, and still being used for simplicity, the technique was surpassed by the following ones.

The Six-step Modulation is also known as Square-wave Modulation, and it is named after the six distinct steps the output phase voltages take over a fundamental cycle (HOLTZ; LOTZKAT; KHAMBADKONE, 1993). It consists in the maximum limit of the DC bus utilization. In other words, if there is the need of a positive output, full V_{dc} is applied to the output, as well as if there is the need of a negative output, the switching occurs and $-V_{dc}$ is applied. Using this simple technique, the fundamental amplitude of the phase voltage is maximized to the limit, and is equal to V_{dc}. Despite this advantage, it generates a considerable amount of harmonics, increasing losses and making torque control difficult.

This work modulation technique is the SVWPM. It is an intermediate solution between SPWM and Six-step modulation, bringing some of the advantages of each. The method generates reduced THD compared to SPWM, improving the efficiency of the system, and also utilizes the DC bus better than SPWM, making use of a zero-sequence triangular voltage. The maximum fundamental amplitude of the phase voltage is equal to $V_{dc}/\sqrt{3}$, which is about 15% higher than SPWM method in the linear region (BROECK; SKUDELNY; STANKE, 1988).

Six-step disadvantages are not so present, but SVPWM does not reach the Six-step

voltage, being usually applied in the linear modulation region, and when the need arises, the converter can enter overmodulation region until reach six-step operation. This method of real-time switching between modulation techniques is commonly applied in the market. Even with the difficulty of accessing information from large automakers, it has been reported by Jurkovic et al. (2015) that General Motors employs this method.

It is also possible to point out that the widespread adoption of DSPs (Digital Signal Processor) and high-speed microcontrollers has enabled low cost implementations (HOLMES; LIPO, 2003). As stated in Section 1.4, one of the objectives of this work is to evaluate if this method can be satisfactorily implemented in a high level language micropython microprocessor.

In relation to other PWM techniques, Hava, Kerkman e Lipo (1999) indicates that discontinuous PWM methods have superior performance at the high-modulation range. Their implementation can be investigated and carried out in future works.

2.7 Software developments

Regarding the state of the art in software, researchers have been developing on different fronts that cooperate for the implementation of the traction converter. Among the development fronts we can mention the programming language and the optimization of code.

Regarding the optimization of the modulation code, some researchers have presented solutions to reduce the SVPWM execution time. Gaballah (2013) features an algorithm that reduces code size and processor usage, in his case resulting in bringing execution time from 25.3μs to 15.3μs. His proposal is to generate the gating drive signals directly from the instantaneous samples of the reference phase amplitudes, basing the algorithm on an equivalence with SPWM.

Regarding the programming language, C still remains the worldwide most used language, with Java also presenting high usage and interest. On the other hand, a great emphasis has been shown on the growth of Python, see Figures 20 and 21.

With developers mass use, and a good cost-benefit in relation to speed and programming complexity, C is also dominant for embedded systems application. Unfortunately, operating on registers and configuring peripherals still requires a considerable learning curve for new developers.

Despite the decline in the search for Java, it is still one of the main programming languages in the world. It is a high-level language, making it easier to implement solutions, and tending to be more robust in the sense that it does not forces the programmer to organize many low-level structures such as registers. The disadvantages of using high-level languages is the lower code execution speed, since the processor tends to execute several internal commands that the programmer is unaware of and has no necessary access to. On embedded systems Java is also used through DevOps tools available such as JVM (Java Virtual Machine), which is a

Figure 20 – Top 50 most popular programming languages TIOBE Index for May 2021 (STATISTICS&DATA, 2022)

	Programming Language	Ratings	Chart Ratings
1	C	13.38%	
2	Python	11.87%	
3	Java	11.74%	
4	C++	7.81%	
5	C#	4.41%	
6	Visual Basic	4.02%	
7	JavaScript	2.45%	
8	Assembly language	2.43%	
9	PHP	1.86%	
10	SQL	1.71%	

Figure 21 – Google web world searches trend in programming language in last five years (GOOGLE, 2022)

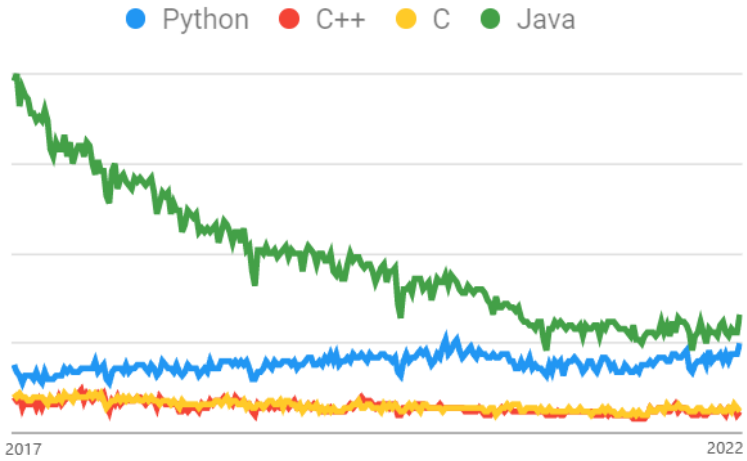

relevant solution in this sense, being a set of threads that execute on top of a RTOS (Real-Time Operating System) by converting the bytecodes into system machine executable code. It's a scalable language, since it uses multi-threading and real-time compiling. Also, it is very secure, with access control and built-in authentication services. Mancoso (2021) points out that Java has not been widely adopted in the development of embedded systems yet, with around 80% of embedded system projects being still written with C or C++. On the other hand, as programmers specialize in high-level languages, they can also be expected to look for high-level programming options for embedded systems, and we can see a shift in this direction in the coming years.

As for Python, it is also a high-level language, so the Java-related comments apply as well. In some ways, Python is even higher level programming than Java, as it provides the programmer with the freedom to use dynamically-typed data, that can be changed with ease, leaving to the interpreter the task of discovering the data type dynamically (ANDERSON, 2022). With the objective of implementing this language in embedded systems, Micropython was

developed, which consists of a compiler from Python to bytecode and a runtime interpreter of that bytecode. Like the JVM, Micropython was developed and optimized to make MCUs application feasible. A very interesting thing about the solution is that in addition to the classic Python libraries, Micropython brings modules that allow access to low-level hardware, giving tools to the programmer who wants to invest more time in speeding up the code. It is also possible to do programming in real-time through the REPL prompt, and the solution is fully open-source, bringing unlimited access to the technology and encouraging development.

Table 2 present a comparison between C, Java and Python. It is clear that there is no ideal language for all applications, and it will depend on what the developer is valuing more in each specific project. In traction converters for automotive applications, usually C will be used for the final system, prioritizing speed and scalability. But it is important to assess whether the development of other languages and embedded solutions has reached a sufficient performance that enables them to enter this market. Even in the worst case, high-level languages are still useful to accelerate the development process and help as didactic materials in the teaching of machine control.

Table 2 – Most prominent programming languages comparison (ANDERSON, 2022; SIDANA, 2021)

	C	Java	Python
Object oriented/Functional	Functional	Object oriented	Object oriented
Interpreted/Compiled	Compiled	Both	Interpreted
Data type	Statically typed	Statically typed	Dynamically typed
Language level	Low	High	Highest
Performance	Best	Mid	Worst
Development cost	Worst	Mid	Best
Scalability	Best	Mid	Worst
Ease of use	Worst	Mid	Best

With the state of the art, several technologies, solutions and developments related to the traction converter were presented, providing relevant information for making the design decisions of this work, and stating its contributions accordingly. At this point, it is necessary to gather the project requirements, to later present the project itself.

3 Design Requirements

This chapter consists of an analysis of the application of the converter that is the object of this work. Performing this analysis prior to the execution of the project is essential, since it sets limits for the design algorithm.

The following items, essential to support the subsequent project, are presented.

- Automobile standards;
- Analysis of torque and power requests;
- External geometric limitations and mass;

3.1 Automotive regulations

As one of the leading global industrial sectors, the automotive industry requires intensive regulation that defines its quality and safety standards.

The implications related to automotive safety are extremely critical. In the United States, it is estimated that more than 38,000 deaths occurred in traffic accidents in the year 2020, an increase of 7.2% compared to the 2019 (NHTSA-USA, 2021) fatalities. In Brazil, the situation is even more tragic. It is a market with around 7 times less vehicle sales, but almost the same amount of traffic fatalities, reaching more than 30,000 fatalities in the year 2020 (CZERWONKA, 2021).

Thus, every system that is developed for automotive application, especially in critical components that can affect safety, must be developed with constant attention to the standards and approved by the competent bodies.

International standards include IATF (International Automotive Task Force) 16949, developed by the industry as an ISO (International Organization for Standardization) technical specification that aligns with and supersedes worldwide existing automotive quality system standards, including american QS-9000, german VDA6.1 (*Verband der Automobilindustrie*), french EAQF (*D' Evaluation D'aptitude Qualite Fournisseurs*), italian AVSQ and ASQ (American Society for Quality) (BSI-GROUP, 2021). It specifies quality system requirements for the design/development, production, installation, and maintenance of automotive products. For most major automotive manufacturers, certification to this specification is a mandatory requirement for doing business.

The standards are very extensive, ranging from electrical, electromagnetic, environmental, mechanical, climatic and chemical requirements. In order to bring some examples of relevant

standards for the development of this type of automotive system, to facilitate future research, a brief survey follows.

- ISO 6469, Electrically propelled road vehicles – Safety specifications;
- ISO 7637:2011 Road vehicles — Electrical disturbances from conduction and coupling;
- ISO 6722, Road vehicles – 60 V and 600 V single-core cables;
- ABNT NBR IEC 60529, Degrees of protection provided by enclosures, 2017;
- AEC-Q100 - Failure Mechanism Based Stress Test Qualification for Integrated Circuits, with emphasis on AEC-Q101 related to active components, such as diodes and transistors;
- AEC-Q200 - Passive components used in the Automotive Industry;
- AEC-Q104 - Multi-Chip Modules (MCM) used in the Automotive Industry;
- ISO 16750-1 (08/2006) and ISO 16750-2 (03/2010) - Road vehicles - Environmental conditions and testing for electrical and electronic equipment;
- ISO 10605 (2008) Road vehicles – Test methods for electrical disturbances from electrostatic discharge;
- ISO 11452-2 (2004) Road vehicles - Component test methods for electrical disturbances from narrowband radiated electromagnetic energy (parts 2, 4, 5, 8, 9 and 11);
- 1999/519/CE Recommendation of the Council of the European Union from 12 July 1999 realted to the limitation of exposure of the public to the electromagnetic fields (from 0 Hz to 300GHz);
- ECE-R10 Uniform limitations concerning the approval of the vehicles withregard to the electro-magnetic compability.

In view of the scope of these regulations, it is clear that validating a component or module for automotive application requires a series of electrical, electromagnetic, mechanical, and thermal tests, among others, that are able to confirm that the system is adequate. Among these tests it is possible to mention:

- Basic functional test;
- Random vibration;
- Drop test;
- Pressure cycles with superimposed temperature;

- Immersion test;
- Temperature shock cycles;
- Resistance to fluids;
- Tightness test;
- Burst pressure;
- Resistance to fire;
- Plating of terminals;
- Endurance to current cycles;
- Resistance to variable atmosphere;
- High pressure wash;
- Dielectric rigidity;
- Connector polarization feature;
- Visual inspection of the connectors;
- Comprehensive terminals review;
- Mechanical endurance;
- Measurement of the terminal; resistance
- Mating force;
- Unmating force;
- Tearing strength of the connector;
- Water sealing under pressure.

In this work for reasons of time and feasibility, these tests were not performed, but it is important to keep in mind that they are critical future development steps, essential for the application of the converter in a vehicle.

Even without carrying out all the tests for the automotive standards now, it is very important during the entire selection of components to observe whether each component complies with the automotive standards, avoiding reworks to adapt the project to the standards in the future.

3.2 Analysis of performance demands

In addition to the statements made about automotive regulations, there are other design requirements, related now to the performance that the powertrain will need to provide. As with the design of electrical machines and energy accumulators, the development of a power converter for automotive traction is closely related to the performance objectives of the vehicle. It is very important to perform this analysis to avoid oversizing or undersizing in the design process, both which negatively affect the cost-effectiveness of the final system. For this project, the following requirements for vehicle performance are established.

When with only two rear motors, the vehicle has to be able to perform:

- Acceleration from 0 to 100 km/h in 10 seconds for a vehicle of 850 kg;
- Maximum speed: 190 kph;
- Traction system to be inserted into 17" wheels;
- PMSM traction motor topology.

In order to transform these requirements into design variables for the motor and powertrain, a longitudinal performance model of the system was developed, and is presented in Appendix B. It is important to consider electrical variables such as the power limits that the battery provides, as well as vehicle dynamics variables, such as load transfer and tire grip with the ground. The vehicle weight is considered 850kg, with a driver of 75kg.

As the motor design was not part of the scope of this work, an estimate of its flux weakening capability was necessary for insertion in the performance model. Ustun et al. (2018) refers to this capability as the Constant Power Speed Ratio (CPSR), which is the ratio between the maximum speed the motor can reach at flux weakening and its rated speed. Figure 22 shows an example of the implications of CPSR in the sizing of the traction system.

With the graphic aid, it is possible to observe the effect of the flux weakening on the powertrain sizing. Ideally for the powertrain design is that at the maximum target speed, the tractive torque is equal to the resistive torque. Beyond that point, any attempt to increase speed is disallowed by forces resisting motion, such as aerodynamic and roll forces. In the example image, this is achieved with CPSR = 4, however this varies from vehicle to vehicle.

The worst case is when flux weakening is not performed (CPSR=1). In this case, the electric machine needs to be dimensioned with its rated speed at the maximum target speed. This method oversizes the powertrain, with considerable amounts of extra power.

Between the ideal CPSR design and the worst case, there is a range of possible values for flux weakening, but all will present a certain level of oversizing.

Figure 22 – Example of torque versus speed curves with variable CPSR.

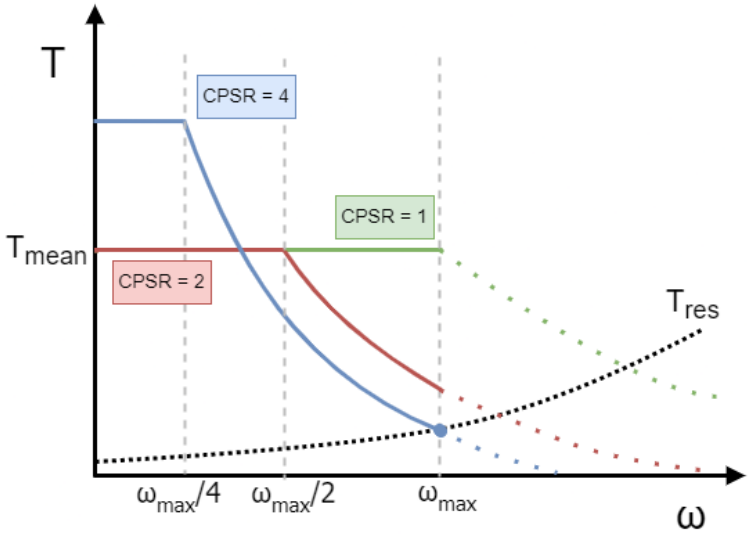

For the powertrain design, the ideal would be to design the machine to obtain its CPSR value, but as this is outside the scope of this work, an estimate of this value is carried out based on the levels found by the scientific community.

Much development has been done to increase the flux weakening capability of PMSMs. Xu et al. (1995) points out that improving this characteristic consists of increasing the direct axis current (I_d) or the direct axis inductance (L_d). But there are issues and risks. Increasing I_d is limited by the convert capability, copper losses of the PM machine and can lead the machine to demagnetization. Increasing L_d is usually performed with geometric modifications but it can be limited due to the low magnetic permeability of the magnets.

The machine topology will also significantly affect the results. Seo e Choi (2014) points out that interior permanent magnets can offer higher reliability and overload ability than surface permanent magnets, which makes them more suitable to traction application.

As for the values found, Ehsani et al. (2018) indicates CPSR<2 for Brushless DC motors, Yang e Ting (2013) reached a CPSR=2.94 with interior permanent magnets and angular displacement estimation techniques, Ustun et al. (2018) arrived in a BLDC at CPSR=3.24 using different sizes of stator teeth and alternate teeth-wound sub-fractional slot-concentrated winding structure, and finally Zhang et al. (2016) reached CPSR=4 with a Buried PMSM V Shaped topology.

Based on this research carried out on the state of flux weakening in PMSMs, a conservative value of CPSR=2 was selected. Again, it is important to point out that it is recommended to design the electric machine in the future, seeking to exceed these values and reiterate the entire design algorithm of this work, so that the sizing fits better the application.

With the CPSR value defined, it is now possible to use the longitudinal performance model. The forces that interact with each other in the vehicle are shown in Figure 23. As can be

seen, with a CPSR=2, the powertrain does not need to be oversized, which is indicated by the resultant force being zero exactly at the point of maximum speed.

Figure 23 – Forces in acceleration, $\mu = 0.8$

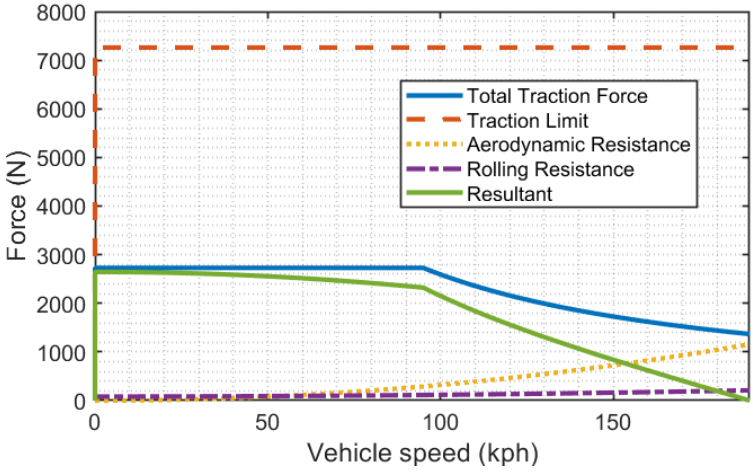

Figure 24 shows the powers during acceleration. As stated in the analysis of Figure 22, the ideal of the automotive application tends to be the machine that allows a long operation at constant power, so that certain maximum speed targets are reached without power oversizing.

Figure 24 – Power in acceleration, $\mu = 0.8$

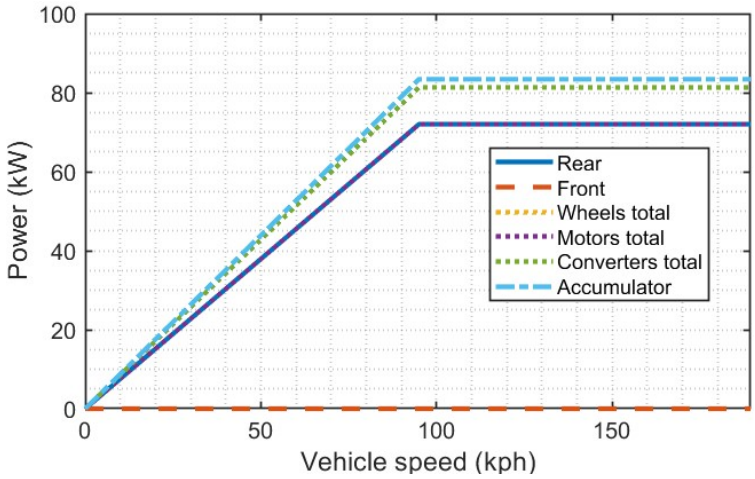

Finally, the speed curve for the acceleration is shown in Figure 25, indicating that the target requirements were duly achieved.

The mass of the vehicle is another factor that greatly affects its performance, see Figure 26. In this way, the more the mass increases, the more torque is necessary to achieve the acceleration target. As the consideration was for an 850kg vehicle and a 75kg driver, the value found for a two rear motor vehicle was $T_m = 380Nm$ per motor. It is also possible to observe that from around 300 Nm per motor, the gains in terms of acceleration time are considerably expensive. A complete cost analysis is proposed in future works, to evaluate how a reduction in the acceleration target can affect the final cost of the powertrain.

Figure 25 – Speed curve in acceleration, $\mu = 0.8$

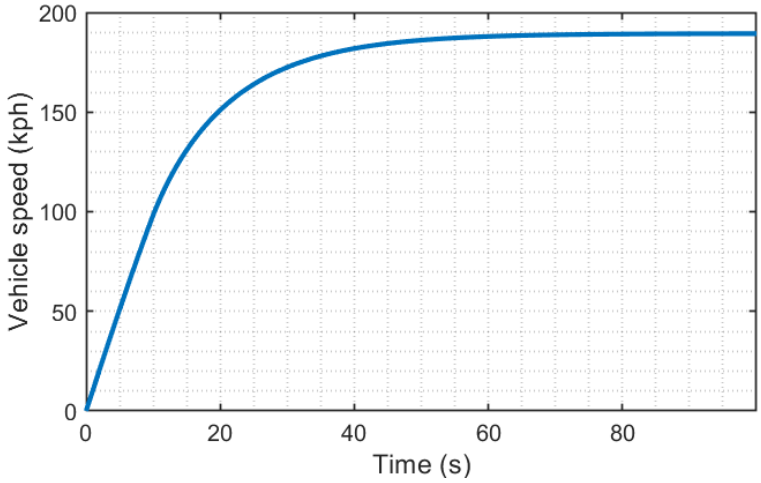

Figure 26 – Acceleration time from 0 to 100 kph, depending on motor torque and vehicle mass

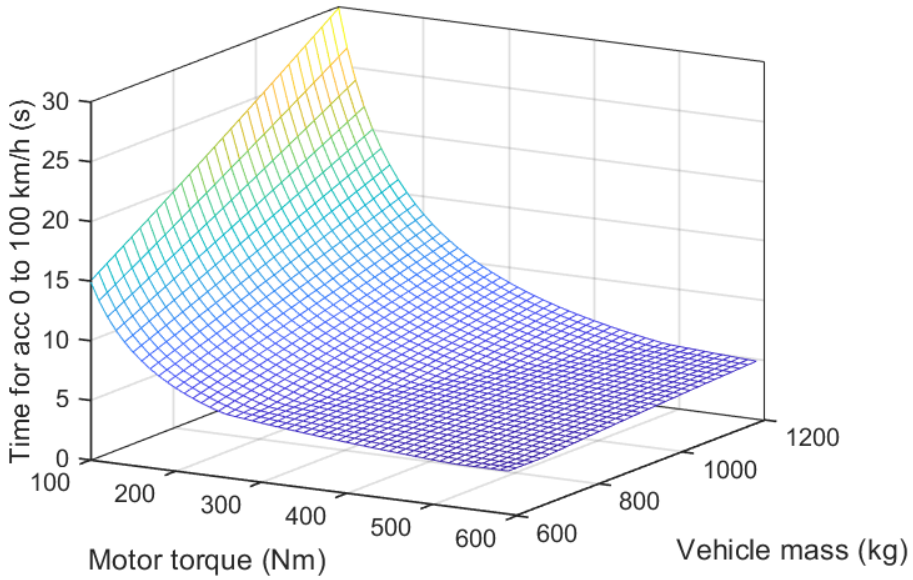

Finally, it is relevant to point out that the characteristics of the vehicle and the consequent design of the electric machine, generate a series of variables correlated to the design of the converter. Among this variables are the powers, voltages, inductances and switching frequency, among others. As for the power, the target of the converter will be associated with the power of the electrical machine. The motor supply voltage also has to be directly related to the converter output and the values present in the accumulator. Another example is the effect of inductances on the switching frequency. The smaller the machine inductances, the more current ripple is present, which may lead to the need to increase the switching frequency to deal with the issue. If this effect is exacerbated and the protection system does not properly account for it, ripple current can sometimes trigger an overcurrent protection. This issue tends to be less observed in industrial applications, since the most used topology in this sector is the IMs (Induction Machine), which have considerably greater inductance values. In BEVs, however, the most common topology is PMSMs (Permanent Magnet Synchronous Machine), where the use of magnets tends to have

lesser inductances than IMs.

As previously stated, the ideal would be to design the converter associated with the electric machine, in order to optimize it for the specific motor. However, as the electric machine design was not in the scope of this work, the variables used here came from different sources, ranging from this writer decisions, the performance demands analysis, works on IPMSM like the one from Li e Liu (2019) and Kiyota e Chiba (2012), to PMSMs datasheets. The machine characteristics are described in Table 3, and based on them, this work's traction converter was developed. All symbols on the table are also present in the symbols appendix before the start of this work text.

Table 3 – Electric machine variables

General data	
Connec.	Star
Slots	27
Poles	26
n,nom	904
f,el,nom	196 Hz
n,max	1808
f,el,max	392 Hz
CSPR	2
Ld	174 uH
Lq	293 uH
Rs	0.05 Ω
J	0.003 kg*m²
b	0.0008 Ns/m

Output	
Ppk,out	36 kW
Tpk,out	380 Nm
Peak time	10 s
P,nom,out	18 kW
T,nom,out	190 Nm
ef,nom	0.95
fp,nom	1
Iph,nom	22.6 A
Iph,max	45.2 A
Vph,nom	280.1 V
Vl,nom	485.2 V
V,dc,nom	685.7 V
V,dc,max	800.0 V

In addition to the requirements analysis presented, it is still important to perform mechanical and geometric analyzes so that the converter fits the application.

3.3 External geometric and mass limitations

Among the biggest arguments against using in-wheel drive is the increase in unsprung mass, and the effects it has on vertical suspension dynamics. The suspension needs to act in such a way that the tire maintains contact with the ground, for performance and vehicle safety reasons, as well as to prevent large vibrations from being transmitted to the passengers, generating discomfort. The increase in unsprung mass implies a greater inertia of this set, making this vertical operation of the suspension harder.

Several studies were conducted in order to evaluate the feasibility of this solution and the limits of additional mass in the wheel set. Bravo et al. (2012) pointed out that, for passenger cars, the additional mass should not exceed 40 kg per wheel, with possible need for suspension redesign. The study of Schalkwyk e Kamper (2006), on the other hand, points out that an increase of 50 kg per wheel is not capable of altering the natural frequencies of the system, to the point of

generating discomfort to the passengers. It is possible to observe that there is no consensus in relation to an exact value, which also depends on the design of the suspension and the type of vehicle analyzed.

In relation to generating damage in the suspension itself, Kulkarni, Ranjha e Kapoor (2016) point out that this is not the case with in-wheel drive, and no life-cycle reduction in the components is observed. Rojas, Niederkofler e Willberger (2010) present suspension systems to reduce the discomfort effects that can be eventually generated by the insertion of in-wheel drive. Even with the variations between researchers, in this work it was decided to limit the insertion of additional mass in the wheel set to a safe range, being defined 40kg per wheel.

Regarding geometrical limitations, the issue can be more complex, since the electrical machine and the traction converter compete for space inside the wheel, together with the brake, suspension and steering systems. A careful analysis needs to be done in this regard, considering a multidisciplinary design, especially including the effects on vehicle dynamics. The 3D model of the wheel, together with the full system is shown in Figures 88 and 89 in Chapter 6.

Within the system geometry, there is radial dimensional freedom and axial dimensional freedom. It is necessary to evaluate both and their implications for the converter design. Axially, the traction assembly is externally limited by the wheel and internally limited by the suspension. It is important not only to consider the suspension as static, but also to include an analysis of its dynamic behavior, evaluating the space it occupies in all operating situations of the vehicle. Large axial changes in the position of the suspension points can affect the vehicle steering capabilities. The objective is to keep them close to the wheel, to allow a minimum scrub radius, with a feasible KPI (Kingpin Inclination), see Figure 27. Increasing the scrub radius has negative effects, such as making the steering heavy and causing the car to lean to its side of greatest grip under braking. Increasing the KPI to reduce this effect is also a limited possibility, but it is very complex to define exact values for this limit.

Figure 27 – KPI and effect on scrub radius

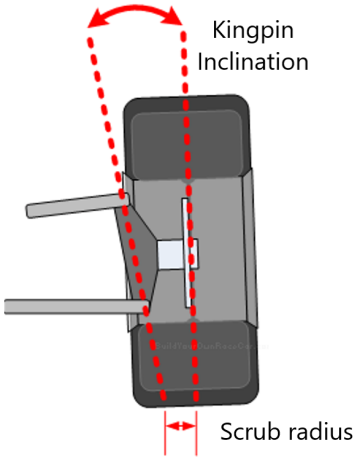

Radially, the outer diameter of the components of the traction assembly is limited by the

wheel. Generally this diameter is not constant, presenting chamfers and other variations. The design can be limited to the smallest inner diameter of the wheel, or can seek to take advantage of the remaining space with conical or more complex shapes. As for the internal diameter of the components of the traction assembly, they are limited in this case by the brake and suspensions systems, inserted inside it. The brake caliper limits it to the 356mm, the brake disk limits it to 298mm and the suspension limits it to 220mm. The final solution was to move the converter away from the brake caliper, so that there is sufficient dimensional freedom.

Having completed all the studies and analyzes that support the development of the traction converter, this work presents now the converter project itself, starting with the hardware and moving on to the software at later stages.

4 Hardware

With the necessary requirements established, this chapter presents the design and sizing of the traction converter hardware. In this development, considerations from the Electrical, Electronics, Mechanical and Heat Transfer knowledge areas are necessary, in order to model, simulate and select components that meet all the necessary specifications.

The development of the following steps is presented.

- System operation modeling;
- Power switch sizing and selection;
- DC bus sizing and selection;
- Gate driver sizing and selection;
- Discharge circuit sizing;
- Power PCB design;
- Control PCB design

4.1 System operation modeling

To start the sizing of a power converter, whose main components are the power switches, it is a good starting point to model the voltage waveforms in it, with the objective to better understand what are the results expected throughout this work. This analysis may not be critical for readers with advanced knowledge in this type of converters, however it is important to point out that this section also brings discussions regarding the effects of DC bus voltage variation, motor efficiency and modulation index.

The voltages modeling includes the switching characteristics and their impacts on the waveforms. In this work a script was developed in Matlab environment, performing the calculations and analysis of electrical voltages, switching and harmonics, using one period of the converter output fundamental. The order of development follows. For a better understanding of what are the following variables, the reader can return to Figure 7.

1. Definitions: DC bus voltage V_{dc}, converter power, modulation index m_a, modulation technique, power factor pf and switching frequency f_{sw};
2. Calculation of V_{ab};

3. Calculation of V_{no};
4. Calculation of V_{ao};
5. Sampling V_{ao};
6. Calculation of phase pulse duration δ_t;
7. Calculation of switched V_{ao};
8. Calculation of switched V_{no};
9. Calculation of switched V_{ab};
10. Calculation of switched V_{an};
11. Harmonic analysis

The block diagram for the system operation modeling is shown in Figure 28, with the letter 'x' meaning a generic phase.

Figure 28 – Algorithm for SVPWM system operation modeling

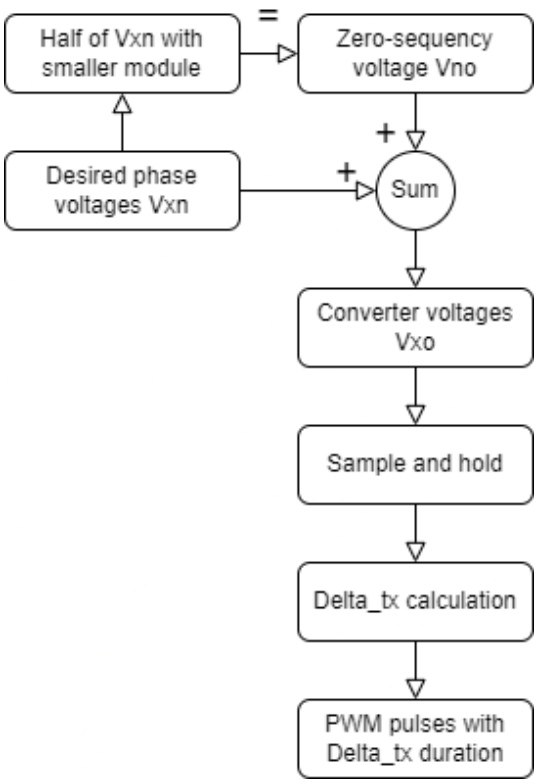

4.1.1 System operation definitions

Some variables are needed as model inputs, such as DC bus voltage V_{dc}, converter power, modulation index m_a, modulation technique, power factor pf and switching frequency f_{sw}. A brief discussion of each follows.

The DC bus voltage was discussed in Section 2.4, being established as a parameter the maximum voltage of $800V_{dc}$. With the maximum DC voltage selected, it is also necessary to consider that DC voltage varies during operation, so that the converter need to be able to support a wide range of input voltages. The main three causes for DC bus voltage variation are the battery discharge, the regenerative braking and the voltage drops across DC bus impedances.

Regarding the voltage variation due to battery discharge, this effect will have a different amplitude for each type of battery chemistry. In the case of this project, Samsung 40T batteries were used, with a INR lithium-ion LiNiMnCoO2 chemistry. The characteristics are presented in Table 4.

Table 4 – DC bus voltage variation due to accumulator discharge, cells in a 190 series connection

	Cell voltage	DC bus voltage
Minimum	3.3 V_{dc}	627.0 V_{dc}
Nominal	3.6 V_{dc}	684.0 V_{dc}
Maximum	4.2 V_{dc}	798.0 V_{dc}
With peak current and 50% SOC	3.3 V_{dc}	627.0 V_{dc}

The issue of regenerative braking effect on DC bus was not addressed in the scope of this work, and will be indicated as part of future developments. However, it can be indicated beforehand that flux weakening can be done to avoid unwanted voltage increases on the DC bus.

The impedances on the DC bus (battery-bus impedance, natural bus impedance, bus-converter impedance) also have voltage drops and affect the observed waveforms. This effect causes variations in the input voltage for the power switches, and must be considered when sizing the DC bus. However, it was disregarded for the initial purposes of electrical and thermal dimensioning of the power switches.

Regarding the converter power, it was discussed in Section 3.2. In this context, different possibilities are presented: thermally dimensioning the converter according to the rated power of its operation, or according to the maximum power. In order to use the rated power, it would be necessary to make an in-depth analysis of the issue, since the thermal constants of the converter are different from the thermal constants of the electric machine. The safest form of dimensioning was used in this case, considering the worst case scenario as the motor maximum power. It is also important to remember that the electric machine has an efficiency, so the power supplied by the converter is even greater than that present in the shaft. The power considered was obtained in a simplified way as being approximately equal to the motor's maximum output power divided by the motor's rated efficiency, see Equation 4.1.

$$P_{max} \approx \frac{P_{m,max}}{\eta_{m,nom}} = \frac{36000}{0.95} = 37.9kW \tag{4.1}$$

where P_{max} is the maximum converter power (W), $P_{m,max}$ is the maximum motor power (W) and $\eta_{m,nom}$ is the rated motor efficiency

At this point it is also important to introduce the concept of modulation index. Given a certain input voltage, the converter is able to control the output voltage amplitude through switching. The modulation index is the variable that will indicate this, being proportional to the amplitude of the output. It is important to take extra care when using this variable, since there are two different and commonly used definitions. Some authors refer to the unit modulation index as being in six-step operation, other authors refer to the unit modulation index as being in SPWM operation. Table 5 presents the values for each definition. This work uses the reference in SPWM, in order to facilitate the scientific community that already operates with the definitions and formulations used in the widely known work of Mohan et al. (1995).

Table 5 – Setting the modulation index on different reference types

	Six-step reference	SPWM reference
SPWM	m_a = 0.785	m_a = 1
SVPWM	m_a = 0.907	m_a = 1.155
Six-step	m_a = 1	m_a = 4/π

The variation in the definition of the modulation index, generates different formulations that relate the voltage at the DC bus, with the output line voltage. Equations 4.2 and 4.3 present the two formulations. In any case, it can be observed that higher modulation ratios generate higher values of line voltage, without changing the need to change DC bus voltage.

$$V_{line,RMS} = V_{dc} \times \frac{\sqrt{3}}{\sqrt{2}} \times \frac{2}{\pi} \times m_a \tag{4.2}$$

where m_a is the modulation index with reference to six-step operation

$$V_{line,RMS} = V_{dc} \times \frac{\sqrt{3}}{\sqrt{2}} \times \frac{1}{2} \times m_a \tag{4.3}$$

where m_a is the modulation index with reference to SPWM operation. Formulation used in this work.

Regarding the modulation technique, it is discussed in Section 2.6. After presenting other modulation methods, the solution adopted was the SVPWM modulation (m_a=1.155), including the possibility of overmodulation, until reaching the six-step operation (m_a=4/π). In this way, the classic SVPWM method can be used, associated with the full utilization of the DC bus voltage present in the six-step. More about the algorithm and the transition between these modulations can be found in the work of Peroutka e Glasberger (2006).

The power factor is a different issue. As this converter feeds a PMSM (Permanent Magnet Synchronous Machine), there is the possibility of stable operation with unity power factor (ANDREESCU et al., 2012), but as previously stated, in automotive application is advantageous to operate in flux weakening region, where the power factor is less than one.

4.1.2 Voltage waveforms

Although the switching frequency of this work is 100kHz, as stated in Section 2.4, the figures are shown with a switching frequency of 20 kHz to facilitate the visualization of the waveforms. The calculation is initiated with the reference phase and line voltages as seen in Figure 29. All analysis will be done with the nominal voltage of Table 4.

Figure 29 – Model reference phase and line voltages

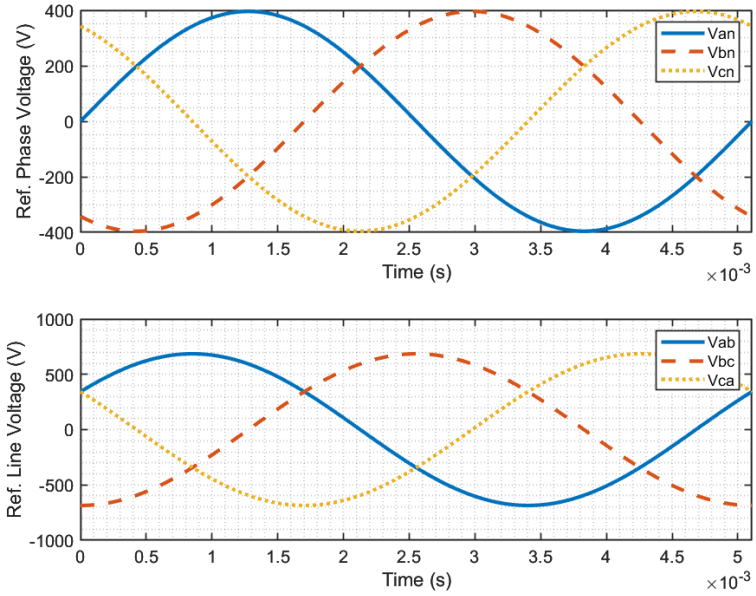

With the basic reference voltages, it is necessary to follow the algorithm presented in Figure 28, observing which phase voltage has the smaller module and dividing it in half to obtain the zero-sequency voltage V_{no}. Finally the converter reference voltage is obtain by the sum of the two, see Equation 4.4 and Figure 29.

$$V_{an} + V_{no} = V_{ao} \tag{4.4}$$

Then the sample and hold process is performed, as seen in Figure 31. The Δt_x waveforms are the same, but related to the period, see Equation 4.5.

$$\Delta t_x = \frac{T_s}{2} \times \left(\frac{V_{xo,samp}}{\frac{V_{dc}}{2}} + 1 \right) \tag{4.5}$$

where Δt_x is the phase pulse duration, T_s is the switching period and $V_{xo,samp}$ is the converter sampled output phase voltage

Figure 30 – Model reference voltages

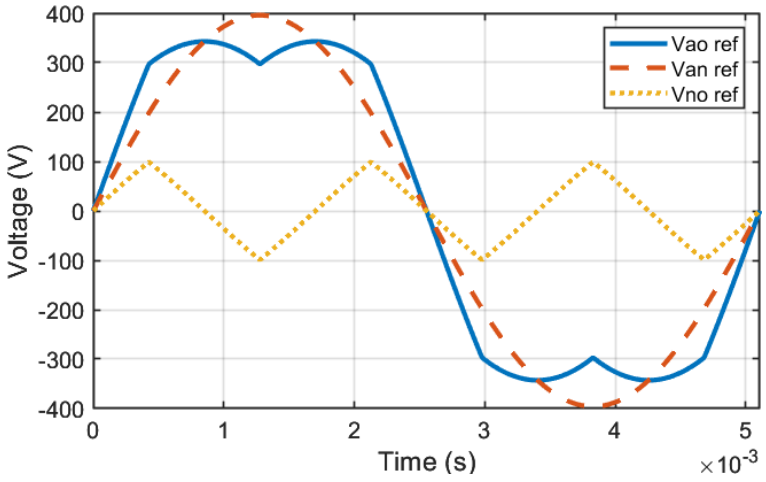

Figure 31 – Model sampled converter voltages $V_{xo,samp}$, ($f_{sw} = 20kHz$ only for visualization)

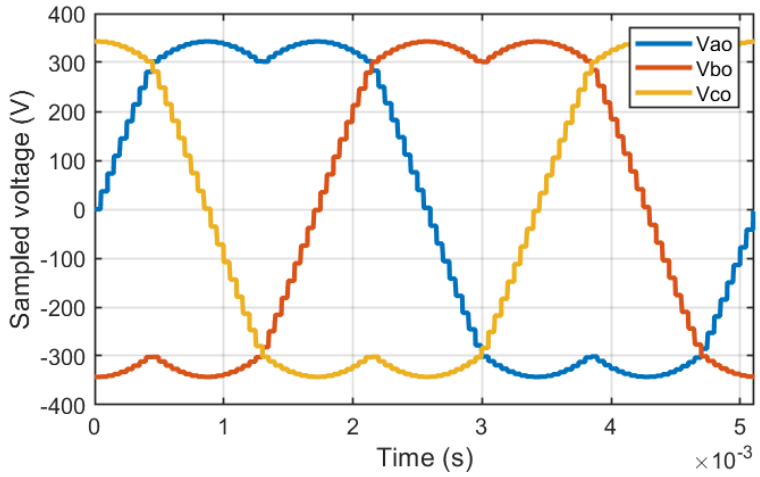

Then the switched converter output voltages V_{xo} are calculated. They are equal to $+V_{dc}/2$ during the centered pulse and $-V_{dc}/2$ otherwise, see Figure 32. It is very interesting to observe the switched waveform to better understand how the system works. When the converter needs to modulate an instantaneously higher voltage, it will use a higher duty cycle (closer to 1), when the output voltage is zero it will use a duty cycle of 0.5 and finally when the instantaneous voltage decreases, the duty cycle will decrease (approaches zero).

The phase and line voltages are obtained based in the previously calculated waveforms, as shown in Figures 33 and 34. It is interesting to observe all these characteristic waveforms, because they are what needs to be observed in the results of this developed converter.

Finally, it is also interesting to observe the converter voltages in the frequency domain, performing the Fourier transform of the signals V_{xo}, as shown in Figures 35 and 36. Here the switching frequency ploted is actually 100kHz. It is possible to observe the third harmonic injection performed in the SVPWM method, with harmonic components in the switching frequency range, effect directly generated by the switching. Also interesting to point out that the

Figure 32 – Model converter output voltage: V_{ao}, ($f_{sw} = 20kHz$ only for visualization)

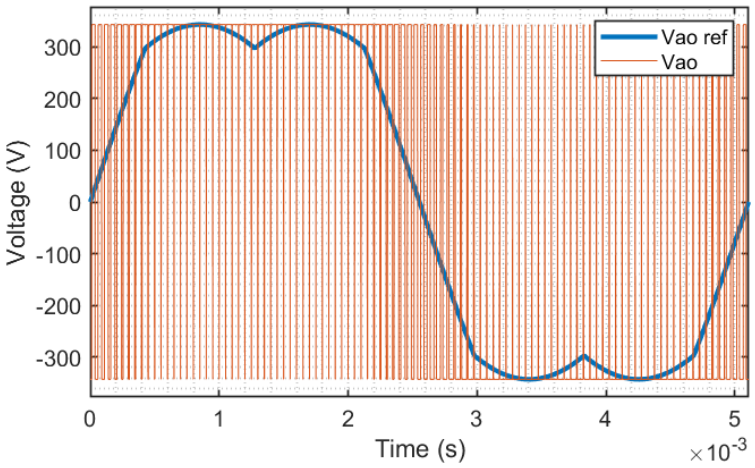

Figure 33 – Model phase voltage: V_{an}, ($f_{sw} = 20kHz$ only for visualization)

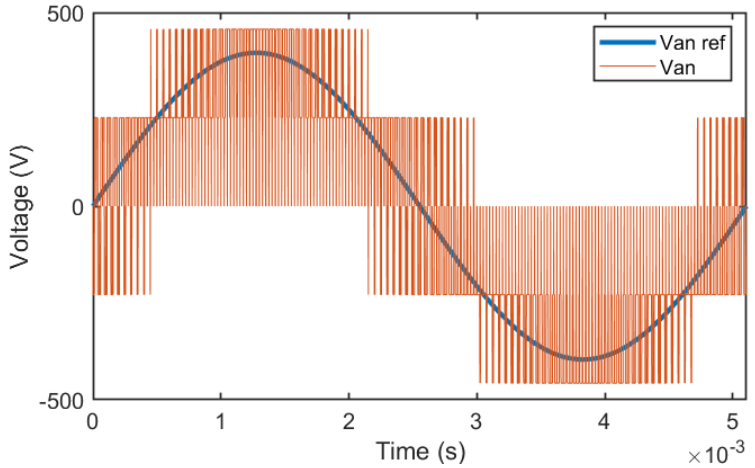

Figure 34 – Model line voltage: V_{ab}, ($f_{sw} = 20kHz$ only for visualization)

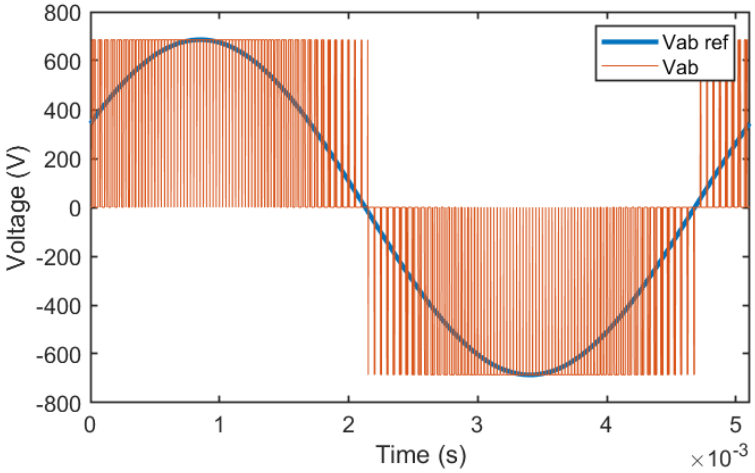

next relevant harmonic injection occurs near the switching frequency, in this case far away of the nominal modulating frequency of 196Hz.

Figure 35 – Model converter output voltage V_{ao} in frequency domain, low frequency spectrum (actually used $f_{sw} = 100kHz$)

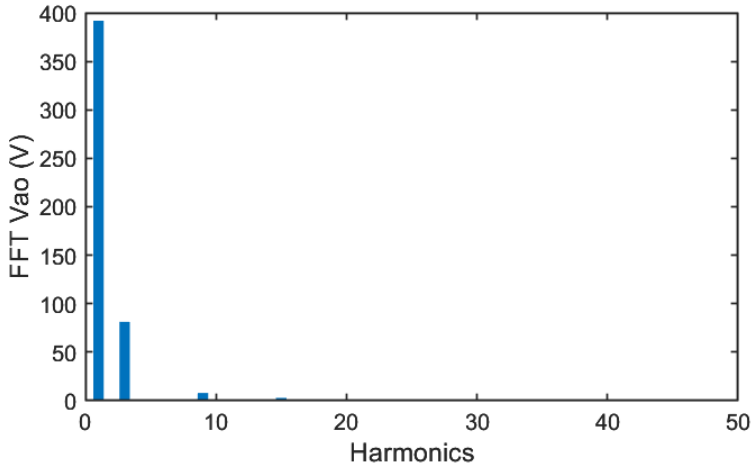

Figure 36 – Model converter output voltage V_{ao} in frequency domain, high frequency spectrum (actually used $f_{sw} = 100kHz$)

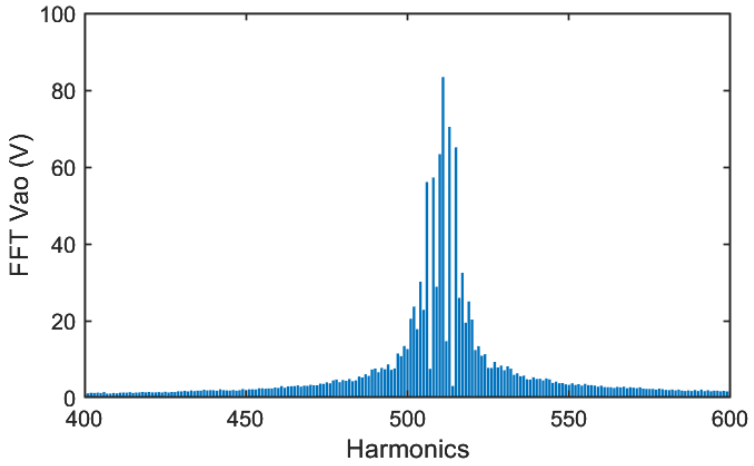

4.2 Power switch

With the system operation model developed and the voltages calculated, it is possible to proceed to the sizing of the power switches. This is a multivariable process, since a wide range of factors must be considered, such as the geometric characteristics of their allocation in the converter, cooling system, chemical technology, cost, among others. A basic algorithm for the switch sizing is shown in Figure 37.

To be able to develop the thermal model, a component needs to be selected. With the volume limitations of the in-wheel system, it is critical to analyze the geometry of the assembly and PCB connections and select an adequate packaging for space saving. Geometry and packaging also have a direct influence in the converter thermal characteristics and cooling solutions. Regarding the power switches packaging, information can be found in Appendix C. Regarding modularity, the possibilities are below.

Figure 37 – Algorithm for power switch sizing

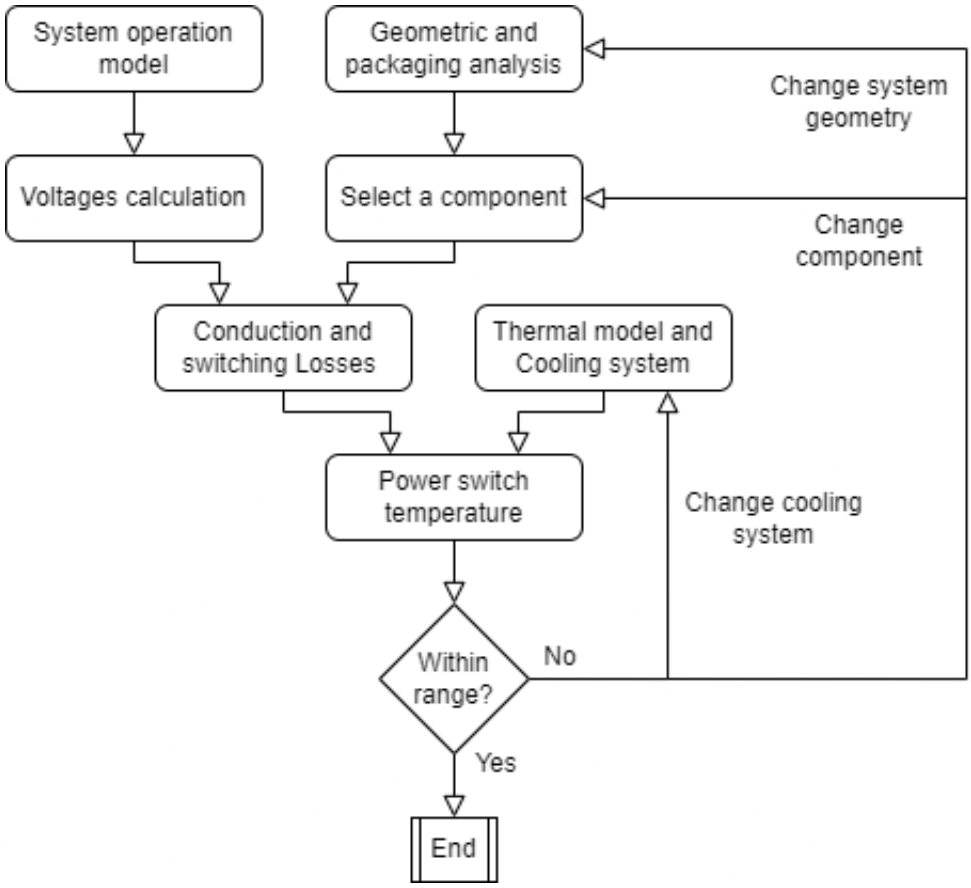

- Discrete components, i.e., one packaging per switch;
- Half-bridge module, packaging with 2 switches;
- Three-phase module, packaging with all 6 switches.

Three-phase modules are very simple to assemble, and are also more robust and have less flexible dimensions, as they have a single case covering all power switches, see Figure 120. Discrete component solutions tend to be more suitable for systems with dimensional constraints, since they give the designer more flexibility in choosing a spatial arrangement. In this case, the designer will have a series of options, such as the classic HiP247 packaging, see Figure 118, solutions that facilitate the use of 3D space, such as the STPAK packaging in Figure 121, and even solutions that optimize space with pins below the IC, such as PowerFLAT packaging in Figure 122.

In this work, a study was carried out of several different spatial arrangements, with different packaging solutions. The least feasible number of the converter assembly planes was tried, for reasons of simplicity and cost. After several iterations, the D3PAK-3 was an option of great interest, since its pin arrangement allows a 2D planar assembly in a reduced space. But at the end, the three major specifications used to select the packaging, was that the switch needed

to have automotive certification, in-depth datasheet informations and Kelvins pins. Kelvin pins are the solution used to separate the power source pin from the source pin connection to the gate driver. More about that will be presented in Section 4.4. A final packaging that fulfilled all this three conditions was the TO-247-4L, being the one chosed in this work.

With the geometry analysis and a packaging selected, a specific component is proposed and the thermal analysis is made. This analysis is critical to indicate if the select power switch is suitable for the application, and is performed to ensure that the maximum temperatures of the component are not exceeded.

4.2.1 Thermal sizing of power switches

Thermal sizing is paramount for power converter design, since junction temperatures are the main variables used to evaluate whether the system can deliver the required power. In this case it is necessary to analyze four sources of losses, as follows.

- Conduction losses in MOSFETs
- Switching losses in MOSFETs
- Conduction losses in diodes
- Switching losses in diodes

As a good starting point for the iterative algorithm, a component can be chosen that had a continuous drain current equal to the DC current they will be sized to drain from the DC bus. If desired, parallel modules can be used to divide this current. In this work, with some selected switches the simulations indicated over-temperatures, with the necessity of 2 components in parallel, including the final solution. It is normal to use even more than this, as in the Tesla's Model 3 inverter, that has 4 switches in parallel.

Here the designer has some options. The first would be to use the model done in Section 4.1, obtain also the switched currents and with the datasheet calculate the losses. Although this is a simple way to move forward, it tends to have low precision in the results, since an in-depth thermal analysis needs to consider other factors such as temperature, gate resistance and motor speed. Therefore, the second way would be to use specific software to the thermal modeling of the switches. If there is the possibility to have access to this kind of software, better precision in the results are expected. The solution used in this work is the PLECS, from PLEXIM GmbH.

The PLECS model is shown in Figure 38. It was developed based on a PLECS example (PLEXIM, 2022), of a PMSM current control, which avoided the need of developing a control only for this thermal simulation, therefore reducing development time. As the consideration made is that the inverter input current ripple is provided by the DC bus capacitors, a high inductance is

placed with the battery voltage source. Without this inductance, the simulated battery voltage source provides all the current ripple, which is not a good model of the real inverter.

Figure 38 – PLECS model for power switches thermal sizing

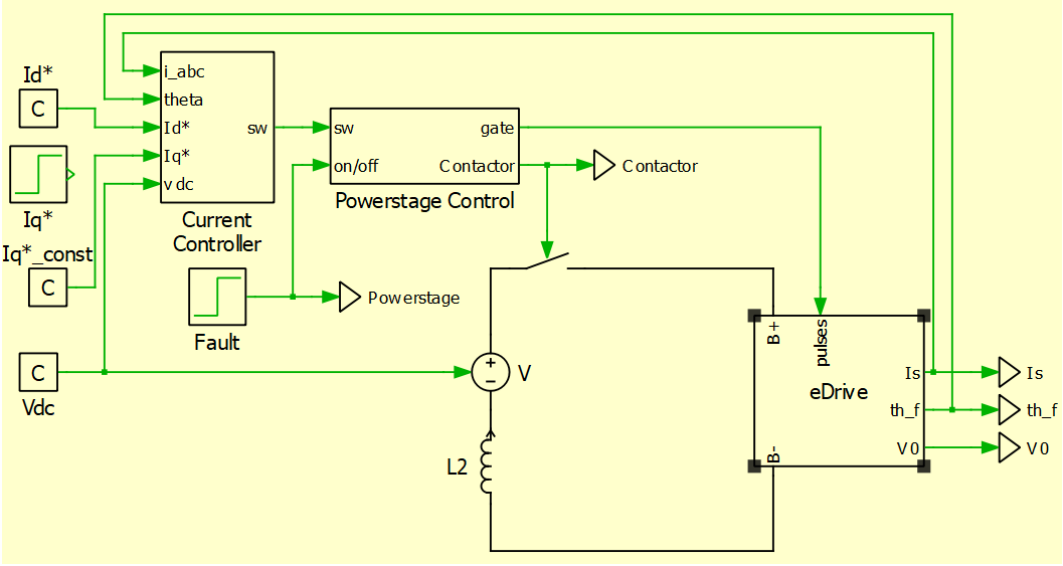

Figure 39 shows what was modeled inside the 'eDrive' block. The example model inverter was substituted by a full descriptive inverter, with the 'MOSFET with diode' block. The thermal analysis may be added with a heat sink involving the six switches, but to be sure that the right calculations are being done, the thermal circuit of each switch was described. At the end, all of them are connected to a thermal capacitor that represents the heat sink per se. Finally it is associated with a thermal resistance, heat flow meter and a grounded constant temperature (representing the exterior temperature). The selected power switch was SCT4018KR (ROHM, 2022).

Figure 39 – PLECS model for power switches thermal sizing, eDrive block

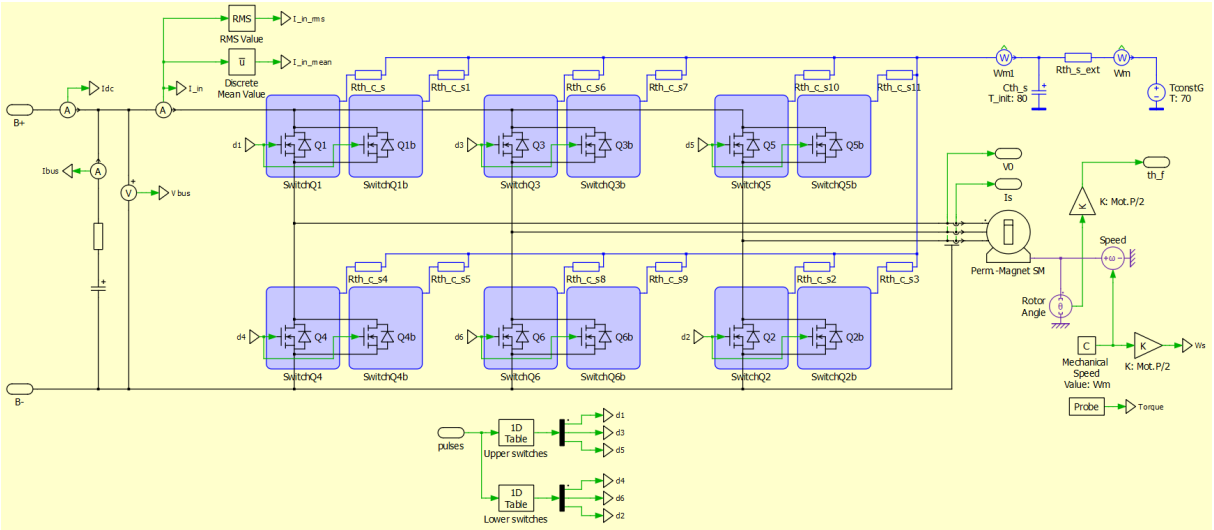

One of the pros of using this types of software, is that a better thermal description of the switch can be considered. The turn-on and turn-off losses are inserted in the model, and shown in Figures 40 and 41. These switching loss curves are not fully provided by the manufacturer, instead it needs to provide 2 curves: "Typical Switching Loss vs. Drain - Source Voltage" and "Typical Switching Loss vs. Drain Current". With this 2 curves, the designer is able to calculate the missing values. The graph is constructed replicating the same 'loss growth with voltage' profile, for the different current levels. It is also important to remember to replicate the data for negative currents, causing this visual mirror effect. If the manufacturer also provides this data at different temperatures, the model can achive even better thermal description.

Figure 40 – Power switch turn-on losses: SCT4018KR

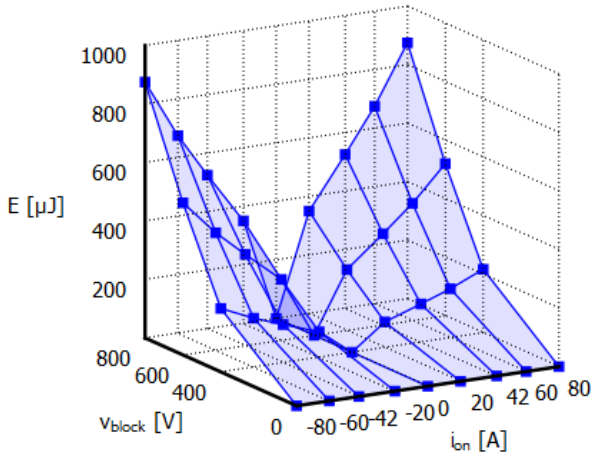

Figure 41 – Power switch turn-off losses: SCT4018KR

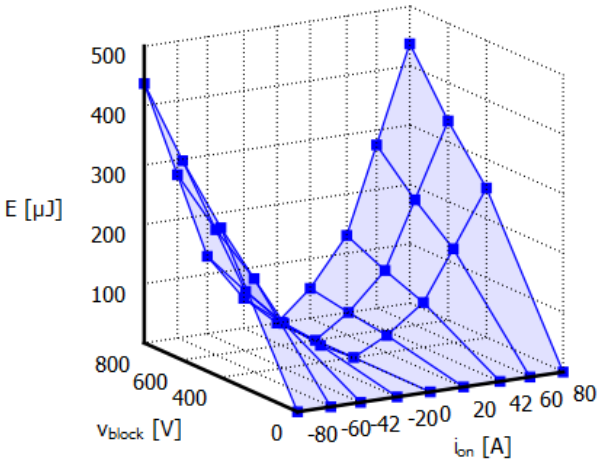

For the conduction losses calculation, the IxV curves for 1st quadrant and 3rd quadrant are needed. In this case the datasheet has curves for different temperatures (25ºC and 150ºC), which is important for a good conduction losses model, see Figure 42.

For the complete thermal model, besides losses, thermal resistances and capacitances are also needed, as follows:

Figure 42 – Power switch IxV curve for conduction losses: SCT4018KR

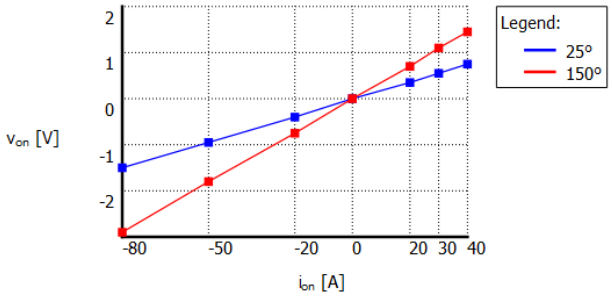

- The junction to case thermal resistance $R_{th,j-c}$;
- The junction thermal capacitance $C_{th,j}$;
- The case to heat sink thermal resistance $R_{th,c-s}$;
- The TIM (Thermal Interface Material) thermal capacitance $C_{th,tim}$;
- The heat sink to exterior thermal resistance $R_{th,s-ext}$;
- The heat sink thermal capacitance $C_{th,s}$.

$R_{th,j-c}$ and $C_{th,j}$ can be extracted from the power switch curve "Typical Transient Thermal Impedance vs. Pulse Width", but also some datasheets have tables for "Typical Transient Thermal Characteristics". Equation 4.6 can be used to extract the capacitance values from the curves, but PLECS is able to do it automatically. Datasheets may also present a wide variety of thermal impedance curves, depending on the duty cycle d_c. In this case, a worst case consideration can be done, and the curve with the bigger duty cycle used (usually $d_c = 0.9$). A lookup table can also be developed by varying these values according to the duty cycle.

$$C_{th,j} = \frac{-t_{Z,th}}{R_{th,j-c}} \times \frac{1}{log\left(\left(\frac{-Z_{th}}{R_{th,j-c}}\right) + 1\right)} \tag{4.6}$$

where $t_{Z,th}$ is a selected time in the curve (s) and Z_{th} is the thermal impedance for that time

The other values are more complicated to be obtained, being highly dependent on multiple factors. The survey or calculation of these thermal resistances and capacitances is a non-trivial task, as they depend heavily on the geometry of the system and the physical characteristics of the materials used. With very simple geometries and in controlled environments, thermal analysis achieves good accuracy, but in systems with complex geometry and variable environment, such as a vehicle wheel, it is very difficult to infer or accurately calculate these variables.

A common path used is modeling in computational fluid dynamics (YANG et al., 2021). These software solutions can be used directly to calculate the system temperatures, but they also demand experience from the designer with the simulation tool, with the results depending on the correct configuration of the boundary variables, the simulation mesh, among other factors

(YUN et al., 2001). Softwares like GT-Suite are other solutions, that are able to include even the cooling system geometry and coolant flow in the power switches model. However, the choice in this work was not to delve into this level in thermal simulations, so as not to depend on the acquisition of these software, as well as to optimize the design time. The variables were selected through datasheets and research of similar systems, so that the objective is not to obtain quantitatively very precise temperature results, but the results order of magnitude. Whatever is needed beyond that, will be adjusted in future developments of the physical system assembly and testing procedures. With the converter under test, it is possible to carry out temperature measurements, correcting and validating the thermal circuit.

Having made all these considerations about the thermal circuit, even if these variables are being obtained through datasheets and research, it is good that they are as close as possible to the real system. The methodology used to estimate the critical variables follows.

- The junction to case thermal resistance $R_{th,j-c}$ were obtained in the datasheet's "Typical Transient Thermal Characteristics" table;
- The junction thermal capacitance $C_{th,j}$ were also obtained in the datasheet's "Typical Transient Thermal Characteristics";
- For the component heat to reach the heat sink, it has to pass through a TIM (Thermal Interface Material), that will constitute a thermal resistance $R_{th,c-s}$. In some cases it is already given in the datasheets. However, for these components it was not given, and research was made to find good considerations for the application. This variable depends on the component packaging and the material used between the component and the heat sink. ST (2018b) work was used to finally infer the value, pointing out that for TO247, a typical value with contact grease is 0.1ºC/W;
- The TIM has also a capacitance $C_{th,tim}$, but as we seek to achieve as minimal TIM thickness as possible, this capacitance is usually disregarded;
- The heat sink to exterior thermal resistance $R_{th,s-ext}$ depend on the heat transfer characteristics of the heat sink and the cooling method. This variable is difficult to find, as well as making considerations with it, since it will depend on the geometry of the system, the flow of coolant fluids, the type of coolant, among others. The best way found to infer this magnitude for the case of liquid cooling was to use data from other heat sinks with liquid cooling (ATS, 2022). As an example, for the supplier researched ATS, $R_{th,s-ext}$ can vary between 0.003 K/W and 0.15 K/W depending on flow rate and geometry. Although large variations are found, this initial research serves to get an idea of the order of magnitude of the values. This work system was compared to the solution with similar dimensions: ATS-TCP-1003, plate heated side, worst-case cooling flow rate of 0.5 gpm, ending up with a considered thermal resistance of 0.015ºC/W;

- Finally the heat sink thermal capacitance $C_{th,s}$, can be directly calculated by the sink's mass times specific heat.

There are also other parameters that will affect power switches temperature, including the use of synchronous rectification as a good solution for reducing losses, and lowering the final temperature. In this work, synchronous rectification was only implemented as a way to increase performance in further design steps, see Chapter 5, and was not included in the thermal model, configuring a worst-case scenario thermal consideration.

Additionally, one of the most relevant variables in the thermal modeling of automotive inverters is the motor speed, and more precisely, the output modulating frequency. If the motor is operating at low speeds, the modulating frequency is also low, so that more time is spent with considerable current on each switch. Therefore, the transitory effect of these low speeds tends to be higher temperatures on the power switches. The solution adopted was to simulate the system at various speed operating points.

Finally, for the external temperature, 70ºC were considered. It is an usual value for the maximum coolant temperature of eDrive components.

4.3 DC bus

With the power switches sized and selected, the next high-impact component in the converter volume is the DC bus. It protects both the accumulator and the power switches from large current and voltage spikes. Hence, the proper dimensioning must include the ripple current requirements and the capacitance calculated from voltage ripple requirements (PEI; ZHOU; KANG, 2014; GUO; YE; EMADI, 2017). Different design algorithms can be used for these components, but the proposed in this work in presented in Figure 43. It is possible to observe that many variables can affect the voltage ripple, fact that links the DC bus design with the gate driver and PCB designs. As there is a relation between different parts of the project, the algorithm necessarily becomes iterative. If one of the variables has not yet been defined, such as the gate resistance, or the dimensions of the PCB traces, initial estimates must be performed, and the algorithm must be iterated. The capacitors selected were 2 parallel and 2 series of the TDK's B58033-SP500 (TDK, 2022). This capacitors are specifically optimized for fast-switching semiconductors and have AEC-Q200 automotive qualification.

Obviously, this methodology described includes simplifications, since a more in-depth methodology would be difficult to understand graphically. A clear example of this is that the rise time of currents not only affects the voltage ripple, but also the efficiency of the converter. In addition to being simplifications for basic explanations of the design process, these methodologies also require future bench validation.

The simplified circuit of the DC bus is no longer sufficient for a correct dimensioning

Figure 43 – Algorithm for DC bus sizing

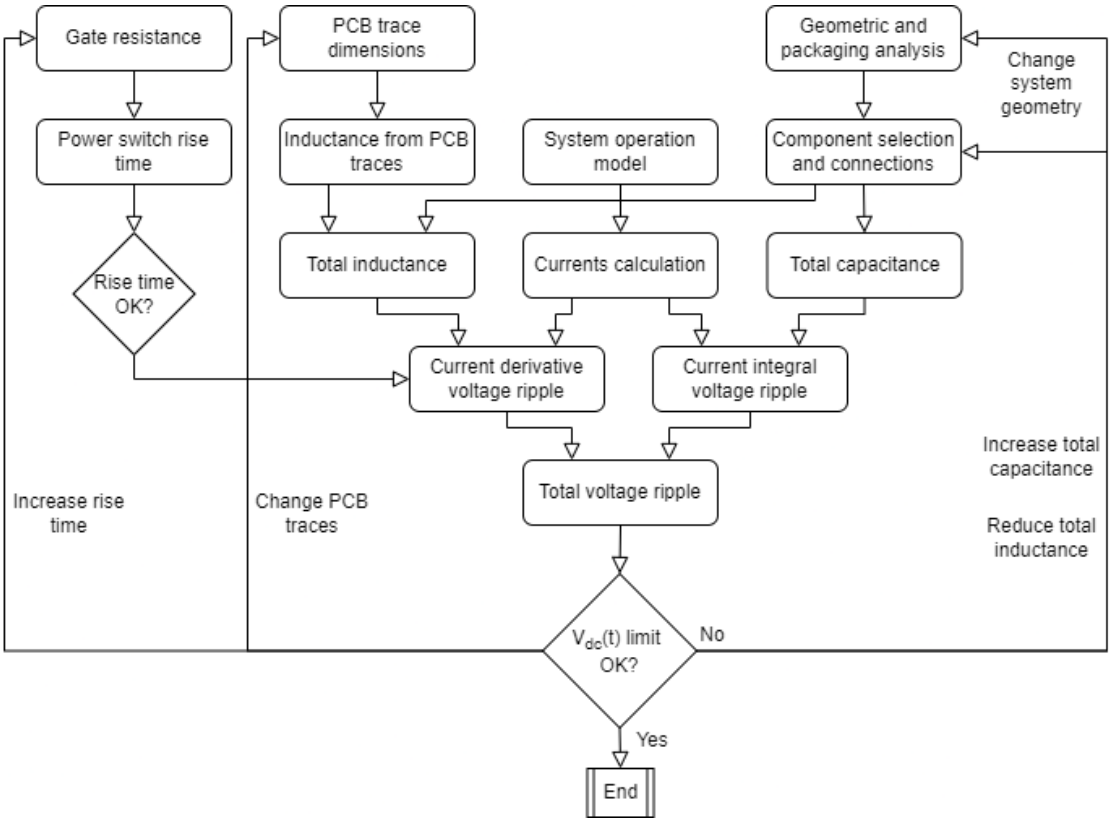

of the components, see Figure 44. The circuit proposed for analysis is presented in Figure 45. The V_{dc} voltage is separated into V_{bat}, V_{bus} and V_{in}. The impedances between V_{bat} and V_{bus} are important for regenerative braking analysis, but they were not considered the scope of this work, being indicated for future development. Therefore, the voltages were considered equal.

Figure 44 – Basic DC bus circuit

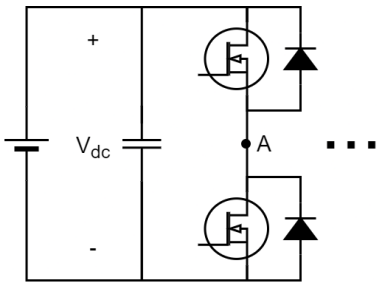

Bus impedances calculation are presented in Equations 4.7, 4.8, 4.9.

$$C_{bus} = \frac{C_{bus,self} \times C_{parallel}}{C_{series}} \tag{4.7}$$

where $C_{bus,self}$ is the capacitance of one capacitor used (F), C_{series} is the number of capacitors in series and $C_{parallel}$ is the number of capacitors in parallel

Figure 45 – Proposed DC bus analysis

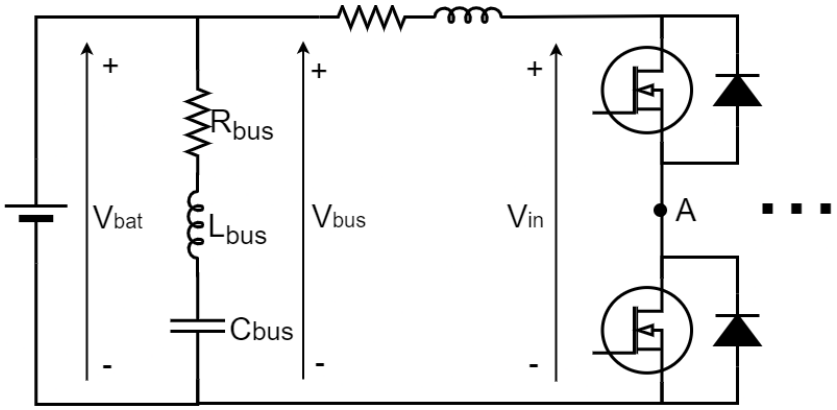

$$L_{bus} = \frac{L_{bus,self} \times C_{series}}{C_{parallel}} \tag{4.8}$$

where $L_{bus,self}$ is the self inductance of the capacitor used (H)

$$R_{bus} = \frac{R_{bus,self} \times C_{series}}{C_{parallel}} \tag{4.9}$$

where $R_{bus,self}$ is the self resistance of the capacitor used (Ω)

For the impedances that connect the DC bus with the switches, an in-depth analysis is recommended. This connection can be done via PCB traces or bus bars. In the case of PCB traces, Hubing, Doren e Drewniak (1994) presents equations for the inductance on the traces, being important to study his work, since the formulations vary according to the general characteristics of the PCB. An example is provided in Equation 4.10.

$$L_{pcb} = \frac{\mu_0 l_{pcb}^2}{2\pi} \ln\left(\frac{s_{pcb}}{a_{pcb}}\right) \tag{4.10}$$

where L_{pcb} is the PCB traces inductance (H), $\mu_0 = 4\pi 10^{-7}$ is the permeability of free space (H/m), l_{pcb} is the lenght of the PCB trace (m), s_{pcb} is the mean separation of PCB traces (m) and a_{pcb} is the transversal area of the PCB trace (m²)

In the case of busbars, which were used in this work, since the format can be non-trivial, an analytical parallel busbar inductance calculation was used (PIĄTEK et al., 2013), but the ideal would be to use CAE modeling for obtaining L_{bar}. A software option that is able to do it is Ansys Q3D Extractor. The resistance can be calculated with Equation 4.11.

$$R_{bar} = \frac{\rho_{bar,ref} \times l_{bar}}{a_{bar}} \times (1 + \alpha(T_{bar} - T_{bar,ref})) \tag{4.11}$$

where R_{bar} is the Bus-to-Switch busbar resistance (Ω), $\rho_{bar,ref}$ is the conductor resistivity in the reference temperature (usually 20ºC) (Ωm), α is the temperature coefficient of resistance, T_{bar} is the Bus-to-Switch busbar temperature and $T_{bar,ref}$ is the reference temperature (usually 20ºC)

With the proposed circuit developed, the specification of capacitors in the d.c. bus is a somewhat non-trivial procedure, involving multiple factors, which follow. The effects will be discussed one at a time.

- Voltage ripple due to the integral of inverter input current
- Voltage ripple due to inverter input current on inductances
- Voltage ripple due to current in resistances
- Current capacity, at switching frequency
- Thermal analysis

Again, software simulation such as PLECS can be used to get a good description of the phenomena related to this sizing process. Here, at first a more in-depth analytical description will be discussed, and after the PLECS implementation will be presented.

Starting with the voltage ripple due to the integral of inverter input current, it is given by Equation 4.12. It is the ripple related to the charge and discharge of the capacitors.

$$V_{C,bus} = \frac{1}{C_{bus}} \int I_{in,rip} dt \tag{4.12}$$

where $V_{C,bus}$ is the voltage ripple due to the integral of inverter input current (V) and $I_{in,rip}$ is the power switches input ripple current (A)

The voltage ripple due to inverter input current on DC bus inductance and DC bus resistance is given by Equations 4.13 and 4.14. The main consideration in this dimensioning is that in the DC bus capacitors, only ripple current $I_{in,rip}$ flows. However, in the PCB impedances, the full current I_{in} flows.

$$V_{L,bus} + V_{R,bus} = L_{bus} \frac{dI_{in,rip}}{dt} + R_{bus} I_{in,rip} \tag{4.13}$$

where $V_{L,bus}$ is the voltage ripple due to inverter input current in L_{bus} (V), $V_{R,bus}$ is the voltage ripple due to inverter input current in R_{bus} (V)

$$V_{Lbar} + V_{Rbar} = L_{bar} \frac{dI_{in}}{dt} + R_{bar} I_{in} \tag{4.14}$$

where V_{Lbar} is the voltage ripple due to inverter input current in L_{bar} (V), I_{in} is the power switches input current (A), V_{Rbar} is the voltage ripple due to inverter input current in R_{bar} (V)

It is essential to understand that the algorithm is concluded when V_{dc} instantaneous limit is not breached. But the proposed circuit shows that this limits needs to be evaluated for two different components: the dc bus (V_{bus}) and the power switches (V_{in}), see Equations 4.15 and 4.16.

Specifically in the case of this work components, $V_{bus,max} = 2 * 500V$ and $V_{in,max} = 1200V$. A worst case of all voltage ripples in phase may be considered, and would be viable for a fast analytical modeling of the system. In reality, this worst case is not reached, since the voltage ripples have a non-zero phase between them, and software solutions like PLECS can do this in-depth simulation.

$$V_{bus,max}(t) > V_{bus,mean}(t) + V_{C,bus}(t) + V_{L,bus}(t) + V_{R,bus}(t) \tag{4.15}$$

where $V_{bus,max}$ is the DC bus voltage limit (V) and $V_{bus,mean}$ is the DC bus mean voltage (V)

$$V_{in,max}(t) > V_{bus,mean}(t) + V_{C,bus}(t) + V_{L,bus}(t) + V_{R,bus}(t) + V_{Lpcb}(t) + V_{Rpcb}(t) \tag{4.16}$$

where $V_{in,max}$ is the power switches voltage limit (V)

Finally, the effects generated by the discharge of the battery in use must be considered, reducing its voltage and increasing the switched current. While bus voltage reduction due to battery discharge tends to generate more freedom for ripple, higher switching current increases ripple.

Finally, a basic thermal analysis is also indicated to get the order of magnitude of the operating temperature. In this case, the selected component's datasheet indicates how to perform this basic thermal analysis (VISHAY, 2021), see Equation 4.17.

$$T_{c,cap} = \left(\left(\frac{I_{in,rip,rms}}{C_{parallel}} \right)^2 \times R_{bus,self} \times R_{th,cap} \right) + T_{amb} \tag{4.17}$$

where $T_{c,cap}$ is the capacitor case temperature (ºC), $R_{th,cap}$ is the capacitor thermal resistance (K/W) and the T_{amb} is the ambient temperature (ºC)

As the voltage equation depend on time, and to get a better thermal model of the DC bus, the PLECS model of Figure 46 was developed. Here the "Mosfet with diode" of the last model cannot be used, since it would force the current in the inductors to change instantaneously. Therefore the components "Mosfet with limited di/dt" and "Diode with reverse recovery" are needed. With a proper configuration of both elements, the simulation can run smoothly.

The capacitor's ESR (Equivalent Series Resistance) and ESL (Equivalent Series Inductance) impact greatly the results of the thermal model, as well as the voltage ripples. Here the designer is faced with another issue: the ESR values vary greatly with frequency, so that a simple value would not be a good model for the capacitor. The solution found was to use a model developed at PLECS that considered this behavior (SCHONBERGER, 2010).

For the complete thermal model, thermal resistances and capacitances are also needed, as follows:

Figure 46 – PLECS model for DC bus sizing, eDrive block

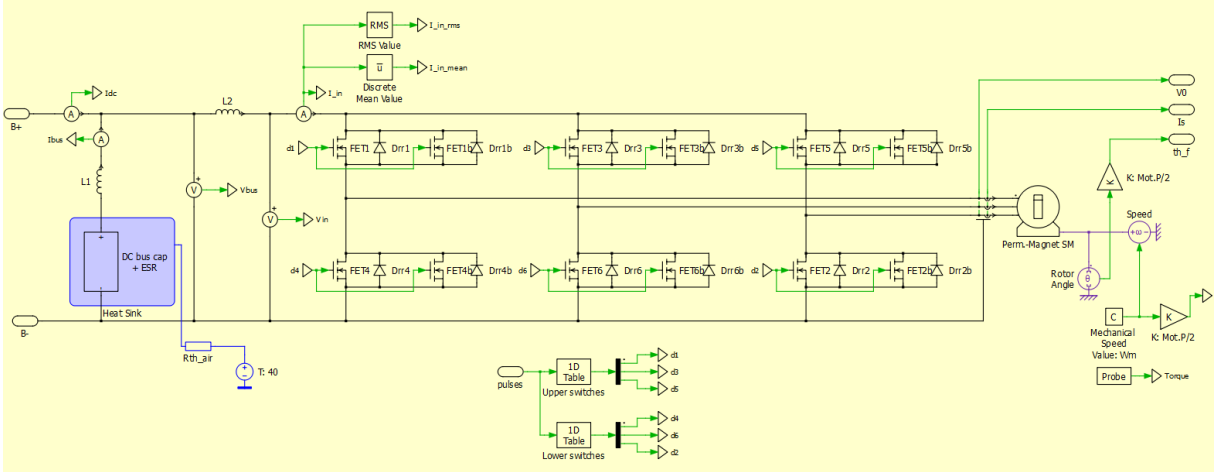

- The DC bus to exterior thermal resistance $R_{th,dc-ext}$. Here the classical convection thermal resistance formula of 1/hA can be used. The area is easy to calculate from the datasheet, and the heat transfer coefficient can be obtained in the work of (KHALIFA, 2001);
- The DC bus thermal capacitance $C_{th,dc}$. It can be directly calculated by the capacitor's mass times specific heat. Mass is easy to find in datasheets, but the specific heat is not a trivial issue, since the capacitor is made of many different materials, including conductors and insulators. A worst case scenario consideration can be done, using the value of the estimated material with lower specific heat of the component, such as copper for example.

Differently from the power switch case, 70ºC for external temperature was not used, since the capacitors are not in contact with the coldplate. The consideration was that they dissipate heat to the external air around them, that will be at 40ºC.

Regarding the current capacity of the capacitors, this is an issue that also needs attention when sizing the DC bus. When talking about application in switched converters, the current levels can be high and the switching are in the order of kHz, generating specific requests for the performance of the capacitors. It is important to observe the ability of capacitors to supply current at the maximum switching frequency used. Generally, datasheets do not provide the data exactly at the desired frequency, so the closest possible data is used. The analysis performed for the current capacity is presented in Equation 4.18.

$$I_{sw,max,cap} > \frac{I_{in,rip,rms}}{C_{parallel}} \tag{4.18}$$

where $I_{sw,max,cap}$ is the capacitor maximum switched current (A) and $I_{in,rip,rms}$ is the inverter RMS input current ripple (A)

At the end, the capacitors are considered sufficient if they do not overheat and the voltage limits are not breached. As previously stated, the component finally selected was the TDK's

B58033-SP50, a CeraLink capacitor. The DC bus was mounted with two of these capacitors in series, since 500V capacitors had the large capacitance needed, but were not able to withstand the DC bus voltages alone. And also two capacitor branches in parallel, due to switched current capacity reasons. There is the option of using, for example, four higher voltage capacitors in parallel. The result would be similar, but in the case of this work it was detrimental to the geometry of the bus bars. Again, the results for the final ripple voltage and temperature are presented in Chapter 6.

4.4 Gate Driver

To perform the specification of the gate drivers it is necessary to have a good understanding of the power switches they will drive, generating the requirements for their operation. In the case of this application with MOSFET SiC's, here are some of the requirements for the gate driver.

- Sufficient peak current for the power switches gates;
- Sufficient mean power for the power switches gates;
- Automotive qualification;
- Isolation between LV and HV;
- High dVds/dt immunity CMTI (Common-Mode Transient Immunity), so that the gate driver remains robust at the high rise times reached by SiC MOSFETs (that can reach more than 100V/ns);
- Active clamping protection;
- "Desaturation" protection or sense overcurrent protection. Fast protection for over-current and short-circuit current, avoiding catastrophic breakdown;
- Miller clamp function;
- High output voltage at the driver, in order to have good noise and interference support;
- May need a negative output voltage in the driver, preventing the Miller effect (together with the low turn-on threshold voltage existing in SiC MOSFETs) from triggering the switch at an undesired moment

To better understand the issues related to the sizing of this critical component for the converter, the simplified circuit of the gate driver and power switches is no longer sufficient, see Figure 47. The circuit proposed for analysis is presented in Figure 48. The additional components in the proposed model are relevant due high values of dV/dt, dI/dt. The discussion

of gate resistances are presented below, as well as the effects of each of these stray capacitances and inductances.

Figure 47 – Basic gate driver circuit

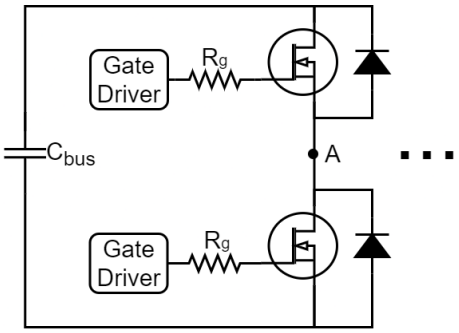

Figure 48 – Proposed gate driver analysis

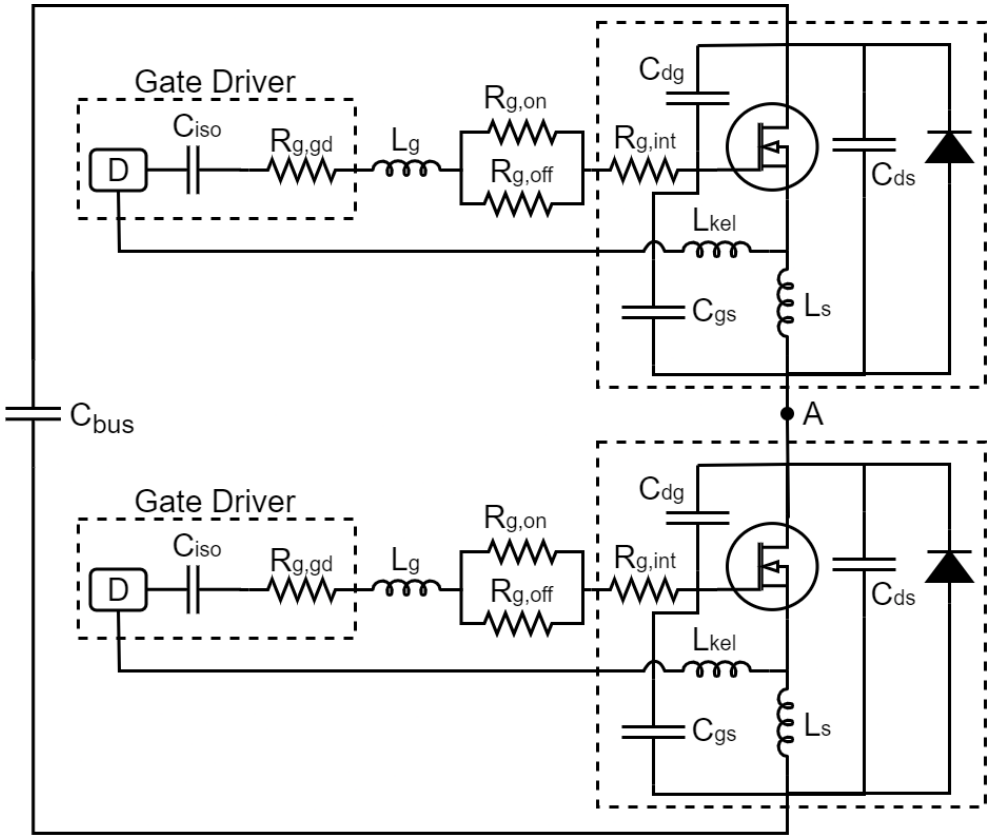

The real gate resistances are composed by three different sources: the gate driver internal resistance, PCB resistors and the power switch gate internal resistance. Besides that, it is useful to separate the PCB resistors for the on and off states, enabling the designer to speed up or slow down the on and off switching process independently. The result for on state is presented in Equation 4.19 and for off state is presented in Equation 4.20.

$$R_{g,on} = R_{g,gd,on} + R_{g,ext,on} + R_{g,int} \tag{4.19}$$

where $R_{g,on}$ is the equivalent gate resistance for on state (Ω), $R_{g,gd,on}$ is the internal gate driver resistance for on state (Ω), $R_{g,ext,on}$ is the external gate resistance for on state (Ω) and $R_{g,int}$ is the internal MOSFET gate resistance (Ω)

$$R_{g,off} = R_{g,gd,off} + R_{g,ext,off} + R_{g,int} \tag{4.20}$$

where $R_{g,off}$ is the equivalent gate resistance for off state (Ω), $R_{g,gd,off}$ is the internal gate driver resistance for off state (Ω) and $R_{g,ext,off}$ is the external gate resistance for off state (Ω)

Selecting the gate resistance depends on several factors. One of them may be the current rise time limit in the power switches that generates voltage ripple on the DC bus, as discussed in Section 4.3. As the gate resistance changes the switching speed, it will also have direct implications for switching losses. Higher gate resistances slow down switching, having opposite effects on MOSFETs and freewheeling diodes. In the case of MOSFETs, decelerating the switching generates more losses, since the crossing of current and voltage transients becomes wider. However, in the case of freewheeling diodes, decelerating the switching reduces the current spikes, also reducing the reverse recovery losses. As a further development, would be interesting to analyze the variation in the switching loss in the MOSFET and in reverse recovery of the diode, with the gate resistance, but a the moment the gate resistance used was the one indicated by the datasheet.

If there would be the need to change the gate driver resistance, it could be specified based on the rise time needed to not exceed the maximum voltage in the power switches, according to Equation 4.16, see Equation 4.21.

$$t_r = \frac{(L_d|\hat{I}_{in,rip}|) + (L_{bar}|\hat{I}_{in}|)}{V_{in,max} - V_{Cd} - V_{Rd} - V_{Rbar}} \tag{4.21}$$

where t_r is the rise time or fall time of the power switches drain current (s)

With the resistances selected, the dimensioning can continue with the analysis of stray effects. The capacitances of the power switch are relevant stray effects to describe the operation of SiC MOSFETs, since the process of turning a switch on and off is related to the charging and discharging of the capacitance C_{gs}. To analyze this process, the circuit is considered an RC, that in charging is composed of $R_{g,on}$ and C_{gs} and in discharge is composed of $R_{g,off}$ and C_{gs}. Therefore, the gate current fed has a peak given by Equation 4.22, that decreases exponentially and needs to be fed by the gate driver. Care must be taken in comparing components when it comes to this peak current, as some manufacturers report this value through quick short circuit tests, while others will report more practical results with realistic gate resistors.

$$\hat{I}_g = n_{par} \times \frac{V_{gs,on} - V_{gs,off}}{R_{g,on}} = 2 \times \frac{15 - (0)}{3.3} = 9.09A \tag{4.22}$$

where $\hat{I}_g$ is the peak gate current (A), n_{par} is the number of parallel power switches, $V_{gs,on}$ is the gate-source voltage for on state (V) and $V_{gs,off}$ is the gate-source voltage for off state (V)

Besides the peak current, the gate power is calculated by Equation 4.23.

$$P_g = n_{par} \times Q_g \times f_{sw} \times (V_{gs,on} - V_{gs,off}) = 2 \times 170e^{-9} \times 100e^{3} \times (15 - (0)) = 0.51W \quad (4.23)$$

where P_g is the gate power (W) and Q_g is the total gate charge (C)

By selecting out the components that are capable of delivering the required peak current, and the required gate power, the analysis can resume with the other stray impedances issues. Regarding the L_g inductance and the C_{iso} capacitance, they will interact and transient effects can generate problems to the LV circuit. The L_g inductance is proportional to the distance from the gate driver to the gate itself, and can be reduced by bringing both components closer together, as they are generally not inserted in the same PCB, for EMI reasons. Sudden current variations in this inductance can generate considerable voltages, affecting V_{gs} and disturbing the switching process. Also, these voltages appear across the capacitor C_{iso}, since it is the gate driver parasitic capacitance present in the isolation between LV and HV. It is interesting to note that high dV/dt values at this capacitance cause considerable currents to flow into the LV circuit: an effect that must be properly taken care of.

The parasitic inductance in the source to gate connection L_{kel} also has the same effect as L_g in generating disturbances for the voltage V_{gs}. There are some solutions that seek to reduce this effect, such as shorter MOSFET terminal pins, as well as Kelvin pins. Kelvin pins are used to separate the power source pin from the source pin connection to the gate driver, in other others, separate L_{kel} from L_s. This solution can affect not only the stray inductances that the gate driver perceives, but the dI/dt derivatives as well, since the Kelvin pins carry lower currents than the main source pins, thus lowering even further the consequent disturbances for the voltage V_{gs}.

In addition to gate resistance considerations, and the effects generated by stray impedances in the circuit, it is necessary to analyze the potential faults and protection systems required for the gate driver. At this point it is important to understand more about MOSFET operating modes and how they compare to IGBTs. The fact that the devices have different operating modes, with different IxV curves, can make classic IGBT protection circuits not effective in MOSFETs. Figures 49 and 50 show the different operation regions and characteristics of the devices.

Although the curves appear to be similar, IGBTs have a clearly defined active region (also called desaturation region), while SiC MOSFET do not technically go into desaturation. The desaturation region in IGBTs aids in fault detection, as small increases in the current generate large increases in voltage across the device. This works similar to a clamping effect, aiding in fault detection and protection. The difference in the case of a SiC MOSFET device is that this plateau is considerably further from the normal operation of the switch. In other words, although the device operates in its non-linear region (in this case called saturation region), the plateau

Figure 49 – MOSFET IxV characteristics and operation regions (TEJA, 2021)

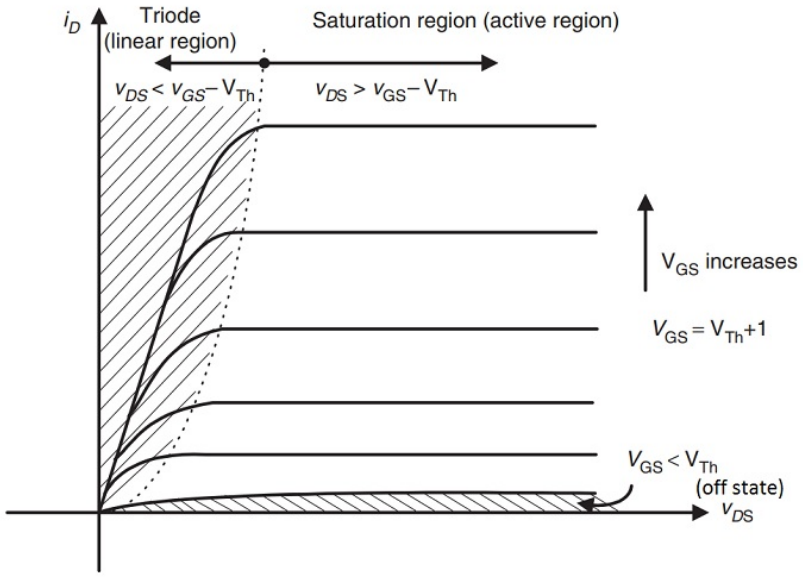

Figure 50 – IGBT IxV characteristics and operation regions (ST, 2014)

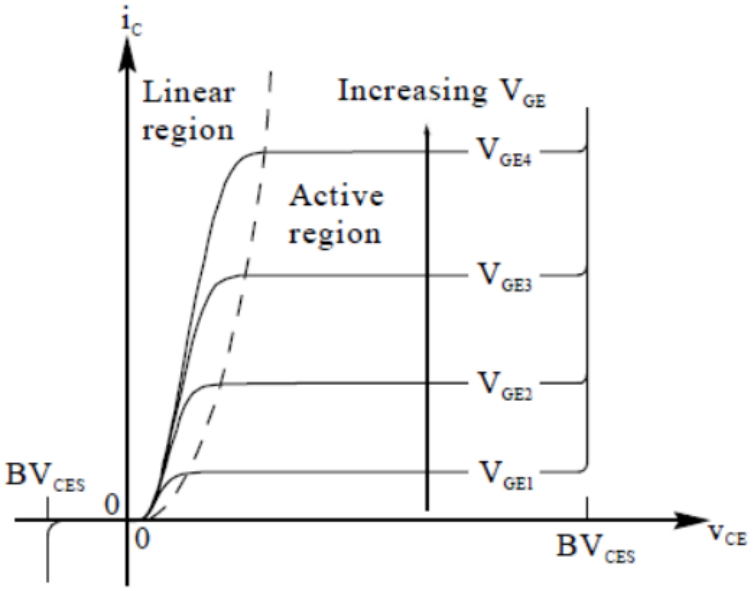

will occur at very large current peaks. This effect makes fault detection difficult, especially in overcurrent protection. Short circuits still tend to be easily detected, but overcurrents are more difficult to detect when compared to IGBTs. Generally, both for silicon carbide and for silicon IGBT applications, it is recommended to use the fast control loop of the MCU to detect overload conditions and leave to the gate driver the protection for short currents. Therefore, the feature known as "desaturation" protection (name used due to the history of its use in IGBTs, although it should be called "saturation protection" when used with MOSFETs), is the protection that monitors the V_{ds} voltage of the switch while it is on, and if the protection threshold is reached, the switch is turned off. It serves exactly to detect the presence of a fault based on the measurement of the voltage V_{ds}.

Another way to perform overcurrent protection is through direct sensing of the current, usually measuring the drain current with a resistor. This solution has a good protection response, but it is not widely used due to the losses in this measuring resistor.

The next feature suitable for the application is the active clamp protection. This protection acts on drain overvoltage spikes, actively clamping during the MOSFET turn-off. With this solution, the maximum turn-off spike drain voltage is limited, which is another safety feature that makes high frequency operation feasible.

Another undesirable effect generated in parasitic impedances is the Miller effect. This is an effect related to the capacitance C_{dg}. The Miller effect is a phenomenon where the activation of one of the MOSFETs of the leg induces the activation of the other MOSFET. To prevent this from happening, it is recommended both the use of a negative voltage for shutdown and the selection of gate drives with the feature of observing the power switch gates and protecting the system from the event.

In addition to fault detection, it is important that the gate driver does not turn off the power switch too quickly. The shutdown must be done in a controlled way, because high values of dI/dt will generate high voltages on the power switch. Without proper care, an overcurrent protection can damage the switch due to overvoltage.

After all the proposed analyses, and the sizing performed, one of the main characteristic that defined the choice of the gate driver was the automotive qualification. The selected component was the STGAP1AS (ST, 2018a), which is the gate driver present in the inverter of the most commercialized electric vehicle in the world: the Tesla Model 3. In addition to being validated for its mass use in automotive systems, it features all robust and qualified safety systems for the application, including active clamping protection, "desaturation" protection, Miller clamp function and deadtime generation. It was also the most efficient gate driver evaluated in the work of Ma e Gu (2021).

4.5 Current Sensors

Regarding the power PCB, the circuits that need to be on them are obviously the power switches and the DC bus, which will have high voltage and high current, but also current sensors, since the main currents go directly through the sensors.

The three-phase circuit needs current measurement, since it is used for the torque control of the electrical machine, which is performed in real time and based on these variables. Some designers, instead of using a sensor for each phase, use the assumption that the three phases are balanced, to calculate the waveform of the third phase digitally, solution also used in this work.

Another current sensor generally applied in power converters is present in the DC bus. Although this current from the battery, which feeds the DC bus, is already measured by the

BMS (Battery Management System), it is recommended that the converter also performs this measurement, especially with the relevance of redundancy in automotive systems. The converter can use this information for fault detection, and can be programmed to protect the system based in a DC current threshold.

Current sensors also considerably affect the dimensions of the converter, since for measurements that can reach hundreds of amperes, the sensors can have a considerable volume. As the volume and dimensions of the converter are critical issues for the in-wheel application, current sensors must also be carefully selected for volume reduction.

When sizing current sensors, it is important to analyze the minimum and maximum currents, as well as the amplitude of the reading distortion, especially at high current values. It is also relevant to select between digital or analog outputs, being more suitable to use digital sensors for reasons of supportability to EMI, however analog solutions have reduced cost.

- Rated output;
- Galvanic isolation;
- Common mode field rejection;
- Linearity and linearity limits;
- Saturation current;
- Output temperature characteristic;
- Response time

Regarding DC current amplitude, in this work all DC current drained from the battery do not reach 100A, so that a sensor from this value is sufficient. However, at regenerative braking, this current will be negative and may reach different values. So to be sure, a regenerative braking analysis must be done and bidirectional sensors are needed.

Regarding AC current amplitude, bidirectional sensors are usual, since positive and negative currents happen all the time. The peaks until nominal speed also do not reach 100A, but the main issue here is the flux weakening operation, since it injects additional direct current. So to be sure, the flux weakening strategy must be known, with the peak of direct and quadrature current injection.

Regarding the sensor technology, the designer can usually decide between a Hall effect measurement or a shunt resistor measurement. Shunt measurements, although conceptually simpler, have their problems. While for efficiency reasons, it is sought to reduce the value of this resistor as much as possible, there are limits to this reduction. Very low resistance values may

not generate voltage signals with sufficient amplitude to be properly measured with an adequate signal-to-noise ratio.

Hall effect measurement technology is widely used. The current to be measured generates a magnetic field by Ampere's Law, which is measured in the Hall sensor in voltage, according to Faraday-Lenz's Law. As the measurement is performed using magnetic fields, external EMI is critical. However, development has already been carried out in this field, as demonstrated by the work of Latham (2019). The solution in this case was the use of two Hall elements, properly positioned inside the sensor to measure the desired current and reject external magnetic fields (common-mode rejection).

Some possible indications to be carried out for the scientific community are measurement solutions involving bars and cables, such as from Kohshin Electric Corporation, IC measurements from the ACS724, ACS725 and ACS773 families from Alegro Microsystems (ALLEGRO, 2022) and finally the MLX91218 and MLX91219 families from Melexis (MELEXIS, 2021). The sensor family chosen was the Allegro MicroSystems ACS773 200kHz Automotive Current Sensor ICs.

Having finished the sizing of the main components and circuits of the converter, it is possible to move on to present and discuss the development of the power and control PCBs.

4.6 Power PCB design

The development of PCB's for a Power Electronics application is not trivial, being relevant a careful geometric and electromagnetic analysis. In this work, as generally indicated for power electronics projects, the power PCB is physically separated from the control PCB, for EMI reasons.

Since the converter is placed inside the wheel, more vibration and harsh conditions are expected, so that automotive qualifications are a must. Not only the components have to attend to AEC standards, but in this case, an in-depth vibration and thermal analysis are needed. A software like Ansys Sherlock is able to do the complete life prediction for the circuit, and would be suitable for this application. However, this in-depth analysis was not in the scope of this work, and is include in future developments.

Following are the main issues related to power PCB design.

- Thickness and width sizing of the traces;
- Minimum distance between traces due to operating voltage;
- Minimum distance between traces to avoid crosstalk;
- Minimum distance of systems from PCB areas with high and low voltage;
- Geometric complexity, volume reduction and component layout

One of the main concerns related to this development is the effects of high dV/dt and dI/dt in the system operation, generating the need of low inductance traces, and avoiding closed loops where occurs the induction of unwanted voltages. At high frequencies, stray capacitances are also relevant, and can generate considerable losses in the converter.

One of the critical points of power PCB design, is the connection between the DC bus and the power switches, as discussed previously in Section 4.3. These suffer from the current switching performed in the MOSFET's, generating high dI/dt values. The DC bus is designed according to these effects, so a reduction of the inductance of these connections is highly relevant to avoid large voltages between the DC bus terminals and the power switch terminals. The dimensions of the busbars that connect the DC bus to the power switches are the most relevant variables in this regard.

The circuit diagram is presented in Figure 51 and the PCB routing is presented in Figure 52.

Figure 51 – Power PCB diagram

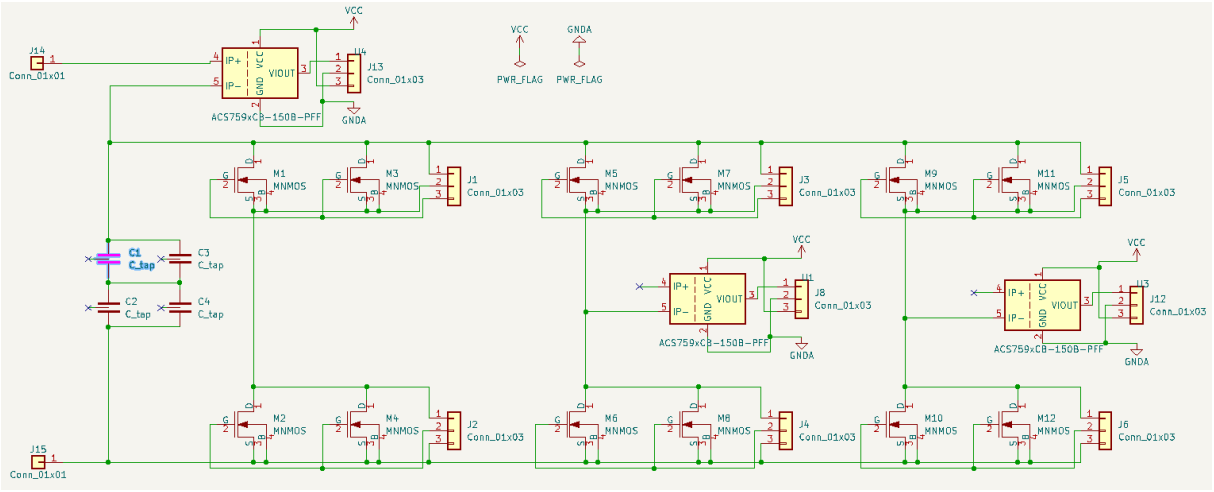

4.6.1 Traces distances

Dealing with high voltages, maybe the first dimension limit that must be defined is the distance limits of the tracks and bus bars. These limits can occur for reasons of operating voltage, crosstalk, or distance from high and low voltage systems.

With long global experience in PCB design, development is permeated with "rule of thumbs". Sharawi (2004) presents the concept of "Crosstalk" as the effect resulting from capacitive coupling (due to electric fields) and inductive coupling (due to magnetic fields) between a group of connections. The interference between traces increases with their proximity, so the author cites the use of $4w_{pcb}$ (separation of adjacent traces by at least 4 times the trace width) in order to reduce the effects of crosstalk.

Figure 52 – Power PCB routing

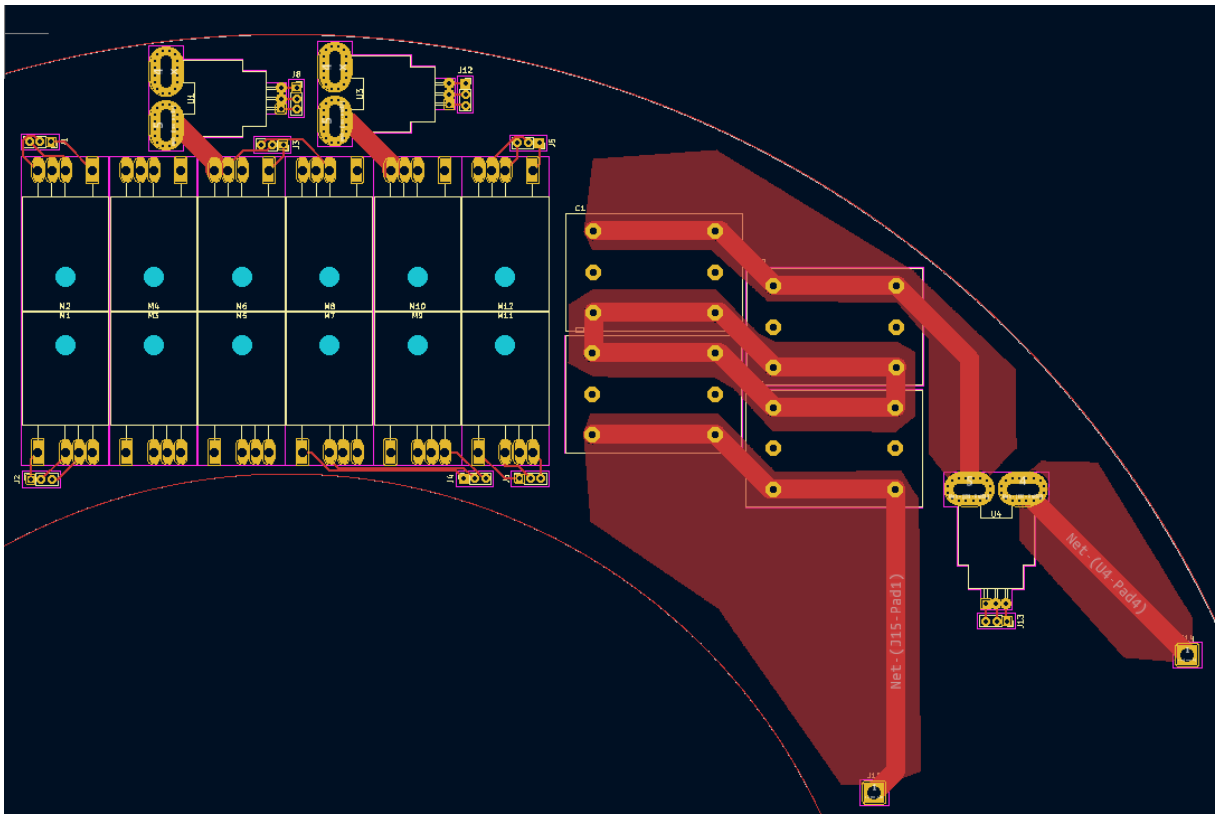

Regarding the operating voltage, there are several relevant regulations to be cited. The two main ones are IEC-60950-1 (2nd edition) and IPC-2221. The IEC standard covers any products with AC main or battery power supply, especially internationally commercialized ones. The IPC-2221 is the generic standard for guidance on PCB, containing a full list of requirements on material quality, traceability, layout guidelines, etc. The distances defined by the standards will be presented either in the form of clearance (distance between the conductors through the air), or in the form of creepage (distance of the conductors through the insulating material of the PCB). The peak value of the DC voltage will determine clearance, and the RMS value of the AC voltage will determine creepage.

There are requirements indicated for safety and requirements indicated for the simple operation of the systems. Where only functional insulation is required, the specific clearance between PCB traces are set only to avoid electric breakdown between them. On the other hand, safety requirements are broader, in order to provide increased protection against electric shock. While IPC-2221 is widely used for functional requirements, IEC-60950 is the standard indicated for finding the safety requirements (ROZENBLAT, 2014). For completeness of information, IEC also provides data for functional isolation, allowing the usage of lesser distance if it withstands the test voltage per Table 5B. UL60950 standard indicates a practical value of 40V/mil (1.57kV/mm). For example, for a peak of 1200Vdc, the IPC-2221 will indicate a clearance of 6mm and the UL60950 will indicate a clearance of 0.76mm.

Regarding the distance from high and low voltage systems, according to IEC 1010, the clearance in air must be 8 mm for overvoltage Cat. III and a working voltage between 600 and 1000 V (DC or RMS). Another interesting documentation on the subject is that of SAE (SAE, 2022), which indicates, in the range of 300 to 600Vdc, to use 12.7mm over surface or 4mm under conformal coating. SAE defines that if HV systems are in the same PCB as LV systems they must be on separate, clearly defined and marked areas of the board. The exception occurs when using ICs such as opto-couplers which are rated for the respective maximum DC voltage, but do not fulfill the required spacing, then they may still be used and the given spacing will not apply.

4.6.2 Traces sizing

Regarding the thickness and width of the traces, formulations for PCB traces are mathematical simplifications of thermal sizing, as they generally include the current in the trace, its thickness, length, temperature rise and ambient temperature. In addition to temperature, voltage drop and trace losses must be evaluated. IPC standards are used, namely IPC-2221A (Generic Standards on Printed Board Design) (IPC, 2003), as shown in Equations 4.24, 4.25, 4.26 and 4.27, with R_{pcb} calculated the in the same way given in Section 4.3 Equation 4.11.

$$a_{pcb} = \left(\frac{I_{pcb}}{k * \Delta T_{pcb}^{0.44}} \right)^{\frac{1}{0.725}} * 6.4516e^{-10} \tag{4.24}$$

where a_{pcb} is the trace transversal area (m²), I_{pcb} is the RMS current in the trace (A), $k = 0.024$ is IPC-2221 constant for internal layers and $k = 0.048$ for external layers, ΔT_{pcb} is the PCB trace temperature rise (ºC)

$$w_{pcb} = \left(\frac{a_{pcb}}{e_{pcb}} \right) \tag{4.25}$$

where w_{pcb} is the trace width (m) and e_{pcb} is the trace thickness (m)

$$V_{pcb} = R_{pcb} * I_{pcb} \tag{4.26}$$

where V_{pcb} is the trace voltage drop (V)

$$P_{pcb} = R_{pcb} * I_{pcb}^2 \tag{4.27}$$

where P_{pcb} is the trace power loss (W)

Therefore, to select trace width and thickness, targets of trace losses, voltage drop and maximum temperature are needed. In the case of losses and voltage drops, obviously they cannot be exorbitant values that make the converter operation unfeasible, but exact values for these variables are difficult to define, being design choices.

In the case of temperature, maximum limits are defined and depend on the type of PCB material used. A very common type of PCB is FR4, where FR4 denotes the grade of the fire-retardant F4 attribute. FR4 PCB is made of multiple layers of glass fiber epoxy laminate material, being preferable amongst manufacturers, due to its consistency of physical properties (CADENCE, 2022). The thermal characteristic of FR4 is denoted by T_g or glass transition temperature, being the temperature where it changes from solid to a soft and rubbery state. Typically, FR4 PCBs are rated to have a T_g of 130°C, but the recommended operating temperature is at least 20ºC lower than T_g, being 110ºC. If a higher PCB temperature is required, there are solutions for that, such as medium T_g PCBs (above 150°C) and high T_g PCBs (above 170°C). For reasons of robustness and safety, a good design decision is to select a high T_g material for the Power PCB, so that it will be considered T_g =170ºC, and the target maximum operating temperature being 150ºC.

Although the maximum operating temperature can be set, it is not trivial to know what the ambient temperature will be to calculate T_{rise}. For simplification, the ambient temperature was considered to be 100ºC, so that ΔT_{pcb} =50ºC. It is essential to validate these values in the converter tests, and to feedback the measured temperatures to this design variables.

With the PCB targets set, the calculation were made with $e_{pcb} = 0.5mm$, resulting in $w_{pcb} = 1.8mm$, $V_{pcb} = 0.15V$ and $P_{pcb} = 5.75W$. These are not obligatory values, instead, these are reference values. Usually, the designer of the PCB should try to increase the width of the high current traces as high as possible, to lower voltage drops and power losses even further. With this in mind, the traces were designed with a base width of $w_{pcb} = 3.5mm$ and copper filled zones were added. At the end, the real traces of the PCB ranged from $w_{pcb} = 7mm$ to $w_{pcb} = 62mm$.

Now, all the calculations can be done in reverse, considering the real minimum value of the trace width to obtain more realistic estimates, resulting in: $w_{pcb} = 7mm$, $T_{pcb} = 105.20$ºC, $V_{pcb} = 0.033V$ and $P_{pcb} = 1.69W$.

4.7 Control PCB design

Having presented the main issues related to the development of the power PCB, a second PCB was developed, with the main function of controlling the power PCB, giving command to the power switches, protecting the system in case of failures and communicating with the vehicle.

Again, since the converter is placed inside the wheel, more vibration and harsh conditions are expected, so that automotive qualifications are a must. Not only the components have to attend to AEC standards, but in this case, an in-depth vibration and thermal analysis are needed. A software like Ansys Sherlock is able to do the complete life prediction for the circuit, and would be suitable for this application. However, this in-depth analysis was not in the scope of this work, and is include in future developments.

Some of the circuits present in this PCB follow.

- MCU circuit
- CAN circuit
- Gate driver circuit
- Voltage sensor circuit
- Current sensor circuit
- Encoder circuit
- Voltage source (or regulator) circuit
- Discharge circuit

High power does not pass through this PCB, but there are areas with high voltage that will follow the requirements previously stated, and areas with low voltage with other requirements. For the IPC-2221 standards, in less than 15V boards the minimum PCB clearance is 0.1 mm for general purpose devices, and 0.13 mm for power conversion devices. With digital signals, the typical rule is to simply follow the $3w_{pcb}$ rule of thumb, where the clearance between traces is triple the width of the trace.

The PCB routing is presented in Figure 53. It has 6 layers, with 3 signal layers and 3 plane layers: ground, 3.3V and 5V.

Figure 53 – Control PCB routing

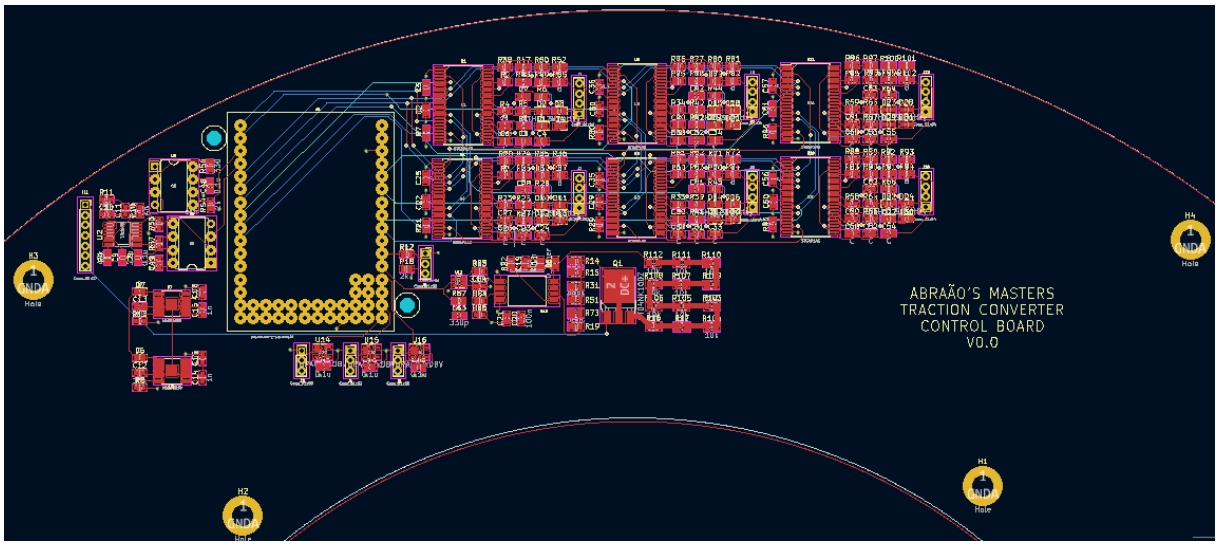

It is also recommended that PCBs developed with analog and digital signals, have a physical separation of the areas where these signals are present, with separate ground planes

also, properly allocated under each respective zone (ROASTO; VINNIKOV; KLYTTA, 2007). If possible, avoid interrupting these ground planes with circuit traces. On the external faces of PCBs, insertion of a ground plane, or power plane, is also indicated, reducing the length of current loops. Figure 54 shows the ground layer planes divided into digital and analog planes.

Figure 54 – Control PCB routing with ground layer visible

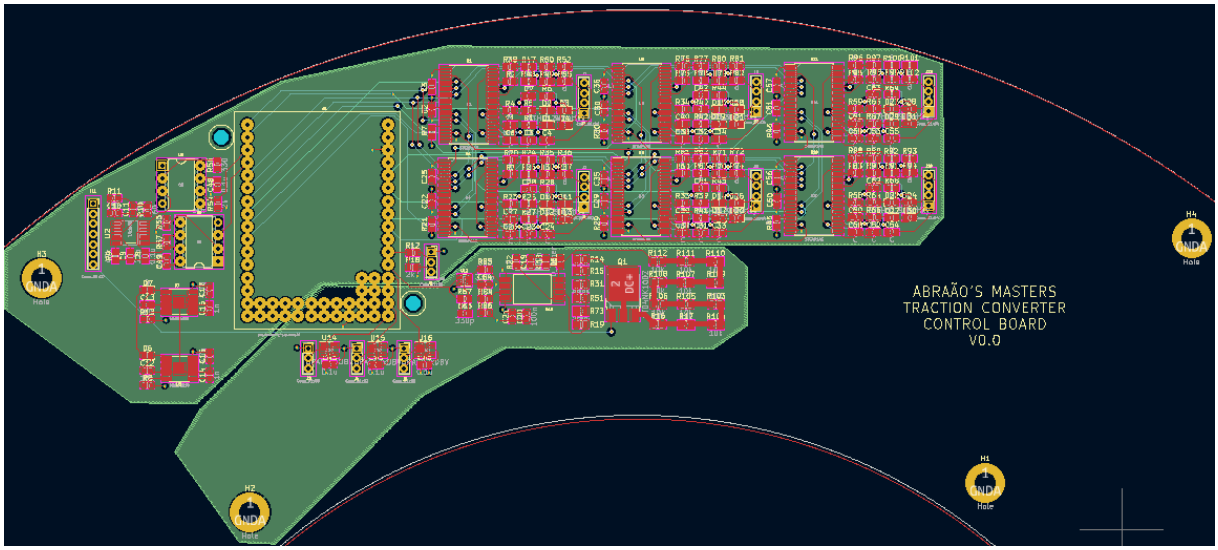

For the current sensors circuit, their signals phases and/or amplitude are critical. Conditioning circuits are needed between the sensors and the MCU A/D converter, as usual. NCV321SN3T1G, an automotive, low power, 1 MHz, rail-to-rail amp-op was used as buffer.

4.7.1 MCU Circuit

To execute the converter command, the central component is the MCU. It is responsible for receiving voltage and current information, running the SVPWM, communicating with the gate drivers and the vehicle. The MCU is the brain of the entire converter, see its diagram in Figure 55.

For commercialization and final version of the converter, it is essential that the MCU has automotive qualification. It needs to have adequate robustness for the application, preferably including a watchdog system for self-assessment of failures. The MCU presented here is not for a commercialized version, but for the first prototype version of the converter, to achieve the specific objective of this work of facilitated power converter prototyping for academia and companies.

The solution selected for prototyping is the Pyboard V1.1, which uses a STM32F405RG microprocessor, and has both a USB flash drive to save your Python scripts and a serial Python prompt for instant programming. Using it, the microcontroller can be programmed

Figure 55 – MCU circuit

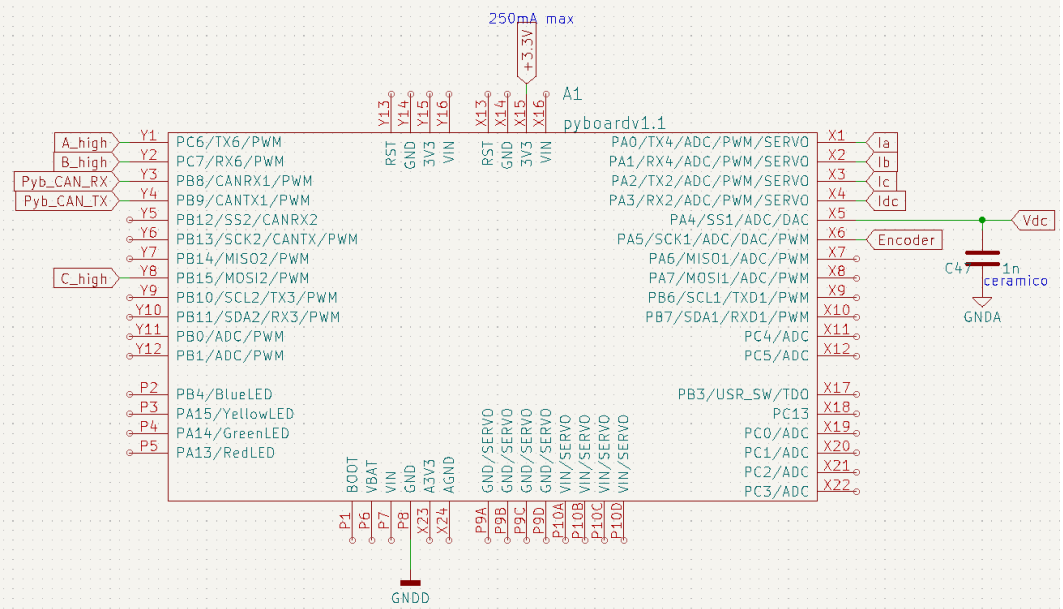

in micropython, following the global trends of programming languages, as presented in Section 2.7.

At a first glance, the Pyboard appears to have all the necessary functionality to carry out this project, in order to inform the scientific community if this type of high-level programming has already reached a sufficient state for advanced control of electrical machines in practical applications. In Chapter 7 the final assessment if the Pyboard was sufficient will be presented.

At its inputs, the board receives the analog signals measuring the currents Ib, Ic and Idc and the voltage Vdc. As previously stated, current Ia is not measured, since it can be calculated using Ib and Ic, and considering that the motor is a balanced circuit. The encoder's digital signal is also received. In addition, it has connections to the vehicle's CAN (Controller Area Network) network and communicates with the gate drivers via SPI (Serial Peripheral Interface).

4.7.2 CAN Circuit

Between the CAN pins of the MCU and the CAN network itself of the vehicle, it is necessary to insert some circuits. Initially an isolation between the two systems is indicated, which is usually performed through optocouplers and finally a CAN transceiver. The development of the CAN circuit was proposed by Yuan et al. (2014), and is shown in Figure 56.

Care must be taken not to share references and supplies, so as not to invalidate the performance of the optocouplers.

Figure 56 – CAN circuit

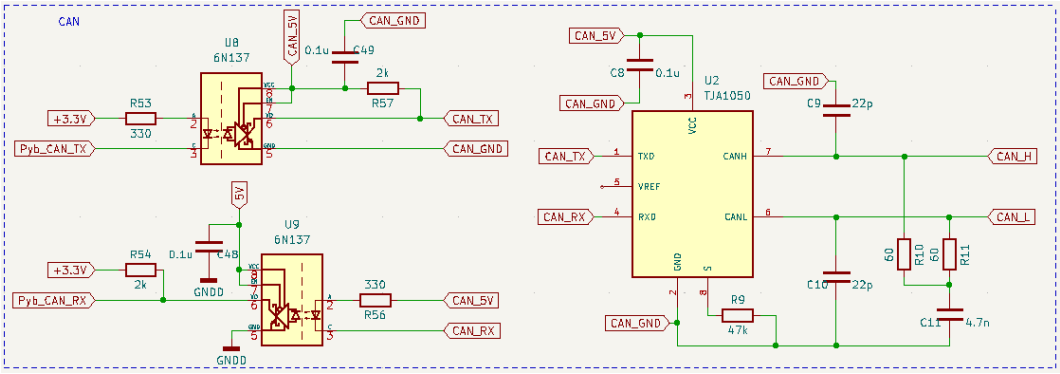

4.7.3 Gate Driver Circuit

The gate driver is a critical converter circuit, as it is responsible for the entire interface between MCU and power switches. All its design and considerations were presented in Section 4.4, with the selection of the automotive STGAP1AS (ST, 2018a). The circuit diagram is shown in Figure 57.

Figure 57 – Gate driver circuit

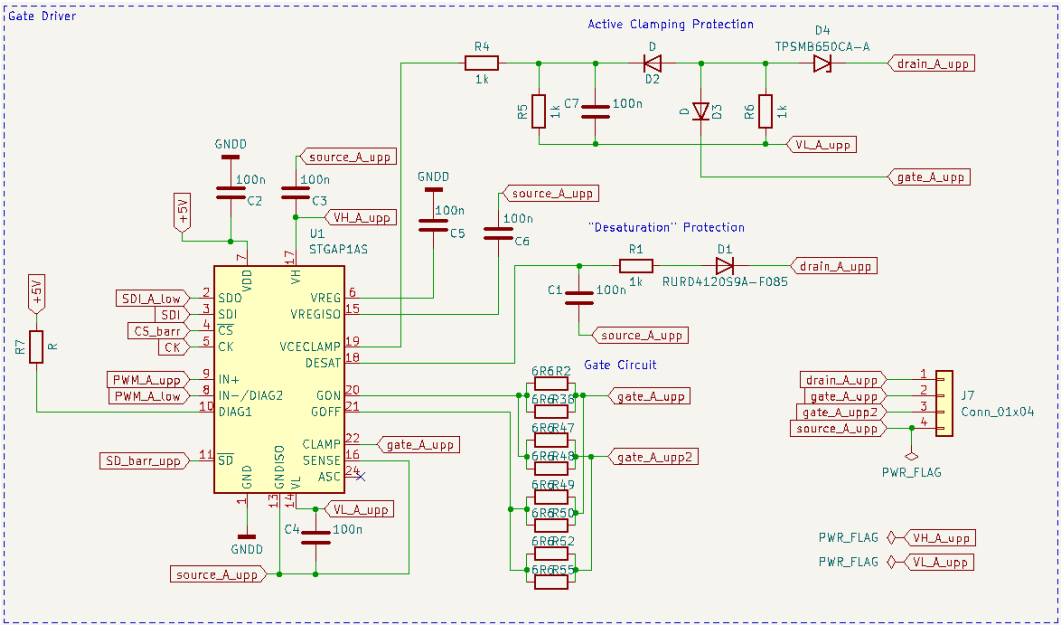

As it is a more complex circuit, another five questions can be raised for the designer to pay due attention to the dimensioning of the IC components and connections, namely, the gate circuit, the SPI communication, the active clamping protection, the "desaturation" protection and the Miller effect clamping.

The gate circuit is critical to the operation of the power switches, affecting the intensity of the dI/dt and dV/dt derivatives in the converter. It should be handled with care, as presented in Section 4.4. If there is a need to decelerate the switching, for reasons of ripple or similar, it is recommended to increase these resistances gradually, always observing the temperature of the

power switches. For redundancy, manufacturers indicate to use different resistors for different parallel switches, and sometimes multiple resistors in parallel to form one, so that in case of failure the gate path can be still somewhat preserved.

In the SPI communication, it is also important to be aware of the way to connect the ICs. The clock and $\overline{CS}$ pins are shared by all 6 gate drivers, but the SDO and SDI pins must be connected in series so that the MCU is able to communicate with all ICs.

The "desaturation" protection circuit is simple, with a capacitor, resistor and diode. Attention however needs to go into this diode, being a critical component, since it will block the entire DC bus voltage, and also need to be automotive qualified.

The active clamping protection circuit main component is also the diode connected to the drain. In this case, a TVS is used. This diode reverse voltage will be the voltage clamped. The remaining voltage will be seen across the resistor right next to it. When the threshold voltage on the VCECLAMP is reached, the gate driver will actively slow down the power switch turn-off to keep a safe condition. The active limiting of the driver's turn-off current strongly reduces the current flowing through the TVS, thus preventing it from operating in overstressing conditions (ST, 2018a).

The Miller effect clamping function is done through the CLAMP pin, without the need of external circuitry. An internal switch in the gate driver pin is activated when gate voltage goes below a voltage threshold, creating a low impedance path between the switch gate and the VL pin, in order to avoid the induced turn-on phenomenon that may occur when the other switch in the same leg is being turned on, due to the C_{gc} capacitance.

4.7.4 Discharge circuit

The specification of the discharge circuit is made based on automotive standards for maintenance and operation safety. The circuit diagram is shown in Figure 58.

Figure 58 – Discharge circuit

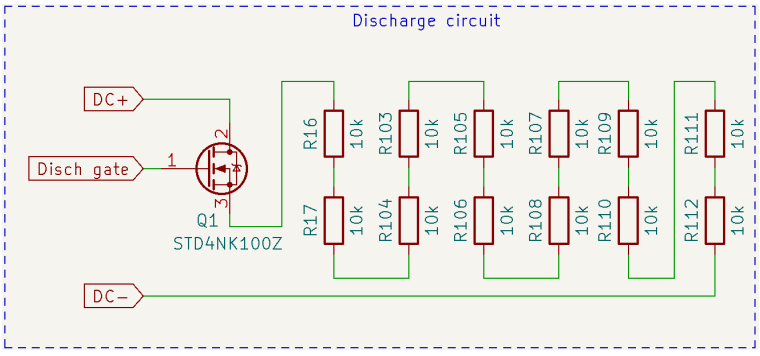

According to (SAE, 2022), the discharge circuit needs to make sure that the voltage in the tractive system drops to under 60Vdc or 25V AC RMS in less than five seconds after

shutdown. The resistance of the discharge circuit is given by a simple RC circuit, as shown in Equations 4.28 and 4.29.

$$V_{dc,disc} < V_{bus,max} \times e^{\frac{-t_{disc}}{R_{disc}C_d}} \tag{4.28}$$

where $V_{dc,disc}$ is the discharged DC voltage (V), t_{disc} is the discharge time (s) and R_{disc} is the discharge resistance (Ω)

$$R_{disc} < \frac{-t_{disc}}{C_{bus} \ln\left(\frac{V_{dc,disc}}{V_{bus,max}}\right)} = \frac{-5}{12e^{-6} \ln\left(\frac{60}{800}\right)} = 160.86k\Omega \tag{4.29}$$

Using twelve 10k resistors in series, the mosfet that drives the discharge circuit has to be able to withstand the $V_{bus,max}$, and a peak current of $V_{bus,max}/R_{disc} = 6.67mA$. As the current is small, virtually any component that supports voltage will have the required current capacity, so that selection can focus on the voltage and the qualification in AECQ101 or AECQ200 norms. The resistors need to withstand the $V_{bus,max}/12 = 66.7V$ and a peak power per resistor of $(V_{bus,max}/12)^2/(R_{disc}/12) = 0.44W$. The resistor chosen was the RA73F2A10KBTDF from TE Connectivity.

Regarding the circuit that triggers the discharge, the discharge circuit switch tends to have large voltage requests, while current requests are reduced. Therefore, one key is not more suitable than the other, and it is possible to use MOSFETs or IGBTs. Anyway, the focus in the case of this application remains on the use of a key with automotive qualification. An interesting feature also for this switch in the case of this project is that the threshold voltage V_{gs} is lower than 5V, allowing the system to be activated with voltages already present on the PCB. A good practice for a critical circuit like this is to be hard-wired, meaning that it does not need microcontrolled logic for its command.

The selected circuit was the STB9NK80Z, which is an automotive MOSFET that supports the DC bus voltage, and has low current, when compared to the other components found. The threshold gate voltage is 3.75V, lower than 5V as desired.

In this circuit, Ansys Sherlock would be particularly relevant, to analyze if the heat dissipated in the resistors would cause further issues for the PCB.

4.7.5 Voltage Sensor Circuit

The challenge of measuring high voltages is considerable. The greater the difference between the measured voltage and the voltage sensor output, the more challenging the task can be, since the percentage errors of the passive components tend to generate greater deviations in the output signal. As indicated earlier, the circuit also needs to be galvanically isolated to protect the LV system. The proposed circuit is shown in Figure 59.

Figure 59 – Voltage sensor circuit

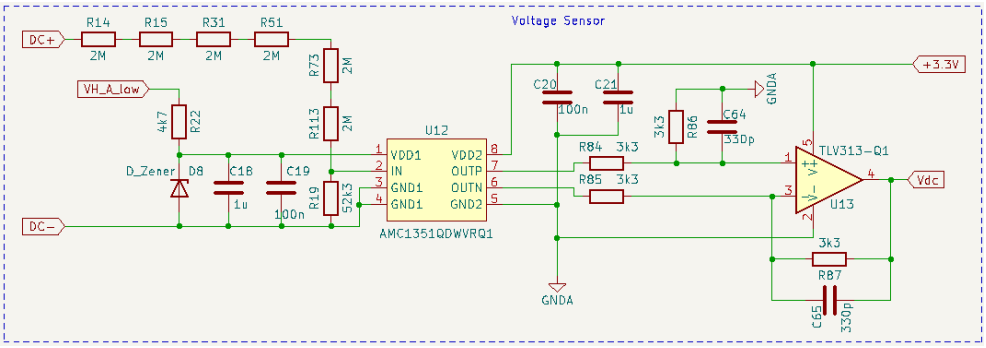

There are different solutions for measuring high voltages. Among them one of the highlights of a classic solution in Power Electronics is the LV25-P from the manufacturer LEM. It is a voltage transducer, which performs galvanic isolation and provides the current output signal. However, in the case of this application, the circuit generates some problems. In addition to its considerable cost, it does not have the proper automotive qualification. The IC also needs +12V and -12V power supplies, two voltages not present on the PCB, which would burden the project with the need to insert two additional sources.

The implemented solution was with the AMC1351-Q1, from Texas Instrument. It is an automotive qualified circuit, which performs galvanic isolation and generates a differential voltage signal. This type of solution also needs a resistive voltage divider at its input, to lower the voltage to the supportable level for measurement (in this case 5V). For the conversion of the differential signal to single-ended output, a TLV313-Q1 automotive rail-to-rail op-amp is used.

At the input side, the sensor is supplied by the low side gate driver. The voltage is clamped to 5V by the Zener and filtered with the capacitors.

Finally, performing voltage division is a task that has its necessary care. Power dissipation and dynamic range issues must be considered. Especially regarding automotive application, as the energy sources are on board the vehicle, energy consumption is critical. The sizing of the voltage divider must prioritize the reduction of losses on it, at the same time that it must generate input voltage and a minimum current sufficient in the IC for it to carry out the measurement. Also, the lower the input voltage of the circuit, the dynamic range becomes an issue. In this project we are in the range of a voltage division by 240, so that 1V on the DC bus will be a signal of only about 4.2mV to be measured.

For selecting the resistors in the voltage divider, the top resistors number is equal to $n_{div} = V_{dc,max}/V_{res,max} = 1200/200 = 6$, not including the lower sensing resistor. Also, the maximum current through the divider is considered to be $I_{div,max} = 100\mu A$, indicated by the datasheet as an example. The sizing calculations follows in Equations 4.30, 4.31 and 4.32.

$$R_{div} = \frac{V_{dc,max}}{n_{div} * I_{div,max}} = \frac{1200}{6 * 100e - 6} = 2M\Omega \tag{4.30}$$

where R_{div} is the resistor value at the voltage divider (Ω)

$$R_{sens,eff} = \frac{V_{dd1}}{(V_{dc,max} - V_{dd1}) \times (R_{div} \times n_{div})} = \frac{5}{(1200 - 5) \times (2e6 \times 6)} = 50.21k\Omega \quad (4.31)$$

where $R_{sens,eff}$ is the sensing resistor effective value (Ω)

$$R_{sens} = \frac{R_{sens,in} \times R_{sens_eff}}{R_{sens,in} - R_{sens_eff}} = \frac{1.25e6 \times 50.21e3}{1.25e6 - 50.21e3} = 52.31k\Omega \quad (4.32)$$

where R_{sens} is the sensing resistor value (Ω) and $R_{sens,in}$ is the internal impedance of the voltage sensor IC (Ω)

The R_{div} resistor chosen was the MCU0805MD2004BP500, $2M\Omega$ automotive high precision solution of 0.1% tolerance, and the R_{sens} chosen was the RG2012P-5232-W-T1, $52.3k\Omega$ automotive high precision solution of 0.05% tolerance. The final power loss of the voltage divider is 120.5mW.

4.7.6 Voltage Regulator Circuit

The converter electronics are powered by the vehicle's low voltage system. However, this power supply is far from an ideal source. The unconditioned rail from the battery is not a simple, steady source of DC current, instead, it is subject to high noise and EMI/RFI. The voltage output of the low voltage battery also change, due to discharging, and the actual supply on the component tends to be lower, due to the impedances of the conductors and connections. All these effects cause the voltage that supplies an automotive system to need great supportability of supply voltage ranges.

Besides all that, the low voltage system of the vehicle supplies only one voltage level, while the PCB circuits needs various voltage supply levels, usually 3.3V, 5V, sometimes 12V and even negative voltages. The best way to deal with these problems is through low power DC/DC regulators and converters.

When selecting one or more circuits to supply power to the converter electronics, it is necessary to pay attention to a series of issues, such as:

- Qualification for automotive applications;
- Quiescent current;
- All circuits supply voltage levels. Minimum, nominal and maximum;
- All circuits supply currents. Minimum, nominal and maximum;

In relation to the quiescent current, it is a critical variable in automotive applications, since in some cases the vehicle can be turned off for dozens of days, draining these currents. High quiescent currents can shorten the life of low-voltage automotive batteries and even cause them to actually fail according to the time the vehicle has been turned off.

A survey of the supply currents of all PCB circuits was carried out, as well as the supportability of the input voltage variation of each component. The 3.3V circuit requires from the source maximum excursion between 3V and 3.6V, and minimum current of 70mA. The 5V circuit requires from the source maximum excursion between 4.75V and 5.25V, and minimum current of 200mA.

Some possible solutions are the LT8603 from Analog Devices and the MAX16930 or MAX16910 from Maxim Integrated, the latter being the one selected in this work as it is currently the cheapest option between the three.

THe MAX16910 proved to be a suitable option for the converter since it operates from a +3.5V to +30V input voltage, with this wide range of supply voltages already been designed to be powered by low voltage batteries in automotive systems. It delivers up to 200mA of load current, so it serves the converter of this project well. If necessary, two can be used in parallel. Regarding quiescent current and shutdown current, it consumes only $20\mu A$ and $1.6\mu A$, respectively. The same circuit can be configured to generate 3.3V or 5V, without the need to use different ICs, which reduces production costs at scale.

With the hardware project of this work developed, now it is time to go to the software and control development.

5 Software and Control

With the hardware development done in the previous chapter, this chapter presents the software and control applied in this project. The programming is done in Micropython, with the application of a FOC (Field Oriented Control) control system for the FSPMSM (Fractional Slot Permanent Magnet Synchronous Machine).

The development of the following items is presented.

- Control topology;
- Electric machine model;
- Speed control;
- Flux weakening control;
- Current control;
- Algorithm implementation.

The PWM generation and code execution time tests were performed using the Typhoon HIL (Hardware in the loop) tool. The tests assembly can be seen in Figure 60.

Figure 60 – Tests assembly using Typhoon HIL and Pyboard V1.1

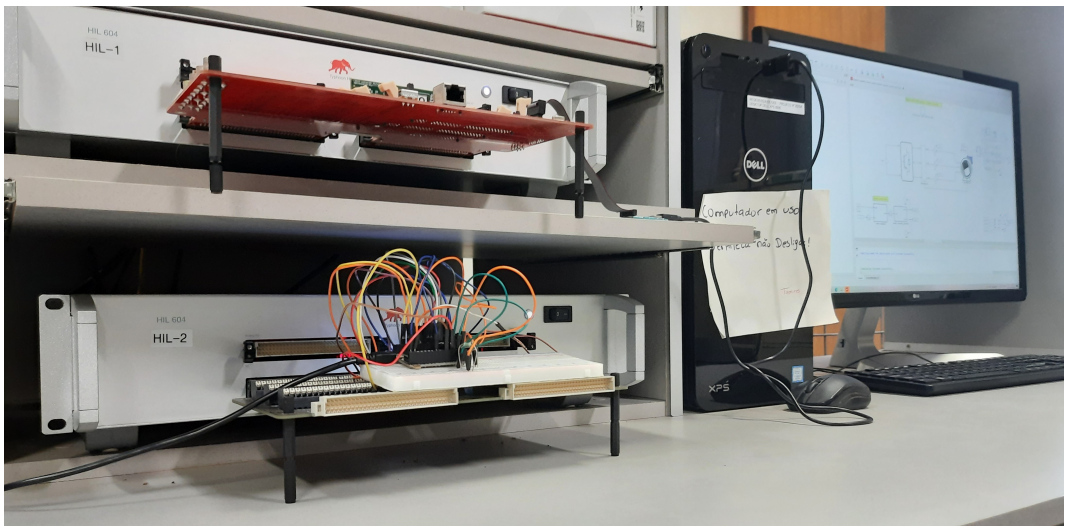

The other codes were tested with the aid of Matlab/Simulink, using Simulink's function block. With this solution, the designer can replace a specific block diagram with a coded function, testing the algorithm coded implementation.

Before the algorithm implementation, the control design is presented. While R&D involving electrical machines is a niche activity, new technologies and improvements to the control system are constantly emerging in all major research centers in Electrical Engineering. From the control of DC machines through the operation of large variable resistors, through the drive of AC motors directly to the grid, to the spread of power electronics. A huge step forward for this sector was vector control, also known as FOC (Field Oriented Control). With mathematical support in the Clark and Park transforms, this proposal makes it possible to decouple the characteristics of torque and flux in the electrical machine, moving from all the electromagnetic complexity of an asynchronous machine to the simplicity of DC machine control.

5.1 Control topology

Researching control technique solutions for electric traction, it is possible to observe that a lot of development has been done in this field. Regarding specifically the control topology for this application, it is important to define the objectives pursued in the development of this system for the vehicle. For each objective, different topologies and control techniques are proposed in the scientific community.

Conceptually analyzing the driver's command in the vehicle, the position of the accelerator pedal informs the vehicle how much torque the driver is requesting. In this sense, it can be argued that the pedal command is to be inserted as the reference to a current control in the electric machine (MORENO-TORRES et al., 2015). The work of Hu et al. (2011) proposes not only the use of torque control with insertion of the pedal signal as a reference, but also a saturation of this torque reference according to tire slip calculations. This technique enables vehicle traction control.

Some authors propose application of speed control. Again, conceptually analyzing the operation of a vehicle, the driver himself generally performs the function of speed controller in closed loop, checking the vehicle's speed and sending an acceleration command through the pedal, with the objective of reaching the desired speed. With the development of autonomous vehicles, the lack of the driver performing this task leaves it to the cruise control, as seen in the work of Lu, Dong e Hu (2019). Vighneswaran e Nair (2018) also proposes the use of speed control. According to the author, cruise control of BEVs increases efficiency, controlling the speed, and maintaining it steady as set by the driver.

Other developments in control systems for electric powertrains are present in the scientific community. The work of Jurca, Ruba e Marţiş (2016) is an example, where a control system is developed to optimize the power factor in electric traction. Another example is the work of Battiston et al. (2014), where the objective is to control the voltage on the DC bus, something that enables regenerative braking implementations. In the same sense, Moreno-Torres et al. (2015) presents solutions for accumulator protection and regenerative braking control using an internal

closed loop of battery current and an external closed loop of DC bus voltage.

Finally, in order to provide the reader with sources for research on the subject, Klerk e Saha (2021) carried out a review of control solutions for automotive electric traction. According to the author, the review indicated that recent literature has focused on efficiency improvements, to increase vehicle range, and ensure motor parameter insensitivity, to develop highly robust and reliable systems.

In this work, speed control, flux weakening control and current control were implemented. These are all options found on commercial traction inverters (EMDRIVE, 2021; PARKER, 2021). Regenerative braking and the analysis related to it, are among the suggestions for future developments. The proposal was to use a cascading solution, with the application of internal current loop, and external speed loop. The development carried out allows the operation through the external speed loop, but also allows bypassing it, with a torque reference externally provided by the pedal, see Figure 61. Color change was used to differentiate the model of the real system from the implemented digital system.

Figure 61 – General control diagram.

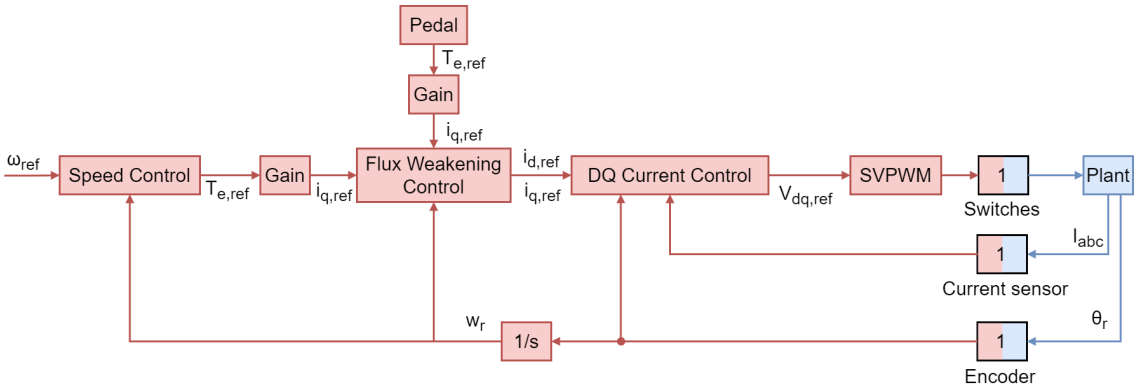

Finally, it is important to point out the differences between the control methodologies called FOC (Field Oriented Control) and DTC (Direct Torque Control). Although both techniques allow torque and flux to be decoupled and controlled independently, (PYE, 2015) points out some differences that are presented in Table 6. The author also comments that this is a basic comparison, and extensive development has been carried out in both techniques to improve their performance.

In this work, FOC was used, due to its better harmonics behavior and familiarity with its implementation. There was no in-depth study beyond that presented in the comparison between FOC and DTC. As the control is done for PMSM, the rotor flux position can be measured via encoder, so that performing the mathematical estimation of this variable is not necessary. Sensorless application is also possible for PMSMs (KIM; EHSANI, 2004), but it was not included in the scope of this work.

Next, a model of the PMSM is presented, based on the work of Novotny e Lipo (1996).

Table 6 – Comparison between FOC and DTC techniques, according to Pye (2015)

	FOC	DTC
Flux control	using current control	directly
Current control	present	absent
Reference	magnetizing flux	stator flux
Dynamic torque response	-	better
Steady state behavior	better	-
Motor current harmonics	fewer, increased efficiency	-
Signal processing time	-	better, lacking modulator stage
Low speed noise	lower noise	-

The control implementation is done considering this mathematical modeling, with disturbance compensation, compensation for internal plant loops and including the use of feedforward.

5.2 Electric machine model

The PMSM modeling is initially presented in Equations 5.1, 5.2, 5.3, 5.4 and 5.5. The model is based on DQ coordinates, with basically two objectives. The first is that using these coordinates it is possible to separate the magnetizing flux generation behavior from the flux behavior directly related to torque, in two different coordinates and axes. The other is that since the reference axis of these coordinates is rotating, in phase with the rotor flux, the variables tend to be continuous, rather than sinusoidal, simplifying the control. The reference to this equations is the work of Novotny e Lipo (1996).

$$V_{ds} = R_s i_{ds} + \frac{d}{dt}\lambda_{ds} - \omega_r \lambda_{qs} \tag{5.1}$$

where V_{ds} is the direct axle voltage (V), R_s is the stator phase resistance (Ω), i_{ds} is the direct axle current (A), λ_{ds} is the direct axle flux linkage (Wb), ω_r is the two-poles model rotor speed (rad/s) and λ_{qs} is the quadrature axle flux linkage (Wb)

$$V_{qs} = R_s i_{qs} + \frac{d}{dt}\lambda_{qs} + \omega_r \lambda_{ds} \tag{5.2}$$

where V_{qs} is the quadrature axle voltage (V) and i_{qs} is the quadrature axle current (A)

$$i_{ds} = \frac{\lambda_{ds} - \lambda_{mag}}{L_{ls} + L_{md}} = \frac{\lambda_{ds} - \lambda_{mag}}{L_d} \tag{5.3}$$

where λ_{mag} is the permanent magnet flux linkage (Wb) and L_d is the direct axle inductance (H)

$$i_{qs} = \frac{\lambda_{qs}}{L_{ls} + L_{mq}} = \frac{\lambda_{qs}}{L_q} \tag{5.4}$$

where L_q is the quadrature axle inductance (H)

$$T_e = \frac{3}{2} P_p(\lambda_{ds} i_{qs} - \lambda_{qs} i_{ds}) \tag{5.5}$$

where T_e is the electromagnetic torque (Nm) and P_p is the number of pole pairs

With these relations, the linkage fluxes can be found, as shown in Equations 5.6 and 5.7.

$$\frac{d}{dt}\lambda_{ds} = V_{ds} - \frac{R_s}{L_d}\lambda_{ds} + \frac{R_s}{L_d}\lambda_{mag} + \omega_r \lambda_{qs} \tag{5.6}$$

$$\frac{d}{dt}\lambda_{qs} = V_{qs} - \frac{R_s}{L_q}\lambda_{qs} - \omega_r \lambda_{ds} \tag{5.7}$$

Newton's Second Law is finally used to find the rotor speed, as shown in Equation 5.8. It is important to note that the electric machine's model rotor speed ω_r needs to be divided by the pole pairs to find the real rotor speed ω.

$$\omega = \int \frac{(T_e - T_L - b\omega)}{J} dt = \frac{\omega_r}{P_p} \tag{5.8}$$

where ω is the rotor speed (rad/s), T_L is the load torque (Nm), b is the viscous damping ($Nm \cdot s$) and J is the rotational inertia ($kg \cdot m^2$)

This equation is modeled and inserted into a simulation tool, as shown in Figure 62, which in the case of this work was Matlab/Simulink. The use of this tool brings the burden of not being free, so for future implementations it is suggested to use another more accessible tool.

Figure 62 – PMSM model developed in Matlab/Simulink

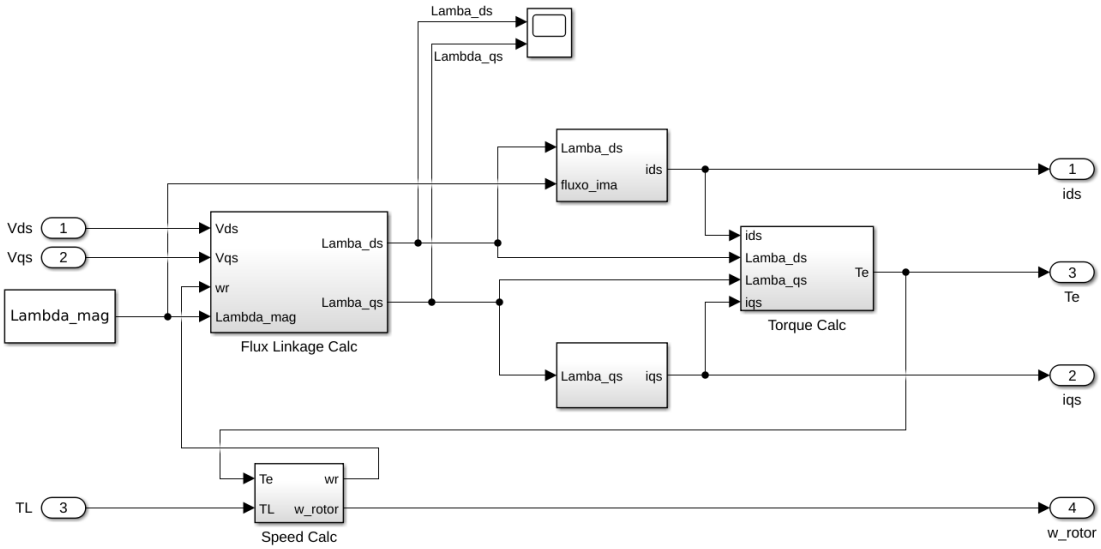

5.3 Speed control

The goal of the speed control is to make the measured speed equal to the reference, even with the perturbation of T_L. The complete speed control diagram is shown in Figure 63. Color change was used to differentiate the model of the real system from the implemented digital system.

Figure 63 – Speed control diagram

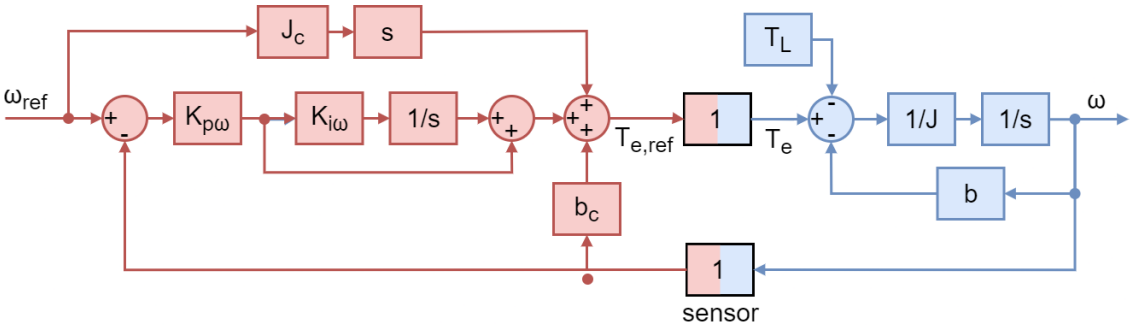

There are two blocks that behave as an interface between the two sides of the model. The lower block represents the speed sensor. It was considered that speed sensing is ideal (with unity gain). The upper block acts as a "torque generator", receiving the torque reference, and generating this torque value. In the real system it is composed by the converter (current control and switching) and the electric motor. All this systems were considered to behave for speed control as ideal, with unity gain. For this consideration to be valid, the system must be in proper working order, and the current control cutoff frequency must be at least a decade above the speed control cutoff frequency.

At the end of the control, it enters a triple adder, indicating that it can be divided into three distinct functions. The lower branch b_c, compensates for the inner loop of the plant b. The central branch is the controller. And finally, the upper branch $J_c s$ is a feedforward that compensates for the open-loop behavior of plant $1/(Js)$. The 'c' subscript refers to the control, and is used to differentiate the variables that are estimated and/or measured, and used in the control, from the variables that are used in the real plant model. This distinction between plant and control variables is relevant, since there is no way to estimate/measure such variables with perfection.

The last effect that lacked compensation was the load torque T_L. The problem here is that load torque measurement is complex and expensive, so naturally speed control implementations avoid compensating for this variable. That is also a reason for the speed control diagrams to generally consider the load torque as a perturbation.

The selection of the PI controller's gains was based on the work of Wilson (2015). Although this selection is sometimes mistakenly treated as somewhat random, an analysis of the system shows that it is a very deterministic process, directly associated with design choices.

5.3.1 Speed control closed loop analysis

To understand the proposed speed control, including the effects of feedforward, compensations and gains, one of the ways of analysis is through the closed loop transfer function. The calculation is presented, giving support to the control analysis and calculation of gains.

As a transfer function, the other entries are considered null, which in this case is $T_L = 0$. The formulation is presented in Equations 5.9, 5.10, 5.11, 5.12 and 5.13.

$$\omega = \frac{1}{sJ}\left[-b\omega + b_c\omega + sJ_c\omega_{ref} + (\omega_{ref} - \omega)\left(K_{p\omega} + \frac{K_{p\omega}K_{i\omega}}{s}\right)\right] \tag{5.9}$$

where b_c is the estimated viscous damping ($Nm \cdot s$), J_c is the estimated rotational inertia ($kg \cdot m^2$), $K_{p\omega}$ is the proportional speed gain ($Nm \cdot s$) and $K_{i\omega}$ is the integral speed gain

$$sJ\omega = -\omega(b - b_c) - \omega\left(K_{p\omega} + \frac{K_{p\omega}K_{i\omega}}{s}\right) + \omega_{ref}\left(K_{p\omega} + \frac{K_{p\omega}K_{i\omega}}{s}\right) + \omega_{ref}sJ_c \tag{5.10}$$

$$\omega\left[sJ + (b - b_c + \left(K_{p\omega} + \frac{K_{p\omega}K_{i\omega}}{s}\right)\right] = \omega_{ref}\left[sJ_c + \left(K_{p\omega} + \frac{K_{p\omega}K_{i\omega}}{s}\right)\right] \tag{5.11}$$

$$\left|\frac{\omega}{\omega_{ref}}\right| = \frac{sJ_c + K_{p\omega} + \frac{1}{s}(K_{p\omega}K_{i\omega})}{sJ + (K_{p\omega} + b - b_c) + \frac{1}{s}(K_{p\omega}K_{i\omega})} \tag{5.12}$$

$$\left|\frac{\omega}{\omega_{ref}}\right| = \frac{s^2J_c + sK_{p\omega} + (K_{p\omega}K_{i\omega})}{s^2J + s(K_{p\omega} + b - b_c) + (K_{p\omega}K_{i\omega})} \tag{5.13}$$

With Equation 5.13, many observations can be made. The first is that the feedforward-related term sJ_c inserts a zero into the transfer function. Another observation is that $K_{p\omega}$ has a viscous damping dimension, adding damping to the system, and the inner loop compensation b_c works against this effect. Finally, if the variable estimates were perfect, with $J_c = J$ and $b_c = b$, the function reduces to unity gain, as expected.

Now to obtain the gains, the analysis is started based on the obtained transfer function.

5.3.2 Speed control integral gain

As previously stated, the methodology used to obtain controller gains was based on the work of Wilson (2015). However, the methodology considers the system without feedforward and compensation, that were inserted as a contribution of this work. Compensation can be inserted into the methodology without too many issues, but feedforward inserts another zero in the function, considerably changing its behavior. Thus, it was decided to present the analysis initially without feedforward, and then insert it, calculating its effects. The transfer function

without feedforward is presented in Equation 5.14 and with numerator and denominator divided by $(K_{p\omega}K_{i\omega})$ in Equation 5.15.

$$\left|\frac{\omega}{\omega_{ref}}\right| = \frac{sK_{p\omega} + (K_{p\omega}K_{i\omega})}{s^2J + s(K_{p\omega} + b - b_c) + (K_{p\omega}K_{i\omega})} \tag{5.14}$$

$$\left|\frac{\omega}{\omega_{ref}}\right| = \frac{s\left(\frac{1}{K_{i\omega}}\right) + 1}{s^2\left(\frac{J}{K_{p\omega}K_{i\omega}}\right) + s\left(\frac{K_{p\omega}+b-b_c}{K_{p\omega}K_{i\omega}}\right) + 1} \tag{5.15}$$

The design philosophy in this state, is to seek to ensure that the poles of the closed current loop are real, avoiding resonance. See Equations 5.16, 5.17 and 5.18.

$$\left(\frac{J}{K_{p\omega}K_{i\omega}}\right)s^2 + \left(\frac{K_{p\omega} + b - b_c}{K_{p\omega}K_{i\omega}}\right)s + 1 = (sC{+}1)(sD{+}1) = (CD)s^2{+}(C{+}D)s{+}1 \tag{5.16}$$

where C and D are constants

$$CD = \frac{J}{K_{p\omega}K_{i\omega}} \tag{5.17}$$

$$C + D = \frac{K_{p\omega} + b - b_c}{K_{p\omega}K_{i\omega}} = \frac{b - b_c}{K_{p\omega}K_{i\omega}} + \frac{1}{K_{i\omega}} \tag{5.18}$$

Now, the proposal is to try to make one of the terms in Equation 5.16, or (1+Cs), or (1+Ds), equal to the numerator of the closed loop. If this is possible, the final system would reduce down to a single pole. To do this, $C = (b - b_c)/(K_{p\omega}K_{i\omega})$ and $D = 1/K_{i\omega}$. To find the integral gain see Equations 5.19 and 5.20 and to reduce the system order, the closed loop denominator is replaced by its (sC+1)(sD+1) version, see Equation 5.21.

$$\frac{J}{K_{p\omega}K_{i\omega}} = CD = \frac{b - b_c}{K_{p\omega}K_{i\omega}} \times \frac{1}{K_{i\omega}} = \frac{b - b_c}{K_{p\omega}K_{i\omega}^2} \tag{5.19}$$

$$K_{i\omega} = \frac{b - b_c}{J} \tag{5.20}$$

$$\left|\frac{\omega}{\omega_{ref}}\right| = \frac{s\left(\frac{1}{K_{i\omega}}\right) + 1}{\left[s\left(\frac{b-b_c}{K_{p\omega}K_{i\omega}}\right) + 1\right]\left[s\left(\frac{1}{K_{i\omega}}\right) + 1\right]} = \frac{1}{s\left(\frac{b-b_c}{K_{p\omega}K_{i\omega}}\right) + 1} = \frac{1}{s\left(\frac{J}{K_{p\omega}}\right) + 1} \tag{5.21}$$

It is possible to observe that with the exact choice of this integral gain, the order reduction of the system is successful, transforming it into a simple first-order system. It is also interesting to note that if the b_c compensation is perfect, the method used indicates null integrative gain, making

the controller only proportional. Anyway, for reasons of not trusting the perfect compensation b_c, for the selection of the gain the worst case was used, with $b_c = 0$ and $K_{i\omega} = b/J$.

With the finalized application of the method, the analysis of the effects of inserting the feedforward can be discussed. The numerator of Equation 5.15 is changed, adding the feedforward zero, see Equation 5.22. In order to maintain the same pole and zero cancellation performed in the presented method, the development is presented in Equations 5.23, 5.24 and 5.25.

$$\left|\frac{\omega}{\omega_{ref}}\right| = \frac{s^2\left(\frac{J_c}{K_{p\omega}K_{i\omega}}\right) + s\left(\frac{1}{K_{i\omega}}\right) + 1}{s^2\left(\frac{J}{K_{p\omega}K_{i\omega}}\right) + s\left(\frac{K_{p\omega}+b-b_c}{K_{p\omega}K_{i\omega}}\right) + 1} \tag{5.22}$$

$$s^2\left(\frac{J_c}{K_{p\omega}K_{i\omega}}\right) + s\left(\frac{1}{K_{i\omega}}\right) + 1 = (sF+1)(sG+1) = (sF+1)\left[s\left(\frac{1}{K_{i\omega}}\right) + 1\right] \tag{5.23}$$

where F and G are constants

$$FG = \frac{J_C}{K_{p\omega}K_{i\omega}} = \frac{J_c}{K_{p\omega}}\frac{1}{K_{i\omega}} \tag{5.24}$$

$$F = \frac{J_c}{K_{p\omega}} \tag{5.25}$$

It is concluded that with this methodology, the feedforward inserts a zero into $J_c/K_{p\omega}$, and the transfer function can be finally complete, as shown in Equation 5.26. Again, if the variable estimates were perfect, with $J_c = J$, the function reduces to unity gain, as expected.

$$\left|\frac{\omega}{\omega_{ref}}\right| = \frac{s^2\left(\frac{J_c}{K_{p\omega}K_{i\omega}}\right) + s\left(\frac{1}{K_{i\omega}}\right) + 1}{s^2\left(\frac{J}{K_{p\omega}K_{i\omega}}\right) + s\left(\frac{K_{p\omega}+b-b_c}{K_{p\omega}K_{i\omega}}\right) + 1} = \frac{s\left(\frac{J_c}{K_{p\omega}}\right) + 1}{s\left(\frac{J}{K_{p\omega}}\right) + 1} \tag{5.26}$$

5.3.3 Speed control proportional gain

The calculation of the proportional gain of the current control has two indicated analyzes. The first is already directly observed by Equation 5.26, since the inverse of the relation $J/K_{p\omega}$ defines the bandwidth of the speed control. An initial bandwidth value a decade before the current control frequency (500Hz/10 = 50Hz) was set, see Equations 5.27 and 5.28. This solution is classic, and works as a good starting point.

$$\omega_{c,\omega} = \frac{K_{p\omega}}{J} \tag{5.27}$$

where $\omega_{c,\omega}$ is the speed control cutoff frequency (rad/s)

$$K_{p\omega,initial} = \omega_{c,\omega} \cdot J = \left(\frac{f_{c,i}}{10} \cdot 2\pi\right) \cdot J \tag{5.28}$$

The second analysis, to finally assess whether the $K_{p\omega}$ gain is adequate for the application, is to evaluate the dynamic stiffness of the system. It is defined by the transfer function of the disturbance over the output, in this case $|T_L/\omega|$. The analysis considers the diagram of Figure 63, being relevant to point out that to obtain the transfer function, other system entries must be zeroed, in this case $\omega_{ref} = 0$. See Equations 5.29, 5.30 and 5.31.

$$\omega = -\frac{T_L}{sJ} - \frac{b\omega}{sJ} + \frac{b_c\omega}{sJ} - \left[\left(K_{p\omega} + \frac{K_{p\omega}K_{i\omega}}{s}\right)\omega\frac{1}{sJ}\right] \tag{5.29}$$

$$(sJ)\omega = -T_L - (b - b_c)\omega - K_{p\omega} \cdot \omega - \frac{K_{p\omega}K_{i\omega}}{s}\omega \tag{5.30}$$

$$\left|\frac{T_L}{\omega}\right| = \left|sJ + (K_{p\omega} + b - b_c) + \frac{K_{p\omega}K_{i\omega}}{s}\right| \tag{5.31}$$

The minimum dynamic stiffness is equal to the value that does not depend on s, in this case $\left|\frac{T_L}{\omega}\right|_{min} = (K_{p\omega} + b - b_c)$. The worst-case scenario here is when $b = 0$, so it is used to set the requirement to $K_{p\omega}$, and the gain need to obey Inequation 5.32.

$$K_{p\omega} \geq \left|\frac{T_L}{\omega}\right|_{min} + b_c \tag{5.32}$$

The final value of the speed control proportional gain needs to considered both analysis, as shown in Equation 5.46.

$$K_{p\omega} = max\left(\left(\frac{f_i}{10} \cdot 2\pi \cdot J\right), \left(\left|\frac{T_L}{\omega}\right|_{min} + b_c\right)\right) \tag{5.33}$$

If the dynamic stiffness requirement asks for a higher $K_{p\omega}$ than previously calculated, the frequency of the speed control $f_{c,\omega}$ increases, consequently increasing also the current control frequency $f_{c,i}$ and switching frequency f_{sw}. A clear gain from increasing the switching frequency is the possibility of better performance in control dynamic stiffness, demonstrating a link between the use of SiC and control performance.

5.4 Flux weakening control

Until the nominal speed of the PMSM, the eDrive system has a well-known classical behavior. Voltages increase with frequency and speed, and the quadrature current controls the torque. Past the nominal speed, a different behavior is needed, since the internal voltage of the

machine reached the maximum voltage that the DC bus can provide. For increasing speed, now this internal motor voltage needs to be lowered, and this can be done with flux weakening.

Flux weakening has to respect two limits: current and voltage. Considering both motor and inverter ratings, these are presented in Equations 5.35 and **??**.

$$i_{d,pu}^2 + i_{q,pu}^2 \leq I_{max,pu}^2 \tag{5.34}$$

where $i_{d,pu}^2$ is the normalized direct current (I), $i_{q,pu}^2$ is the normalized quadrature current (I), $I_{max,pu}$ is the normalized maximum current (I)

$$V_{d,pu}^2 + V_{q,pu}^2 \leq V_{max,pu}^2 \tag{5.35}$$

where $V_{d,pu}^2$ is the normalized direct voltage (V), $V_{d,pu}^2$ is the normalized quadrature voltage (V), $V_{max,pu}$ is the normalized DC-link voltage (V)

This is the general idea, however, how to do it is a totally different issue. There are a wide variety of technological solutions for implementing this, even including direct mechanical solutions, moving the magnets away from the air gap to decrease the flux perceived by the stator, or even pieces of the stator itself (ZHU et al., 2014).

The more usual solutions are done purely electrically, with the work of (LU; KAR, 2010) showing a wide review of this techniques for PMSM. All the techniques were divided into four categories: feedback, feed-forward, hybrid and non-linear.

Feed-forward techniques generally have good stability and transient responses, but they are strongly dependent on the motor parameters and the accuracy of the motor model, see example in Figure 64. This type of solution calculates the direct current as a function of the operating speed, and the quadrature current command is calculated from the torque command, but without surpassing the total current limits of the system. The dependence on motor parameters can cause issues from multiple reasons, with one being the need of careful measurement of the motor parameters, but the other being maybe even more complex: parameter variation of the machine associated with either temperature, changing of the material characteristics with time, and saturation effects. All this variations affect the control response, and can even deteriorate the behavior completely.

On the other hand, feedback techniques are generally slower solutions, however the upsides include a more efficient utilization of the DC-link voltage, and lesser dependence on the motor parameters, see example in Figure 65. The solution involves measuring the motor voltage and/or speed, and use the voltage error (KWON; SUL, 2006) or the speed error (SUE; PAN, 2008) to adjust the direct current to track the voltage limit at increasing speed. Along with the slower transient response, this type of control also has the issue of defining the gains, which can be a non-trivial task.

Figure 64 – Example of flux weakening feed-forward control (LU; KAR, 2010)

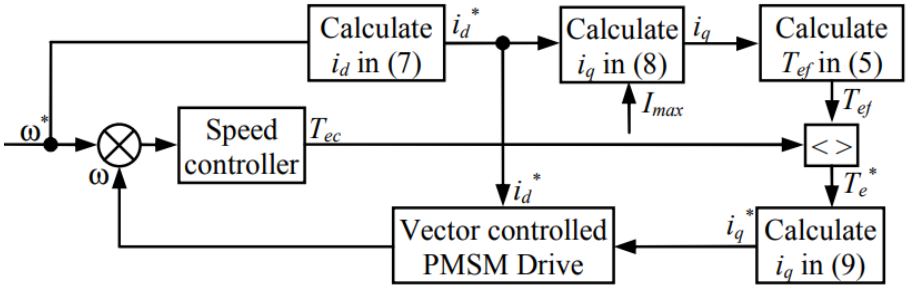

Figure 65 – Example of flux weakening feedback control (LU; KAR, 2010)

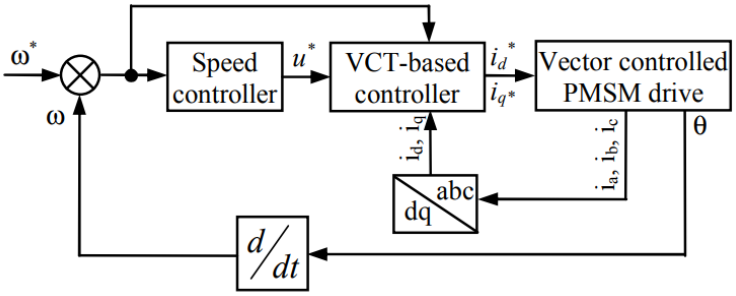

Hybrid techniques seek to obtain the advantages of both previous solutions. The direct current is pre-calculated for MTPA (Maximum Torque Per Ampere), while the quadrature current command is calculated from the torque command, but without surpassing the total current limits of the system (achieved using feedback of the direct current). Another other way to implement a hybrid solution is that the feed-forward current references calculated for MTPA are modified through the feedback flux output of the integrator in the current controller.

Finally, the non-linear techniques are based on control theory, simplifying the controller structure, being also robust to the variation of the motor parameters. It includes adaptive solutions, such as combining speed and current controllers together instead of keeping the conventional cascade structure, and the system and controller parameters are tuned on-line (BOLOGNANI et al., 2008). One disadvantage of this methods is the computational complexity.

In the case of this work, the focus was not to implement the world's highest performing flux weakening control, but to present the advantages and disadvantages of each solution, and implement a functioning one. The option was to pre-calculate the direct currents needed for each motor speed, since the torque x speed curve is already obtained in Section 3.2. As is shown in the general control diagram of Figure 61, the flux weakening block will receive the torque reference, or direct current reference, will observe the speed of the motor, and decide how much direct current it has to command from the system, for it to be capable to reach higher speeds.

Finally, if the motor speed is lesser than nominal, this calculation does not need to be done, leaving the quadrature current as the torque times a gain, and the direct current always equal to zero. Only when the motor reaches higher speeds than nominal, the new values of direct

and quadrature current need to be calculated.

Using the torque x speed calculated curve, along with Equations 5.5 and 5.35, the direct currents of each speed beyond nominal are defined, see Equation 5.36. This equation can be solved computationally for each speed, or a less performing solution can be done by linearization.

$$T_e = \frac{3}{2} P_p \sqrt{I_{max}^2 - i_d^2} \times (\lambda_{mag} + id \times (L_d - L_q)) \tag{5.36}$$

With the flux weakening done, the direct and quadrature current references are sent to the current control.

5.5 Current control

The current control will receive the current references, and will work so that the inverter actually injects these currents. In practice, it seeks to generate the voltage reference for the converter that it understands will result in the desired currents.

As in Section 5.2, the Park transformed is utilized, allowing this separate control of torque and flux. Torque is commanded in the quadrature axis, and flux is commanded in the direct axis.

As for the direct axis, since this is a permanent magnet synchronous machine, the main flux is already present, and the motor usually does not need magnetizing current. Flux weakening operations have not been included in the scope of this work, but can be performed to reach speeds beyond the nominal, provided great care is taken to avoid demagnetization.

The quadrature axle becomes the object of the loop operation, enabling direct control of the machine torque through the i_{qs} current.

To present the current control topology step by step, making it easier for the reader to understand, a simple circuit is presented in Figure 66. It is a classic simplified representation of a synchronous machine, being an RL circuit with the addition of a counter electromotive force. The control of this this circuit is proposed in Figure 67.

Figure 66 – Example of simple circuit for current control

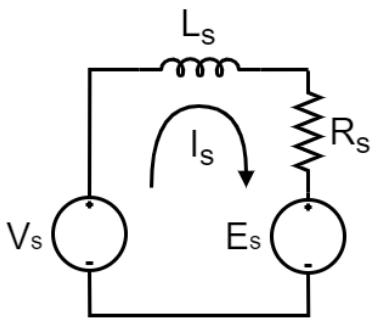

Figure 67 – Current control for simple circuit

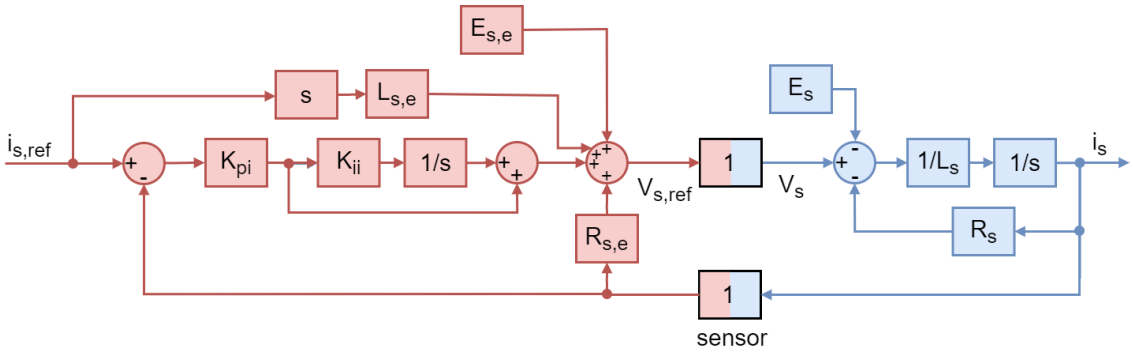

All control elements noted in Section 5.3 are also present here. Again, there are two blocks that behave as an interface between the two sides of the model. The lower block represents the current sensor. It was considered that current sensing is ideal (with unity gain). The upper block acts as a "voltage generator", receiving the voltage reference, and generating this voltage value. In the real system the converter switching process is responsible for this, through an algorithm like SVPWM. This process was considered to behave for current control as ideal, with unity gain. For this consideration to be valid, the system must be in proper working order, and the switching frequency must be at least a decade above the current control cutoff frequency.

At the end of the control, it enters a quadruple adder, indicating that it can be divided into four distinct functions. The lower branch $R_{s,c}$, compensates for the inner loop of the plant R_s. The central branch is the PI controller. Above it, is the feedforward $L_{s,c}s$ that compensates for the open-loop behavior of plant $1/(L_s s)$. Again, the 'c' subscript refers to the control, and is used to differentiate the variables that are estimated and/or measured, and used in the control, from the variables that are used in the real plant model.

Finally, the upper branch $E_{s,c}$ is the element that is different from the speed control, acting as a compensation for the disturbance E_s. As stated in Section 5.3, in a speed control, measuring the load torque T_L is complex and expensive, so naturally speed control implementations avoid compensating for this disturbance. The current control situation is different, since the behavior of the counter electromotive force is widely studied, and mathematically modeled.

Once this simplified circuit is analyzed, understanding the real DQ current control is facilitated, since it will have these same elements, see Figures 68 and 69.

The first thing that can be observed is that the DQ model has a cross-relationship between the D axis and the Q axis. This effect comes naturally from Park's transform. Equations 5.1 and 5.2 are applied, being represented in the plant model with the insertion of the $\omega_r \lambda$ terms. The same is done in the controller, with the signals inverted, so that there is compensation.

Another observation is that on the internal voltage E_s entry, the behavior of the direct and quadrature axle differ. In the DQ modeling proposed for the PMSM this term will not be present for the direct axle. On the other hand, it appears in the quadrature axle as $\omega_r \lambda_{pm}$, which

Figure 68 – Direct axle current control. Sensor not represented

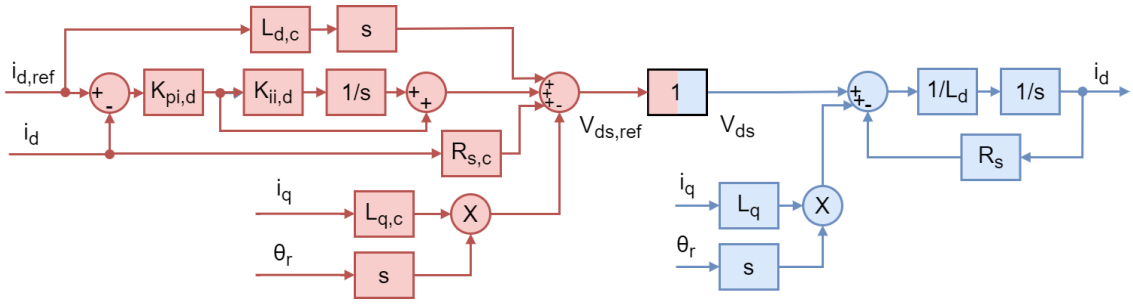

Figure 69 – Quadrature axle current control. Sensor not represented

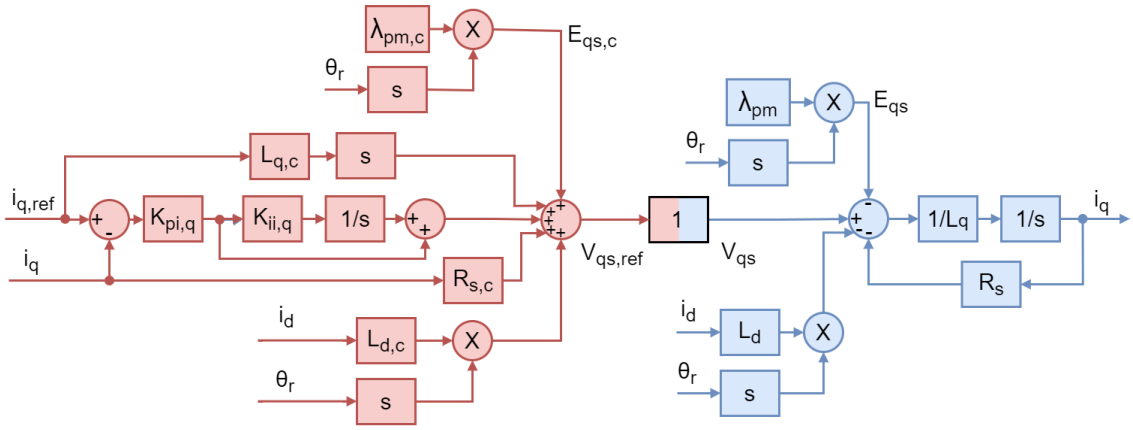

is exactly related to the internal voltage generated by the flux linkage of the permanent magnets.

The closed loop analysis of the current control, is similar to the speed control analysis done in Subsection 5.3.1, so will not be fully presented, to avoid repeating content. Some equations will be presented to show the similarity, and carry out the discussions. The Q axis was used as an example, since it is responsible for the torque actuation. The results are presented in Equation 5.37. In this case the inputs that are zeroed to obtain the transfer function are $E_{qs} = 0$, $E_{qs,c} = 0$ and the cross coupling signals.

$$\left|\frac{i_q}{i_{q,ref}}\right| = \frac{s^2\left(\frac{L_{q,c}}{K_{pi,q}K_{ii,q}}\right) + s\left(\frac{1}{K_{ii,q}}\right) + 1}{s^2\left(\frac{L_q}{K_{pi,q}K_{ii,q}}\right) + s\left(\frac{K_{pi,q}+R_s-R_{s,c}}{K_{pi,q}K_{ii,q}}\right) + 1} \tag{5.37}$$

Again, the feedforward inserts another zero in the transfer function, and the same methods are used, resulting in the integral gains presented in Equations 5.38 and 5.39.

$$K_{ii,d} = \frac{R_s - R_{s,c}}{L_d} \tag{5.38}$$

$$K_{ii,q} = \frac{R_s - R_{s,c}}{L_q} \tag{5.39}$$

Again, if the $R_{s,c}$ compensation is perfect, the method used indicates null integrative gain, making the controller only proportional. Anyway, for reasons of not trusting the compensation

$R_{s,c}$, for the initial selection of the gain the worst case was used, with $R_{s,c} = 0$, $K_{ii,d} = R_s/L_d$ and $K_{ii,q} = R_s/L_q$.

When using the two control loops, namely, speed and torque control, it is necessary to assess whether the integral gain of the internal loop is not disturbing the external loop. This concern does not exist in the case of bypassing the external loop, with direct torque command coming from the pedal.

5.5.1 Current control proportional gain

The calculation of the proportional gain of the current control is similar to what was presented for the speed control Subsection 5.3.3, having also the same two indicated analyzes, being its effect on the current loop cutoff frequency and on the dynamic stiffness.

Current control is initially inserted at a frequency a decade below the switching frequency, see Equations 5.40 and 5.41.

$$\omega_{c,iq} = \frac{K_{pi,q}}{L_q} \tag{5.40}$$

where $\omega_{c,iq}$ is the Q current control cutoff frequency (rad/s)

$$K_{pi,q,initial} = \omega_{c,iq} \cdot L_q = \left(\frac{f_{sw}}{10} \cdot 2\pi\right) \cdot L_q \tag{5.41}$$

In the second analysis, related to dynamic stiffness, there are small changes due to the presence of a perturbation compensation. In this case the inputs that are zeroed to obtain the transfer function are $i_{q,ref} = 0$ and cross coupling signals. See Equations 5.42, 5.43 and 5.44.

$$i_q = -\frac{E_{qs}}{sL_q} - \frac{R_s i_q}{sL_q} + \frac{R_{s,c} i_q}{sL_q} + \frac{E_{qs,c}}{sL_q} - \left[\left(K_{pi,q} + \frac{K_{pi,q}K_{ii,q}}{s}\right) i_q \frac{1}{sL_q}\right] \tag{5.42}$$

$$(sL_q)i_q = -(E_{qs} - E_{qs,c}) - (R_s - R_{s,c})i_q - (K_{pi,q})i_q - \left(\frac{K_{pi,q}K_{ii,q}}{s}\right) i_q \tag{5.43}$$

$$\left|\frac{E_{qs} - E_{qs,c}}{i_q}\right| = \left|sL_q + (K_{pi,q} + R_s - R_{s,c}) + \frac{K_{pi,q}K_{ii,q}}{s}\right| \tag{5.44}$$

The resulting dynamic stiffness equation is similar to Equation 5.31, but the effect of compensation is observed. Instead of having to account for all the perturbation torque T_L, the dynamic stiffness of current needs to account for the perturbation compensation error $(E_{qs} - E_{qs,c})$. The gain $K_{pi,q}$ actually has a unit of resistance, bringing the information of the

current that will be "injected" to solve a voltage error arising from the difference between the real induced voltage and the estimate of the induced voltage.

The minimum dynamic stiffness is equal to the value that does not depend on s, in this case $\left|\frac{E_{qs}-E_{qs,c}}{i_q}\right|_{min} = (K_{pi,q} + R_s - R_{s,c})$. The worst-case scenario here is when $R_s = 0$ and $E_{qs,c}$, so it is used to set the requirement to $K_{pi,q}$, and the gain need to obey Inequation 5.45.

$$K_{pi,q} \geq \left|\frac{E_{qs}}{\omega}\right|_{min} + R_{s,c} \tag{5.45}$$

The final value of the current control proportional gain needs to considered both analysis, as shown in Equation 5.46.

$$K_{pi} = max\left(\left(\frac{f_{sw}}{10} \cdot 2\pi \cdot L_q\right), \left(\left|\frac{E_{qs}}{i_q}\right|_{min} + R_{s,c}\right)\right) \tag{5.46}$$

If the dynamic stiffness requirement asks for a higher K_{pi_q} than previously calculated, the frequency of the current control $f_{c,i}$ increases, consequently increasing also the switching frequency f_{sw}. Again, a clear gain from increasing the switching frequency is the possibility of better performance in control dynamic stiffness, demonstrating a link between the use of SiC and control performance.

With the development of the control is finished, this work moves on to the modulation itself and the implementation of the algorithms.

5.6 Modulation

Receiving the direct and quadrature voltage references from the current control, the system still need to convert them into gate signals for the power switches. For that purpose the modulation is set.

With the modulating techniques presented in Section 2.6, the advantages and disadvantages of each solution where presented. This works seeks to implement the center-aligned solution of SVPWM, and also exploring overmodulation if needed.

Some other issues regarding the modulation need to be addressed, such as synchronous rectification and deadtime compensation.

5.6.1 Synchronous rectification

One of the advantages of using SiC switching solutions, is the synchronous rectification. In normal IGBT inverters operation, when the AC current is in one direction, it flows through the IGBT and when it changes the direction, it flows through the freewheeling diode.

Since MOSFETs can conduct current in either direction, a different option is presented. Synchronous rectification consists of the technique of turning on the MOSFET when the diode is conducting the freewheeling current, so that the MOSFET shares this current with the diode.

With the MOSFET sharing the current with the diode, the overall converter losses are reduced, improving efficiency and power density. Being a relevant technique for MOSFET power converters, this work sought to implement it.

5.6.2 Deadtime compensation

While synchronous rectification is a technique to improve the MOSFET converter efficiency, the deadtime effects are undesired phenomena that occurs in the system. Figure 70 shows a classical sinusoidal PWM solution with deadtime.

Figure 70 – Classical PWM implementation with deadtime (YAN; YUAN, 2020)

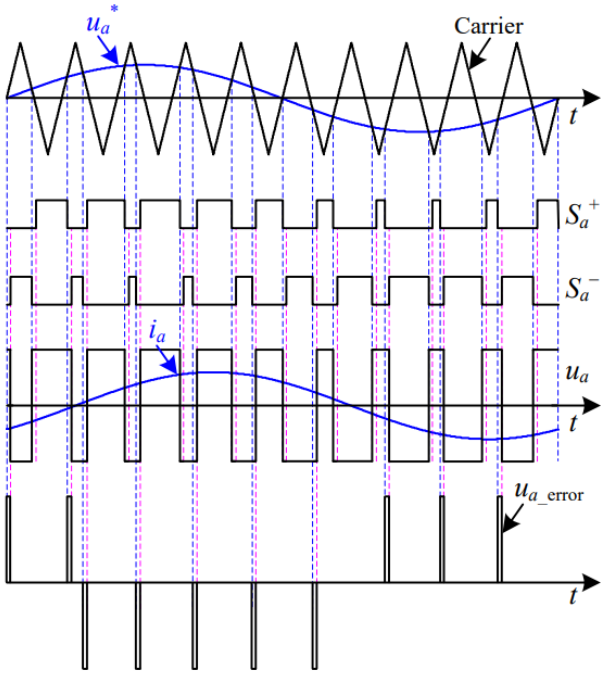

As previously stated, power switches in one leg cannot be on at the same time, because it would short circuit the DC bus, causing disastrous effects. Since the switching process is not instantaneous, the commands have to pass through this deadtime without any switch being commanded to turn on, just waiting for the other switch to turn off first.

The problem here is that this deadtime can cause voltage losses, generate low frequency current/voltage harmonics (mainly in 5th and 7th harmonics) and decrease the DC-link voltage utilization. This phenomena becomes aggravated with the increase in switching frequency.

With all this problems, deadtime compensation is a subject of high interest in the scientific community, and with increasing negative effects. A possible solution for it is the "Deadtime

Elimination PWM" shown in Figure 71. This solution consists of the drive pulses in half of the fundamental period being enabled or disabled according to the polarity of the reference current.

Figure 71 – Deadtime Elimination PWM (YAN; YUAN, 2020)

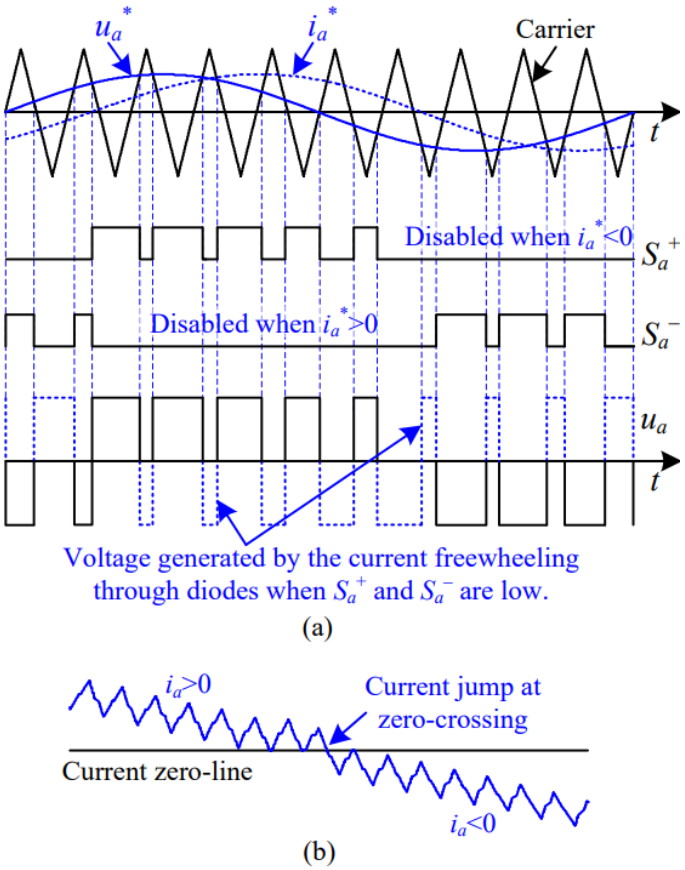

The deadtime elimination PWM has mainly two problems. First, as the drive pulses in the current freewheeling stage are disabled, synchronous rectification does not exists. Second, due to this abrupt alternation between the upper and lower switches, there is not a gradual transition for current ripples across the zero-line, generating a current jump at the zero-crossing.

5.6.3 Implemented modulation

As shown, regarding modulation in power converters, multiple objectives compete with each other, and a final perfect solution for all does not exist.

At the end, this work opted for using a modulation proposed in the work of Yan e Yuan (2020). This solution seeks to at the same time implement deadtime compensation and some synchronous rectification as well. This was achieved by using two modulation waves, see Figure 72.

It is possible to observe that this is a intermediate solution between classical deadtime implementation and the deadtime elimination PWM. Smaller pulses are generated in the free-

Figure 72 – Double-Modulation-Wave PWM for Dead-Time Effect Elimination and Synchronous Rectification (YAN; YUAN, 2020)

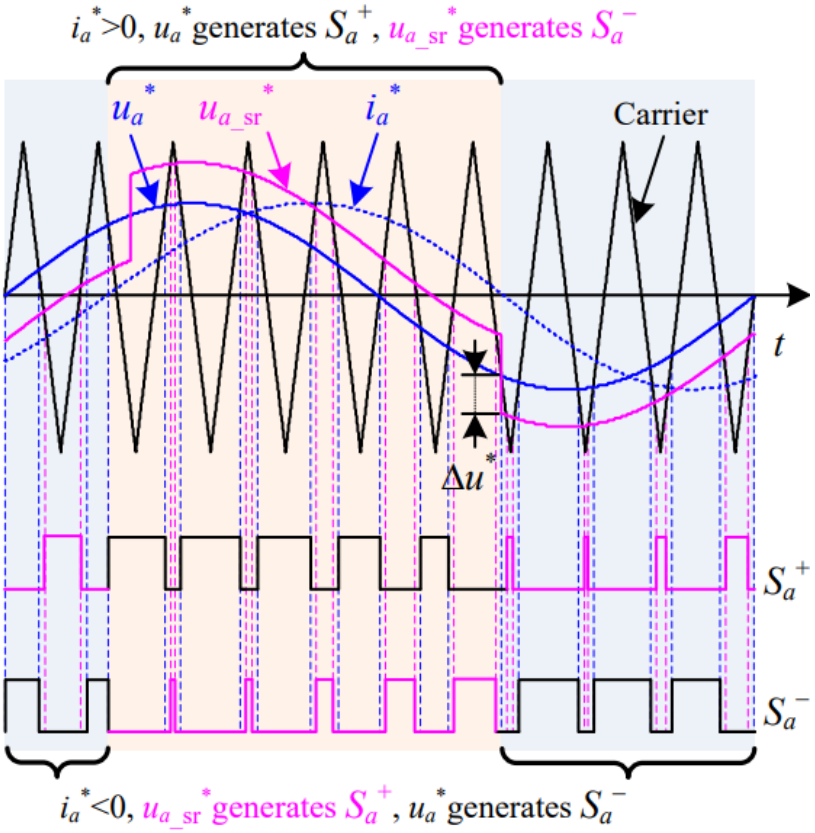

wheeling stage, not sufficient to generate deadtime effects problems, whilst implementing some synchronous rectification.

This technique increases the converter efficiency and lowers the current jump at the zero-crossing, but also has its downsides. The pros come with some DC-link voltage cost and as the algorithm decides the state of all switches, if the gate driver is not developed to implement this algorithm, the MCU has to implement it and provide the 6 switch commands ready for the gate drivers.

The examples in the figures are presented with sinusoidal PWM, but the algorithm can and is implemented with SVPWM as well.

5.7 Algorithm implementation

With the hardware development done, as well as an analysis of the control system, the next step is the implementation through the programming of the MCU. Each programming language has its specificities, and as previously mentioned, this work chose to demonstrate the direct programming of the MCU at a high level, with the objective of accelerating and cheapening the prototyping and learning process in industry and academia.

The macro items of this implementation can be seen in Figure 73. This work proceeds with the specifics necessary for in-depth understanding of each macro step of the algorithm.

Figure 73 – Algorithm macro structure

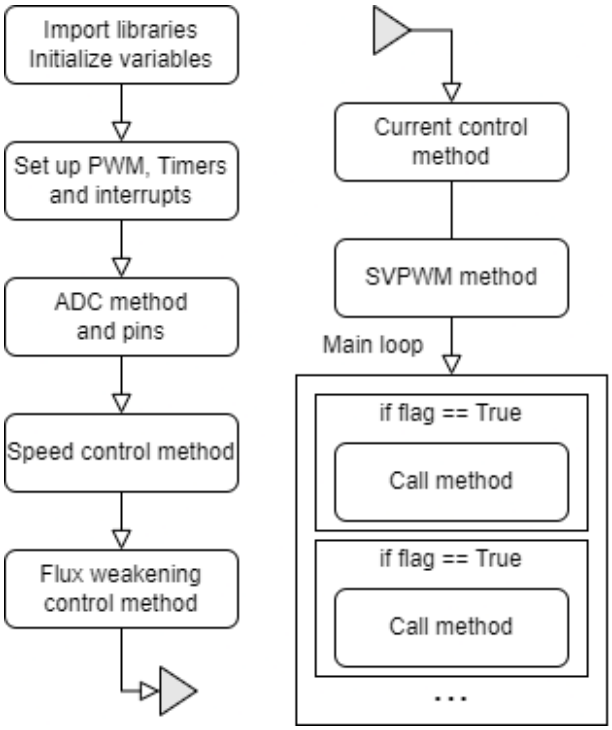

The MCU hardware used in this work was a Pyboard V1.1, which uses a STM32F405RG microprocessor. This board is an overall good solution for micropython application, as shown in the hardware comparison made by (ELECTRONICS, 2022). Code can be executed in it by a USB flash drive to save your Python scripts or a serial Python prompt for instant programming. Code stored in flash is generally used for more complex applications, but quick command testing is accelerated by prompt access. The code can be seen in Appendix D.

At this point, a problem was encountered. Despite the microprocessor having a good amount of channels and Timers for PWM, the Pyboard v1.1 itself does not make all of them available to the user. This made the "Double-Modulation-Wave PWM" code unfeaseble on the Pyboard v1.1. In fact, the lack of pins and channels to do so caused complications even for simple SVPWM implementation.

The objective of this work to program the algorithms in micropython and implement them at a high level continued, but already with the advanced conclusion that despite the use of Pyboard v1.1, it is not an adequate solution, not even for the prototyping of this converter.

5.7.1 Libraries and variables

Starting the code it is necessary to import libraries and initialize variables. Regarding libraries the only ones needed are machine, math and pyb, the latter being used for Timer, Pin

and ADC (analog to digital converter). Also few variables are needed to be initialized globally, since it is good practice to use local variables (variables present only within functions). The local implementation allows the variable to be found quickly, since it does not have to be searched up in the global dictionary. Examples of possible global variables are return vectors of functions. Quantities that will not change during code execution, like the switching frequency, can be initialized as constants with const() declaration. This works in a similar way as #define in C in that when the code is compiled to bytecode the compiler substitutes the numeric value for the identifier (GEORGE; SOKOLOVSKY, 2022).

Another good practice is to initialize the variables already with the format that they will be used, so that memory allocation is not performed during execution.

With the variables properly set, below are other code elements that need to be programmed before the main loop.

5.7.2 PWM, timers and interrupts

As previously stated, electrical machines control have a few MCU activities that need to be timed. The first that can be mentioned is the PWM (pulse-width modulation) itself. For the converter command, 6 PWM are required. The work of generating these signals is divided between the MCU and the gate driver. In general, the minimum that the MCU needs to deliver is 3 PWMs with 120º phases between them, since the market has gate drivers for generating complementary signals and dead times. Although, as previously stated, this would not allow the implementation of the "Double-Modulation-Wave PWM". An enable signal will also be necessary for turning off all switches when desired.

It is relevant to point out that in the MCU, the PWM is not usually programmed or executed on the main processor, since this would occupy its processing capacity. Therefore, it is relevant for the PWM generation to be done peripherally, being a critical feature for the MCU to be able to control the powertrain. Another feasible option is to use MCUs with multiple cores, working in parallel. As with the Pyboard, some common MCUs also have a peripheral system for PWM generation, allowing calculations to be performed at higher frequencies. To use these peripherals, it is necessary to configure Timers for this function, usually informing which Timer, its frequency and mode of operation (center-aligned, etc.).

In addition to the timer for PWM, the converter needs to perform other timed functions, such as sampling, current control, flux weakening control and speed control. If the frequencies are multiples of each other, it is possible to use a single Timer, iterating within it to trigger the other functions or using clock scaling. For the switching frequency, some considerations have to be made. First, the ripple interference to the control dynamic can work as a noise and disturb the control loop, therefore is preferable to make f_{samp}=f_{sw}, or at least be down scaled with switching frequency, because the sampled value will be the averaged value at the switching

period (KAZMIERKOWSKI; MALESANI, 1998; BUSO, 1999). The problem to implement this in the microcontroller can be the read time of the ADCs. (ITOH; KAWAUCHI, 1991) shows that in his analysis the condition for control stability is the ADC read time to be equal or less than $0.35xT_{sw}$ (switching period). This issue was kept in mind, but initially the current was considered perfectly sinusoidal, for focusing the design efforts in the funcionalities and implementation of the SVPWM.

The speed control was done with a separate timer, to avoid the memory allocation of an iterator. For future developments, a further analysis is suggested, to assess if the final code will really be faster with this separate timer for speed control, or if would be better using other methods mentioned before.

For the current control and speed control timers, interrupts functions are defined with their respective flags. Their purpose is to stop the execution of the main loop at a defined frequency so that the codes are always executed at that frequency. The interrupt function has its callback when the counter of its timer overflows, characterizing an event. It is very important to pay attention to these functions, since they will hinder the processor and can generate issues, such as problems with interrupts happening while others are executing. It is generally recommended limiting the code of these functions to a flag trigger, leaving to the main loop the task of observing the state of these flags and performing the calculations.

As there were problems with the number of pins, PWM and channels in Pyboard v1.1, and also for comparative reasons between the solutions, the classic SVPWM method was also implemented.

5.7.3 SVPWM classical algorithm

The SVPWM development is the central element of the machine drive algorithm. A representation for better understanding the classical algorithm is shown in Figure 74.

The code receives as inputs $V_{d,ref}$, $V_{q,ref}$ and θ, being responsible for calculating the duty cycle of each phase. To perform this task, the algorithm is presented in Figure 75.

Initially the MCU is informed which global variables will be used in the function. As previously stated, it is good to avoid this method, since the process to look up the variables in the global dictionary takes longer than if done locally. Besides local variables, another way to speed up the code is to perform local preloading of frequently used methods, such as sines and cosines, in order to also reduce the amount of times these functions are looked up in the global dictionary.

Dq0 to alpha-beta transform is then applied, see Equation 5.47. Some authors run the SVPWM method directly on dq0 (GABALLAH, 2013; BADRAN; TAHIR; FARIS, 2013), but in this work the analysis is made using alpha-beta, and a direct application in dq0 is proposed for future speed increase development.

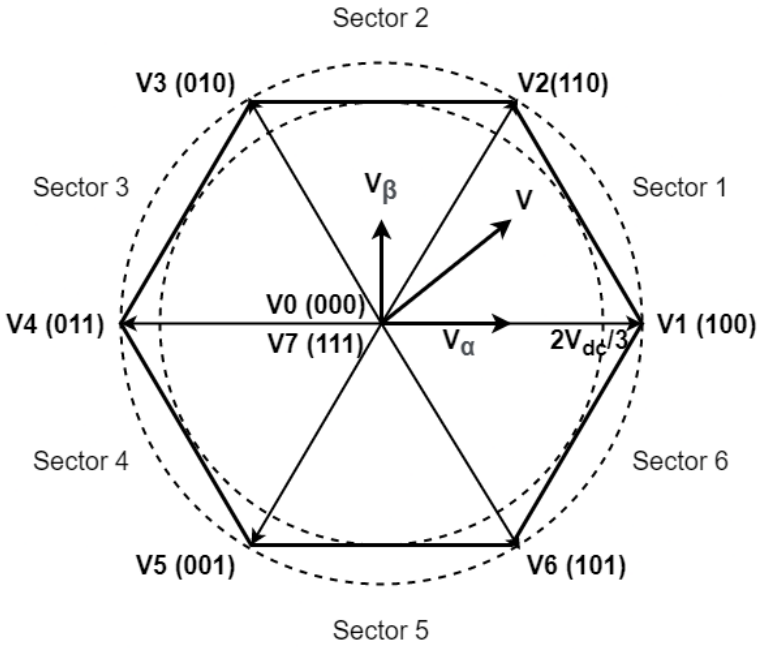

Figure 74 – SVPWM representation. Module of adjacent vector is $2V_{dc}/3$

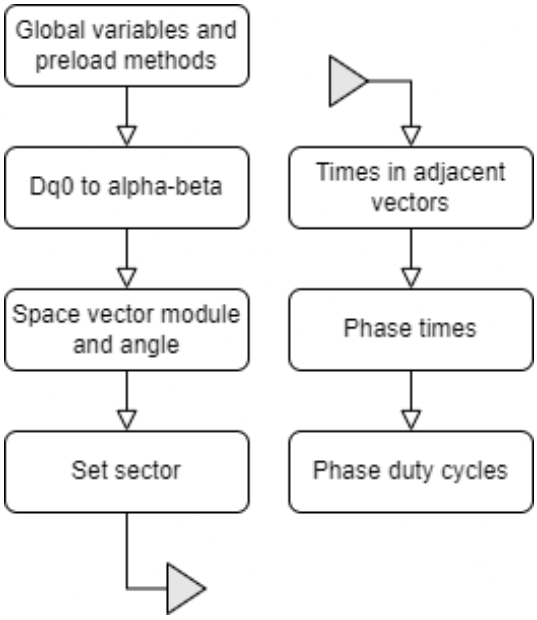

Figure 75 – SVPWM algorithm diagram

$$\begin{bmatrix} V_{\alpha,ref} \\ V_{\beta,ref} \end{bmatrix} = \begin{bmatrix} cos(\theta) & -sin(\theta) \\ sin(\theta) & cos(\theta) \end{bmatrix} \begin{bmatrix} V_{d,ref} \\ V_{q,ref} \end{bmatrix} \tag{5.47}$$

To obtain the space vector $V_{ref}\angle\gamma$, it is used a simple implementation presented in Equation 5.48. For the angle, a deeper analysis needs to be done of the function to be implemented. In this case the arccosine was chosen, see Equation 5.49, and some conditionals needed to be

programmed to guarantee that the four quadrants are contemplated, since the function only returns values from 0 to π.

$$|V_{ref}| = \sqrt{V_{\alpha,ref}^2 + V_{\beta,ref}^2} \tag{5.48}$$

$$\gamma = \arccos \frac{V_{\alpha,ref}}{|V_{ref}|} \tag{5.49}$$

In possession of the angle γ of the space vector, 6 conditionals are implemented to select in which sector the vector is present. To optimize the speed of the next phase, it is recommended to use these conditionals to set the sine and cosine of the angles γ_1 and γ_2 of the adjacent vectors. These are fixed values that do not need to be calculated by the MCU, example: for sector 1, $\gamma_1 = 0$ and $\gamma_2 = \pi/3$.

For the execution of SVPWM it will be necessary to finally calculate the times in each adjacent vector. The equation for this is presented in Equations 5.50, 5.51, 5.52, 5.53, 5.54 and 5.55.

$$\overline{V_{ref}} = \frac{T_1}{T_{sw}}\overline{V_1} + \frac{T_2}{T_{sw}}\overline{V_2} \tag{5.50}$$

with $\overline{V_1}$ and $\overline{V_2}$ being the adjacent vectors and T_1 and T_2 being the times spent on them

$$\begin{bmatrix} V_{\alpha,ref} \\ V_{\beta,ref} \end{bmatrix} = \begin{bmatrix} V_{1,\alpha} & V_{2,\alpha} \\ V_{1,\beta} & V_{2,\beta} \end{bmatrix} \begin{bmatrix} \frac{T_1}{T_{sw}} \\ \frac{T_2}{T_{sw}} \end{bmatrix} \tag{5.51}$$

$$\begin{bmatrix} V_{\alpha,ref} \\ V_{\beta,ref} \end{bmatrix} = \begin{bmatrix} |V_1|\cos\gamma_1 & |V_2|\cos\gamma_2 \\ |V_1|\sin\gamma_1 & |V_2|\sin\gamma_2 \end{bmatrix} \frac{1}{T_{sw}} \begin{bmatrix} T_1 \\ T_2 \end{bmatrix} \tag{5.52}$$

$$\begin{bmatrix} V_{\alpha,ref} \\ V_{\beta,ref} \end{bmatrix} = \frac{2}{3}V_{dc} \begin{bmatrix} \cos\gamma_1 & \cos\gamma_2 \\ \sin\gamma_1 & \sin\gamma_2 \end{bmatrix} \frac{1}{T_{sw}} \begin{bmatrix} T_1 \\ T_2 \end{bmatrix} \tag{5.53}$$

$$\begin{bmatrix} T_1 \\ T_2 \end{bmatrix} = \frac{3}{2}\frac{T_{sw}}{V_{dc}} \begin{bmatrix} \cos\gamma_1 & \cos\gamma_2 \\ \sin\gamma_1 & \sin\gamma_2 \end{bmatrix}^{-1} \begin{bmatrix} V_{\alpha,ref} \\ V_{\beta,ref} \end{bmatrix} \tag{5.54}$$

$$\begin{bmatrix} T_1 \\ T_2 \end{bmatrix} = \frac{1}{V_{dc}}\frac{3T_{sw}}{2}\left(\frac{1}{\cos\gamma_1\sin\gamma_2 - \cos\gamma_2\sin\gamma_1}\right) \times \begin{bmatrix} \sin\gamma_2 & -\cos\gamma_2 \\ -\sin\gamma_1 & \cos\gamma_1 \end{bmatrix} \begin{bmatrix} V_{\alpha,ref} \\ V_{\beta,ref} \end{bmatrix} \tag{5.55}$$

For all the 6 cases, the expression in parentheses in Equation 5.55 is always equal to $\sqrt{3}/2$. Finally the resulting formula is presented in Equation 5.56.

$$\begin{bmatrix} T_1 \\ T_2 \end{bmatrix} = \frac{1}{V_{dc}} \frac{3T_{sw}}{2} \frac{\sqrt{3}}{2} \times \begin{bmatrix} \sin\gamma_2 & -\cos\gamma_2 \\ -\sin\gamma_1 & \cos\gamma_1 \end{bmatrix} \begin{bmatrix} V_{\alpha,ref} \\ V_{\beta,ref} \end{bmatrix} \tag{5.56}$$

Once again to speed up the code execution, these fixed multiplier factors can be previously calculated, preferably outside the function itself, so that the same calculation is not performed multiple times by the microprocessor. Regarding the $1/V_{dc}$ factor, it can be considered constant in some applications, but this is not the case with automotive, which have a battery powered converter that varies its output voltage depending on SOC (state of charge) and I_{dc}. Since the switching frequency does not vary, the factor $(3xT_{sw}x\sqrt{3})/(2*2)$ is constant and can be calculated in advance and outside the function.

With the adjacent vectors times, it is possible to calculate the times for each phase, according to Table 7. To understand how this table is built it can be seen in Figure 74. Take for example Sector 3, where the adjacent vectors are V3(010) and V4(011). The three numbers represent the state of which phase. So in this case Phase A will be off (V3(0$\underline{1}$0) V4(0$\underline{1}$1)), phase B will be on (V3(0$\underline{1}$0) V4(0$\underline{1}$1)), and phase C will be only on during T2 (V3(01$\underline{0}$) V4(01$\underline{1}$)). For optimal switching, always half of the "dead time" T0, will be spent on vector V0 and half will be spent on vector V7, causing T0/2 to be added in every case.

Table 7 – Phase times calculation, using adjacent vectors times

Sector	T_a	T_b	T_c
1	T1+T2+T0/2	T2+T0/2	T0/2
2	T1+T0/2	T1+T2+T0/2	T0/2
3	T0/2	T1+T2+T0/2	T2+T0/2
4	T0/2	T1+T0/2	T1+T2+T0/2
5	T2+T0/2	T0/2	T1+T2+T0/2
6	T1+T2+T0/2	T0/2	T1+T0/2

The full classical SVPWM code in micropython can be seen in Appendix D.

With the times in each phase at hand, the duty cycles are calculated by dividing by T_{sw}. Since division costs the microprocessor a lot of cycles, it can be replaced by a multiplication by f_{sw}.

It is important to remember here that for this case, the amplitude of the output of SVPWM function cannot be 0 to 1. It is important to note on what scale the microcontroller needs to receive these values, where in the case of the Pyboard V1.1 they need to be scaled and received from 0 to 100, with 0 generating the most negative output, 50 generating the zero voltage output and 100 generating the most positive output.

5.7.4 Main loop and execution time

With the previous steps completed, the main loop can be set with continuous execution (e.g. while True). Inside it are macro if-else type conditionals, with blocks of code that are triggered by the interruption flags. That is, the main loop works by evaluating the interrupt flags, that will indicate the execution of their respective code blocks. As mentioned before, this solution is implemented to keep the code execution frequency constant.

Controlling real-time systems, especially when there is a need to execute code at a fixed frequency f_{code}, implies that the execution duration of this code must be limited to period $T_{code}=1/f_{code}$. The situation worsens when multiple codes compete for the microprocessor at different frequencies, being recommended to use two or more cores in parallel execution. A basic analysis of the situation indicates that a core execution is limited by the code with the shortest period (highest frequency) running on it. This condition for proper system operation is described for only one core in Equation 5.57. Attention in keeping this condition is necessary, so that serious execution issues do not occur.

$$(t_{svpwm} + t_{cc} + t_{fwc} + t_{sc}) < \min(\frac{1}{f_{svpwm}}, \frac{1}{f_{cc}}, \frac{1}{f_{fwc}}, \frac{1}{f_{sc}}) \tag{5.57}$$

where t_{svpwm}, t_{cc}, t_{fwc} and t_{sc} are the code execution times for SVPWM, current control, flux weakening control and speed control, respectively

Here is important to understand a phenomena. The SVPWM code (that indicates the duty cycles to the MCU), which is the lowest level of the codes here, uses the current control results. Therefore if it runs faster than the current control itself, it won't be doing anything but calculating the same thing over and over again. So basically, the codes need to run in the current control frequency, 10 times slower than the switching frequency.

The code called SVPWM should not be confused with what the MCU is doing on the peripheral, which is building the PWM itself based on the duty cycle set.

Finally, with the use of just one core, and no parallel processing, all this 4 codes have to run in less than $100\mu s$ (for f_{sw} =100kHz).

Once the main loop is implemented, with its control codes triggered by the interrupt flags, the proposed programming is finished, and the HIL tests can be performed.

5.7.5 Code testing

Jumping from theory straight to microcontroller implementation tends to be difficult, as debugging the code with the MCU already directly connected to the HIL proved to be a frustrating task.

Thus, an intermediate step was to advance in the Matlab/Simulink model used for testing the control, and also use it to test the codes.

With the aid of Simulink's function block, the designer can replace a specific block diagram with a coded function, testing the algorithm coded implementation, see current control example in Figures 76 and 77.

Figure 76 – Current control block diagram

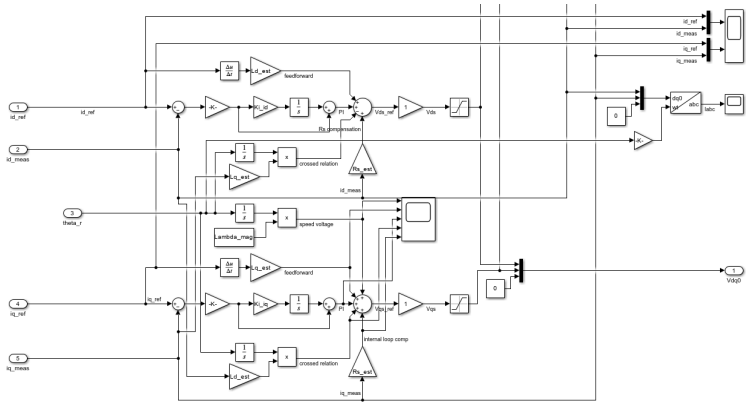

Figure 77 – Current control function block for code testing

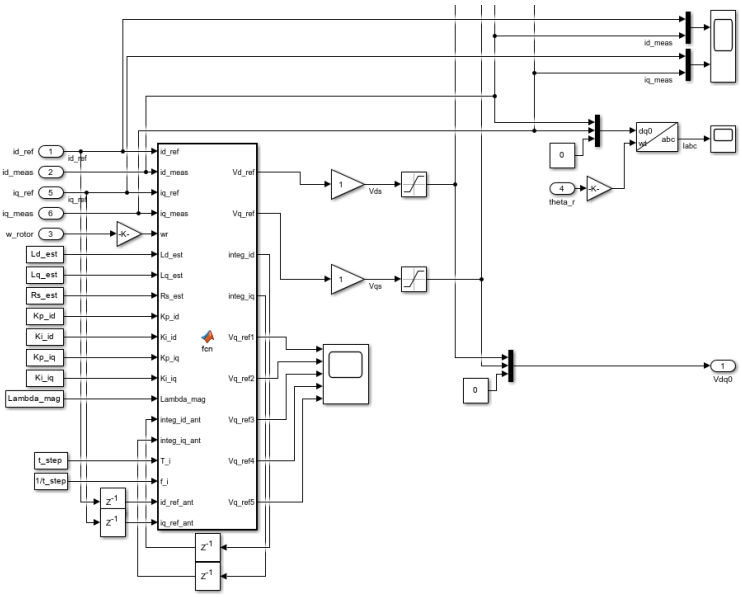

As python and Matlab are very similar languages, with microalterations the same codes programmed in Pyboard could be tested using this method. This greatly accelerated the code debugging process, making it possible to find specific problems, turning to be a suitable step for the development of this type of system.

5.7.6 Hardware in the loop

With the previous step done, PWM generation and code execution times were tested in a Hardware-in-the-Loop environment.

Testing of the system operation can be done in a physical plant or a simulated plant. The discussion regarding the cost comparison of the two solutions is beyond the scope of this work, but in this case, the tests and results were obtained in a simulated HIL (hardware-in-the-loop) plant. It is a simulation environment, similar to other solutions such as Matlab/Simulink and Plexim/PLECS, but with a structure for direct interaction with an external system through analog and digital inputs and outputs.

In this work its function is primarily to replace the physical system, allowing the MCU code to be tested without the need to finish the physical assembly of the inverter and the electrical machine, but additional advantages can be indicated below.

- System changes can be made with reduced time and less effort;
- The system can be easily controlled from a distance, since it is fully commanded by a computer;
- Since it is a simulation, power tests can be performed without risks of equipment damage, including short circuits;

It is relevant to point out that changes in the Pyboard V1.1 code are performed from a reset of the board. Using a digital output from the Typhoon HIL, it was possible to activate this reset and perform all tests remotely, speeding up the development process.

The methodology used to perform the tests was to initially model the system entirely in the HIL environment, including electrical machine, power converter, SVPWM module, current control, and speed control. The system can be seen in Figure 5.7.6.

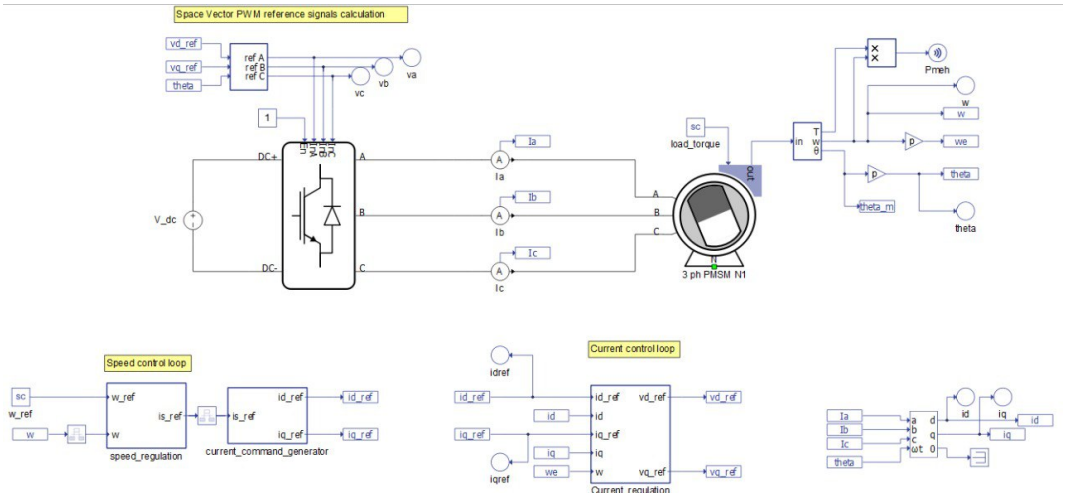

Figure 78 – HIL squematic for closed loop

This simulation allows the behavior of the system to be observed and serves as a basis for comparison for further developments. Based on the results obtained in it, the modules can be step by step replaced by the external MCU, so that the functionality can be tested block by block.

With the analyzes carried out, this work moves onto the results and discussions.

6 Results and Discussion

This chapter presents the results and discussions after executing the proposed design methodologies. It includes the following results.

- Model simulation;
- Assembly results;
- Control simulation results;
- HIL operation;
- Code execution time.

6.1 Model simulation results

The model simulation initial results were already partially presented with voltages, currents and command signals in Section 4.1. In this section the final results will be presented, starting with the power switches.

6.1.1 Power switch results

The sizing process was carried out, resulting in a 2-parallel solution with the power switch SCT4018KR (ROHM, 2022). The component junction temperature were obtained through the PLECS simulation, and the profile is presented in Figure 79.

Figure 79 – MOSFETs junction temperatures, 2-parallel SCT4018KR solution, 50RPM, discharged battery (3.3V per cell)

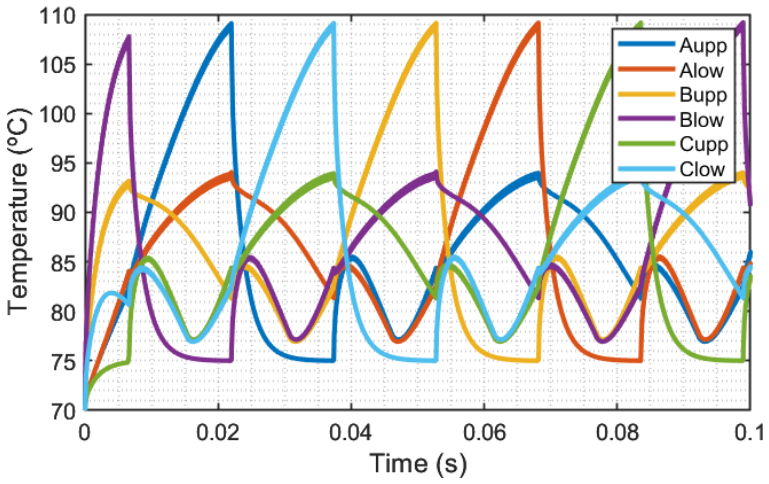

Since the junction thermal capacitance is low, it is possible to observe that the power switches are fast to reach steady-state operation. This facilitates the simulation process, allowing to run the simulation with a short time span. However, this also shows that a bad fault control strategy can be devastating to the converter. A short circuit, or even an over current situation would not take long to overheat the power switch and damage the component.

The same simulation done without the parallelization, reached a temperature junction of 197ºC. With the 2-parallel solution, and with the considerations made in the thermal model, there is still more than 40ºC of gap to reach the junction maximum temperature, which is not necessarily a oversizing of the system. Again, It is important to remember that when a fault occurs, such as a short circuit, the switches tend to overheat fast, so a design that is too tight in terms of temperature may not be a robust choice.

As the vehicle runs and discharge the battery, the DC voltage decreases, increasing DC current and affecting conduction losses, so these temperatures have to also be obtained for different battery voltages. This temperatures will also change with the motor RPM, since when the motor is at a lower RPM, the converter operates at a lower modulating frequency, giving more time to the switches to heat. Figure 80 shows the maximum junction temperature results considering these different factors, being possible to observe that in this case the temperature can vary 15ºC with this variables.

Figure 80 – MOSFETs junction temperatures, varying motor RPM and battery voltage

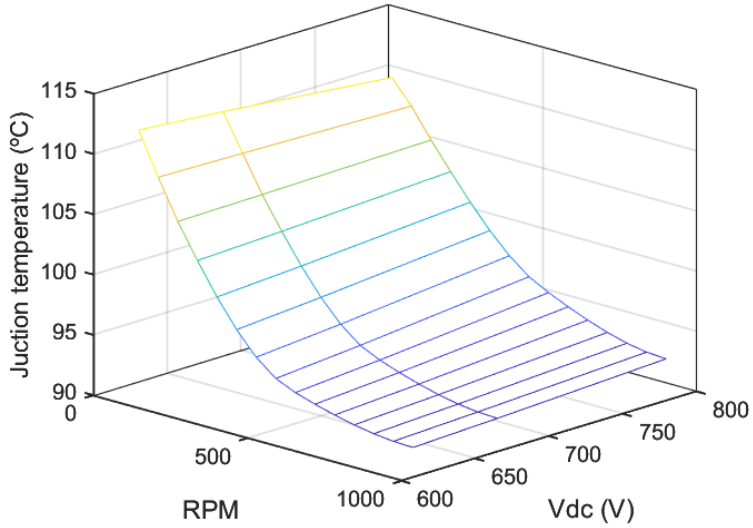

Regarding the losses, they will change with the battery voltage. There is also a low indirect dependence on the motor RPM, since it will change the instantaneous temperatures of the power switches, and the tendency is to have lower efficiency at higher temperatures. The total losses of the 12 switches are added and presented in Figure 81. The DC bus losses will also be include before finally stating the converter efficiency.

One interesting aspect that becomes clear in the losses plot, that was not that clear in the temperatures plot, is an inversion in its behavior. Both conduction and switching losses are

Figure 81 – Total MOSFETs losses, varying motor RPM and battery voltage

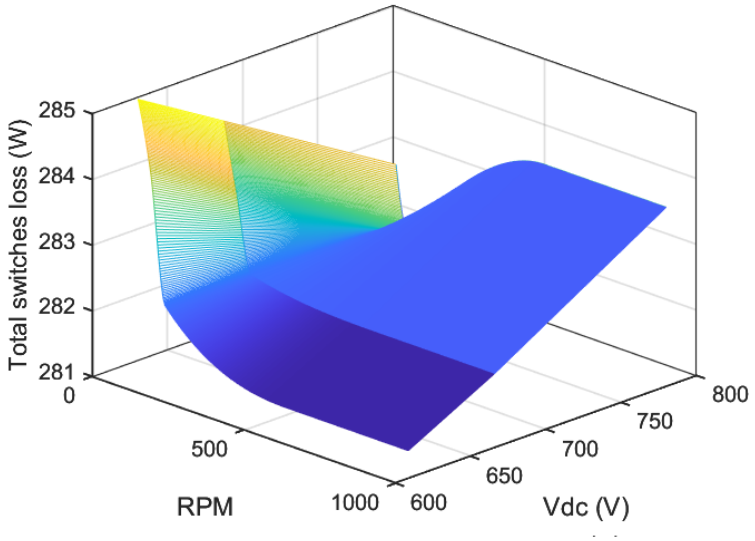

dependent on the current and voltage flowing through the switch, but their relation is different. The effect is that at low speeds, the conduction losses makes so that more losses occur with high currents (low battery voltages). At higher speeds, the behavior inverts, with the conduction and switching losses more balanced. Although this is an interesting effect, the losses did not vary in a absurd way, and for the desired 380Nm generation were kept around 283W.

The design loop was concluded, demonstrating success in thermal sizing, since the junction temperature did not exceed the limits established by the datasheet. This result means that any cooling system with thermal characteristics equal to or greater than the considerations made will be sufficient for the converter operation.

It is essential that in carrying out the tests, extra care is taken in slowly increasing the power, continuously measuring the temperature of the power switches. In addition, also check via oscilloscope if the current derivatives dI/dt are within the expected, operating on the gate resistance values $R_{g,ext,on}$ and $R_{g,ext,off}$ if necessary, so that the switching losses are not higher than expected.

6.1.2 DC bus results

For the DC bus, regarding losses, they will be affected on the RMS current that passes through it. Therefore, they will vary with the power drained by the inverter and also with the battery voltage. When the motor RPM is low, the power drained by the inverter is also low, so that in the DC bus, the currents are less intense, and the capacitors have less probability of overheating. Regarding battery voltage, when the battery discharges, higher currents are needed for providing the same power, and the capacitors are put in a more difficult thermal situation.

The final simulated losses for the selected DC bus capacitor, as it is designed for operating in high frequencies, were considerably low, since the ESR reaches values as low as $4m\Omega$, the

mean losses during a switching period do not surpass 5W, even with all the variation previously stated. Therefore, there is not much relevance in presenting them graphically here. These low loss values are the result of a good selection of capacitors, which must have a low ESR at the operating frequency.

As previously stated, the DC bus was designed based on the consideration that it carries only the ripple current of the inverter, with the zero-frequency current being provided by the battery. It is also important to notice that with regenerative braking, this is not the case, and the DC bus will charge (positive zero-frequency current) and discharge in the battery (negative zero-frequency current).

As the thermal capacitance of the DC-link is considerable, the thermal simulation generally may take long to run. The solution here was to define the initial temperature as the maximum datasheet temperature, and if it lowers with time, the capacitors are within the correct thermal operating range.

As only the thermal transfer via convection in the external area of the capacitors was considered, the temperatures tended to be inflated. However, even so, a convective heat transfer coefficient of 4W/m²K was sufficient to maintain the temperature within acceptable range.

Now regarding ripple voltages, the design loop also ended with values within the limits, both for the power switches (1200V) and DC-link (2x500V), see Figures 82 and 83.

Figure 82 – DC voltages for power switches input and DC-link, with fully charged battery

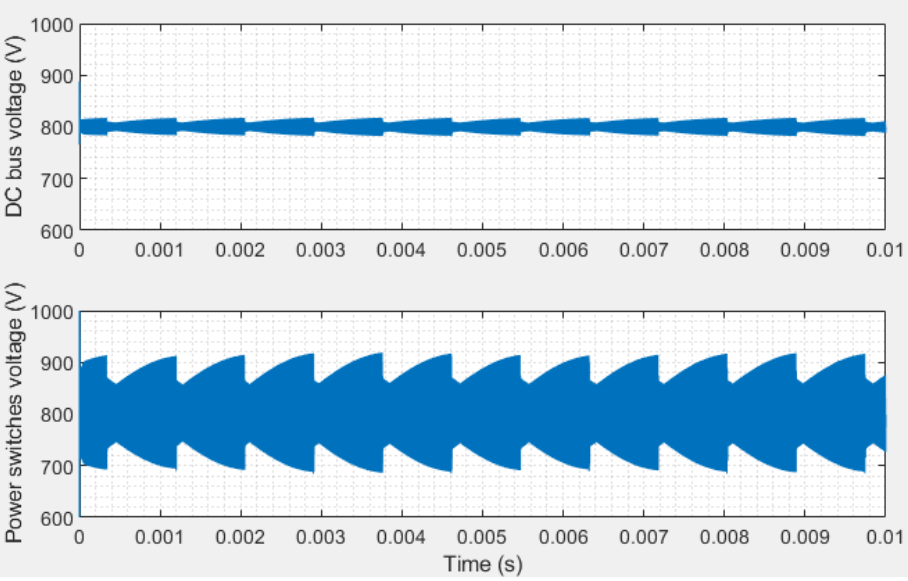

As expected, the power switches suffer with a higher ripple voltage, due to the switching current flowing through the DC bus bar inductance that connects them to the capacitors. Also, in both capacitors and power switches, with a charged battery more than 150V of range are still available to a further regenerative braking implementation and with a discharged battery, this goes up to more than 400V available.

Figure 83 – DC voltages for power switches input and DC-link, with fully discharged battery

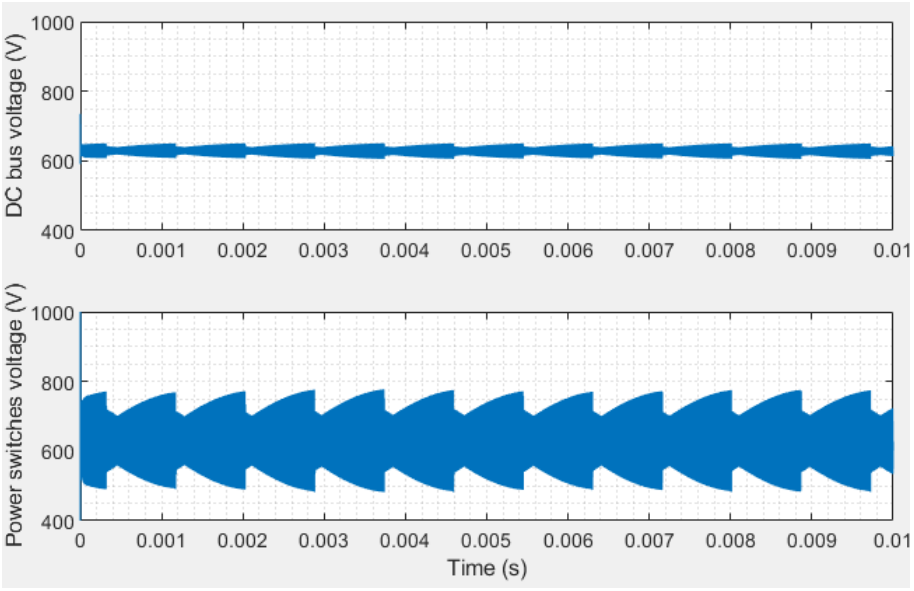

The sizing of the DC bus ripple has a curious effect. When battery discharges the tendency is that a lower DC voltage is present, but with the discharge, the DC current increases, increasing the ripple in the inductances. Therefore, this simulation really has to be done in different battery state of charges. In this work, this interesting phenomena was not predominant, and the fully charged battery were still presented the greatest DC voltage peak.

The results demonstrate the need to carry out the analysis for all battery load values, as well as the criticality of the parasitic inductances in the converter, especially the inductances in the connections between the DC bus and power switches.

6.1.3 General model simulation results

The converter efficiency is shown in Figure 84. With very low speeds the efficiency declines rapidly, due to natural high decline in power outputs. However, over most of the operating range is considerably higher, with 99.2% of nominal value.

In the efficiency plot, the dependency on the battery voltage is almost lost, since the variation in losses is very small compared to the output power.

6.2 Assembly results

With the previous analysis completed, the 3D CAD results can be presented. The Control and Power PCBs CAD can be seen in Figures 85 and 86.

In the Control PCB, the main issue was routing multiple signals between the MCU and the gate drivers, positioning the components in a way that separates analog from digital areas,

Figure 84 – Converter nominal efficiency, varying motor RPM and battery voltage

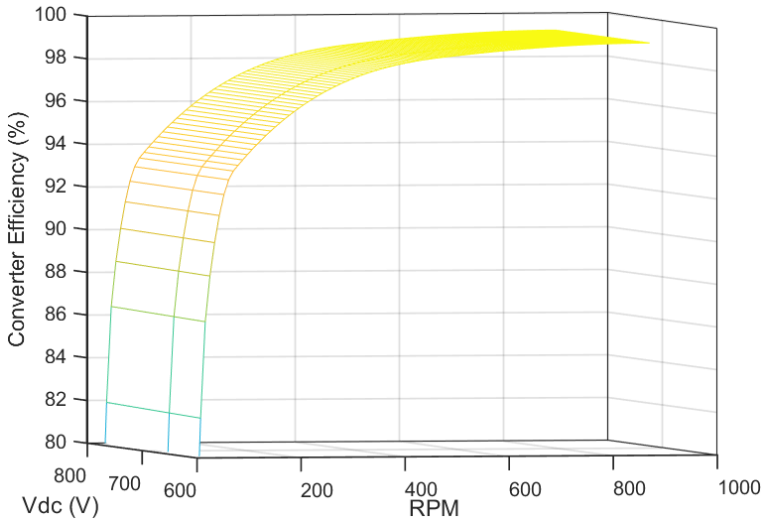

Figure 85 – Control PCB design CAD

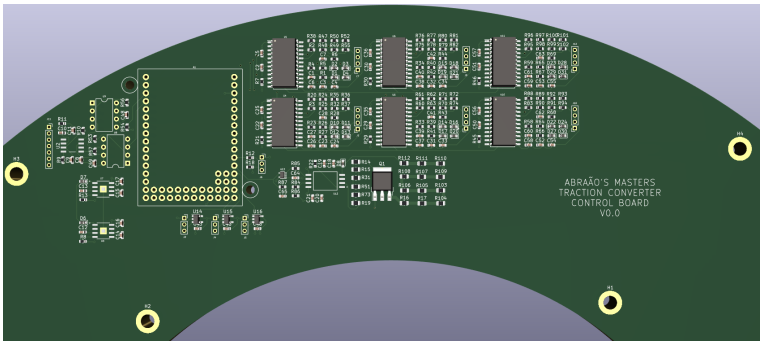

Figure 86 – Power PCB design CAD

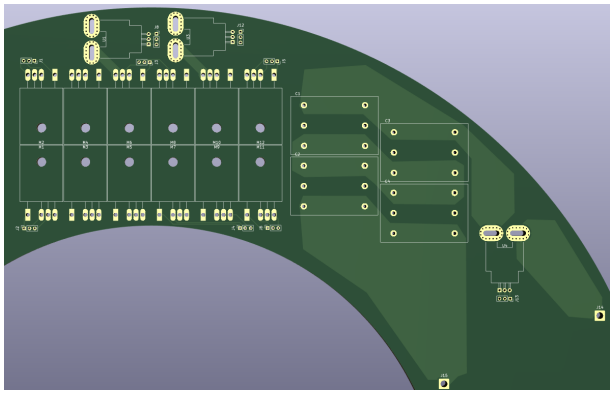

and also allocating the gate drivers on top of the power switches, for reducing the inductances in the gate path.

In the power PCB the most critical dimension was the radial. While around the perimeter the dimensional freedom is bigger, the converter competes for space with other vehicle systems in the radial dimension. Little can be done about the power switches themselves, apart from perhaps continuing analysis on different footprints. Improvements in this regard can also be seek with different equivalent solutions for current measurement, perhaps bringing current sensors to

another plane.

The power PCB exploded view showing the busbars geometry is in Figure 87.

Figure 87 – Power PCB exploded view

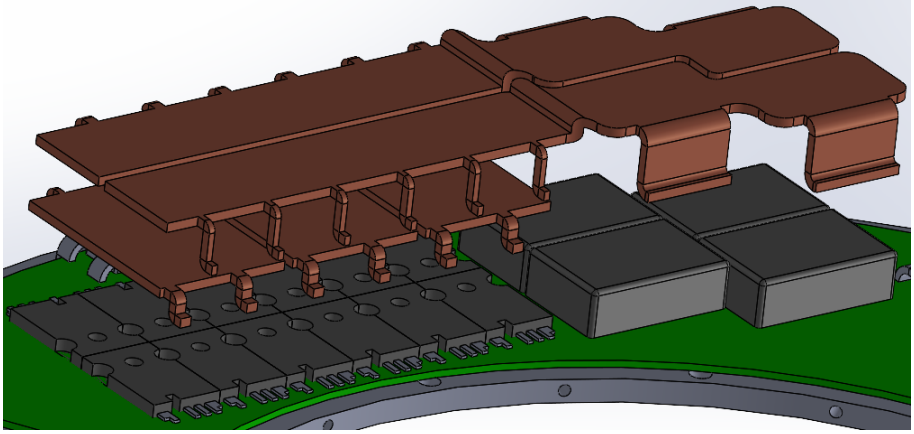

For reducing the inductance both in the AC busbars as well as in the DC-link busbars, multiple planes were defined, as follows.

- Coldplate;
- Power switches / Power PCB;
- DC-link capacitors and other components;
- 3-phase AC busbars;
- DC-link busbars;
- Control PCB;
- Cover.

Finally the full wheel assembly is presented in Figures 88 and 89.

In the front view it is possible to observe that the brake caliper does not allow the converter to be radially uniform. As the converter backplate also acts as a motor housing, it had to be extended by 360º, with the necessary internal radius variations. The decision made in relation to PCBs was to use only half of the angular space, which in addition to keeping them away from the heat generated in the brake system, also distances the electrical connections from the brake pressure lines.

In the superior plane cut view, several other considerations can be made about system packaging. The backplate is fixed together with the stator support. The motor housing was developed with the aim of following the wheel profile, in order to make better use of the available internal space. This allows the motor as well as the converter to be axially better inserted into the

Figure 88 – Full wheel assembly render, front view

Figure 89 – Full wheel assembly, superior plane cut view

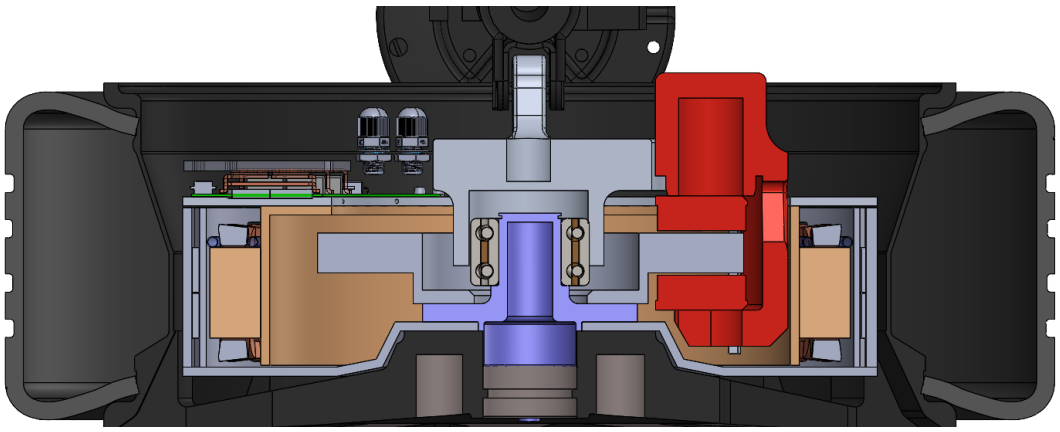

available internal space. The limit of this was defined by the brake disc. The radial dimension of the PCBs also competes for space with the brake disc, so the stator support needed to be expanded to move the PCB away from the disc.

Again, several analyses still need to be done on such a system before it goes on production, with the help of CAE software, like Ansys Sherlock, including vibration and further thermal analyses.

6.3 Speed control simulation results

The proposed speed control system was simulated in Matlab/Simulink, starting a reference speed ramp in 0.1s, with 6s duration, and nominal torque load applied at 6.5s, all according to the design requirements of Section 3.2. The controller time response is shown in Figure 90. The results of the complete control and of the PI only control were compared. It is possible to observe that the answers are similar, so that to visualize the differences it was necessary to present a zoom of the graph.

Figure 90 – Speed controller time response. Speed ramp from 0.1s to 6.1s. Maximum torque step at 6.5s

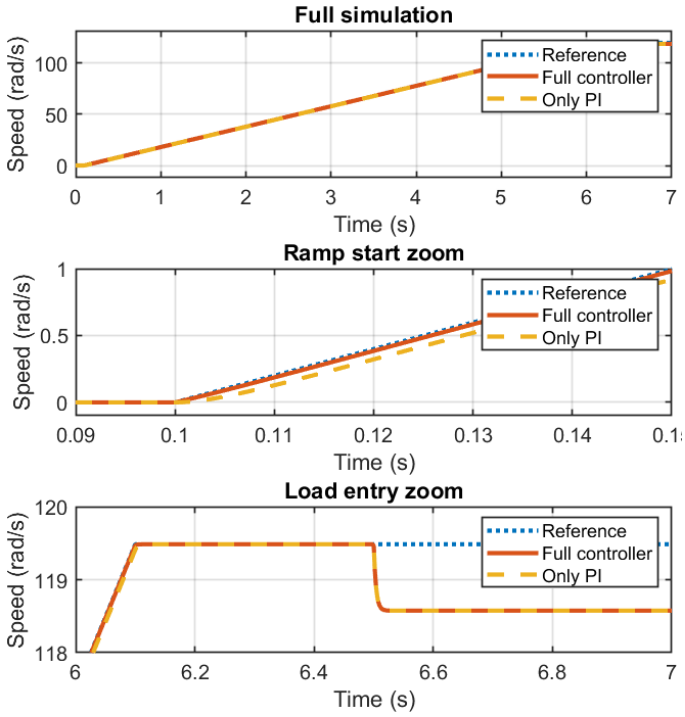

With the zoom, it was possible to observe that the complete control (with the insertion of friction compensation and feedforward) responds faster, getting closer to the reference. With this result, it remains for the system designer to assess whether these gains in the temporal response are worth the computational expense of the complete speed control implementation.

Figure 91 shows how each speed control section behaved. It is possible to observe that in the speed ramp, and consequently in any change of the reference speed, the feedforward acted in a relevant way. The PI acted mainly with the insertion of the load. Finally, the friction compensation acts proportionally to the speed, but its amplitude was considerably smaller than the others.

Finally, a sensitivity analysis to parameter variation is performed. As mentioned before, the parameter estimation/measurement is not perfect, so knowing the effects of these imperfections on the control performance is relevant.

Figure 91 – Speed controller operation. Speed ramp from 0.1s to 6.1s. Maximum load torque step at 6.5s

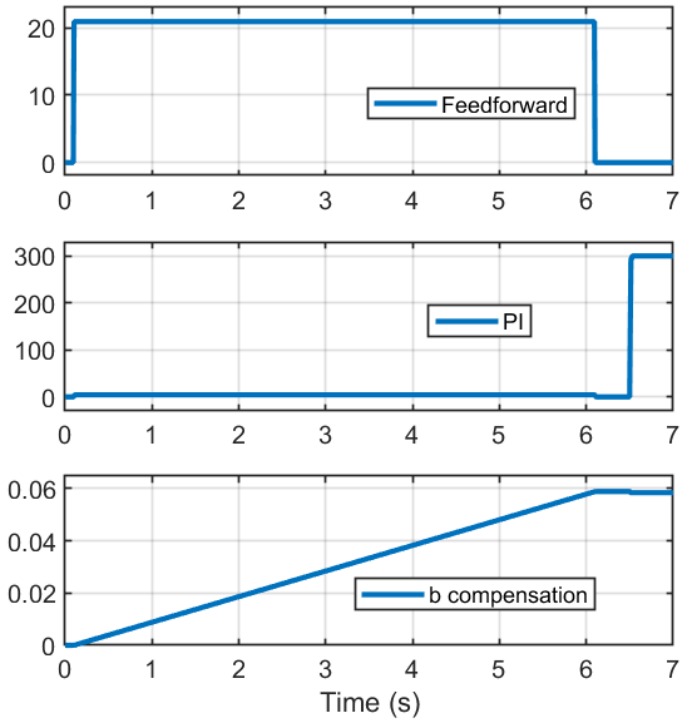

Figure 92 shows the results for the rotational inertia variation. It is possible to observe that if the designer overestimates the value of rotational inertia, that is, the control understands that the system has more inertia than it actually has, it commands more torque than necessary and the system ends up with a more aggressive behavior. On the other hand, if the designer underestimates this value, the system behaves slower, and the speed is lower than the reference. The full variation in the simulated range was around 0.5RPM, which for this nominal 905RPM system, none of these effects are expected to be noticeable to the vehicle crew.

Figure 92 – Speed controller rotational inertia variation sensitivity.

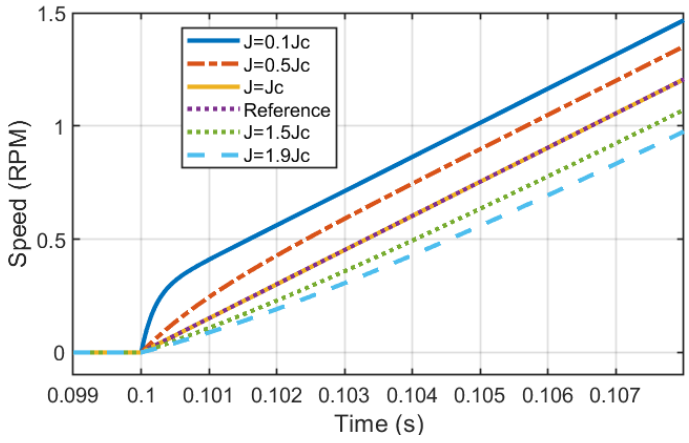

Figure 93 shows how feedforward relates to the effects of rotational inertia variation. As it is shown, the feedforward is based on the understanding of the control over the inertia of the plant, to advance a torque command. The simulated results indicate that depending on the parameter estimate, the feedforward implementation can move the system away from or closer to the reference. For example, under the specific conditions of the simulation performed, in the lower part of the figure, the system had more inertia than estimated, so the feedforward tends to bring the result closer to the reference. On the other hand, in the upper part of the figure, the system had less inertia than estimated, so that advancing an even greater torque command tends to distance the result from the reference.

Figure 93 – Speed controller rotational inertia variation sensitivity, and the effect of feedforward.

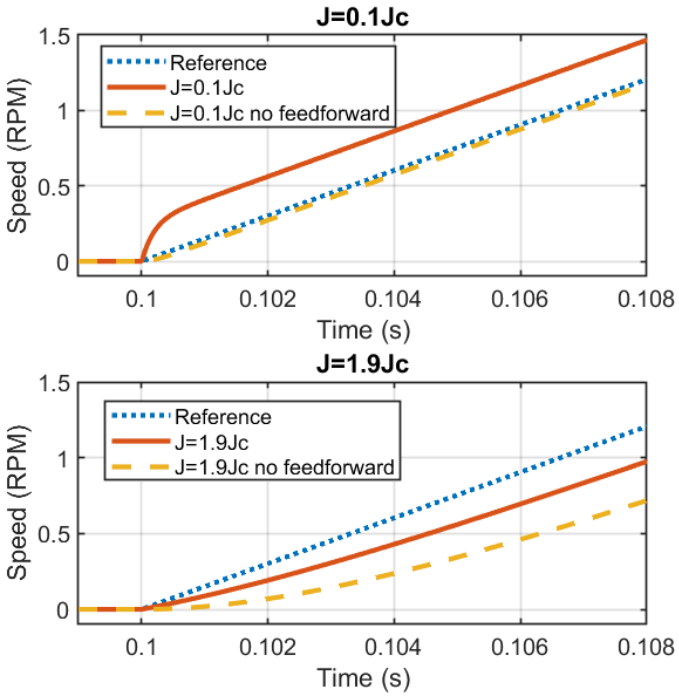

The same analysis procedure was performed for viscous damping, see Figure 94. The effect is similar to rotational inertia, but for this project, it happens on a reduced scale. A greater zoom was necessary to observe the effect, and the variations found were in the range of 1mRPM.

After presenting the results and discussing the speed control, this works moves on to the current control.

6.4 Flux weakening control simulation results

The flux weakening control was also simultaed in MATLAB/Simulink environment. The development here was directly to insert a maximum torque reference via pedals, and let the machine accelerate to its maximum speed, observing all the behavior of the control in its entire

Figure 94 – Speed controller viscous damping variation sensitivity. Speed reference above this data, with unfeasible simultaneous visualization.

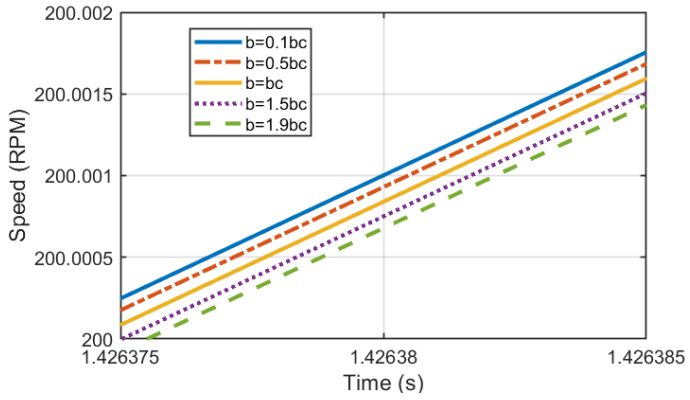

motor speed range. The results are shown in Figures 95 and 96. It is important to remember that the torque per motor is 380Nm, so that the double rear motor powertrain will have 760Nm.

Figure 95 – Id and Iq with constant full torque request from pedals

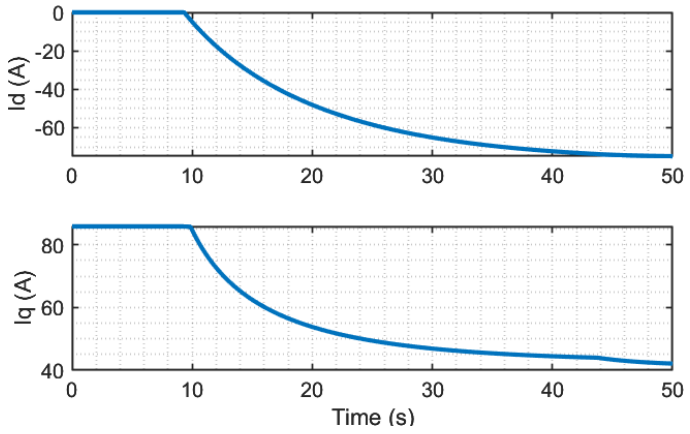

Figure 96 – Flux weakened torque with constant full torque request from pedals, with 2 rear motors powertrain

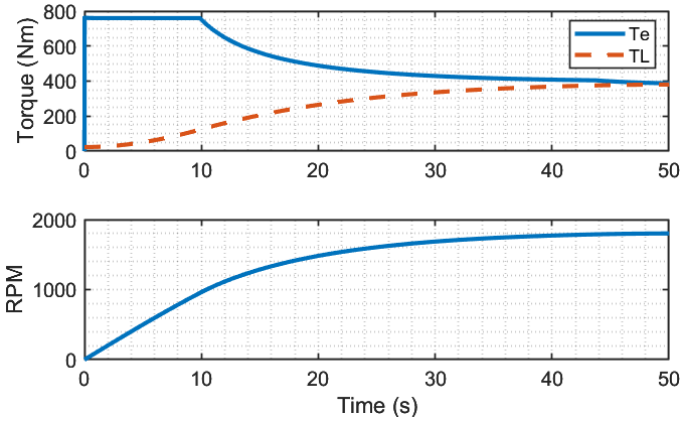

It is possible to observe the expected behavior. Until the nominal speed, the direct current is equal to zero and the quadrature current keeps equal to the torque reference times a gain. The torque is converted to machine, causing acceleration and with the increasing speed, the resisting forces grow.

Beyond nominal speed, a negative direct current is injected, with the negative signal representing that it will act against the magnets flux linkage. In this simulation case, the maximum current was considered to already be reached, so that quadrature current is also lowered with increased speed. This Iq behavior were a simulation example and does not have to occur this way. The designer will set the maximum current according to the limits of the converter and the electrical machine in its specific application.

With the flux weakening, the machine's torque is lowered, and the speed can increase further. The resisting torque keeps increases until both torques become equal and the vehicle reaches its maximum speed.

A sensitivity analysis to parameter variation is also indicated to be performed in future developments. Now this work resumes going to the current control simulations.

6.5 Current control simulation results

The proposed current control system was simulated in Matlab/Simulink, starting a reference current ramp in $10\mu s$, with $10\mu s$ duration, and nominal torque load applied at $30ms$. The results of this subsection will be presented for the current I_q, since it is related to the torque generation. The controller time response is shown in Figure 97. The results of the complete control, the control without feedforward and the PI only control were compared.

Figure 97 – Current controller time response. Current ramp from $10\mu s$ to $20\mu s$

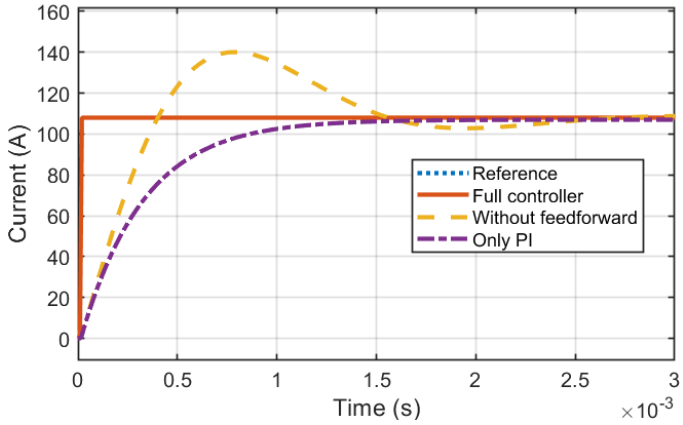

It was possible to observe that the complete control responds faster and that a considerable part of this response speed is in the feedforward. With this result, it remains for the system

designer to assess whether these gains in the temporal response are worth the computational expense of the complete current control implementation.

Figure 98 shows how each current control section behaved. It is possible to observe that in the current ramp, and consequently in any change of the reference current, the feedforward acted in a relevant way. The other control elements have reduced amplitudes.

Figure 98 – Current controller operation. Current ramp from $10\mu s$ to $20\mu s$

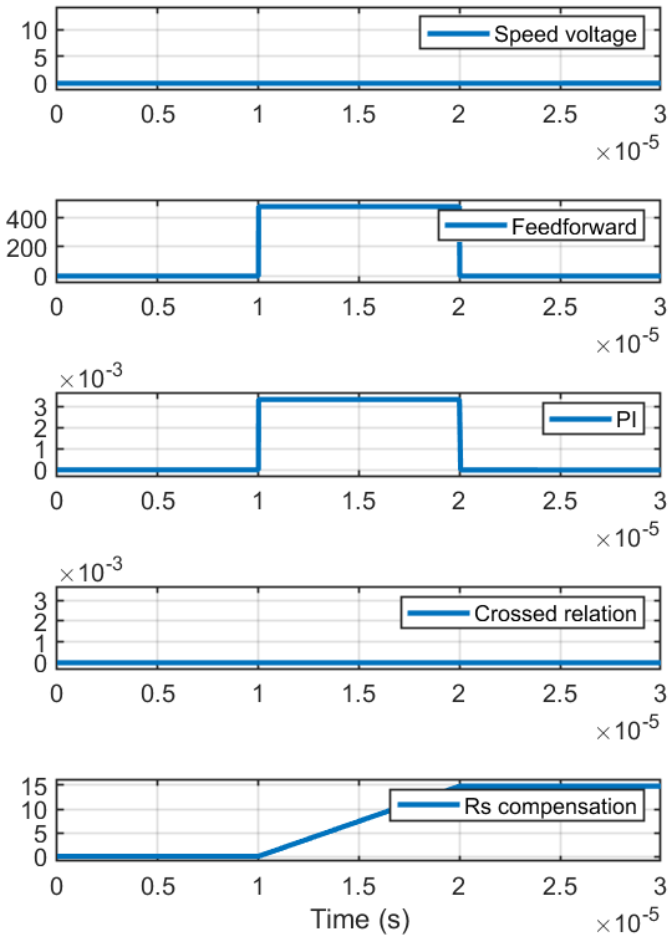

This result is interesting to demonstrate that in current control without feedforward, the controller actuation may be happening largely to compensate for the internal voltage disturbance. The effect of the disturbance depends on the mechanical speed, which takes considerably longer than the current to change.

Finally, a sensitivity analysis to parameter variation is also performed. Figure 99 shows the results for the inductance variation. It is possible to observe that if the designer overestimates the value of inductance, that is, the control understands that the system has more inductance than it actually has, it commands more voltage than necessary and the system ends up with a more aggressive behavior. On the other hand, if the designer underestimates this value, the system behaves slower. Unlike the relatively small speed control system variations, the range of

inductance estimates resulted in this case in variations of up to around 900% in the peak transient current.

Figure 99 – Current controller inductance variation sensitivity.

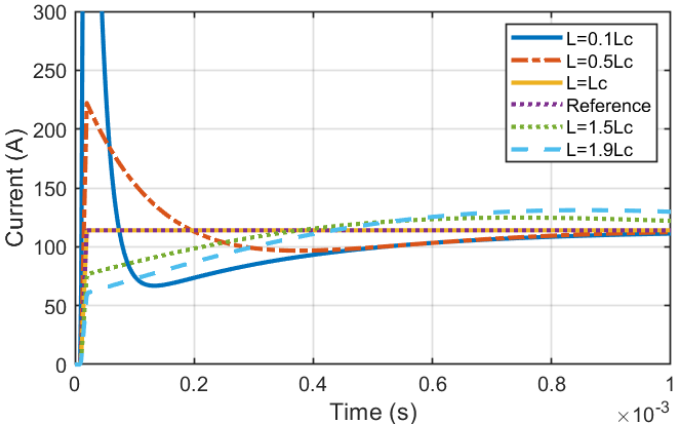

Figure 100 shows how feedforward relates to the effects of inductance variation. As it is shown, the feedforward is based on the understanding of the control over the inductance of the plant, to advance a voltage command. The simulated results indicate that depending on the parameter estimate, the feedforward implementation can can make the system more aggressive or slower. For example, under the specific conditions of the simulation performed, in the lower part of the figure, the system had more inductance than estimated, so the feedforward tends to bring the result closer to the reference. On the other hand, in the upper part of the figure, the system had less inductance than estimated, so that advancing an even greater voltage command tends to distance the result from the reference, in this case generating a considerable transient current spike.

The same analysis procedure was performed for stator resistance, see Figures 101. During the ramp, the effect linearly worsens with increasing current, as expected, reaching a maximum difference of 5A in this simulation. But again the biggest impacts are seen in the transients afterwards. The current peaks observed in this case were smaller than in the inductance, but still considerable. Underestimating the value of R_s showed the best results under the specific conditions of the simulation. Overestimating R_s raises the voltage commands, and transient current spikes are observed.

Figure 102 analyzes the effects of compensation, indicating again that the result of compensations can improve or worsen performance, depending on the operating condition and the precision in the estimation of the variables. The stator resistance, specifically, can be easily measured with an ohmmeter, so initially the errors in its estimate will depend on the quality of the measuring equipment. However, it should be remembered that it varies with temperature, so an interesting solution is to correct this estimate with temperature measurements of the coils.

Finally, for current control, another variable is interesting to be evaluated: the magnets

Figure 100 – Current controller inductance variation sensitivity, and the effect of feedforward.

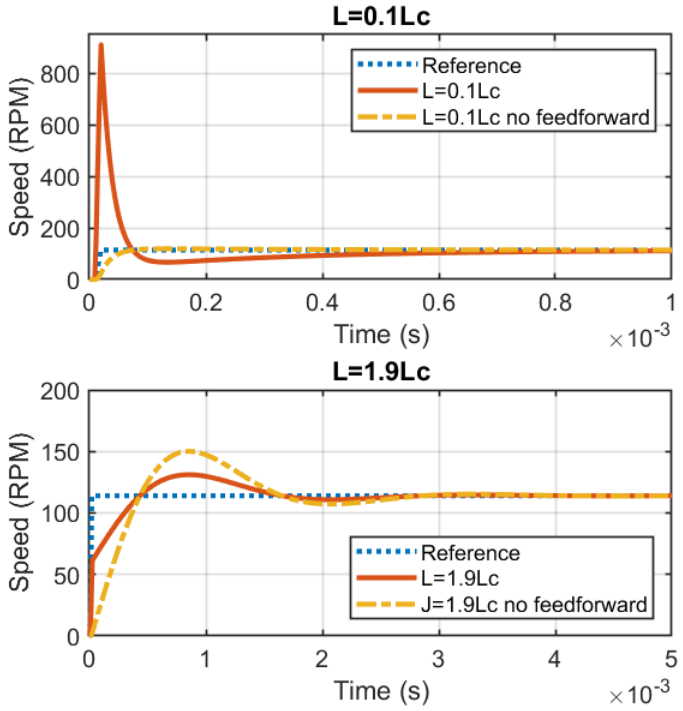

Figure 101 – Current controller stator resistance variation sensitivity.

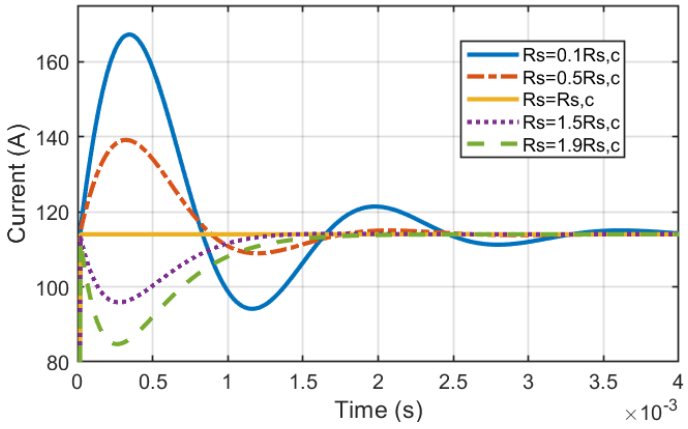

flux linkage. During the ramp, the variations found were reduced, with a maximum of 1mA. Figure 103 demonstrates that again the most noticeable changes were after the end of the ramp, where the magnet flux link estimation errors generate a steady state error.

Figure 104 analyzes the effects of compensation, with similar conclusions to the previous analysis. Clearly for the specific conditions of the simulation performed, the variations found were greater when the flux linkage value is underestimated. The level of variation found in the case of the flux linkage of this machine was considerably smaller than in the case of inductance and stator resistance.

With the proposed evaluations for the control system finalized, it is time to proceed to an

Figure 102 – Current controller stator resistance variation sensitivity and compensation effects.

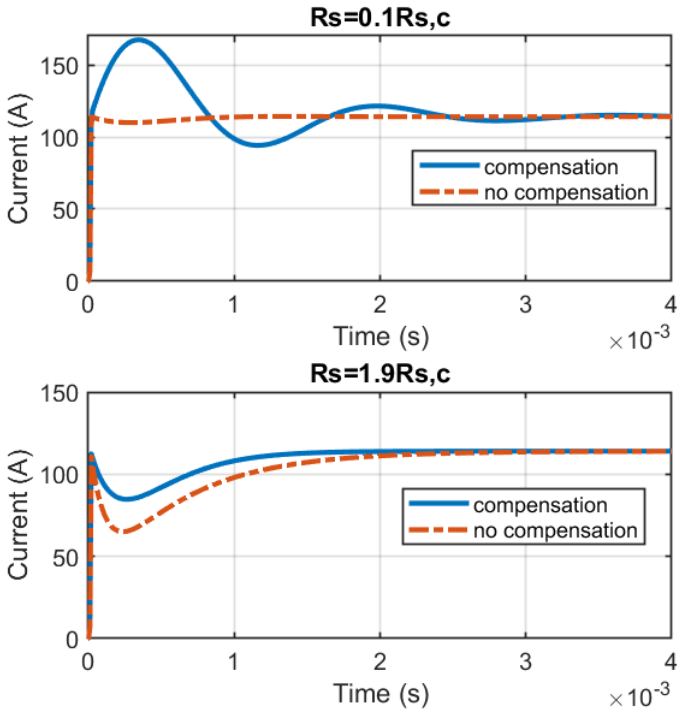

Figure 103 – Current controller magnets flux linkage variation sensitivity.

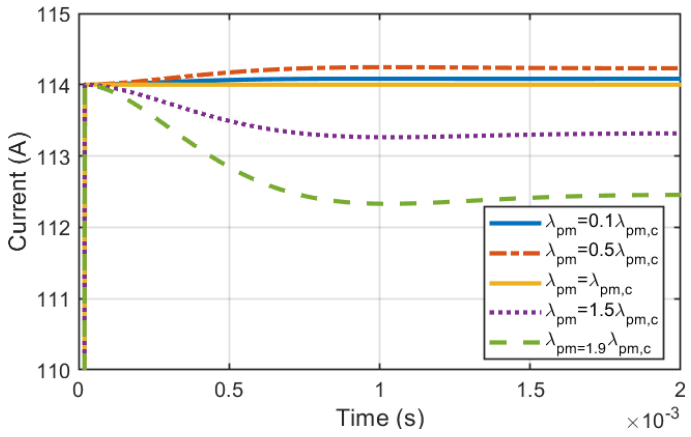

analysis of the code execution times, to evaluate the performance in its implementation in the proposed prototyping MCU.

6.6 HIL operation

As previously stated, a Hardware-in-the-Loop solution was used to test both the PWM operation and the code execution times. Due to the issues with pins, number of PWM and channels of the Pyboard v1.1, the full "Double-wave Modulation" could not be tested, just the classical SVPWM implementation.

Figure 104 – Current controller magnets flux linkage variation sensitivity and compensation effects.

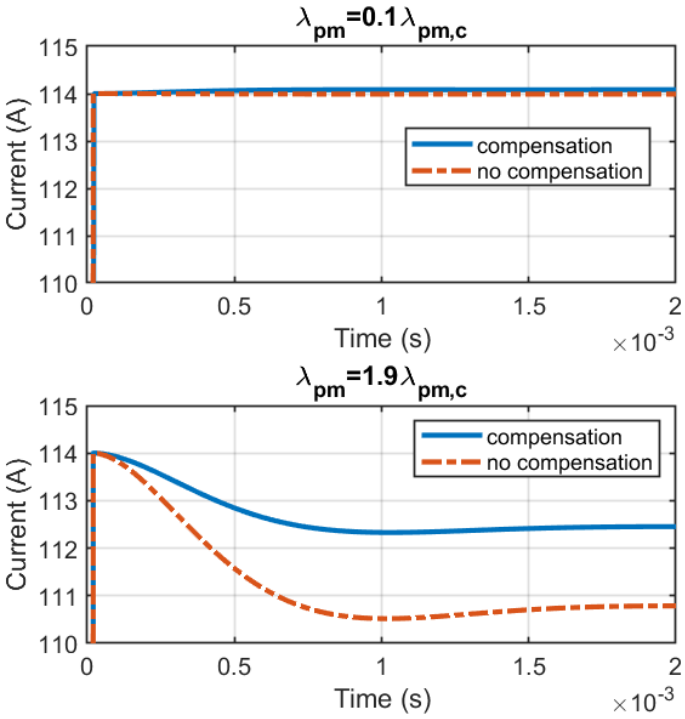

The results with the aid of the HIL, allowed visualizing the system operation performed directly by the MCU. The SVPWM generated phase and line voltages are shown in Figures 105 and 106, respectively.

Figure 105 – SVPWM phase voltages

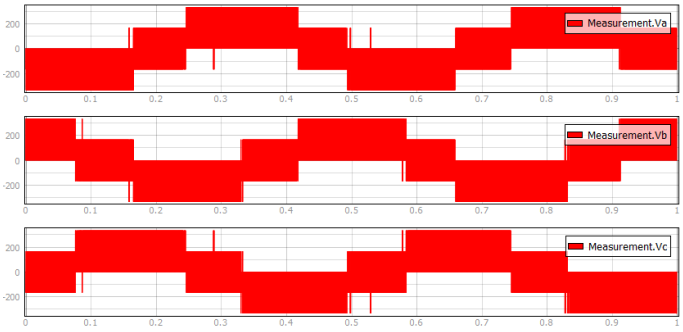

With the observation of the expected phase voltage and line voltage waveforms for the SVPWM, the presentation of the results proceeds for the duration of the codes.

6.7 Code execution time

For time measurement a digital output of the MCU was used, being set to high before the section of the measured code, and at the end set to low. This digital output was connected to

Figure 106 – SVPWM line voltages

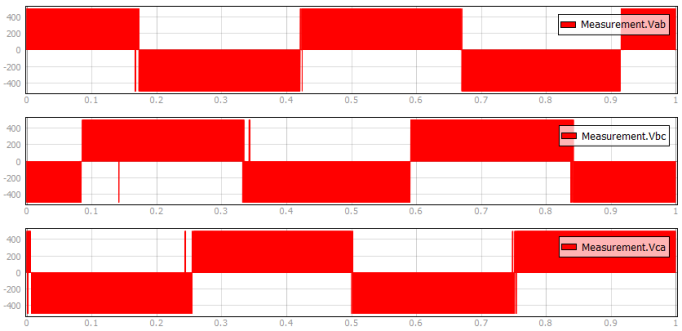

the Typhoon HIL, and observed in the project scopes.

The codes were optimized to reduce execution time, and an example case study on how to do it is presented in Subsection 6.7.1. The results of the code execution time follow.

- Classical SVPWM: $623\mu s$;
- SVPWM carrier-based implementation (without set duty cycle): $231\mu s$;
- Double-wave Modulation SVPWM carrier-based implementation (without set duty cycle): $367\mu s$;
- Current control: $344\mu s$;
- Flux weakening control: $60\mu s$;
- Speed control: $81\mu s$.

Considering that we can operate the SVPWM in the current control frequency, in other words, 10 times slower than the switching frequency, we can now calculate if this code execution times would be sufficient for reaching the 100kHz desired. With only this codes, using Equation 5.57 for only one core, without parallel execution, the maximum switching frequency is 11737 Hz, see Equation 6.1. Even after optimizing the code execution time, this switching frequency is still 8.52 times lower than the 100kHz objective.

$$(367e^{-6} + 344e^{-6} + 60e^{-6} + 81e^{-6}) = 852e^{-6} < \frac{1}{f_{svpwm}} = \frac{1}{f_{sw}/10} = \frac{1}{11737/10} \tag{6.1}$$

Considering a possibility of operating with 2 parallel operating cores, with 1 only for the SVPWM code, and the second core executing the other codes, the switching frequency could be increased to 20618 Hz, still 4.85 times lower than the 100kHz objective.

6.7.1 Execution time optimization: Classical SVPWM code case study

Initially the SVPWM code was run and the result after a round of optimizations is described in Table 8.

Table 8 – Classical SVPWM code sections execution time

Code section	Exec time (us)
Interrupt & runtime measurement	10
Global variables, preload methods, return	40
Read 3 ADCs	154
Scale and shift ADCs	29
Dq0 to alpha beta	109
Vmodulus calculation	27
acos and conditionals	64
Set sector & preset sin cos $\gamma_1\gamma_2$	31
T1,T2,T0	55
ta, tb, tc	17
Scale and set duty cycle	87
Full SVPWM code	623

Considerable time is used reading the ADCs and performing the dq0 to alpha-beta transform. The acos implementation and calculation of times also spent quite some processing time. Based on this type of analysis it is possible to prioritize optimizations of particular code sections. Following, are explanations of some of the work done to decrease runtime.

The first task performed was the use of local variables and preload methods, the results are seen in Table 9.

Table 9 – Local variables and preload method analysis

	Full exec time (μs)	Gain (μs)	Gain %
Original code	1024		
Local variables	845	179	17,48%
Preload methods	832	13	1,27%

The performance increase in using local variables was demonstrated, indicating that the time for the microprocessor to find these variables in the global dictionary was considerable. The impact of the preload methods was not so expressive in comparison, mainly because within the SVPWM algorithm, the functions are not used repetitively, at most three times each.

The ADCs issue was also analyzed, testing other functions present in micropython, namely read_timed() and read_timed_multi(). The results are seen in Table 10. Buffer sizes tested were 1, 3 and 5. In the cases of 3 and 5 buffers, a simple average was calculated and their runtime is included in the "Code(μs)" column.

Table 10 – ADCs methods analysis

	Code (μs)	Read (μs)
Read	469	154
Read timed, buffer size 1	441	2525
Read timed, buffer size 3, mean	503	8475
Read timed, buffer size 5, mean	516	14462
Read timed multi, buffer size 1	443	1524
Read timed multi, buffer size 3, mean	480	3487
Read timed multi, buffer size 5, mean	497	5469

Interestingly enough, the read_timed() and read_timed_multi() functions presented worse results. The rest of the code may eventually have execution time reductions, but the ADC reading becomes extremely time consuming. Unfortunately this functions also have a blocking characteristic, which causes the microprocessor to stop its main execution to read the ADCs anyway. For this application, no advantage was found in using these functions, and the previous simple read() implementation was kept. Once again: a future micropython implementation of this reading process in a peripheral system is relevant for improving the performance of the embedded SVPWM.

Finally, parts of the code that were in the main loop were also inserted into separate functions, prioritizing local memory allocation and local dictionaries searches. Associated with it, the micropython's Native function was evaluated, which allows the code to be pre-allocated in memory and speeds up its execution. The results are seen in Table 11.

Table 11 – Code in functions and micropython.native analysis

Optimization step	Full runtime (μs)	Gain %
SVPWM code, without native	714	
SVPWM code, with native	665	6,86%
ADCs method in function	646	2,66%
ADCs method in native	642	0,56%
Set duty cycle in function	640	0,28%
Set duty cycle in native	623	2,38%
Total		12,75%

The final execution time of the classical SVPWM algorithm was 623us.

In addition to this analysis, it is interesting to comment about the garbage collector issue. When memory is being allocated on the heap, at some point the memory limits may be reached. In this case, a procedure that lasts a few milliseconds is executed to clean the memory references, freeing these "garbage" for use again. Future development needs to be done to evaluate the effects of the garbage collector on machine drive operation.

An interesting way to drastically reduce the runtime is to use a hybrid programming solution. The SVPWM code is programmed in C, while the other (less frequent) codes are programmed in micropython. In this way, the SVPWM code can be used as a fast executed library function for the python programmer.

7 Conclusion and Future Developments

This work's main objective was the design of a Bidirectional Three-Phase Converter for automotive traction application. The project was presented with its specific nuances of an automotive application.

The development was made from the justification of the relevance of the work, and the use and growth of technology in electric traction, going through the state of the art of related solutions, topologies of the powertrain, the converter and the state of the components.

The project requirements were presented, focusing on the specifics of the automotive application, and based on acceleration and maximum speed targets, the traction system modeling was developed, finding power, torque, voltage and current targets.

Then the hardware project itself was presented, from all the main components of the converter, to more specific details about the PCBs project. The packaging within the in-wheel system was a considerable challenge, being very multivariable, requiring consideration of suspension, brakes, motor and converter designs. Several iterations were carried out to achieve a viable system for the in-wheel application, with considerably simple packaging to facilitate scale production and maintenance.

The software and control project followed, presenting solutions for machine control with full algorithm development and programming in a high-level environment. Currently, it is not possible to use micropython for real-time control of electrical machines in an automotive practical environment, proving to still be limited to simple proof-of-concept implementations. When the language is compared with C, it is a higher level solution, therefore presenting slower execution time. Slower code means a limit on the frequency of controls, mainly current control. Optimizations allow increasingly higher frequencies to be reached, but still not enough for a fast switching like the one in this project. For possible future implementation in automotive systems, the engineering community awaits the development of higher speed systems that follow the appropriate automotive regulations.

The development and presentation of many of the main issues related to the design of an automotive traction converter were completed, seeking to generate relevant documentation to considerably accelerate the future design of any similar system by the scientists and engineers who have contact with this work.

Regarding the specific objectives presented in Chapter 1, it is worth concluding here how they were treated and reached.

- The development of solution suitable for automotive application was a major focus of development, seeking to select components and ICs that were qualified for the application.

A considerable geometric effort was also made to make it possible to mount this system inside the vehicle's wheel;

- To increase the efficiency of the traction system as a whole, the direct driven in-wheel solution was selected, removing the need to use mechanical reduction, which has losses. SiC MOSFETs were also used, being a solution that tends to reduce system losses, compared to Si IGBTs. Synchronous rectification were also a solution to improve even further the efficiency of the system;
- To facilitate vehicle electrification procedures and/or vehicle volume reduction, the motors were inserted in-wheel, as well as the converter, further modularizing the in-wheel solution, and further increasing the vehicle's internal space, which can be used for other purposes;
- To reduce the volume and mass of the traction system, this work sought to share the packaging of the motor and the converter, as well as future studies on sharing the cooling system. The SiC MOSFET solution also tends to reduce this final volume, since with less losses the components tend to be smaller;
- And finally to facilitate power converter prototyping for academia and companies, the development was carried out in a prototyping proposal with a high level MCU programmed in micropython. Although it was observed that this solution is still not enough for prototyping beyond a simple proof-of-concept, in the future this solution can turn out to accelerate learning about Power Electronics, as well as helping small and medium-sized companies in the development of algorithms and implementation of traction converters.

Here are suggestions for further development.

7.1 Future Developments

This project is intensely related to the area of Power Electronics, so that extensive contents of the postgraduate courses in Electrical Engineering at UFMG were applied. This enabled the development well, despite it having been concomitant with distance learning due to the COVID-19 pandemic. A huge shortage in the supply of components and ICs occurred in this period, making the assembly of PCBs and subsequent bench tests unfeasible. The solution was to focus mainly on the design process and develop deep into the function/thermal/electrical/control simulations. The proposed future developments to continue this research follow.

Regarding general propositions:

- Assemble the converter and perform bench tests;
- Advance in bench tests of flux weakening operation, taking care to avoid demagnetization;

- To further describe the correlation between the electrical machine and the traction converter design algorithms;
- Analyze feasibility of developing the solution for rims smaller than 17", and if the brake system could still be allocated radially to the traction assembly (internally to the motor and inverter);
- Submit the converter to the tests of the necessary regulations, to formally qualify it for the automotive application;
- Include battery voltage sag analysis for DC-link design;
- Full design of the converter with Si IGBT technology, including cost and performance comparisons.

Regarding thermal issues:

- Multiphysics computational modeling of the power converter and validation;
- Thermal tests of the power switches and validation of the developed model;
- Thermal tests of the bus capacitors and validation of the developed model;
- Analysis of effects of power factor variation on power switches thermal sizing.

Regarding costs analysis:

- An in-depth cost analysis of the developed converter;
- Review of all ICs and components in an extensive search for cheaper equivalent solutions;
- Mathematical cost description and optimization, based on design decision;
- Include how a reduction in the acceleration target can affect the final cost of the powertrain for more popular consumers.

Regarding regenerative braking:

- Full regenerative braking analysis;
- Include in the analysis the effects of impedances between V_{bat} and V_{bus};
- Analyze whether it will be necessary to use DC bus power switches and capacitors with greater voltage withstand

Regarding software:

- Implement the control model in a free and more accessible software/tool, providing an alternative option to Matlab/Simulink;
- Develop sensorless control, with no encoder;
- Develop DTC control and compare results with FOC;
- Develop regenerative braking control, with internal battery current loop and external DC bus voltage loop;
- Evaluate the effects of the garbage collector on machine drive operation;
- Compare code execution time with speed control done with a separate timer and done inside current control interruption;
- Implement SVPWM function in C inside Pyboard, generating a library and comparing performance;
- Implement the entire system in C with an automotive microcontroller optimized for the application and commercialization of the solution

Bibliography

ALLEGRO. *ACS724 and ACS725: High-Accuracy, Isolated Current Sensor with Stray Field Rejection*. 2022. Disponível em: <https://www.allegromicro.com/en/products/sense/current-sensor-ics/zero-to-fifty-amp-integrated-conductor-sensor-ics/acs724-5>. Citado na página 97.

ALVES, L. F. et al. Sic power devices in power electronics: An overview. In: IEEE. *2017 Brazilian Power Electronics Conference (COBEP)*. [S.l.], 2017. p. 1–8. Citado 3 vezes nas páginas 10, 49, and 50.

ANDERSON, S. *Python vs. Java: A Deep Dive Comparison*. 2022. Disponível em: <https://streamsets.com/blog/python-vs-java-comparison/>. Citado 3 vezes nas páginas 15, 58, and 59.

ANDREESCU, G.-D. et al. Stable v/f control system with unity power factor for pmsm drives. In: IEEE. *2012 13th international conference on optimization of electrical and electronic equipment (OPTIM)*. [S.l.], 2012. p. 432–438. Citado na página 74.

ATS. *Tubed Cold Plates*. 2022. Disponível em: <https://www.qats.com/Products/Liquid-Cooling/Tubed-Cold-Plates>. Citado na página 83.

BADRAN, M. A.; TAHIR, A. M.; FARIS, W. F. Digital implementation of space vector pulse width modulation technique using 8-bit microcontroller. *World Applied Sciences Journal*, Citeseer, v. 21, p. 21–28, 2013. Citado na página 133.

BARNES, C. M.; TUMA, P. E. Practical considerations relating to immersion cooling of power electronics in traction systems. In: IEEE. *2009 IEEE Vehicle Power and Propulsion Conference*. [S.l.], 2009. p. 614–621. Citado na página 44.

BATTISTON, A. et al. A control strategy for electric traction systems using a pm-motor fed by a bidirectional z-source inverter. *IEEE Transactions on Vehicular Technology*, IEEE, v. 63, n. 9, p. 4178–4191, 2014. Citado na página 112.

BERA, T. K.; BHATTACHARYA, K.; SAMANTARAY, A. K. Evaluation of antilock braking system with an integrated model of full vehicle system dynamics. *Simulation Modelling Practice and Theory*, Elsevier, v. 19, n. 10, p. 2131–2150, 2011. Citado 2 vezes nas páginas 14 and 186.

BIELA, J. et al. Sic versus si—evaluation of potentials for performance improvement of inverter and dc–dc converter systems by sic power semiconductors. *IEEE transactions on industrial electronics*, IEEE, v. 58, n. 7, p. 2872–2882, 2010. Citado 2 vezes nas páginas 37 and 50.

BLAND, D. *Electric is good, but ethanol seen better in Brazil*. 2022. Disponível em: <https://www.globalfleet.com/en/fleet-strategy/latin-america/features/electric-good-ethanol-seen-better-brazil>. Citado na página 27.

BOILLAT, D. O. et al. Volume minimization of the main dm/cm emi filter stage of a bidirectional three-phase three-level pwm rectifier system. In: IEEE. *2013 IEEE Energy Conversion Congress and Exposition*. [S.l.], 2013. p. 2008–2019. Citado na página 45.

BOLOGNANI, S. et al. Combined speed and current model predictive control with inherent field-weakening features for pmsm drives. In: IEEE. *MELECON 2008-The 14th IEEE Mediterranean Electrotechnical Conference*. [S.l.], 2008. p. 472–478. Citado na página 122.

BRAVO, D. M. et al. *Estudo da influência do aumento da massa não suspensa em um veículo híbrido com motores elétricos nas rodas*. [S.l.]: CONEM, 2012. Citado 2 vezes nas páginas 35 and 67.

BROECK, H. W. V. D.; SKUDELNY, H.-C.; STANKE, G. V. Analysis and realization of a pulsewidth modulator based on voltage space vectors. *IEEE transactions on industry applications*, IEEE, v. 24, n. 1, p. 142–150, 1988. Citado na página 56.

BROUGHTON, J. et al. Review of thermal packaging technologies for automotive power electronics for traction purposes. *Journal of Electronic Packaging*, American Society of Mechanical Engineers, v. 140, n. 4, p. 040801, 2018. Citado na página 44.

BRUBAKER, M. et al. Integrated dc link capacitor/bus enables a 20% increase in inverter efficiency. In: VDE. *PCIM Europe 2014; International Exhibition and Conference for Power Electronics, Intelligent Motion, Renewable Energy and Energy Management*. [S.l.], 2014. p. 1–8. Citado na página 54.

BRUBAKER, M. A. et al. Optimized dc link for next generation power modules. In: VDE. *PCIM Europe 2016; International Exhibition and Conference for Power Electronics, Intelligent Motion, Renewable Energy and Energy Management*. [S.l.], 2016. p. 1–9. Citado na página 54.

BSI-GROUP. *IATF 16949 - Indústria Automotiva*. 2021. Disponível em: <https://www.bsigroup.com/pt-BR/IATF-16949-Industria-Automotiva/>. Citado na página 60.

BUCCELLA, C.; CECATI, C.; LATAFAT, H. Digital control of power converters—a survey. *IEEE Transactions on Industrial Informatics*, IEEE, v. 8, n. 3, p. 437–447, 2012. Citado na página 37.

BUSO, S. *Digital Control of Three-Phase DC/AC Converters: Current Control Techniques*. 1999. Disponível em: <https://www.dsce.fee.unicamp.br/~antenor/pdffiles/lez3.pdf>. Citado na página 133.

CADENCE. *Fr4 Maximum Temperature and Thermal Dissipation*. 2022. Disponível em: <https://resources.pcb.cadence.com/blog/2020-fr4-maximum-temperature-and-thermal-dissipation>. Citado na página 101.

CHAN, C. et al. *Modern electric vehicle technology*. [S.l.]: Oxford University Press on Demand, 2001. v. 47. Citado na página 33.

CHAPMAN, R. *New, 800V, electric cars, will recharge in half the time*. 2021. Disponível em: <https://www.economist.com/science-and-technology/new-800v-electric-cars-will-recharge-in-half-the-time/21803666>. Citado na página 48.

CONCARI, L. et al. H8 architecture for reduced common-mode voltage three-phase pv converters with silicon and sic power switches. In: IEEE. *IECON 2017-43rd Annual Conference of the IEEE Industrial Electronics Society*. [S.l.], 2017. p. 4227–4232. Citado 2 vezes nas páginas 10 and 45.

CZERWONKA, M. *Dados preliminares mostram queda no número de mortes no trânsito brasileiro em 2020*. 2021. Disponível em: <https://www.portaldotransito.com.br/noticias/dados-preliminares-mostram-queda-no-numero-de-mortes-no-transito-brasileiro-em-2020/>. Citado na página 60.

DIAO, L. et al. An efficient dsp–fpga-based implementation of hybrid pwm for electric rail traction induction motor control. *IEEE Transactions on Power Electronics*, IEEE, v. 33, n. 4, p. 3276–3288, 2017. Citado na página 55.

DOE-USA, U. D. o. E. *The Hystory of the Electric Car*. 2014. Disponível em: <https://www.energy.gov/articles/history-electric-car>. Citado na página 30.

DOE-USA, U. D. o. E. *How Much Air Pollution Comes From Cars?* 2021. Disponível em: <https://auto.howstuffworks.com/air-pollution-from-cars.htm>. Citado na página 28.

EHSANI, M. et al. *Modern electric, hybrid electric, and fuel cell vehicles*. [S.l.]: CRC press, 2018. Citado na página 64.

ELECTRONICS, C. *MicroPython Board Comparison*. 2022. Disponível em: <https://core-electronics.com.au/guides/micropython-board-comparison/>. Citado na página 131.

EMDRIVE. *emDRIVE User Manual*. 2021. Disponível em: <https://www.emdrive-mobility.com/downloads/>. Citado na página 113.

ENGINEERING, E. mobility. *Elaphe L1500 in-wheel motor*. 2021. Disponível em: <https://www.emobility-engineering.com/elaphe-l1500-in-wheel-motor/>. Citado 2 vezes nas páginas 10 and 42.

EPA-USA. *Sources of Greenhouse Gas Emissions*. 2020. Disponível em: <https://www.epa.gov/ghgemissions/sources-greenhouse-gas-emissions>. Citado na página 27.

F-S, B.; J-M, T. et al. An environmental analysis of fcev and h2-ice vehicles using the ecoscore methodology. *World Electric Vehicle Journal*, Multidisciplinary Digital Publishing Institute, v. 3, n. 3, p. 635–646, 2009. Citado na página 28.

FUKUDA, K.; AKATSU, K. 5-phase double winding pmsm with integrated sic inverter for in-wheel motor. In: IEEE. *2019 22nd International Conference on Electrical Machines and Systems (ICEMS)*. [S.l.], 2019. p. 1–5. Citado 3 vezes nas páginas 34, 46, and 183.

FUNDEP. *Rota 2030 - Linha V – Biocombustíveis, Segurança Veicular e Propulsão Alternativa à Combustão*. 2021. Disponível em: <https://rota2030.fundep.ufmg.br/linha5/>. Citado na página 27.

GABALLAH, M. M. Design and implementation of space vector pwm inverter based on a low cost microcontroller. *Arabian journal for science and engineering*, Springer, v. 38, n. 11, p. 3059–3070, 2013. Citado 2 vezes nas páginas 57 and 133.

GARCIA, M. M. *PWM centered vs. left-aligned mode*. 2019. Disponível em: <https://marcelmg.github.io/pwm_left_vs_centered/>. Citado na página 56.

GEORGE, D. P.; SOKOLOVSKY, P. *Maximising MicroPython speed*. 2022. Disponível em: <https://docs.micropython.org/en/latest/reference/speed_python.html>. Citado na página 132.

GILLESPIE, T. D. *Fundamentals of vehicle dynamics*. [S.l.], 1992. Citado na página 184.

GITLIN, J. M. *Here's the first of Hyundai's new 800-volt EVs—the Ioniq 5*. 2021. Disponível em: <https://arstechnica.com/cars/2021/02/this-crisp-looking-crossover-is-hyundais-next-ev-the-ioniq-5/>. Citado na página 48.

GOOGLE. *Programming Language: Google Trends*. 2022. Disponível em: <https://www.google.com/trends>. Citado 2 vezes nas páginas 10 and 58.

GUO, J.; YE, J.; EMADI, A. Dc-link current and voltage ripple analysis considering antiparallel diode reverse recovery in voltage source inverters. *IEEE Transactions on Power Electronics*, IEEE, v. 33, n. 6, p. 5171–5180, 2017. Citado na página 84.

GUO, S. *How to drive SiC MOSFET.... The right way !!* 2017. Disponível em: <https://training.ti.com/how-drive-sic-mosfet-right-way>. Citado 6 vezes nas páginas 10, 49, 50, 51, 52, and 53.

HADDEN, T. et al. A review of shaft voltages and bearing currents in ev and hev motors. In: IEEE. *IECON 2016-42nd Annual Conference of the IEEE Industrial Electronics Society*. [S.l.], 2016. p. 1578–1583. Citado na página 45.

HASANZAD, F.; RASTEGAR, H.; PICHAN, M. Performance analysis of reduced common-mode voltage space vector modulation techniques for three-phase four-leg voltage-source inverter. In: IEEE. *2018 9th Annual Power Electronics, Drives Systems and Technologies Conference (PEDSTC)*. [S.l.], 2018. p. 65–70. Citado 2 vezes nas páginas 10 and 45.

HAVA, A. M.; KERKMAN, R. J.; LIPO, T. A. Simple analytical and graphical methods for carrier-based pwm-vsi drives. *IEEE transactions on power electronics*, IEEE, v. 14, n. 1, p. 49–61, 1999. Citado na página 57.

HE, N. et al. 20-kw zero-voltage-switching sic-mosfet grid inverter with 300 khz switching frequency. *IEEE Transactions on Power Electronics*, IEEE, v. 34, n. 6, p. 5175–5190, 2018. Citado na página 48.

HELMS, H. et al. Electric vehicle and plug-in hybrid energy efficiency and life cycle emissions. In: CITESEER. *18th International Symposium Transport and Air Pollution, Session*. [S.l.], 2010. v. 3, p. 113. Citado na página 29.

HOLMES, D. G.; LIPO, T. A. *Pulse width modulation for power converters: principles and practice*. [S.l.]: John Wiley & Sons, 2003. v. 18. Citado 2 vezes nas páginas 56 and 57.

HOLTZ, J.; LOTZKAT, W.; KHAMBADKONE, A. M. On continuous control of pwm inverters in the overmodulation range including the six-step mode. *IEEE transactions on power electronics*, IEEE, v. 8, n. 4, p. 546–553, 1993. Citado na página 56.

HU, J.-S. et al. Electric vehicle traction control: a new mtte methodology. *IEEE Industry Applications Magazine*, IEEE, v. 18, n. 2, p. 23–31, 2011. Citado na página 112.

HUBING, T. H.; DOREN, T. P. V.; DREWNIAK, J. L. Identifying and quantifying printed circuit board inductance. In: IEEE. *Proceedings of IEEE Symposium on Electromagnetic Compatibility*. [S.l.], 1994. p. 205–208. Citado na página 86.

HUNT, E. *Choosing FPGA or DSP for your Application*. 2016. Disponível em: <http://hunteng.co.uk/info/fpga-or-dsp.htm>. Citado na página 55.

IEA, I. E. A. *Global EV Outlook 2021*. 2021. Disponível em: <https://www.iea.org/reports/global-ev-outlook-2021>. Citado 4 vezes nas páginas 10, 30, 31, and 32.

IEA, I. E. A. *Net Zero by 2050*. 2021. Disponível em: <https://www.iea.org/reports/net-zero-by-2050>. Citado na página 30.

IPC. Ipc-2221a generic standard on printed board design. IPC, 2003. Citado na página 100.

ITOH, Y.; KAWAUCHI, S. Easy digital control of three-phase pwm convertor. In: IEEE. *[Proceedings] Thirteenth International Telecommunications Energy Conference-INTELEC 91*. [S.l.], 1991. p. 727–734. Citado na página 133.

JENKINS, J. *Why did Porsche go to the trouble of designing an 800 V Taycan EV?* 2019. Disponível em: <https://chargedevs.com/newswire/why-did-porsche-go-to-the-trouble-of-designing-an-800-v-taycan-ev/>. Citado na página 48.

JIN, N.; GAN, C.; GUO, L. Predictive control of bidirectional voltage source converter with reduced current harmonics and flexible power regulation under unbalanced grid. *IEEE Transactions on Energy Conversion*, IEEE, v. 33, n. 3, p. 1118–1131, 2017. Citado na página 44.

JOHNSON, E. *Introduction to Electric Vehicle Battery Systems*. 2019. Disponível em: <https://www.allaboutcircuits.com/technical-articles/introduction-to-electric-vehicle-battery-systems>. Citado na página 48.

JURCA, F. N.; RUBA, M.; MARŢIŞ, C. Design and control of synchronous reluctances motors for electric traction vehicle. In: IEEE. *2016 International Symposium on Power Electronics, Electrical Drives, Automation and Motion (SPEEDAM)*. [S.l.], 2016. p. 1144–1148. Citado na página 112.

JURKOVIC, S. et al. Next generation chevy volt electric machines; design, optimization and control for performance and rare-earth mitigation. In: IEEE. *2015 IEEE Energy Conversion Congress and Exposition (ECCE)*. [S.l.], 2015. p. 5219–5226. Citado na página 57.

KAZMIERKOWSKI, M.; MALESANI, L. Current control techniques for three-phase voltage-source pwm converters: A survey. *Industrial Electronics, IEEE Transactions on*, v. 45, p. 691 – 703, 11 1998. Citado na página 133.

KHALIFA, A.-J. N. Natural convective heat transfer coefficient–a review: I. isolated vertical and horizontal surfaces. *Energy conversion and management*, Elsevier, v. 42, n. 4, p. 491–504, 2001. Citado na página 89.

KIM, T.-H.; EHSANI, M. Sensorless control of the bldc motors from near-zero to high speeds. *IEEE transactions on power electronics*, IEEE, v. 19, n. 6, p. 1635–1645, 2004. Citado na página 113.

KIYOTA, K.; CHIBA, A. Design of switched reluctance motor competitive to 60-kw ipmsm in third-generation hybrid electric vehicle. *IEEE Transactions on Industry Applications*, IEEE, v. 48, n. 6, p. 2303–2309, 2012. Citado na página 67.

KLERK, M. L. D.; SAHA, A. K. A comprehensive review of advanced traction motor control techniques suitable for electric vehicle applications. *IEEE Access*, IEEE, 2021. Citado 2 vezes nas páginas 37 and 113.

KLIMOV, A. *Protean Electric lift motor-wheel to the OEM-Level*. 2021. Disponível em: <https://irim3.com/autonews/drones/protean-electric-podnimet-motor-koleso-do-oem-urovnya/>. Citado 2 vezes nas páginas 10 and 42.

KULKARNI, A.; RANJHA, S. A.; KAPOOR, A. Fatigue analysis of a suspension for an in-wheel electric vehicle. *Engineering Failure Analysis*, Elsevier, v. 68, p. 150–158, 2016. Citado na página 68.

KURZWEIL, P. Gaston planté and his invention of the lead–acid battery—the genesis of the first practical rechargeable battery. *Journal of Power Sources*, Elsevier, v. 195, n. 14, p. 4424–4434, 2010. Citado na página 30.

KWON, T.-S.; SUL, S.-K. Novel antiwindup of a current regulator of a surface-mounted permanent-magnet motor for flux-weakening control. *IEEE Transactions on industry applications*, IEEE, v. 42, n. 5, p. 1293–1300, 2006. Citado na página 121.

LAJUNEN, A.; YANG, Y.; EMADI, A. Recent developments in thermal management of electrified powertrains. *IEEE Transactions on Vehicular Technology*, IEEE, v. 67, n. 12, p. 11486–11499, 2018. Citado na página 44.

LAKKA, M.; KOUTROULIS, E.; DOLLAS, A. Development of an fpga-based spwm generator for high switching frequency dc/ac inverters. *IEEE Transactions on power electronics*, IEEE, v. 29, n. 1, p. 356–365, 2013. Citado na página 55.

LATHAM, A. Common mode field rejection in coreless hall-effect current sensor ics. *Allegro MicroSystems, LLC*, 2019. Citado na página 97.

LI, L.; LIU, Q. Research on ipmsm drive system control technology for electric vehicle energy consumption. *IEEE Access*, IEEE, v. 7, p. 186201–186210, 2019. Citado na página 67.

LIU, P. et al. A survey of the psychological state and neurobehavioral function of traffic policemen. *China Occup Med*, v. 28, p. 7–9, 2001. Citado na página 28.

LOBSIGER, Y.; KOLAR, J. Closed-loop di/dt and dv/dt igbt gate drive concepts. *ECPE Tutorial, Zurich, Power Semiconductor Devices and Technologies*, 2013. Citado na página 54.

LU, C.; DONG, J.; HU, L. Energy-efficient adaptive cruise control for electric connected and autonomous vehicles. *IEEE Intelligent Transportation Systems Magazine*, IEEE, v. 11, n. 3, p. 42–55, 2019. Citado na página 112.

LU, D.; KAR, N. C. A review of flux-weakening control in permanent magnet synchronous machines. In: IEEE. *2010 IEEE Vehicle Power and Propulsion Conference*. [S.l.], 2010. p. 1–6. Citado 3 vezes nas páginas 12, 121, and 122.

MA, C.-T.; GU, Z.-H. Review on driving circuits for wide-bandgap semiconductor switching devices for mid-to high-power applications. *Micromachines*, Multidisciplinary Digital Publishing Institute, v. 12, n. 1, p. 65, 2021. Citado na página 95.

MACHADO, F. A. et al. Multi-speed gearboxes for battery electric vehicles: Current status and future trends. *IEEE Open Journal of Vehicular Technology*, IEEE, v. 2, p. 419–435, 2021. Citado 2 vezes nas páginas 180 and 181.

MALFAIT, A.; REEKMANS, R.; BELMANS, R. Audible noise and losses in variable speed induction motor drives with igbt inverters-influence of the squirrel cage design and the switching frequency. In: IEEE. *Proceedings of 1994 IEEE Industry Applications Society Annual Meeting*. [S.l.], 1994. v. 1, p. 693–700. Citado na página 43.

MANCOSO, K. *Java for Embedded Systems: Advantages and Disadvantages*. 2021. Disponível em: <https://embeddedcomputing.com/technology/software-and-os/ides-application-programming/java-for-embedded-systems-advantages-and-disadvantages>. Citado na página 58.

MCINTOSH, J. *How It Works: Regenerative Braking*. 2021. Disponível em: <https://driving.ca/column/how-it-works/how-it-works-regenerative-braking>. Citado na página 33.

MEHRABADI, N. R. et al. Busbar design for sic-based h-bridge pebb using 1.7 kv, 400 a sic mosfets operating at 100 khz. In: IEEE. *2016 IEEE Energy Conversion Congress and Exposition (ECCE)*. [S.l.], 2016. p. 1–7. Citado na página 48.

MELEXIS. *Melexis Unveils Automotive 200-2000A Current Sensors with integrated overcurrent detection*. 2021. Disponível em: <https://www.melexis.com/en/news/2021/24jun2021-melexis-unveils-automotive-200-2000a-current-sensors-with-integrated-overcurrent-detection>. Citado na página 97.

MOHAN, N. et al. Power electronics: Converters, applications, and design. *J. Wiley*, v. 199, 1995. Citado na página 73.

MORENO, G. et al. Electric-drive vehicle power electronics thermal management: Current status, challenges, and future directions. *Journal of Electronic Packaging*, American Society of Mechanical Engineers Digital Collection, v. 144, n. 1, 2022. Citado na página 44.

MORENO-TORRES, P. et al. Educational project for the teaching of control of electric traction drives. *Energies*, MDPI, v. 8, n. 2, p. 921–938, 2015. Citado na página 112.

NEUDECK, P. G.; OKOJIE, R. S.; CHEN, L.-Y. High-temperature electronics-a role for wide bandgap semiconductors? *Proceedings of the IEEE*, IEEE, v. 90, n. 6, p. 1065–1076, 2002. Citado na página 50.

NHTSA-USA. *2020 Fatality Data Show Increased Traffic Fatalities During Pandemic*. 2021. Disponível em: <https://www.nhtsa.gov/press-releases/2020-fatality-data-show-increased-traffic-fatalities-during-pandemic>. Citado na página 60.

NING, P.; WANG, F.; ZHANG, D. A high density 250ºc junction temperature sic power module development. *IEEE Journal of Emerging and Selected Topics in Power Electronics*, IEEE, v. 2, n. 3, p. 415–424, 2013. Citado na página 50.

NOVOTNY, D. W.; LIPO, T. A. *Vector control and dynamics of AC drives*. [S.l.]: Oxford university press, 1996. v. 41. Citado 2 vezes nas páginas 113 and 114.

PARKER. *GVI Global Vehicle Inverter*. 2021. Disponível em: <https://www.parker.com/Literature/Electromechanical%20Europe/User%20Guides/192_300303_GVI_Configuration_Manual.pdf>. Citado na página 113.

PEI, X.; ZHOU, W.; KANG, Y. Analysis and calculation of dc-link current and voltage ripples for three-phase inverter with unbalanced load. *IEEE Transactions on Power Electronics*, IEEE, v. 30, n. 10, p. 5401–5412, 2014. Citado na página 84.

PENG, F. Z. Z-source inverter. *IEEE Transactions on industry applications*, IEEE, v. 39, n. 2, p. 504–510, 2003. Citado 3 vezes nas páginas 10, 46, and 47.

PEROUTKA, Z.; GLASBERGER, T. Comparison of methods for continuous transition of space vector pwm into six-step mode. In: IEEE. *2006 12th International Power Electronics and Motion Control Conference*. [S.l.], 2006. p. 925–930. Citado na página 73.

PIĄTEK, Z. et al. Inductance of a long two-rectangular busbar single-phase line. *Przegl. Elektrotech*, v. 89, n. 6, p. 290–292, 2013. Citado na página 86.

PLEXIM. *Motor Drive with Failure Modes*. 2022. Disponível em: <https://www.plexim.com/content/motor-drive-failure-modes>. Citado na página 79.

PYE, A. *DTC or FOC - which is better?* 2015. Disponível em: <https://www.controlsdrivesautomation.com/page_624258.asp>. Citado 3 vezes nas páginas 15, 113, and 114.

RASHID, M. H. *Power electronics handbook*. [S.l.]: Butterworth-Heinemann, 2017. Citado 2 vezes nas páginas 10 and 46.

REBER, V. e-power new possibilities with 800-volts charging. *Porsche Engineering magazine*, 2016. Citado na página 48.

REIMERS, J. et al. Automotive traction inverters: Current status and future trends. *IEEE Transactions on Vehicular Technology*, IEEE, v. 68, n. 4, p. 3337–3350, 2019. Citado 5 vezes nas páginas 10, 36, 44, 46, and 54.

ROASTO, I.; VINNIKOV, D.; KLYTTA, M. Emc considerations on pcb design for a high-power converter control system. In: IEEE. *2007 Compatibility in Power Electronics*. [S.l.], 2007. p. 1–4. Citado na página 103.

RODRIGUES, C. G. et al. Projeção da mortalidade e internações hospitalares na rede pública de saúde atribuíveis à poluição atmosférica no estado de são paulo entre 2012 e 2030. *Revista Brasileira de Estudos de População*, Associação Brasileira de Estudos Populacionais, 2015. Citado na página 27.

ROGERS, S. *FY13 annual progress report for the advanced power electronics and electric motors program*. [S.l.], 2013. Citado na página 54.

ROHM. *SCT4018KR N-channel SiC power MOSFET*. 2022. Disponível em: <https://fscdn.rohm.com/en/products/databook/datasheet/discrete/sic/mosfet/sct4018kr-e.pdf>. Citado 2 vezes nas páginas 80 and 141.

ROJAS, A. E. R.; NIEDERKOFLER, H.; WILLBERGER, J. *Comfort and safety enhancement of passenger vehicles with in-wheel motors*. [S.l.], 2010. Citado na página 68.

ROZENBLAT, L. *Calculating spacing between PCB traces for various voltage levels*. 2014. Disponível em: <https://www.smps.us/pcbtracespacing.html>. Citado na página 99.

SAE. *Low Voltage Battery Cable J1127 202012*. 2020. Disponível em: <https://www.sae.org/standards/content/j1127_202012/>. Citado na página 48.

SAE. *Formula SAE Rules*. 2022. Disponível em: <https://fsaeonline.com/cdsweb/gen/DocumentResources.aspx>. Citado 2 vezes nas páginas 100 and 106.

SAWYER, E.; BRUBAKER, M.; HOSKING, T. Understanding the contribution of switch input connection geometry to overall dc link inductance. In: IEEE. *2015 17th European Conference on Power Electronics and Applications (EPE'15 ECCE-Europe)*. [S.l.], 2015. p. 1–8. Citado na página 54.

SCHALKWYK, D. V.; KAMPER, M. Effect of hub motor mass on stability and comfort of electric vehicles. In: IEEE. *2006 IEEE vehicle power and propulsion conference*. [S.l.], 2006. p. 1–6. Citado 2 vezes nas páginas 35 and 67.

SCHONBERGER, J. Modeling a supercapacitor using plecs. *Plexim GmbH, version*, v. 3, 2010. Citado na página 88.

SEO, J. H.; CHOI, H. S. Cogging torque calculation for ipm having single layer based on magnetic circuit model. *IEEE Transactions on Magnetics*, IEEE, v. 50, n. 10, p. 1–4, 2014. Citado na página 64.

SHARAWI, M. S. Practical issues in high speed pcb design. *IEEE Potentials*, IEEE, v. 23, n. 2, p. 24–27, 2004. Citado na página 98.

SHEN, M. et al. Comparison of traditional inverters and z-source inverter for fuel cell vehicles. *IEEE Transactions on power electronics*, IEEE, v. 22, n. 4, p. 1453–1463, 2007. Citado na página 46.

SIDANA, U. *Python vs C: Know what are the differences*. 2021. Disponível em: <https://www.edureka.co/blog/python-vs-c/>. Citado 2 vezes nas páginas 15 and 59.

ST. *AN4544 Application note - IGBT datasheet tutorial*. 2014. Disponível em: <https://www.st.com/resource/en/application_note/dm00122161-igbt-datasheet-tutorial-stmicroelectronics.pdf>. Citado 2 vezes nas páginas 11 and 94.

ST. Automotive galvanically isolated advanced single gate driver. 2018. Citado 3 vezes nas páginas 95, 105, and 106.

ST. Rectifiers thermal management, handling and mounting recommendations. 2018. Citado na página 83.

STATISTICS&DATA. *Programming Language: Google Trends*. 2022. Disponível em: <https://statisticsanddata.org/data/the-most-popular-programming-languages-1965-2021/>. Citado 2 vezes nas páginas 10 and 58.

STMICROELECTRONICS. Overcoming the multi-discipline design challenges behind ev traction inverters. 2021. Citado 2 vezes nas páginas 187 and 188.

SUE, S.-M.; PAN, C.-T. Voltage-constraint-tracking-based field-weakening control of ipm synchronous motor drives. *IEEE Transactions on Industrial Electronics*, IEEE, v. 55, n. 1, p. 340–347, 2008. Citado na página 121.

TDK. *B58033 CeraLink Capacitors for fast-switching semiconductors*. 2022. Disponível em: <https://product.tdk.com/system/files/dam/doc/product/capacitor/ceramic/ceralink/data_sheet/20/10/ds/b58033_sp.pdf>. Citado na página 84.

TEJA, R. *MOSFET as a switch*. 2021. Disponível em: <https://www.electronicshub.org/mosfet-as-a-switch/>. Citado 2 vezes nas páginas 11 and 94.

TOOLBOX, E. *Rolling Resistance*. 2008. Acesso: 2019-05-01. Disponível em: <https://www.engineeringtoolbox.com/rolling-friction-resistance-d_1303.html>. Citado na página 185.

USTUN, O. et al. On field weakening performance of a brushless direct current motor with higher winding inductance: why does design matter? *Energies*, MDPI, v. 11, n. 11, p. 3119, 2018. Citado 2 vezes nas páginas 63 and 64.

VIGHNESWARAN, G.; NAIR, K. S. Speed control of electric vehicle with sliding mode controller. *International Research Journal of Engineering and Technology (IRJET)*, v. 5, n. 05, p. 388–391, 2018. Citado na página 112.

VISHAY, R. Metallized polypropylene film capacitors dc-link capacitor. 2021. Citado na página 88.

VOGELSBERGER, M. A.; WIESINGER, T.; ERTL, H. Life-cycle monitoring and voltage-managing unit for dc-link electrolytic capacitors in pwm converters. *IEEE Transactions on Power Electronics*, IEEE, v. 26, n. 2, p. 493–503, 2010. Citado na página 53.

WAKEFIELD, E. H. *History of the electric automobile-hybrid electric vehicles*. [S.l.: s.n.], 1998. v. 187. Citado na página 30.

WANG, F. et al. Advances in power conversion and drives for shipboard systems. *Proceedings of the IEEE*, IEEE, v. 103, n. 12, p. 2285–2311, 2015. Citado na página 50.

WANG, S. et al. Association of traffic-related air pollution with children's neurobehavioral functions in quanzhou, china. *Environmental health perspectives*, National Institute of Environmental Health Sciences, v. 117, n. 10, p. 1612–1618, 2009. Citado na página 28.

WARD, D. et al. Fundamentals of semiconductors for hybrid-electric powertrain. *Infeneon Technologies North America Corp*, 2013. Citado na página 54.

WEG. Induction motors fed by pwm frequency inverters. WEG, p. 11, 2022. Citado na página 48.

WEN, H. et al. Analysis and evaluation of dc-link capacitors for high-power-density electric vehicle drive systems. *IEEE Transactions on Vehicular Technology*, IEEE, v. 61, n. 7, p. 2950–2964, 2012. Citado na página 53.

WILSON, D. *Teaching Your PI Controller to Behave*. 2015. Disponível em: <https://e2e.ti.com/blogs_/b/industrial_strength/archive/2015/07/20/teaching-your-pi-controller-to-behave-part-i>. Citado 2 vezes nas páginas 116 and 117.

WU, Z.; SU, G.-J. High-performance permanent magnet machine drive for electric vehicle applications using a current source inverter. In: IEEE. *2008 34th Annual Conference of IEEE Industrial Electronics*. [S.l.], 2008. p. 2812–2817. Citado na página 46.

XU, L. et al. A new design concept of permanent magnet machine for flux weakening operation. *IEEE Transactions on Industry Applications*, IEEE, v. 31, n. 2, p. 373–378, 1995. Citado na página 64.

YAN, Q.; YUAN, X. A double-modulation-wave pwm for dead-time-effect elimination and synchronous rectification in sic-device-based high-switching-frequency converters. *IEEE Transactions on Power Electronics*, IEEE, v. 35, n. 12, p. 13500–13513, 2020. Citado 4 vezes nas páginas 12, 128, 129, and 130.

YANG, Y. et al. A fast and accurate thermal-electrical coupled model for sic traction inverter. In: IEEE. *2021 IEEE Transportation Electrification Conference & Expo (ITEC)*. [S.l.], 2021. p. 496–501. Citado na página 82.

YANG, Y.-P.; TING, Y.-Y. Improved angular displacement estimation based on hall-effect sensors for driving a brushless permanent-magnet motor. *IEEE Transactions on Industrial Electronics*, IEEE, v. 61, n. 1, p. 504–511, 2013. Citado na página 64.

YE, X.; FU, H.; GUIDOTTI, T. Environmental exposure and children's health in china. *Archives of environmental & occupational health*, Taylor & Francis, v. 62, n. 2, p. 61–73, 2007. Citado na página 28.

YUAN, Q. et al. An ultra-low frequency modal testing suspension system for high precision air pressure control. *Sensors & Transducers*, Citeseer, v. 170, n. 5, p. 208, 2014. Citado na página 104.

YUN, C.-S. et al. Thermal component model for electrothermal analysis of igbt module systems. *IEEE Transactions on Advanced Packaging*, IEEE, v. 24, n. 3, p. 401–406, 2001. Citado na página 83.

ZAH, R. et al. Life cycle assessment of energy products: environmental impact assessment of biofuels. 2007. Citado na página 28.

ZENG, Z. et al. Stepwise design methodology and heterogeneous integration routine of air-cooled sic inverter for electric vehicle. *IEEE transactions on power electronics*, IEEE, v. 35, n. 4, p. 3973–3988, 2019. Citado 6 vezes nas páginas 10, 39, 43, 51, 52, and 53.

ZHANG, H.; TOLBERT, L. M.; OZPINECI, B. Impact of sic devices on hybrid electric and plug-in hybrid electric vehicles. *IEEE transactions on industry applications*, IEEE, v. 47, n. 2, p. 912–921, 2010. Citado na página 50.

ZHANG, R. et al. Advanced emergency braking control based on a nonlinear model predictive algorithm for intelligent vehicles. *Applied sciences*, MDPI, v. 7, n. 5, p. 504, 2017. Citado 2 vezes nas páginas 13 and 180.

ZHANG, Y. et al. Design and flux-weakening control of an interior permanent magnet synchronous motor for electric vehicles. *IEEE Transactions on Applied Superconductivity*, IEEE, v. 26, n. 7, p. 1–6, 2016. Citado na página 64.

ZHU, Z. Q. et al. A mechanical flux weakening method for switched flux permanent magnet machines. *IEEE Transactions on Energy Conversion*, IEEE, v. 30, n. 2, p. 806–815, 2014. Citado na página 121.

Appendix

APPENDIX A – Vehicle topology

The popularization of electric mobility is a recent issue in a market previously completely dominated by ICEVs. Thus, it was decided in this work to start the explanation about the topology solutions in electric traction, starting with the ICEV itself, then demonstrating some step-by-step changes and other possibilities made feasible with this emerging technology.

An ICEV is defined as a vehicle driven by a pure internal combustion solution, be it through fossil fuels such as Diesel and gasoline, or biofuels such as ethanol and biodiesel. Figure 107 demonstrates a schematic for such a vehicle.

Figure 107 – Topology of an ICEV. From left to right: fuel tank, engine, clutch/torque converter, multispeed gearbox, differential.

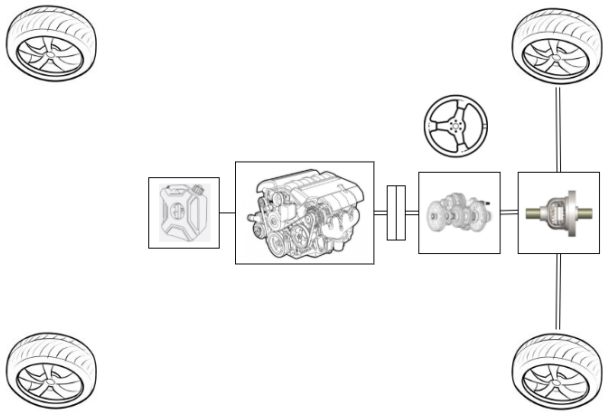

The topology of an ICEV does not present much variability, eventually varying between front and rear wheel drive, but not bringing to the market many relevant solutions with different major topology changes. This is also due to the volume of a combustion engine required to drive a vehicle, even if it is a small-passenger car, usually the engine occupies the entire front or rear space. However, when it comes to electric traction, the situation is different. The greater power density of electric motors opens up various arrangement possibilities, even including multiple motors, generating a huge range of powertrain topologies that are viable and present on the market.

Figure 108 shows a possible simple beginning of a transition from a ICEV to an BEV. It is generally used in Retrofits (conversion).

This solution is usually not the most suitable, since some of the components present in an ICEV are not needed in a BEV. The first to be removed tend to be the multispeed gearbox and clutch/torque converter. The discussion about this is multivariable and extensive, but it is possible to briefly discuss it. The multispeed gearbox is present in ICEVs for two basic reasons:

1. Resumption of torque at higher revs

Figure 108 – Common topology for an ICEV converted to an BEV. From left to right: accumulator, inverter, motor, clutch/torque converter, multispeed gearbox, differential.

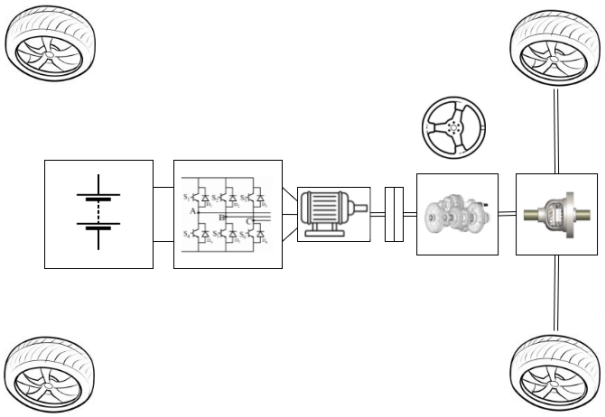

2. Higher speed range

Figure 109 visually points out its necessity, using a torque x speed graph. It is shown that its presence exists exactly in order to approximate an ICE performance to the torque curve characteristics of an electric motor electronically controlled. This analysis indicates that for an electric motor that has constant power in a long speed range, a fixed gearing can replace the multispeed gearbox and reduce the need for a clutch/torque converter. Although, there is still a technological debate about it. Machado et al. (2021) points out that multispeed gearboxes have several potential benefits for BEVs, including enabling the electric traction machine and inverter to operate in a more efficient region, increasing vehicle acceleration, gradeability, and top speed, and reducing overall traction system mass and volume. The autor also there are just two electrified vehicles currently being manufactured, which have more than one gear ratio, the BMW i8 and Porsche Taycan, both using a two-speed gearbox with the aim of improving acceleration and top speed rather than efficiency. Moreover, electric vehicles that have undersized power for their application can indeed increase their maximum speed with the use of multispeed gearboxes, so that designers tend to return to this discussion in some cases.

Figure 109 – Comparison between torque x speed curve of an ICEV with gearbox and a BEV without gearbox (ZHANG et al., 2017)

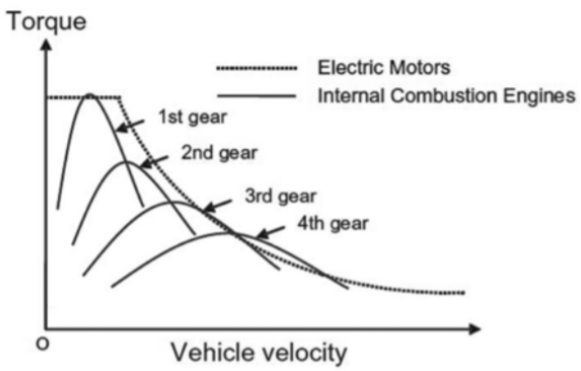

As for the clutch/torque converter, are the component that disconnects the motor from the drive shaft. It is also present in ICEV's for two basic reasons:

1. To allow the combustion engine to maintain a minimum rotational speed, avoiding the need to restart it after the vehicle is stopped;
2. Facilitate the gear shifting process.

The first reason is not applicable to BEVs, since electric motors do not have a minimum speed to operate. The second reason depends on the presence of the multispeed gearbox, which was previously discussed. Finally, considering all these factors, BEVs usually arrive on the market without a clutch/torque converter and without a multispeed gearbox (MACHADO et al., 2021), see Figure 4.

Another solution very present on the market is to position the motors, single-speed gearbox and differential in parallel to the wheel shafts, optimizing the packaging, see Figure 110. This step, so to speak, is already a specific technology for BEVs, since generally the volume of a combustion engine makes this configuration unfeasible.

Figure 110 – Topology of BEV, with motorization, single-speed gearbox and differential parallel to the wheel shafts

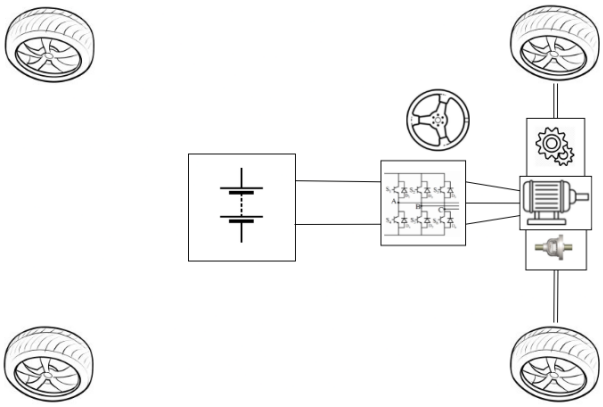

Next, multiple motors can be used, such as the dual-drive solution shown in Figure 111. With two inverters, two motors and two single-speed gearboxes present, the differential is no longer necessary. The differential effect is implemented electronically, initially sending the same torque reference to both wheels, and then allowing for high-level vehicle dynamics optimizations. The cost analysis of this solution is also multivariable and non-trivial, since the cost tends to be higher due to multiple traction components, but at the same time each component can be sized with less power. The differential is also a mechanically complex system, with considerable cost, and will weight in this design decision.

With the possibility of multiple motorization, the in-wheel solution is also made possible. The motors do not necessarily need to be attached to the chassis IBM (In-Board Motors), but

Figure 111 – BEV topology, with front twin motor. Mechanical differential removed, electronic differential implemented.

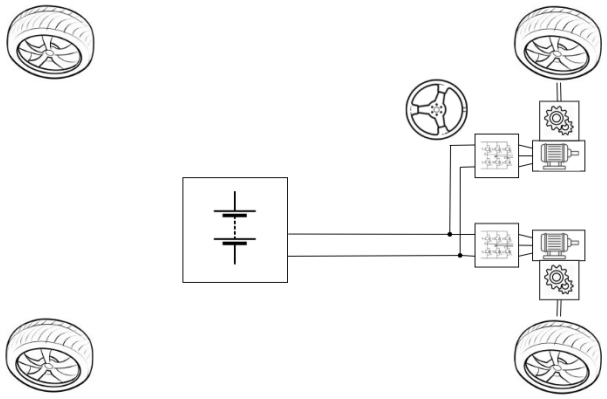

can be inserted directly inside the wheels. In this configuration they are called IWM (In-Wheel Motors), also known as Hub Motors or Wheel-Hub Motors, see Figure 112. In this case, the motors are already designed specifically for the application, and can be implemented without gearbox, with the designers operating on the number of poles of the machine to adjust its rotation to the wheel. Again, one less component, resulting in greater system efficiency.

Figure 112 – BEV topology, with dual front in-wheel motorization

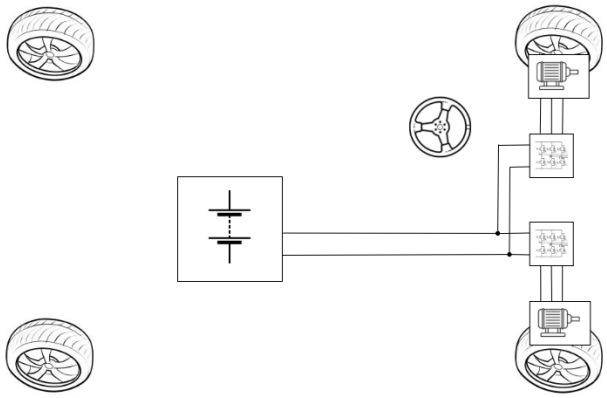

IWM solutions, like IBM solutions, can be applied for AWD (all-wheel drive), using either 3 or 4 motors, see Figure 113. It's also known as 4WD (four wheel drive) and informally called "4x4", but this last designation creates confusion with block differentials ICEV solutions, very common in off-roads.

Finally, the topology proposed in this work goes one step further: the inverters are attached to the motors, and the entire assembly is inserted into the wheels, see Figure 114.

In the proposal of this work to use the converter integrated to the in-wheel electric machine, there are the following advantages:

- Reducing the length of the electrical connection between inverter and motor;

Figure 113 – BEV topology, with AWD-IWM motorization

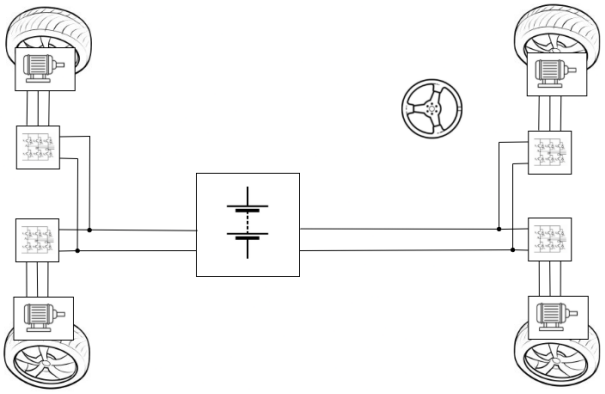

Figure 114 – Topology of this work: BEV with AWD-IWM motorization and in-wheel inverters.

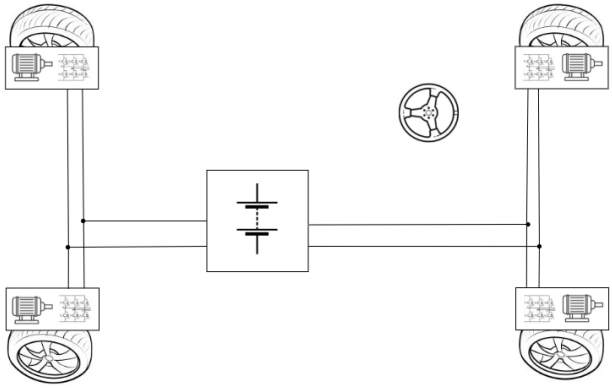

- Reduction of Joule losses in the electrical connection between inverter and motor (FUKUDA; AKATSU, 2019);
- Need to bring only 2 power cables to the wheel (positive and negative of the accumulator), instead of three cables (the three phases of the electric machine);
- Reduction of mass and volume of the motor-inverter set, due to shared use of housing;
- Release of internal space in the vehicle, enabling BEVs size reduction, or facilitating ICEVs hybridization processes.

APPENDIX B – Longitudinal Performance Model

This appendix includes basic equations used to model longitudinal vehicle performance under acceleration for the purpose of gathering parameters for this Project. Extensive documentation on this type of model can be found in the work of Gillespie (1992).

The algorithm developed for modeling and performance analysis is limited to longitudinal effects, disregards track elevation, considers fixed system efficiency and brings the simplification of all mass concentrated in the CG, similar to the force diagram in Figure 115 (with zero inclination angle of the track). On the other hand, the algorithm achieves notoriety for being temporal and including an iterative process for load transfer and acceleration convergence, considering tire-ground friction limits, power limitation, maximum speed and maximum available torque. The algorithm is shown in Figure 116.

Figure 115 – Force diagram of a vehicle

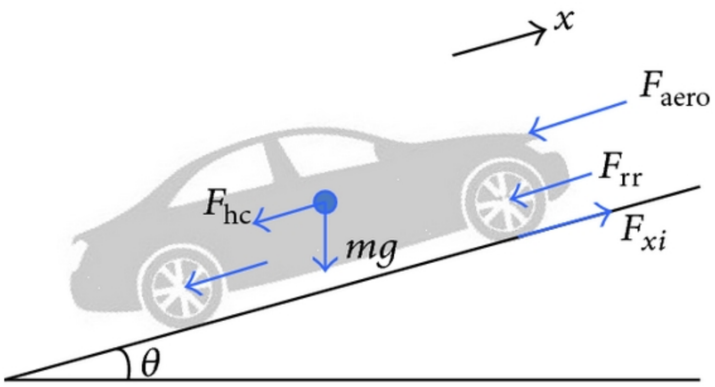

With this procedure we can easily visualize a series of relevant quantities in relation to the time variable, from simpler variables such as traction force, power, and speed, to more complex ones such as rear and front power ratio, aerodynamic resistance, rolling resistance, among others. The following are basic equations.

- General traction equation:

$$F_{tr} - F_{aero} - F_{roll} - F_{inertia} = m \times a \tag{B.1}$$

where m is the mass of the vehicle with pilot (kg), a is the acceleration, F_{tr} is the traction force, F_{aero} is the aerodynamic drag force, F_{roll} is the rolling resistance force and $F_{inertia}$ is the force related to the polar moment of inertia of the rotating assembly

Figure 116 – Longitudinal performance model algorithm

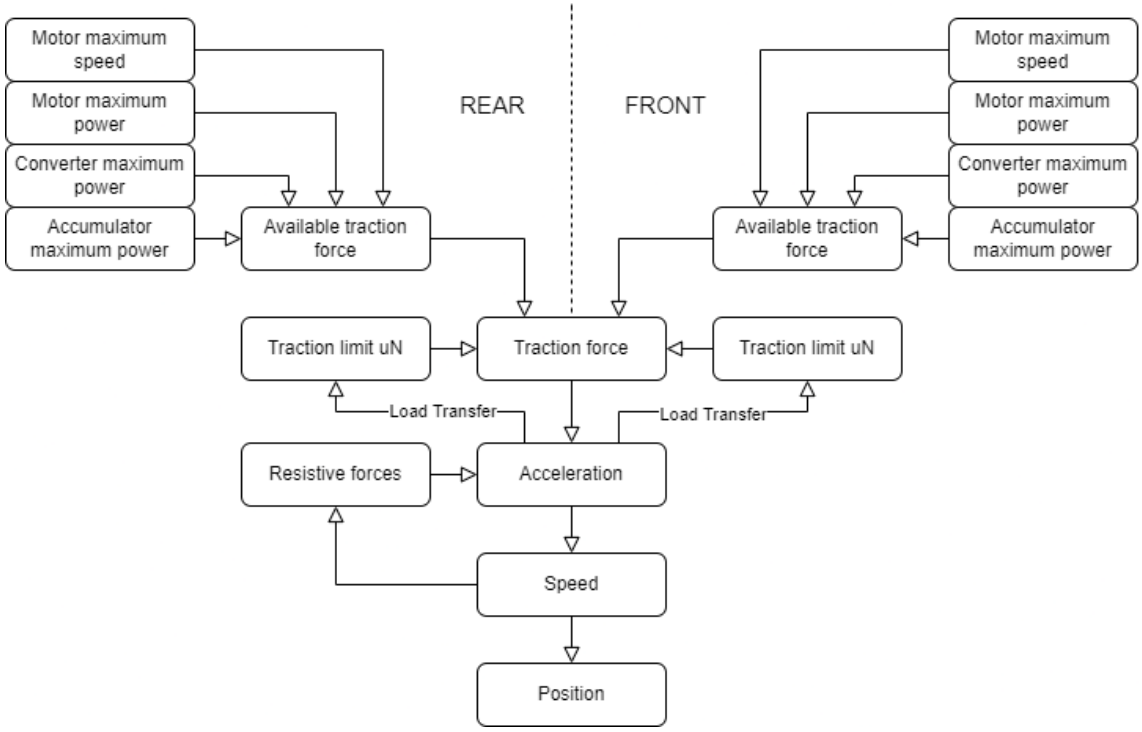

- Aerodynamic drag force:

$$F_{roll} = 0,5 \times c_d \times A \times \rho \times v^2 \tag{B.2}$$

where c_d is the drag coefficient, A is the frontal area (m^2), ρ is the air density (kg/m^3) and v is the velocity (m/s).

- Rolling resistance force:

$$F_{roll} = m \times g^* \times \{0.005 + \frac{1}{p} \times [0,01 + 0.0095 \times (\frac{v_{kph}}{100})^2]\} \tag{B.3}$$

where the term in brackets is the rolling coefficient, g^* is the gravity acceleration (m/s^2), p is the tire pressure (bar), v_{kph} is the speed (km/h). (TOOLBOX, 2008)

- Force related to the polar moment of inertia of the rotating assembly:

$$F_{inertia} = 4 \times \frac{J \times a}{r_{din}^2} \tag{B.4}$$

where J is simplified by the polar moment of inertia of the wheel-set, a is the acceleration of the vehicle (m/s^2) and r_{din} is the dynamic radius of the tire.

- Load transfer force:

$$F_{load} = m \times a \times \frac{h_{cg}}{wb} \tag{B.5}$$

where h_{cg} is the height of the center of gravity (m) and wb is the wheelbase (m).

The reliability of the model depends on a number of variables and considerations. Among them is the coefficient of tire-soil friction (μ), which together with the normal on the tire defines the traction limit (μN). Obtaining a value for this coefficient is one of the biggest challenges. Although its estimation is relevant, it is an extremely complex process, since it depends on a number of factors such as tire pressure, temperature, soil condition (debris, moisture) and even the normal force on the tire itself. General relationships for common applications can be found in the literature, such as the one in Figure 117. The dependence of μ with the *slip ratio* is ignored in the model, considering TCS application.

Figure 117 – Tire-soil friction coefficients in relation to slip ratio, considering common application for different soil types (BERA; BHATTACHARYA; SAMANTARAY, 2011)

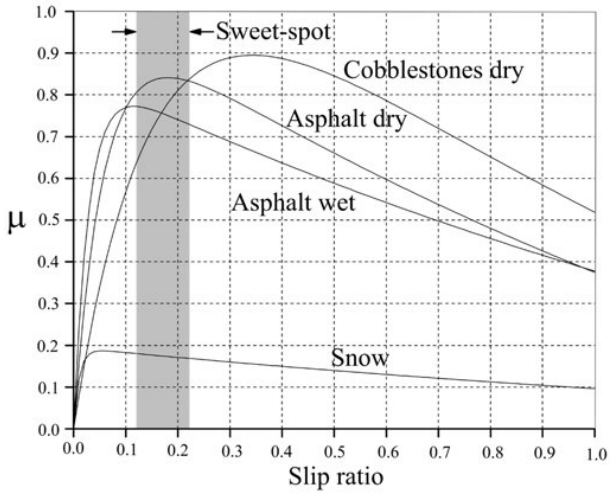

It is important to note that a number of variables need to be evaluated separately in the rear and the front. Examples are the traction force, the normal force, the limits of motor power and speed, the reduction ratio, and others.

APPENDIX C – Power Switches Packaging

This appendix includes information of packaging for power switches. There are also a number of possibilities. To list a few:

- HiP247;
- TO-247;
- ACEPACK SMIT;
- ACEPACK DRIVE;
- STPAK;
- PowerFLAT;
- Bare Die;
- H2PAK-7;
- D3PAK-3 (or TO-268).

The HiP247 and HiP247 long-lead, are very common packages used in different types of transistors. They allow vertical mounting and attachment to a metal frame for cooling, see Figure 118. They have a similar geometry to the TO-247. The vertical installation of these components is not well suited for the in-wheel, small-space application.

Figure 118 – HiP247 package

The ACEPACK SMIT features surface mount with top cooling, providing high electrical insulation (2500 VRMS) and low thermal resistance, see Figure 119 (STMICROELECTRONICS, 2021). Conceptually it is a viable solution, but as the cooling geometry planned in this Project is on the face directed to the electrical machine, the installation of this component would have

Figure 119 – ACEPACK SMIT packaging

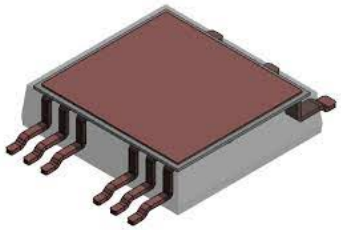

to be directed to the other face of the PCB, generating unnecessary complications in its design. Thus, this was not the selected option.

ACEPACK DRIVE is a power module optimized for hybrid and electric vehicles and traction applications in a power range from 100 to 300 kW, see Figure 120 (STMICROELECTRONICS, 2021). While the solution is interesting in simplifying assembly, the power range is not suitable and no module found met the volumetric and geometric needs of the in-wheel application in question.

Figure 120 – ACEPACK DRIVE packaging

The STPAK package is the solution used in the Model 3 inverters from Tesla Motors. The solution with the presence of contact buses and bottom cooling, with perpendicular output of the gate contacts, proves to be a valid option for simple and efficient assembly, see Figure 121.

Figure 121 – STPAK packaging

PowerFLAT is a viable encapsulation for small volume applications, featuring low thickness and very small pin sizes, see Figure 122. The solutions known as "Bare Die" are conceptually similar to this.

Figure 122 – PowerFLAT packaging

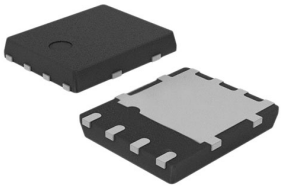

The H2PAK-7 and D3PAK-3 packages, as well as the HiP247, are common solutions, easily available in the market. However, they have curved contacts, designed for direct horizontal PCB application, and are better suited to the needs of this Project than the HiP247, see Figure 123. The shape of the pins allows easy access for soldering.

Figure 123 – D3PAK-3 packaging

Finally, initial analysis has shown that for this Project, feasibility exists in STPAK, PowerFLAT, Bare Die, H2PAK-7, D3PAK-3 and similar solutions.

APPENDIX D – Micropython code

This appendix includes the python code for the converter. The code is subdivided in the following sections, for better understanding:

- Classical SVPWM function;
- SVPWM carried-based function;
- Current control function;
- Flux weakening control function;
- Speed control function.

D.1 Classical SVPWM function code

Listing D.1 – SVPWM python code

```
# SVPWM:
Vdc = 600
svpwm_multiplier = (T_sw/Vdc)*1.732050808
#multiplier = (T_sw/Vdc)*1.5/ad_minus_bc, ad_minus_bc always =
    0.86602540378
#ad_minus_bc = math.cos(alpha1)*math.sin(alpha2)-math.cos(alpha2)*math.sin(
    alpha1)
@micropython.native
def svpwm(Vd, Vq, theta):

    global T_sw
    global svpwm_multiplier
    # Preload methods
    sin_f = math.sin
    cos_f = math.cos
    # Dq0 to alpha beta
    #Valpha = math.cos(theta)*Vd-math.sin(theta)*Vq
    #Vbeta = math.sin(theta)*Vd+math.cos(theta)*Vq
    Valpha = cos_f(theta)*Vd-sin_f(theta)*Vq
    Vbeta = sin_f(theta)*Vd+cos_f(theta)*Vq
    # Space vector module and angle
    V_modulus = math.sqrt(Valpha*Valpha+Vbeta*Vbeta)
    if V_modulus == 0:
        alpha = 0
    else:
```

```
24          alpha = math.acos(abs(Valpha)/V_modulus)
25      if Valpha<0 and Vbeta>0:
26          alpha = 3.14159265359-alpha
27      elif Valpha<0 and Vbeta<0:
28          alpha = 3.14159265359+alpha
29      elif Valpha>0 and Vbeta<0:
30          alpha = 6.28318530718-alpha
31      # Set which sector
32      if alpha>=0 and alpha<1.0471975512: # alpha1 = 0 alpha2 = pi/3
33          sector = 1
34          sin_alpha1 = 0
35          cos_alpha1 = 1
36          sin_alpha2 = 0.86602540378
37          cos_alpha2 = 0.5
38      elif alpha>=1.0471975512 and alpha<2.09439510239: # alpha1 = pi/3,
            alpha2 = 2*pi/3#
39          sector = 2
40          sin_alpha1 = 0.86602540378
41          cos_alpha1 = 0.5
42          sin_alpha2 = 0.86602540378
43          cos_alpha2 = -0.5
44      elif alpha>=2.09439510239 and alpha<3.14159265359: # alpha1 = 2*pi/3,
            alpha2 = pi
45          sector = 3
46          sin_alpha1 = 0.86602540378
47          cos_alpha1 = -0.5
48          sin_alpha2 = 0
49          cos_alpha2 = -1
50      elif alpha>=3.14159265359 and alpha<4.18879020479: # alpha1 = pi,
            alpha2 = 4*pi/3
51          sector = 4
52          sin_alpha1 = 0
53          cos_alpha1 = -1
54          sin_alpha2 = -0.86602540378
55          cos_alpha2 = -0.5
56      elif alpha>=4.18879020479 and alpha<5.23598775598:#(5*math.pi/3)
57          sector = 5
58          sin_alpha1 = -0.86602540378
59          cos_alpha1 = -0.5
60          sin_alpha2 = -0.86602540378
61          cos_alpha2 = 0.5
62      else: #alpha>=5.23598775598 and alpha<6.28318530718:#(2*math.pi)
63          sector = 6
64          sin_alpha1 = -0.86602540378
65          cos_alpha1 = 0.5
66          sin_alpha2 = 0
67          cos_alpha2 = 1
```

```
68      # Equations for times
69      T1 = svpwm_multiplier*(sin_alpha2*Valpha-cos_alpha2*Vbeta)
70      T2 = svpwm_multiplier*(-sin_alpha1*Valpha+cos_alpha1*Vbeta)
71      T0 = T_sw-T1-T2
72      T0_over_2 = T0*0.5
73      # Conditions for guaranteed minimum switching
74      # Ref: Mahmoud M. Gaballah, Design and Implementation of...
75      if sector == 1:
76          t_A = T0_over_2
77          t_B = T1+T0_over_2
78          t_C = T1+T2+T0_over_2 #ou T_sw-(T0/2)
79      elif sector == 2:
80          t_A = T2+T0_over_2
81          t_B = T0_over_2
82          t_C = T1+T2+T0_over_2
83      elif sector == 3:
84          t_A = T1+T2+T0_over_2
85          t_B = T0_over_2
86          t_C = T1+T0_over_2
87      elif sector == 4:
88          t_A = T1+T2+T0_over_2
89          t_B = T2+T0_over_2
90          t_C = T0_over_2
91      elif sector == 5:
92          t_A = T1+T0_over_2
93          t_B = T1+T2+T0_over_2
94          t_C = T0_over_2
95      else: #sector == 6
96          t_A = T0_over_2
97          t_B = T1+T2+T0_over_2
98          t_C = T2+T0_over_2
99      # Return times
100     return [t_A, t_B, t_C]
```

D.2 Double-wave modulation SVPWM carrier-based function code

Listing D.2 – Double-wave modulation SVPWM carrier-based control python code

```
1  t_d = 0.3e-6 # Dead time (s)
2  delta_u = 4*t_d*f_sw
3  def svpwm(Van_ref_pu, Vbn_ref_pu, Vcn_ref_pu, sign_Ia_pos, sign_Ib_pos,
       sign_Ic_pos):
4      global delta_u
5      if abs(Van_ref_pu)<=abs(Vbn_ref_pu) & abs(Van_ref_pu)<=abs(Vcn_ref_pu):
6          Vno_ref_pu = 0.5*Van_ref_pu
```

```
    elif abs(Vbn_ref_pu)<=abs(Van_ref_pu) & abs(Vbn_ref_pu)<=abs(Vcn_ref_pu
        ):
        Vno_ref_pu = 0.5*Vbn_ref_pu
    else:
        Vno_ref_pu = 0.5*Vcn_ref_pu
    # Set values:
    Vao_ref_svpwm_pu = Van_ref_pu+Vno_ref_pu
    Vbo_ref_svpwm_pu = Vbn_ref_pu+Vno_ref_pu
    Vco_ref_svpwm_pu = Vcn_ref_pu+Vno_ref_pu
    # Paper method:
    if sign_Ia_pos == True:
        Vao_ref_svpwm_pu_paper = Vao_ref_svpwm_pu+delta_u
        duty_A_upp = Vao_ref_svpwm_pu
        duty_A_low = Vao_ref_svpwm_pu_paper
    else:
        Vao_ref_svpwm_pu_paper = Vao_ref_svpwm_pu-delta_u
        duty_A_upp = Vao_ref_svpwm_pu_paper
        duty_A_low = Vao_ref_svpwm_pu
    if sign_Ib_pos == True:
        Vbo_ref_svpwm_pu_paper = Vbo_ref_svpwm_pu+delta_u
        duty_B_upp = Vbo_ref_svpwm_pu
        duty_B_low = Vbo_ref_svpwm_pu_paper
    else:
        Vbo_ref_svpwm_pu_paper = Vbo_ref_svpwm_pu-delta_u
        duty_B_upp = Vbo_ref_svpwm_pu_paper
        duty_B_low = Vbo_ref_svpwm_pu
    if sign_Ic_pos == True:
        Vco_ref_svpwm_pu_paper = Vco_ref_svpwm_pu+delta_u
        duty_C_upp = Vco_ref_svpwm_pu
        duty_C_low = Vco_ref_svpwm_pu_paper
    else:
        Vco_ref_svpwm_pu_paper = Vco_ref_svpwm_pu-delta_u
        duty_C_upp = Vco_ref_svpwm_pu_paper
        duty_C_low = Vco_ref_svpwm_pu
```

D.3 Current control function code

Listing D.3 – Current control python code

```
Kp_id = 0
Ki_id = 0
Kp_iq = 0
Ki_iq = 0
integ_id = 0
integ_iq = 0
def current_control(id_meas,iq_meas,id_ref,iq_ref,id_ref_anterior,
    iq_ref_anterior,f_samp_id_ref,f_samp_iq_ref,w_r):
```

```
8       global Kp_id
9       global Ki_id
10      global Kp_iq
11      global Ki_iq
12      global integ_id
13      global integ_iq
14      global Lambda_mag
15      global Ld
16      global Lq
17      global Rs
18      global T_current_control
19      global one_over_Vdc
20      # Error:
21      id_error = id_ref-id_meas
22      iq_error = iq_ref-iq_meas
23      # Integration:
24      integ_id = integ_id+(Kp_id*Ki_id*id_error)*T_current_control
25      integ_iq = integ_iq+(Kp_id*Ki_iq*iq_error)*T_current_control
26      # Derivation:
27      #deriv_id_ref = (id_ref-id_ref_ant)*f_current_control
28      #deriv_iq_ref = (iq_ref-iq_ref_ant)*f_current_control
29      # Controller:
30      Vd_ref = (Kp_id*id_error+integ_id)-(Lq*iq_meas*wr)+(id_meas*Rs)#+(Ld*
            deriv_id_ref)
31      Vq_ref = (wr*Lambda_mag)+(Kp_iq*iq_error+integ_iq)+(Ld*id_meas*wr)+(
            iq_meas*Rs)#+(Lq_est*deriv_iq_ref)
```

D.4 Flux weakening control function code

Listing D.4 – Flux weakening control python code

```
1  def flux_weak(w_motor, Te_speed_control):
2      global rpm_nom
3      global Ld
4      global Lq
5      global Imax
6      global Vmax
7      global Lambda_mag
8      global pole_pairs
9      global T_const
10     global id_max_speed
11     if w_motor > (94.7387): # rpm_nom*pi/30 = 94.7387
12         Pnom = 36000
13         Tmax = Pnom/w_motor
14         if Te_speed_control>Tmax:
15             Te_speed_control=Tmax
```

```
16              id_ref = id_max_speed*(0.0105553479)*w_motor-id_max_speed # 1/(
                    rpm_nom*pi/30) = 0.0105553479
17              iq_ref = sqrt(Imax^2-id_ref^2)
18              Te = (1.5)*pole_pairs*iq_ref*(Lambda_mag+id_ref*(-0.000119)) #
                    Ld-Lq = -0.000119
19          if Te_speed_control<Te:
20              Te = Te_speed_control
21          iq_ref = Te/( (1.5)*pole_pairs*(Lambda_mag+id_ref*(-0.000119)) ) #
                Ld-Lq = -0.000119
22      else:
23          id_ref = 0
24          iq_ref = Te_speed_control*(0.225880839) # 1/T_const = 0.225880839
25      return [id_ref,iq_ref]
```

D.5 Speed control function code

Listing D.5 – Speed control python code

```
1  def speed_control(w_meas,w_ref):
2      global J
3      global b
4      global Kp_w
5      global Ki_w
6      global integ_w
7      global T_speed_control
8      # Error:
9      w_error = w_ref-w_meas
10     # Integration:
11     integ_w = integ_w+(Kp_w*Ki_w*w_error)*T_speed_control
12     # Derivation:
13     #deriv_w_ref = (w_ref-w_ref_ant)*f_speed_control
14     # Controller:
15     Te_ref = (Kp_w*w_error+integ_w)+(w_meas*b)#+(J*deriv_w_ref)
16     return(Te_ref)
```